



New luminescent hybrid materials: synthesis and properties

Youssef Atoini

► To cite this version:

Youssef Atoini. New luminescent hybrid materials: synthesis and properties. Other. Université de Strasbourg, 2017. English. NNT: 2017STRAF004 . tel-01624485

HAL Id: tel-01624485

<https://theses.hal.science/tel-01624485>

Submitted on 26 Oct 2017

HAL is a multi-disciplinary open access archive for the deposit and dissemination of scientific research documents, whether they are published or not. The documents may come from teaching and research institutions in France or abroad, or from public or private research centers.

L'archive ouverte pluridisciplinaire **HAL**, est destinée au dépôt et à la diffusion de documents scientifiques de niveau recherche, publiés ou non, émanant des établissements d'enseignement et de recherche français ou étrangers, des laboratoires publics ou privés.

ÉCOLE DOCTORALE DES SCIENCES CHIMIQUES

Institut de Science et d'Ingénierie Supramoléculaires (ISIS)

THÈSE présentée par :

Youssef ATOINI

soutenue le : **25 janvier 2017**

pour obtenir le grade de : **Docteur de l'université de Strasbourg**

Discipline/ Spécialité : **CHIMIE**

**Nouveaux matériaux hybrides
luminescents : synthèse et propriétés**

THÈSE dirigée par :

Mme DE COLA Luisa

Professeur, université de Strasbourg

RAPPORTEURS :

Mr BASSANI Dario

Docteur, université de Bordeaux

Mr MARTIN LEON Nazario

Professeur, universidad Complutense de Madrid

AUTRES MEMBRES DU JURY :

Mr WEISS Jean

Docteur, université de Strasbourg

Mme DE COLA Luisa

Professeur, université de Strasbourg

Nouveaux matériaux hybrides luminescents : synthèse et propriétés

Résumé

L'objectif de cette thèse est la synthèse, la caractérisation et l'étude de complexes métalliques luminescents, en particulier de Pt (II), leurs propriétés d'agrégation en solution, mais également dans un espace confiné ainsi qu'en surface. L'incorporation de complexes de métaux de transition dans la structure poreuse, et ainsi que leur dépôt à la surface de nanoparticules et dans un cadre métallo-organique (MOF), par greffage post-synthétique, ont été étudiés. Sont également étudiés la corrélation entre les propriétés de films d'une série de complexes de Pt(II) avec leur morphologie, leur mobilité électronique et la simulation de leur structure auto-assemblée par diffraction aux rayons-X. Les propriétés de luminescence de complexes amphiphiles de Pt(II) sont améliorées à l'intérieur de nanoparticules de silice mesoporeuse par la création d'un d'espace confiné. Un effet similaire est observé par le dépôt de complexes de Pt(II) fonctionnalisés sur une surface de nanoparticules d'or. La luminescence d'un cadre organométallique a été modifiée par greffage post-synthétique de complexes d'Ir(III) et de Pt(II).

Mots-clés : complexes de Pt(II), auto-assemblage, luminescence, nanoparticules de silice mesoporeuse, nanoparticules d'or, cadre organométallique

Résumé en anglais

The aim of this thesis is the synthesis, characterization and investigation of luminescent metal complexes, and in particular of Pt(II) compounds, their aggregation properties in solution but in confined space as well. The incorporation of transition metal complexes in porous structure, and in particular in a metal-organic framework (MOF), by post-synthesis grafting, have been investigated. Luminescence properties of amphiphilic Pt(II) complexes were enhanced inside mesoporous silica nanoparticles by the creation of a confined space. Similar effect is observed by deposition of functionalized Pt(II) complexes on gold nanoparticles surface. Luminescence of metal organic framework was tuned by post-synthetic grafting of Ir(III) and Pt(II) complexes.

Keywords: Pt(II) complexes, self-assembly, luminescence, mesoporous silica nanoparticles, gold nanoparticles, metal organic framework

Table of Contents

Résumé de Thèse.....	3
Summary of the Thesis.....	20
CHAPTER 1: General Introduction	37
1.1. Introduction on photophysics and photochemistry	38
1.2. Introduction to transition metal complexes	42
1.3. Introduction on platinum complexes and their assemblies.....	45
1.4. Introduction to self-assembly	48
1.5. Introduction on mesoporous silica nanoparticles	50
1.6. Introduction to gold nanoparticles	53
1.7. Introduction to metal organic frameworks.....	56
1.8. Aim of the thesis.....	58
1.9. References	61
CHAPTER 2: Cationic Pt(II) Complexes and their Assemblies.....	69
2.1. Introduction	70
2.2. Results and discussion	72
2.3. Conclusion.....	84
2.4. Experimental section	85
2.4.1. Materials and methods.....	85
2.4.2 Photophysical measurements	85
2.4.3. Synthetic procedures.....	86
2.5. References	97
CHAPTER 3: Hybrid Pt(II) Complexes-Silica Nanoparticles Materials: Synthesis and Properties.....	99
3.1. Introduction	100
3.2. Results and discussion	101
3.3. Conclusion.....	115
3.4. Experimental procedure.....	115
3.4.1. Materials and methods.....	115
3.4.2. Synthesis of 1a-d and 2a-d	116
3.4.3. Synthesis of 1e and 2e	117
3.5. References	117
CHAPTER 4: Self-Assembly of Pt(II) on Gold Nanoparticles for Surface Enhanced Photoluminescence	119
4.1. Introduction	120
4.2. Results and discussion	122
4.3. Conclusion.....	130
4.4. Experimental section	130
4.4.1. Materials and methods.....	130
4.4.2. Synthetic procedures.....	132
4.5. References	139

CHAPTER 5: Pt(II) Complexes: Photophysical Properties, Packing mode and Electronic Mobility.....	141
5.1. Introduction	142
5.2. Results and discussion	143
5.3. Conclusions	161
5.4. Powder X-ray diffraction: basics and data treatment	161
5.5. Experimental Section	164
5.5.1 Materials and methods.....	164
5.5.2 Photophysical measurements	165
5.5.3 Scanning electron microscopy.....	165
5.5.4. Powder X-ray diffraction.....	166
5.5.5. Synthetic procedures.....	166
5.6. References	167
CHAPTER 6: Tuning Luminescent Properties of Metal-Organic Framework by Metal Complex Inclusion.....	169
6.1. Introduction	170
6.2. Results and Discussion	173
6.3. Conclusion.....	189
6.4. Experimental section	189
6.4.1. Materials and methods.....	189
6.4.2. Synthesis of MOF-253.....	191
6.4.3. Synthesis of Ir(III) precursors	191
6.4.4. Procedure for metal inclusion inside MOF-253.....	197
6.5. References	197
CHAPTER 7: Instrumental Techniques.....	201
7.1. Nuclear Magnetic Resonance (NMR)	202
7.2. Electrospray Ionization-Mass Spectrometry (ESI-MS)	203
7.3. UV-Visible absorption spectroscopy (UV).....	205
7.4. Steady-state emission spectroscopy	206
7.5. Absolute photoluminescence quantum yield	207
7.6. Time-resolved emission spectroscopy	208
7.7. X-ray photoelectron spectroscopy (XPS)	210
7.8. Scanning electron microscopy (SEM)	211
7.9 Transmission electron microscopy (TEM).....	213
7.10. Scanning transmission electron microscope (STEM)	214
7.11. Confocal microscope	215
7.12. Dynamic light scattering (DLS)	216
7.13. Thermogravimetric analysis (TGA)	218
7.14. References.....	219
Acknowledgement.....	220

Résumé de Thèse

1. Introduction

Les complexes de métaux de transition luminescents, et en particulier ceux contenant des éléments lourds tels que Ru,¹ Ir² et Pt,³ si leur conception est appropriée, disposent d'un rendement quantique de photoluminescence (PLQY) élevé, d'une longue durée de vie à l'état excité vie (ESLT), d'une couleur d'émission modifiable, et, pour la plupart d'entre eux, d'une certaine stabilité.⁴ Ils sont donc utilisés dans différents domaines tels que la photo catalyse,⁵ bio-imagerie,⁶ ou comme émetteurs pour les diodes électroluminescentes organiques (OLEDs).⁷

En raison de leur configuration électronique d^8 , les complexes de platine (II) ont une géométrie carrée plane, leur permettant de s'auto-assembler par des interactions non covalentes telles que le π - π stacking (entre les ligands) ou les interactions métal -métal (par recouvrement des orbitales $5dz^2$)^{8,9}. Dans ce dernier cas, de nouvelles transitions électroniques peuvent survenir, par exemple, par photo-excitation, par la formation de nouvelles orbitales moléculaires. Comme cela est représenté sur la **figure 1**, les transitions électroniques entre la HOMO, localisée sur les métaux, et la LUMO, impliquant les ligands peuvent se produire. Ces transitions sont donc des transferts de charge singulet métal-métal à ligand ($^1\text{MMLCT}$) (**figure 1**). Les nouveaux états excités correspondants sont, en raison de la présence de l'atome lourd, de type triplet par nature et peuvent ainsi conduire à des changements spectaculaires dans les propriétés de luminescence des agrégats formés par rapport au monomère.¹⁰⁻¹²

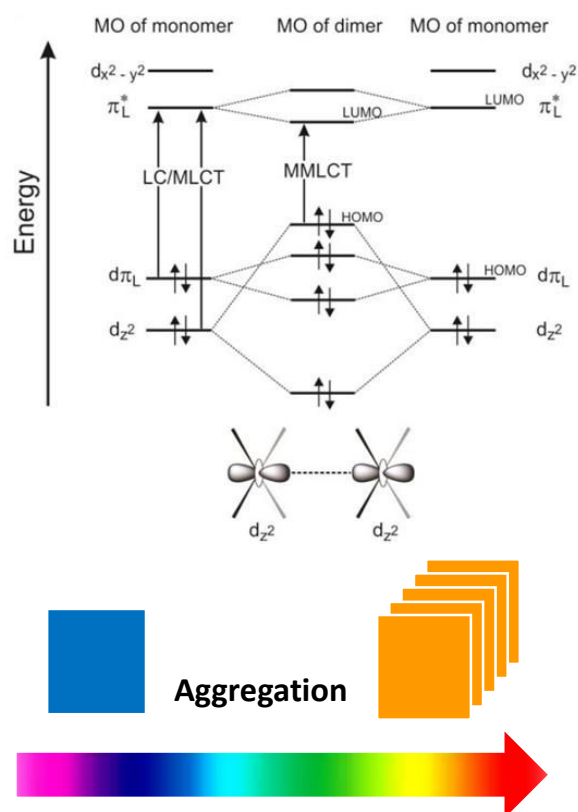


Figure 1. Diagramme d'orbitales moléculaires simplifié montrant l'effet des interactions et du recouvrement orbitalaire (haut). Représentation schématique de l'agrégation des complexes de Pt(II) (bas).

La formation et la stabilisation de ces agrégats peuvent être obtenus, entre autres, en créant un espace confiné réalisé par des nanoparticules de silice mésoporeuse (MSNs),¹³ ou par dépôt sur surface sur des nanoparticules métalliques, par exemple ceux d'or (AuNPs).¹⁴ Les MSNs sont une classe de matériaux qui sont de plus en plus étudiés dans la recherche en raison de leur stabilité, leur forme accordable et la taille accordable de leurs pores, leur étroite distribution de pores, le fait qu'ils sont approuvés par l'agence américaine des produits alimentaires et médicamenteux FDA, leur ratio taille de pores sur taille de matériau élevé. Ils sont donc utilisés dans la catalyse,¹⁵ les capteurs chimiques,¹⁶ les systèmes de délivrance de médicaments,¹⁷ la séparation moléculaire.¹⁸ En ce qui concerne les AuNPs, grâce à leurs propriétés optiques et physiques uniques, ainsi que leur biocompatibilité relative, sont largement utilisées dans de nombreux domaines tels que la diffusion Raman amplifiée par surface,¹⁹ la catalyse,²⁰ la bio-imagerie, la bio-détection ou l'étiquetage biologique.²¹

2. Objectif

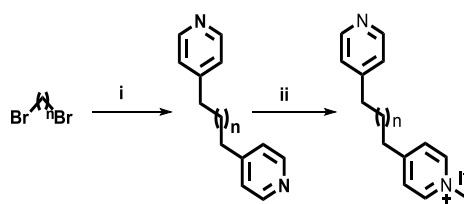
L'objectif de cette thèse est la synthèse, la caractérisation et l'étude de complexes métalliques luminescents, en particulier de Pt (II), leurs propriétés d'agrégation en solution, mais également dans un espace confiné ainsi qu'en surface. L'incorporation de complexes de métaux de transition dans la structure poreuse, et ainsi que leur dépôt à la surface de nanoparticules et dans un cadre métallo-organique (MOF), par greffage post-synthétique, ont été étudiés. Sont également étudiés la corrélation entre les propriétés de films d'une série de complexes de Pt(II) avec leur morphologie, leur mobilité électronique et la simulation de leur structure auto-assemblée par diffraction aux rayons-X.

3. Résultats et discussion

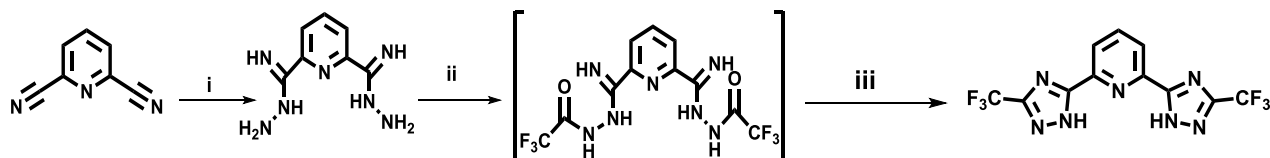
Le premier chapitre de ma thèse est une introduction générale expliquant les principes de la photoluminescence et illustrant l'état de l'art des différents sujets. En particulier, une introduction sur les MSNs, les AuNPs et les MOFs est donnée.

Le deuxième chapitre présente la synthèse, la caractérisation et les propriétés photophysiques de complexes de Pt(II) portant un ligand cationique de type pyridinium. La synthèse des ligands et des complexes est représentée dans le **Schéma 1**.^{11,22,23}

Plusieurs ligands avec différentes longueurs de chaîne carbonée (C2, C5, C8, C11, C14) ont été synthétisés pour deux raisons principales. En premier lieu, les sels de pyridinium ont été décrits dans la littérature comme bons désactivateurs de photoluminescence en raison de leur faible densité électronique et donc de leur comportement électro-attracteur, ce qui les rend appropriés pour un efficace transfert d'électrons.^{24, 25} Par conséquent, la corrélation entre d'une part la distance entre le groupement pyridinium et le centre de platine et, d'autre part l'influence sur le rendement quantique d'émission serait très intéressant à étudier. La deuxième raison est l'étude de la formation des systèmes micellaires en fonction de la longueur de la partie hydrophobe, la partie hydrophile ayant dans tous les cas de la même taille.



i) 4-picoline, LDA, THF, -78°C then RT, overnight ii) CH₃I, chloroform, RT, overnight



i) NH₂-NH₂.H₂O, EtOH, RT, overnight ii) TFA, reflux, overnight iii) ethylene glycol, 130°C, 3h

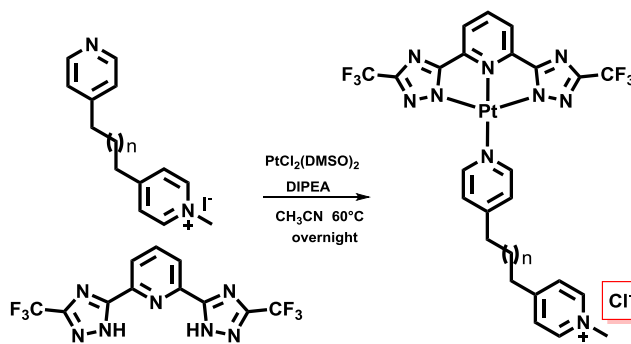


Schéma 1. Représentation schématique de la synthèse des ligands organiques et des complexes de Pt(II)

Après la caractérisation des molécules par résonance magnétique nucléaire (RMN) et spectroscopie de masse à ionisation par électro-pulvérisation (ESI-MS), leurs propriétés photophysiques ont été étudiées. **La figure 2** montre les spectres d'émission et d'excitation des complexes dans l'eau (concentration 10⁻⁵ M) et à l'état solide. Fait intéressant, la longueur du ligand auxiliaire n'a pas d'effet sur la longueur d'onde d'émission dans l'eau ou à l'état solide. De plus, même à de très faibles concentrations (10⁻⁷ M), la longueur d'onde d'émission des complexes reste la même.

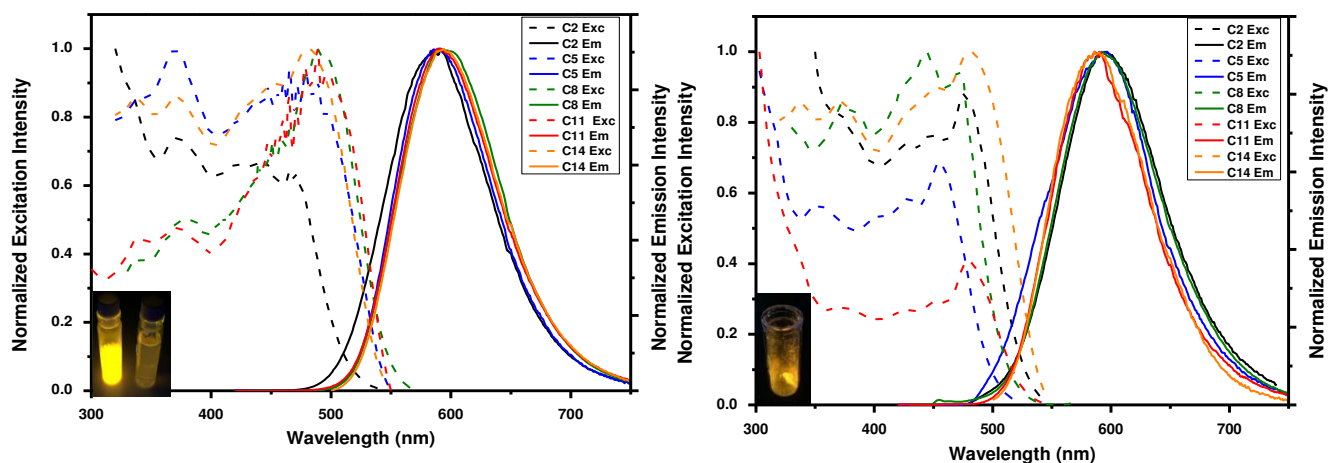


Figure 2. Spectres d'émission (ligne continue) et d'excitation (ligne discontinue) des complexes étudiés en solution (H_2O , 10^{-5}M) (gauche) et à l'état solide (droite). Insérés : spectre de gauche : photographies du complexe **C2** sous irradiation (366nm) en solution dans l'eau, à 10mM (droite) et à 0.01 mM (gauche) ; spectre de droite : photographie du complexe **C2** sous irradiation (366nm) à l'état solide

Le troisième chapitre traite de l'encapsulation des complexes décrits dans le *chapitre 2* à l'intérieur de nanoparticules de silice mésoporeuse (MSNs) afin de stabiliser les agrégats formés. La synthèse de MSNs nécessite la polymérisation, dans des milieux acides ou basiques, d'une source de silice (tétraéthylorthosilicate, TEOS) autour micelles faites par un agent tensio-actif,¹³ qui est habituellement le bromure de cetyltriméthylammonium (CTAB). Le matériau résultant est appelé MCM-41.¹⁴ L'idée est d'utiliser les complexes décrits dans le *chapitre 2* en tant que modèles pour la synthèse de nanoparticules de silice mésoporeuses suivant une procédure similaire à celle décrite précédemment (**Figure 3**).^{26, 27} La formation de cet espace confiné doit fournir une protection contre une indésirable extinction de luminescence du complexe après irradiation due à la présence d'oxygène, ainsi que d'une plus grande rigidité et donc une distorsion moindre, conduisant à une amélioration des propriétés luminescentes.

Tout d'abord, la synthèse de MCM-41 a été réalisée.²⁸ Ce dernier sera utilisé comme référence pendant le reste du chapitre (**Schéma 2**). Ce matériau a été caractérisée par microscopie électronique à balayage (SEM), entre autres techniques, montrant des particules de 100 nm de diamètre (**Figure 4**).

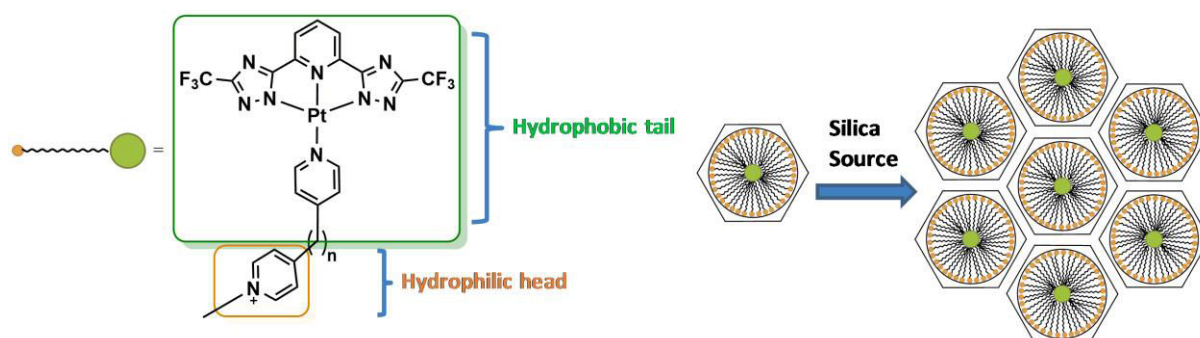


Figure 3. Stratégie utilisant des complexes de Pt(II) cationiques en tant que modèles pour la synthèse de MSNs

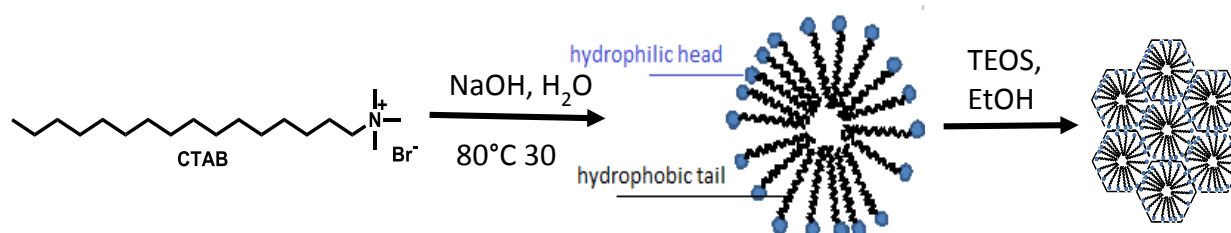


Schéma 2. Approche synthétique pour MCM-41

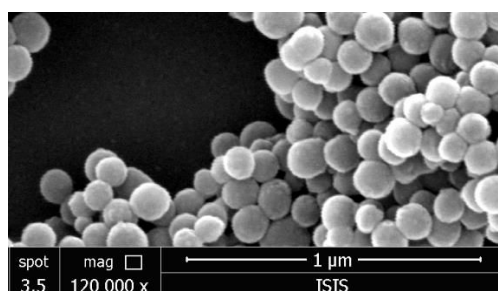


Figure 4. Images SEM de MCM-41

Les complexes de Pt (II) ont été ensuite incorporés dans la synthèse de la silice avec différents rapports complexe / CTAB, comme indiqué dans le **Tableau 1**. La **Figure 5** montre les images SEM de l'ensemble **1 a.-d.** et **2 a.-d.**, et la **Figure 6** montre les propriétés photophysiques des matériaux respectifs.

Les particules présentent une forme sphérique avec une taille qui est beaucoup plus grande que MCM-41, et cela peut être expliqué par la grande taille des complexes par rapport au CTAB. Les profils d'émission et d'excitation (**Figure 6**) ne sont pas dépendants de la concentration complexe / CTAB, mais pour les composés **1a** et **2a**, ayant une très faible concentration du complexe (10^{-3} mM), il est intéressant de noter une émission à énergie plus élevée, typique des complexes de Pt (II) dissous

moléculairement. Il est important de rappeler que le complexe seul montre l'émission de l'agrégat, même à 10^{-4} mM.

Tableau 1. Systèmes étudiés, “**Sample 1**” représentant le complexe C14, alors que “**Sample 2**” représente le complexe C11

	[Pt(II) Complex](mM)	[CTAB](mM)
Sample 1a/2a	10^{-3}	2.75
Sample 1b/2b	0.02	2.75
Sample 1c/2c	0.1	2.25
Sample 1d/2d	0.2	2

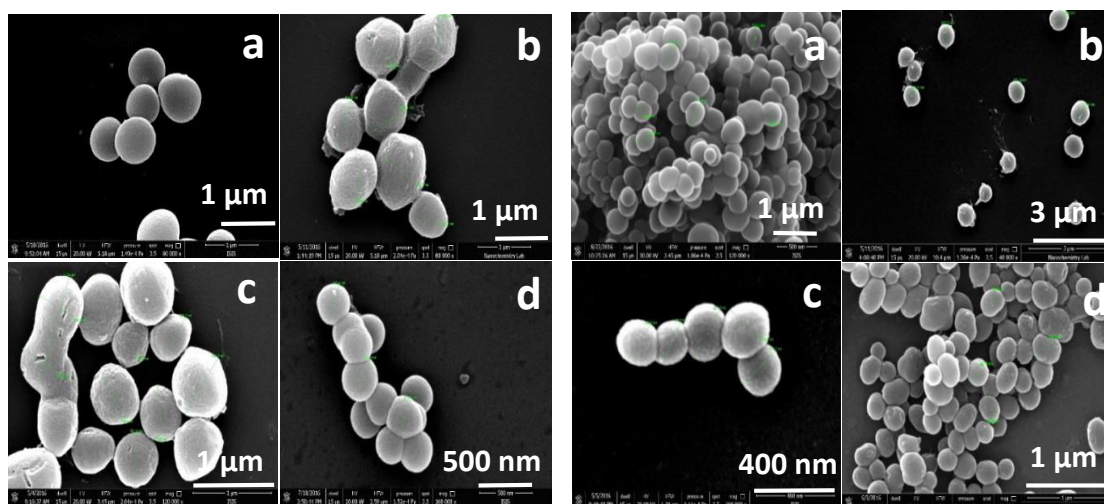


Figure 5. Images SEM des systèmes **1a-1d** (gauche), et **2a-2d** (droite)

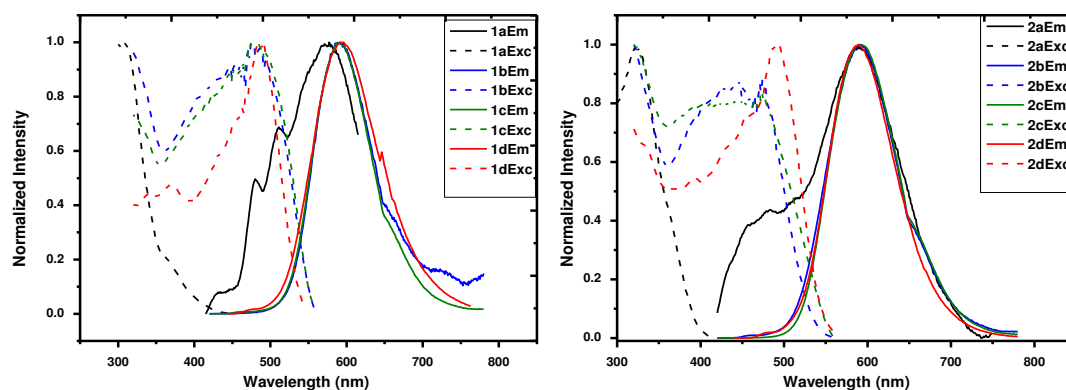


Figure 6. Spectres d'émission (ligne continue) et d'excitation (ligne discontinue) des échantillons **1a-1d** (gauche) et **2a-2d** (droite)

Encouragé par ces résultats, nous avons développé un nouveau matériau de type silice uniquement basé sur le complexe surfactant, sans CTAB. Nous avons décidé d'utiliser la même procédure que celle mentionnée ci-dessus, à l'aide du complexe **1** (C14) et **2** (C11) avec une concentration de 6mM. Les images SEM ainsi que les spectres d'émission et d'excitation du matériau résultant sont représentés sur la **Figure 7**. Le matériau de silice ainsi obtenu (**1e** et **2e**, respectivement) est sphérique et très grand (5 μ m), nous pouvons également observer la haute émission de la forme agrégée. (**Figure 8**).

Le **tableau 2** montre un récapitulatif de toutes les propriétés photophysiques de **1a** - **1e** et **2a** - **2e**. Comme nous pouvons le voir à partir de ces tables, les PLQY sont plus élevés, mais encore plus intéressant, les durées de vie de l'état excité (ESLT) sont beaucoup plus longues. On peut donc conclure une amélioration de la luminescence de cette classe de complexes de Pt (II) par encapsulation dans des matrices de silice mésoporeuse.

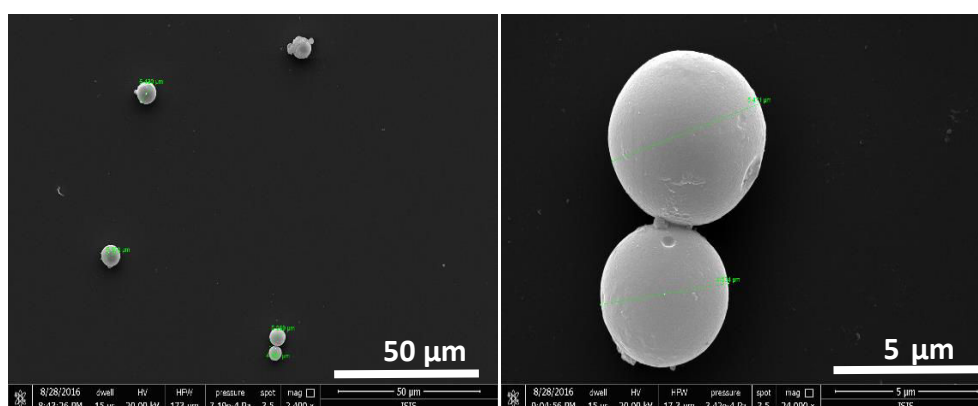


Figure 7. Images SEM de **2e**

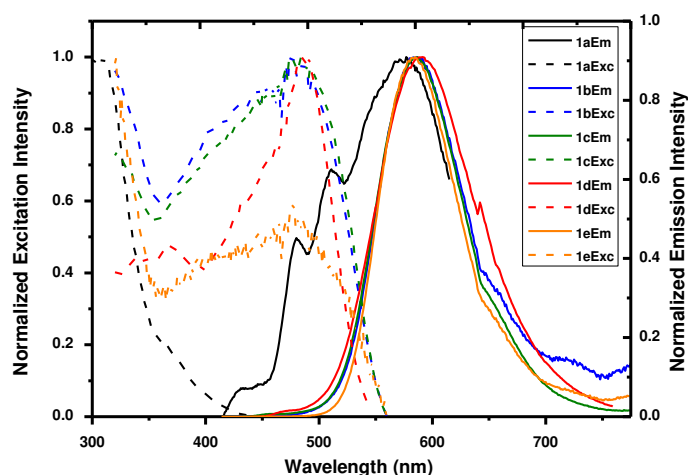
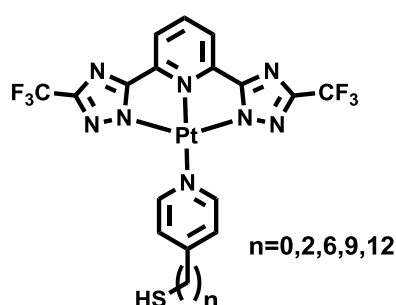


Figure 8. Spectres d'émission (lignes continues) et d'excitation (lignes discontinues) des échantillons **1a-1e**.

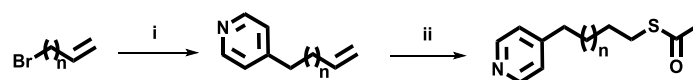
Tableau 2. Tableau récapitulatif des propriétés photophysiques de **1a-1e.** et **2a-2e.**

Material	$\lambda_{em}(nm, \lambda_{exc}=400nm)$	$\phi(\%)$	$\tau(\mu s)$
1a	481-510-576	-	0.171(39%) 0.010(61%)
1b	587	28	0.911 (42%) 0.405 (58%)
1c	587	37	0.936(34%) 0.386(66%)
1d	589	41	0.961(40%) 0.363(60%)
1e	592	28	0.662(26%) 0.281(74%)
2a	476-590	-	0.160(31%) 0.008(69%)
2b	590	44	1.247 (19%) 0.706 (81%)
2c	590	45	1.325 (19%) 0.754 (81%)
2d	590	39	0.991(63%) 0.218(37%)
2e	590	28	0.744(30%) 0.331(70%)

Le quatrième chapitre de cette thèse porte sur l'étude de l'auto-assemblage de Pt (II) sur des nanoparticules d'or (AuNPs) et l'effet conséquent sur les propriétés de photoluminescence.²⁹ Pour atteindre notre objectif, une nouvelle série de complexes a été synthétisée, avec le même ligand tridentate dianionique de type N⁻N⁻N reporté précédemment mais portant différents ligands auxiliaires. En effet, l'affinité bien connue de l'or pour les groupements thiols et plus généralement pour le soufre nous a amené à utiliser des groupements thiol en bout de chaîne des ligands auxiliaires comme le montre la **Figure 8**.

**Figure 8.** Structure des complexes de Pt(II) étudiés dans le *chapitre 4*

Comme la synthèse du ligand tridentate et le procédé de complexation ont été décrits précédemment, seule la synthèse du ligand monodentate est présentée ci-dessous (**Schéma 3**).³⁰



i) 4-picoline, lithium diisopropylamide, Et₂O, -78°C then r.t., overnight

ii) thioacetic acid, 4,4'-Azobis(4-cyanovaleric acid), THF, UV light, r.t., 96h

Schéma 3. Voie de synthèse du ligand auxiliaire

Après la caractérisation des molécules par RMN et MS-ESI, les propriétés photophysiques ont été étudiées (**Figure 9**). Dans le dichlorométhane à $c = 10^{-4}$ M, les complexes affichent l'émission des espèces monomères, tandis que à l'état solide, nous observons une forte émission pour la forme auto-assemblée en raison de la transition ³MMLCT.

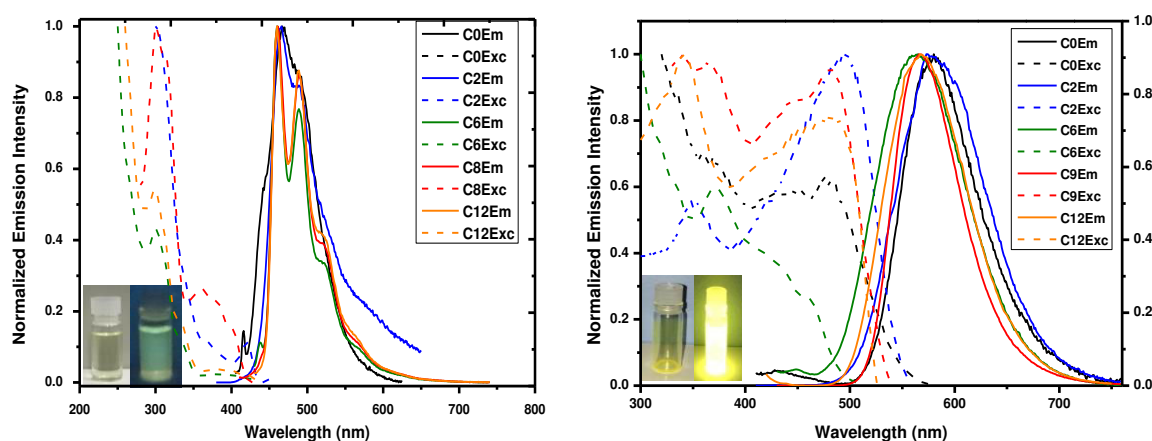


Figure 9. Spectres d'émission et d'excitation des complexes étudiés dans le *chapitre 4*.

Le PLQY de ces complexes en solution sont très faibles (1 %). Cependant, à l'état solide, ils sont fortement émissifs grâce à la formation d'agrégats (59 %). L'émission de complexes s'éteint de façons bi- exponentielle dans les deux cas, en solution (CH₂Cl₂, $c = 10^{-4}$ M) et à l'état solide. Par exemple, pour complexe **C6** : $\tau_1 = 6$ ns (92%) et $\tau_2 = 187$ ns (8 %) en solution, alors que $\tau_1 = 753$ ns (90%) et $\tau_2 = 317$ ns (10 %) à l'état solide. Après déprotection du groupement thiol dans des conditions basiques (MeOD),³⁰ les complexes ont été liés à la nanoparticule. Les caractérisations par (XPS) et par microscopie électronique à balayage par transmission (STEM) ont été effectuées (**Figure 10**, par exemple, pour le complexe de **C6**). A partir l'analyse XPS du soufre, nous pouvons observer deux pics à 164 eV (pour le S libre) et à 168 eV (S lié). L'image STEM

ci-dessous montre la AUNP (environ 100nm) entourée d'une couche du complexe agrégé. En ce qui concerne le PLQY, nous pouvons observer une extinction de luminescence quand le complexe est très proches des AuNPs (C0 et C2). En revanche, pour les chaînes carbonées plus longues, le PLQY augmente avec la taille de la chaîne carbonée pour finalement atteindre 25% dans le cas de C12

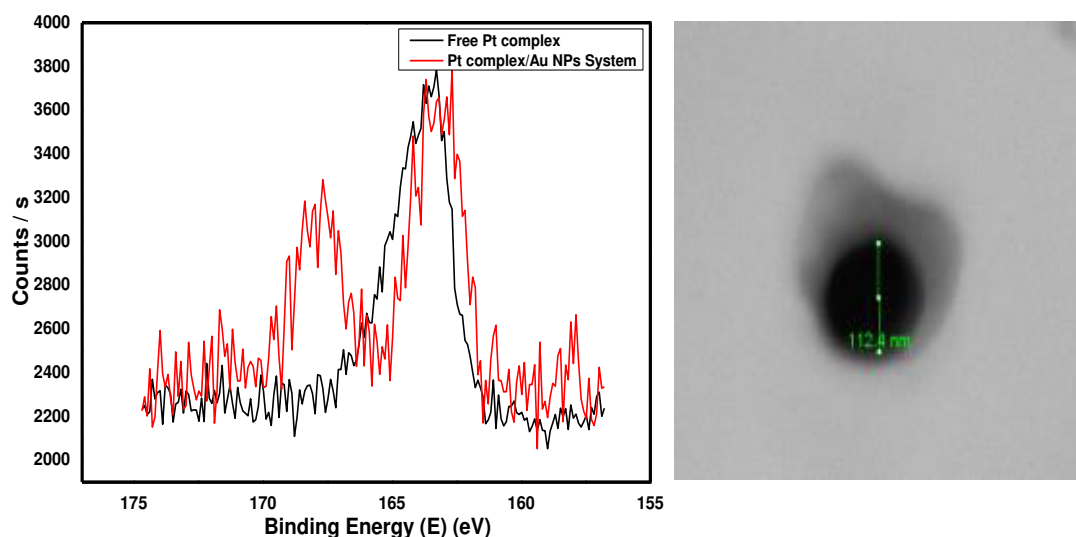


Figure 10. Spectre XPS du soufre du complexe **C6** (gauche) , Image STEM du complexe C6 sur les AuNPs (droite)

Dans le chapitre 5, une série de complexes de Pt (II) contenant des substituants oligothiophènes a été synthétisée et caractérisée. Les complexes contiennent le même ligand tridentate dianionique $N^+N^+N^-$ que précédemment, et des dérivés de type pyridine fonctionnalisée par des groupements thiophène sont utilisés comme ligands auxiliaires (**Schéma 4**). La mise en place d'interactions intermoléculaires π - π et/ou Pt-Pt a donné lieu à d'intéressantes propriétés photophysiques à l'état de film. Ces dernières ont été étudiées et les résultats ont été corrélés à leurs propriétés de transport de charge, à leur morphologie et à la structure simulée de leur auto-assemblage.

Après la synthèse de ces complexes, en fonction des résultats observés, les complexes présentant les meilleures morphologie et valeurs de mobilité, à savoir des complexes **3a**, **3b**, **3c** et **3d** ont été par la suite étudiés. Les spectres d'émission des films pour **3a**, **3b**, **3c**, **3d** sont présentés dans la **Figure 11**.

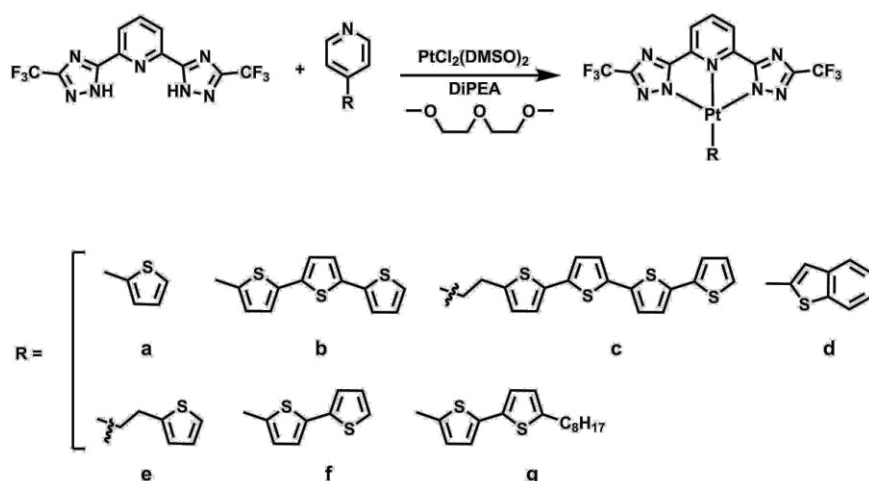


Schéma 4. Voie de synthèse pour les complexes **3a-g**

L'état d'agrégat moléculaire des complexes auto-assemblés a été étudié par simulation et mis en corrélation avec la mobilité des électrons. A cet effet, nous avons choisi les structures correspondant à **3a**, **3b**, **3c** et **3d** et mesuré le diagramme de diffraction rayons X sur poudre (PXRD). La structure géométrique a été optimisée avec le programme Gaussian.³¹ En utilisant le logiciel d'analyse Total Pattern Analysis Solution (TOPAS, Bruker AXS)³², le diffractogramme a été indexé sur 20 pics au maximum au sein d'une valeur de 2θ entre 5° et 40° , et une analyse minutieuse a été réalisée afin de nous permettre de déterminer les systèmes cristallins. Grâce au même logiciel, un raffinement a été effectué pour chaque structure, puis nous avons pu obtenir les paramètres de réseau des structures étudiées, avec des profils pondérés de Rietveld (Rwp) allant de 18 % à 10 % (**Tableau 4**). Un exemple de PXRD mesuré et le modèle raffiné est représenté dans la figure 12.

L'agrégation moléculaire simulée de chaque complexe a été déterminée par le programme Materials Studio, Module Reflex. Pour les complexes **3b** et **3c**, qui disposent d'une mobilité relativement modérée, nous ne constatons aucune interaction Pt-Pt.

Tableau 3. Paramètres de maille des complexes **3a-3d**

Complex	Crystal system	Space group	A(Å)	B(Å)	C(Å)	Alpha(°)	Beta(°)	Gamma(°)	Cry (nm)	Rwp
3a	Monoclinic	P21(4)	15.353	3.790	13.567	90	128.770	90	333	18.1
3b	Triclinic	P-1(2)	2.999	24.897	40.0052	89.653	90.129	90.078	366	14.9
3c	Orthorhombic	P222(16)	35.4967	12.1729	5.0067654	90	90	90	156	10.2
3d	Triclinic	P-1(2)	13.5495	22.4959	27.0455	83.99	87.85	90.7	60	11.5

En effet, la distance est beaucoup plus longue que les 3,5 Å nécessaires afin d'avoir cette interaction (6,71 Å). Probablement, ceci est dû à la conformation inclinée du groupement oligo-thiophène qui empêche l'agrégation proche des molécules. En particulier, **3c** a un groupement éthyle comme agent de liaison entre la pyridine et les groupements oligothiophènes, induisant une rotation libre et donc une possible déformation de la géométrie. Les spectres d'émission du film **3b** est en accord avec ce fait en montrant l'émission monomère des molécules à 440nm, indiquant la présence de monomères qui empêchent la formation de l'agrégation moléculaire étroite. Le complexe **3d** propose un spectre d'émission du film qui de très faible énergie. Ce résultat a été mis en adéquation d'une part car ce complexe présente la meilleure mobilité parmi tous les complexes étudiés, et d'autre part avec la distance intermoléculaire Pt-Pt de 3,21 Å (**Figure 13**).

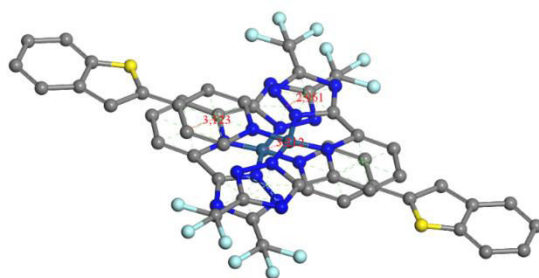


Figure 13. Structure simulée de l'auto-assemblage de **3g**, montrant clairement la présence d'interactions Pt-Pt

Dans le chapitre 6, nous montrons la préparation de nouveaux matériaux émissifs basée sur l'inclusion de complexes de Pt(II) et d'Ir(III) à l'intérieur du MOF³³ Al(OH)(bipyridinedicarboxylate) (**MOF-253**) (**Figure 14**)

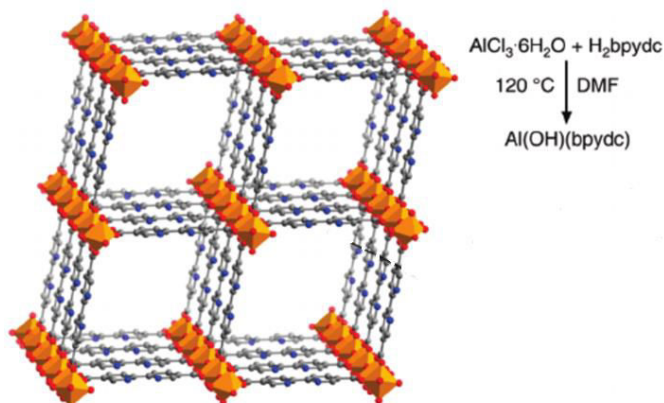


Figure 14. Structure et voie de synthèse du **MOF-253**, le MOF utilisé dans ce chapitre

Le **MOF-253** a été synthétisé en premier selon les travaux de Yaghi et al.³⁴ L'extraction Soxhlet dans le méthanol permet l'élimination de molécules de DMF, solvant utilisé lors la réaction, afin d'obtenir un matériau avec des pores complètement vides. Les matériaux obtenus ont été caractérisés par analyse thermogravimétrique (TGA), N₂ adsorption-désorption, TEM et PXRD. Les propriétés photophysiques du **MOF-253** ont été étudiées, le matériau étant émissif dans la région du jaune ($\lambda_{\text{max}} = 555\text{nm}$), avec un rendement quantique d'émission très faible (1%) et une très courte durée de vie de l'état excité, 6ns (87%) et 3ns (13 %). L'inclusion est réalisée par substitution d'un ligand, conduisant à la formation d'une liaison de coordination, prouvée par XPS, qui offre une robustesse au système.

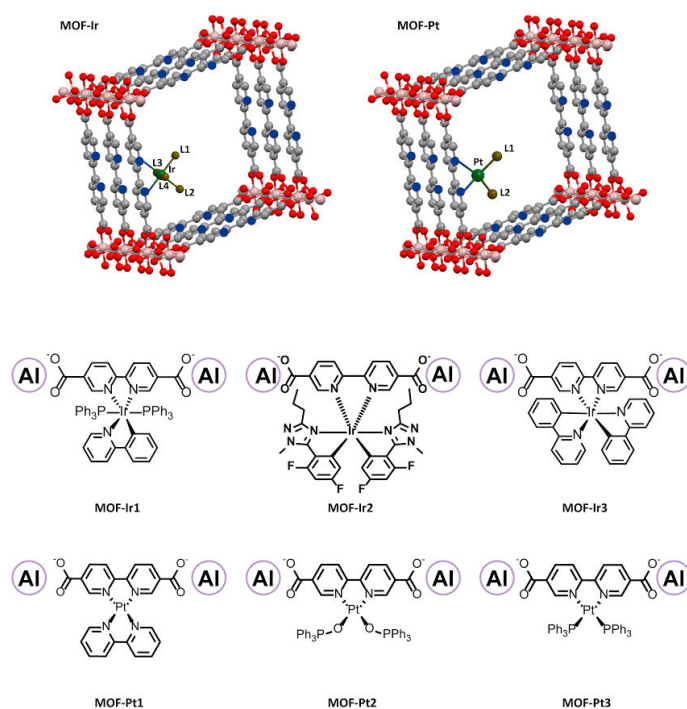


Schéma 5. Systèmes MOF-complexes métalliques étudiés

Afin de prouver la formation de cette liaison de coordination, des expériences XPS ont été effectuées en utilisant l'analyse N1s, sachant que les énergies de liaison d'azote coordonné et non coordonné pour le ligand bipyridine sont différentes. La **Figure 15** montre les spectres XPS N1s à haute résolution de **MOF-253** (A) et **MOF-Pt3** (B).

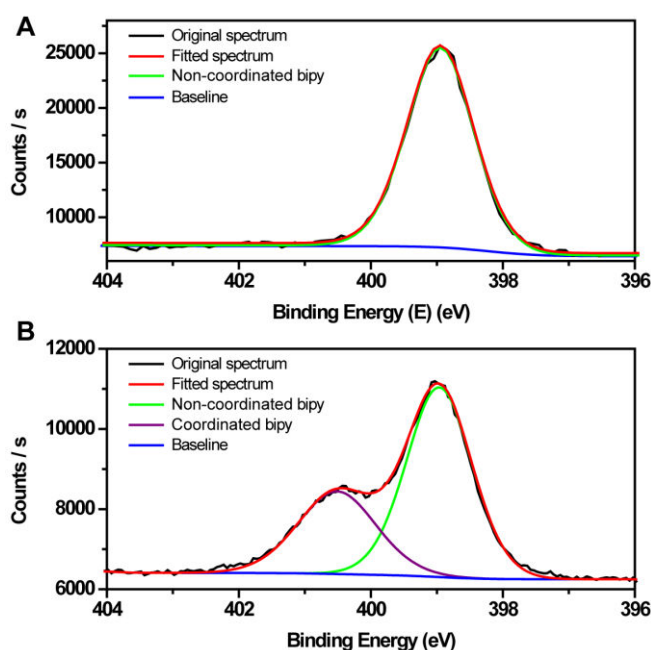


Figure 15. Spectres XPS N1_s haute résolution de **MOF-253** (haut) et **MOF-Pt3** (bas).

En plus des analyses XPS, l'analyse PXRD met en évidence le degré de cristallinité élevé des matériaux, avec une modification complète des paramètres de maille avant et après chaque insertion d'un complexe métallique. De plus, les propriétés photophysiques des matériaux obtenus ont été soigneusement étudiés. En utilisant cette technique, nous sommes en mesure de modifier les propriétés d'émission des matériaux du bleu au rouge, en passant par le vert et le jaune (**Figure 16**). Cependant, nous n'avons pas observé d'augmentation très significative des PLQY après inclusion des complexes métalliques, les matériaux les plus émissifs ayant 5 % de PLQY.

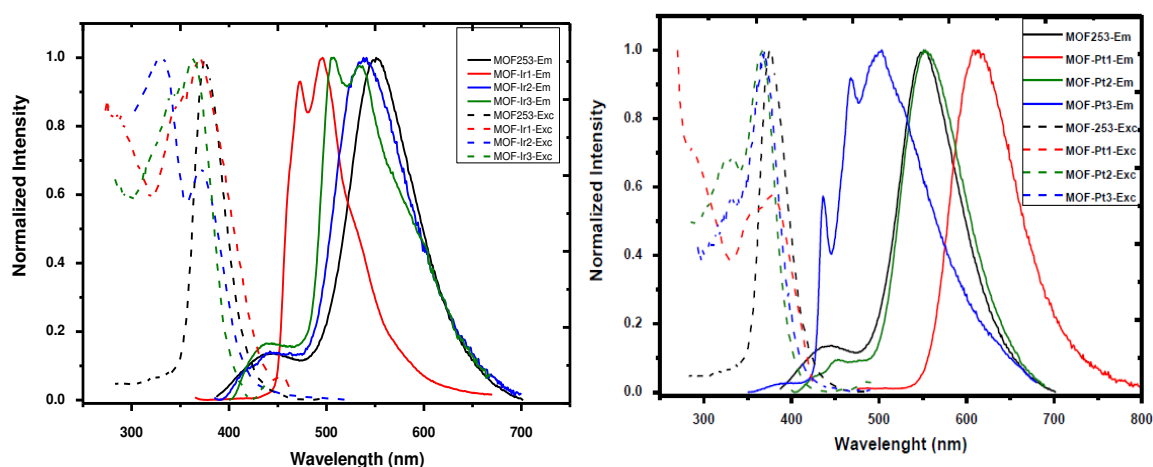


Figure 16. Spectres d'émission (ligne continue) et d'excitation (ligne discontinue) des matériaux MOF-Ir (gauche) et MOF-Pt (droite)

Afin de mener à bien toutes les études, la chimie expérimentale nécessite beaucoup de techniques de caractérisation physique. Selon le produit donné (molécule unique, auto-assemblage, nanomatériau) et à l'information que l'on veut obtenir, la méthode d'analyse choisie, et ainsi l'instrument analytique est différent. Dans le septième et dernier chapitre de cette thèse, nous décrivons les différents principes de caractérisation, ainsi que les instruments utilisés pour effectuer ces expériences analytiques.

4. Conclusion

Dans cette thèse, nous avons synthétisé avec succès et caractérisé des complexes de platine (II) portant un ligand dianionique tridentate $N \wedge N \wedge N$. Selon la conception du ligand auxiliaire, nous avons été en mesure d'appliquer le complexe pour des applications différentes, afin de stabiliser les agrégats d'auto-assemblage, pour améliorer les propriétés de photoluminescence ou même de comprendre la formation l'agrégat moléculaire. L'incorporation de complexes de Pt (II) et d'Ir (III) par une liaison de coordination afin de régler la couleur d'émission sont également étudiés.

5. Références

1. S. Campagna, F. Puntoriero, F. Nastasi, G. Bergamini, V. Balzani *Top. Curr. Chem.* **2007**, 280, 117
2. L. Flamigni, A. Barbieri, C. Sabatini, B. Ventura, F. Barigelletti *Top. Curr. Chem.* 2007, 281, 143
3. J. A. G. Williams *Top. Curr. Chem.* **2007**, 281, 205
4. A. J. Lees *Chem. Rev.* **1987**, 87, 711
5. D.P. Shelar, T.-T. Li, Y. Chen, W.-F. Fu *ChemPlusChem* **2015**, 80, 1541
6. M. Mauro, A. Aliprandi, D. Septiadi, N. S. Kehr, L. De Cola *Chem. Soc. Rev.* **2014**, **43**, 4144
7. C. Cebrian, M. Mauro, D. Kourkoulos, P. Mercandelli, D. Hertel, K. Meerholz, C. A. Strassert, L. De Cola *Adv. Mater.* **2013**, 25, 437
8. Miskowski, V. M.; Houlding V. H. *Inorg. Chem.* **1989**, 28, 1529
9. W. Lu, M. C. W. Chan, N. Zhu, C.-M. Che, C. Li, Z. Hui *J. Am. Chem. Soc.* **2004**, 12, 7639
10. M. Mauro, A. Aliprandi, C. Cebrián, D. Wang, C. Kübel, L. De Cola *Chem. Commun.* **2014**, 50, 7269
11. A. Aliprandi, M. Mauro, L. De Cola *Nat. Chem.* **2016**, 8, 10

12. B. Ma, J. Li, P. I. Djurovich, M. Yousufuddin, R. Bau, and M. E. Thompson *J. Am. Chem. Soc.* **2005**, 127, 29
13. C. T. Kresge, M. E. Leonowicz, W. J. Roth, J. C. Vartuli, J. S. Beck *Nature* **1992**, 359, 5
14. M.-C. Daniel, D. Astruc *Chem. Rev.* **2004**, 104, 293
15. E. A. Prasetyanto, N.-U. H. Khan, H.-U. Seo, S.-E. Park, *Top. Catal.* **2010**, 53, 1381
16. Y. Suto, H. Kumata, M. Tsuzukil, K. Fujiwara, *Anal. Sci.* **2011**, 27, 2;
17. A. Bertucci, E. A. Prasetyanto, D. Septiadi, A. Manicardi, E. Brognara, R. Gambari, R. Corradini, L. De Cola, *Small* **2015**, 11, 5687
18. M. Grün, A. A. Kurganov, S. Schacht, F. Schiith, K.K. Unger, *J. Chromatogr. A* **1996**, 740, 9
19. S. Schlcker, *Angew. Chem. Int. Ed.* **2014**, 53, 4756
20. L. Guczi, D. Horvath, Z. Paszti, G. Peto, *Catal. Today* **2002**, 72, 101
21. Y.-C. Yeh, B. Creran, V. M. Rotello *Nanoscale* **2012**, 4, 1871
22. J.-P. Collin, J. Frey, V. Heitz, J.-P. Sauvage, C. Tock, L. Allouche *J. Am. Chem. Soc.* **2009**, 131, 5609
23. B. J. Coe, S. P. Foxon, E. C. Harper, M. Helliwell, J. Raftery, C.A. Swanson, B. S. Brunshwig, K. Clays, E. Franz, J. Garín, J. Orduna, P. N. Horton, Michael B. Hursthouse *J. Am. Chem. Soc.* **2010**, 132, 1706
24. H. J. Pownall, L. C. Smith *Biochem.* **1974**, 13, 2590
25. M. M. Velázquez and Silvia M. B. Costa *J. Chem. Soc., Faraday Trans.* **1990**, **86**, 4043 710
26. J. S. Beck, J. C. Vart Uli, W. J. Roth, M. E. Leonowicz, C. T. Kresge, K. D. Schmitt, C. T-W. Chu D. H. Olson E. W. Sheppard, S. B. McCullen, J. B. Higgins, and J. L. Schlenkert *J. Am. Chem. Soc.* **1992** 27, 10834
27. M. B. Silva Botelho, J. M. Fernandez Hernandez, T. B. de Queiroz, H. Eckert, L. De Cola A. Simone Stucchi de Camargo *J. Mater. Chem.* **2011**, 21, 8829
28. A. Bertucci, E. A. Prasetyanto, D. Septiadi, A. Manicardi, E. Brognara, R. Gambari, R. Corradini, and L. De Cola *Small* **2015**, 11, 5687
29. S. A. M. Osborne, Z. Pikramenou *Faraday Discuss.* **2015**, **185**, 219
30. J. Poppenberg, S. Richter, E. Darlatt, C. H.-H. T, Hyegeun Min, W. E.S. Unger C. A. Schalley *Surf. Sci.* **2012**, 606 367.
31. Gaussian, Inc., Wallingford CT, 2004.
32. A. A. Coelho *J. Appl. Cryst.* **2003**, 36, 86
31. J. L.C. Rowsell, O. M. Yaghi *Microporous and Mesoporous Mater.* **2004**, 73, 3
32. E. D. Bloch, D. Britt, C. Lee, C. J. Doonan, F. J. Uribe-Romo, H. Furukawa, J. R. Long, O. M. Yaghi, *J. Am. Chem. Soc.* **2010**, 132, 14382

Summary of the Thesis

1. Introduction

Luminescent transition metal complexes feature high photoluminescence quantum yield (PLQY), long excited state lifetime (ESLT), tunable emission colour, and a certain stability.¹ They have been therefore used for different areas such as bio-imaging,² or active materials in organic light emitting diodes (OLEDs).³

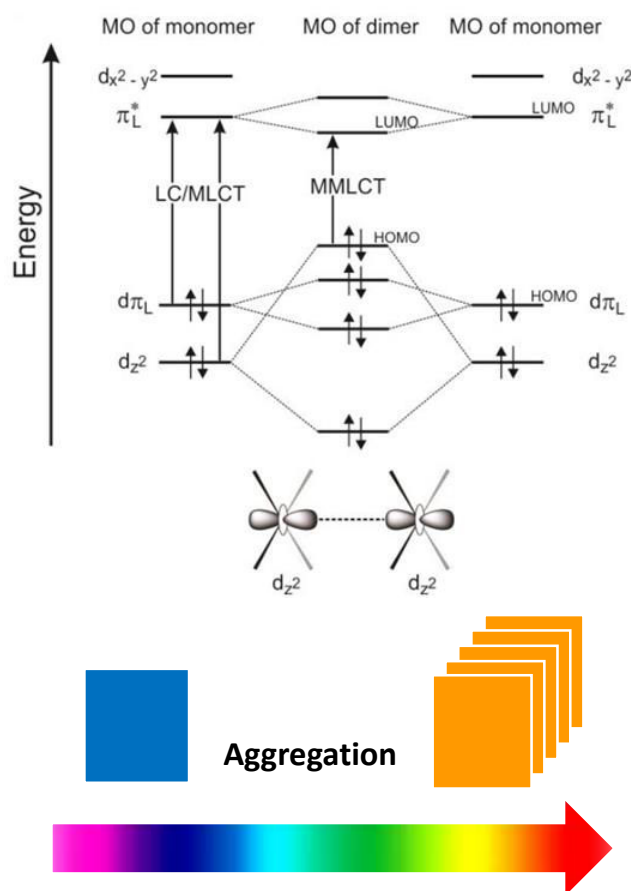


Figure 1. Simplified frontier molecular orbital showing the effect of interactions and intermolecular orbital overlap (top); Schematic representation of Pt(II) complex aggregation (bottom)

In particular, due to its d^8 electronic configuration, platinum (II) complexes have a square planar geometry, allowing them to self-assemble by non-covalent interactions such as pi-pi stacking (between the ligands) or metal-to-metal interactions (by the overlap of the $5d_{z^2}$ orbitals).^{4,5} A new electronic transition is hence formed, so-called

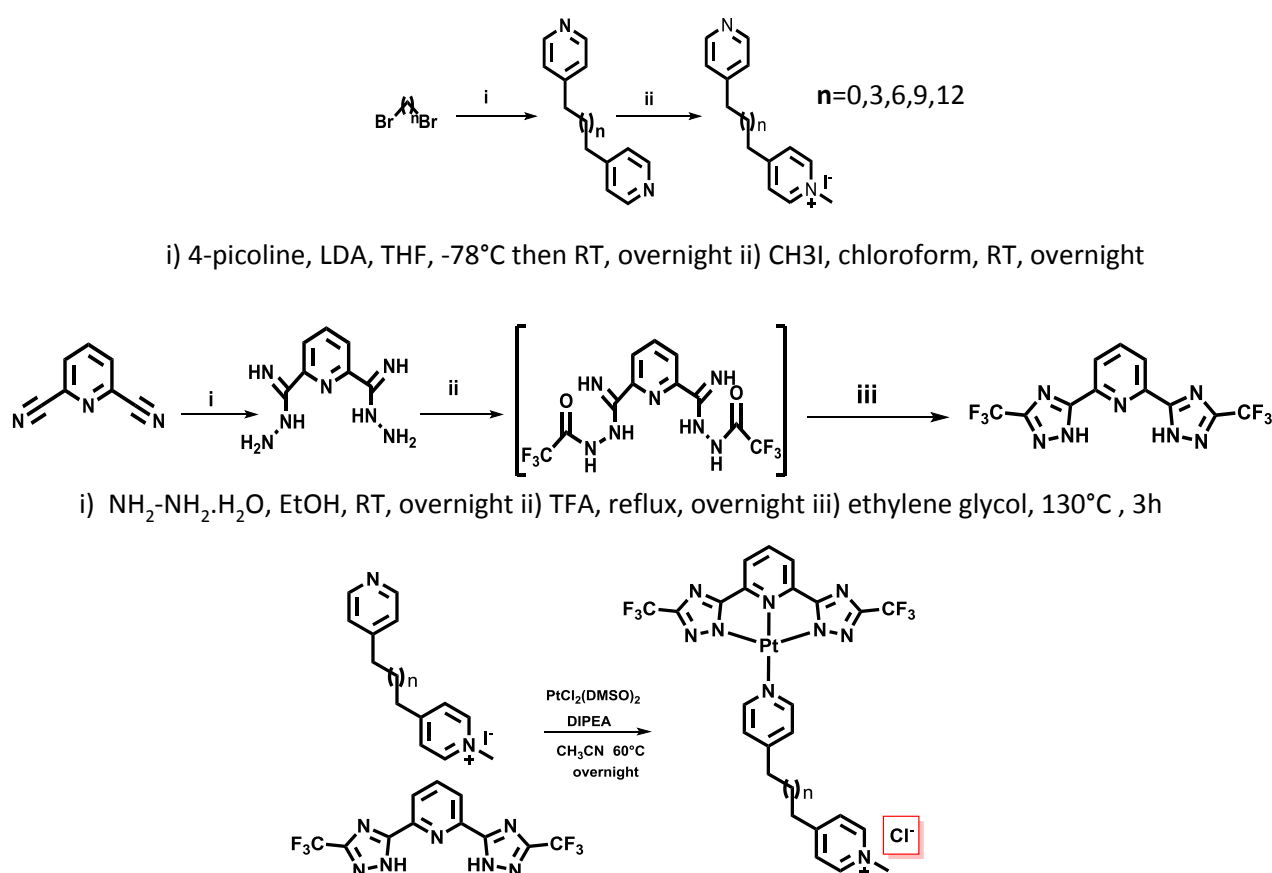
triplet metal-metal to ligand charge transfer ($^3\text{MMLCT}$) (**Figure 1**) This new transition results in dramatic changes in their luminescent properties.⁶⁻⁸

2. Aim of the thesis

The aim of this thesis is the synthesis, the characterization and the investigation of luminescence properties of luminescent hybrid organic-inorganic materials based on the self-assembly properties of Pt(II) complexes.

3. Results and Discussion

The first chapter of my thesis is a general introduction explaining clearly the principle of luminescence and stating each chapter one by one, with a well described state of the art. The second chapter shows the synthesis, the characterization and the photophysical properties of platinum(II) complexes bearing a cationic pyridinium ligand. The synthesis of the ligands and the complexes is shown in **Scheme 1**.^{7,9,10}



Scheme 1. Schematic representation of the synthesis of Pt(II) complexes

The different length of the carbon chain ligand (C2, C5, C8, C11, C14) have been synthesized for two main reasons. The first one is that, as it is known from the literature, pyridinium salts are good photoluminescence quenchers, due to their low electronic density, and therefore their electro-withdrawing behaviour allowing an efficient electron transfer.^{11,12} Hence, the correlation of the distance between the pyridinium moiety and the platinum centre, and on the other hand the emission quantum yield are interesting to study. The second reason is the investigation of the formation of micellar systems according to the length of the hydrophobic moiety, the hydrophilic part having in any case the same size.

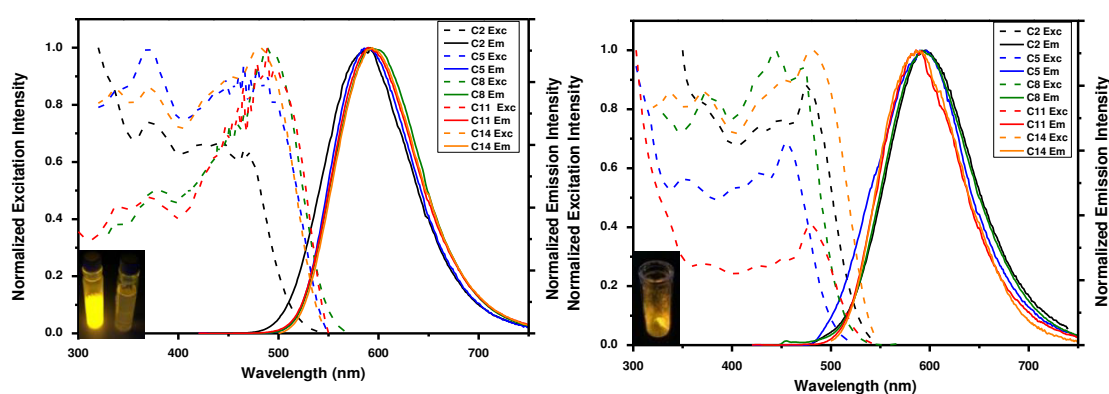


Figure 2. Emission (full line) and excitation (dashed line) of the discussed complexes in solution (water; 10⁻⁵M) (left) and in solid state (right)

After the characterization of the molecules by NMR and ESI-MS, the photophysical properties have been investigated. **Figure 2** shows the emission and the excitation spectra of the complexes, in water (concentration: 10⁻⁵M) and in solid state. Interestingly, the length of the ancillary ligand does not have any effect on the emission wavelength, in water or in solid state. Moreover, even at very low concentration (10⁻⁷M), the emission of complexes stays the same.

The third chapter deals with the encapsulation of the complexes discussed in *chapter 2* inside mesoporous silica nanoparticles (MSNs) in order to stabilize them. The synthesis of MSNs requires the polymerization, in acidic or basic media, of a silica source (Tetraethylorthosilicate, TEOS) around micelles made by surfactant.¹³ Most of the time, in our lab we use cetyltrimethylammonium bromide (CTAB).¹⁴ The idea is to use the complexes discussed in *chapter 2* that are then used as templates for the synthesis of mesoporous silica nanoparticles following a procedure similar to the one

described previously (**Figure 3**).^{15,16} The formation of this confined space should provide a protection from oxygen quenching to the complex after irradiation, as well as more rigidity and therefore less distortion, leading to an improvement of the luminescent properties.

Firstly, the synthesis of MCM-41 has been performed.¹³ This lately plays the role of a reference for the following of this chapter (**Scheme 2**). This material has been characterized by, among others, SEM, showing 100 nm diameter particles (**Figure 4**).

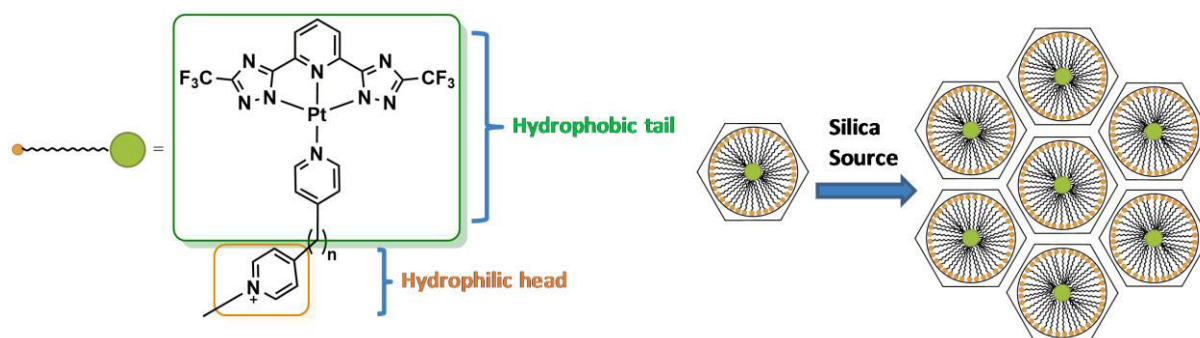
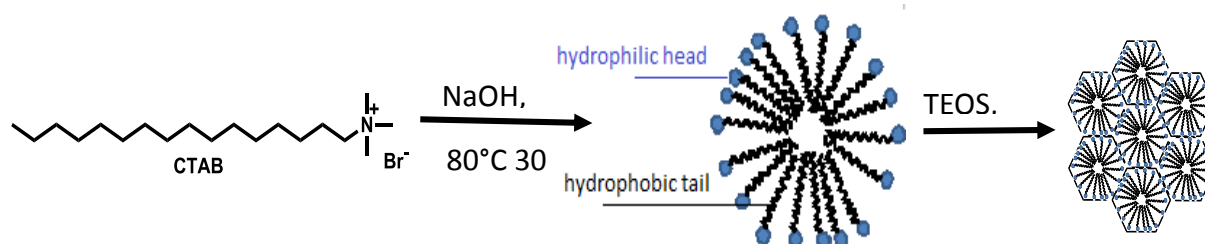


Figure 3. Synthetic strategy using cationic Pt(II) complexes as templates for the synthesis of mesoporous silica nanoparticles.



Scheme 2. Synthetic pathway of MCM-41 MSNs

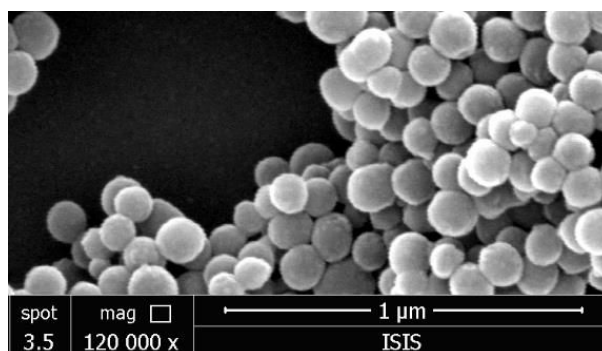


Figure 4. SEM image of MCM-41 MSNs

Table 1. Studied complexes, “**Sample 1**” represents the C14 complex, while “**Sample 2**” the C11 complex

	[Pt(II) Complex](mM)	[CTAB](mM)
Sample 1a/2a	10^{-3}	2.75
Sample 1b/2b	0.02	2.75
Sample 1c/2c	0.1	2.25
Sample 1d/2d	0.2	2

Figure 5. displays the SEM pictures of all **1 a.-d.** and **2 a.d.**, as well as the photophysical properties of the respective materials. The Pt(II) complexes have been then incorporated in the silica synthesis with different ratios complex/CTAB , as shown in **Table 1**.

The particles feature a spherical shape with a size that is much bigger than the regular MCM-41, and this can be explained by the big size of Pt(II) in respect to CTAB. The emission and excitation profiles (**Figure 6**) are not dependent on the concentration of Complex/CTAB, but for samples a, that have a very low concentration of the complex (10^{-3} mM), we interestingly observe the emission at higher energy, typical for the molecularly dissolved Pt(II) complexes. It is important to remind that the complex alone shows the emission of the aggregate, even at 10^{-4} mM.

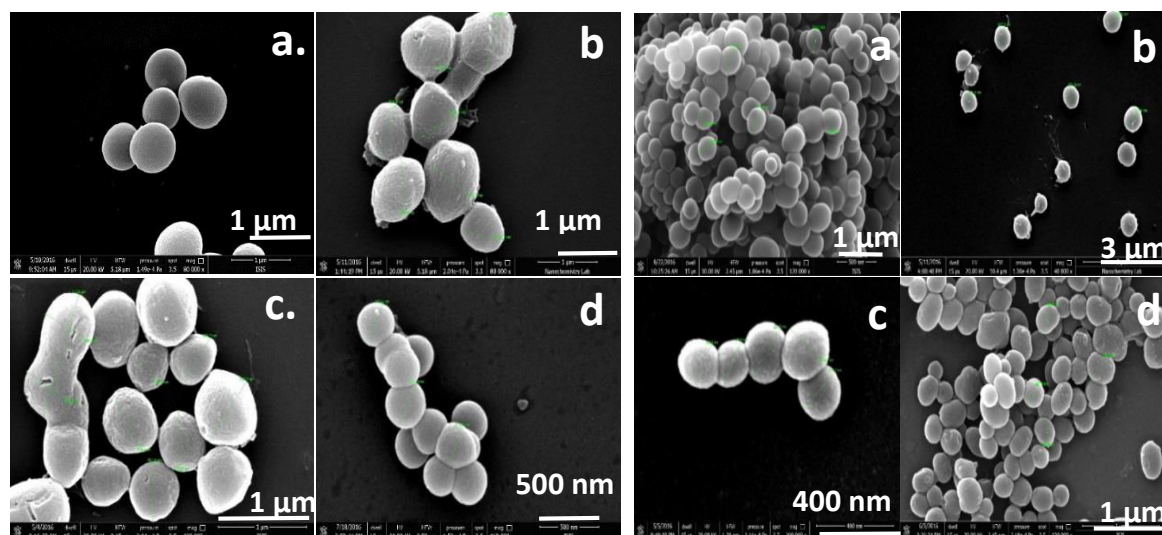


Figure 5. SEM images of samples **1a** to **1d** (left); and samples **2a** to **2d**.

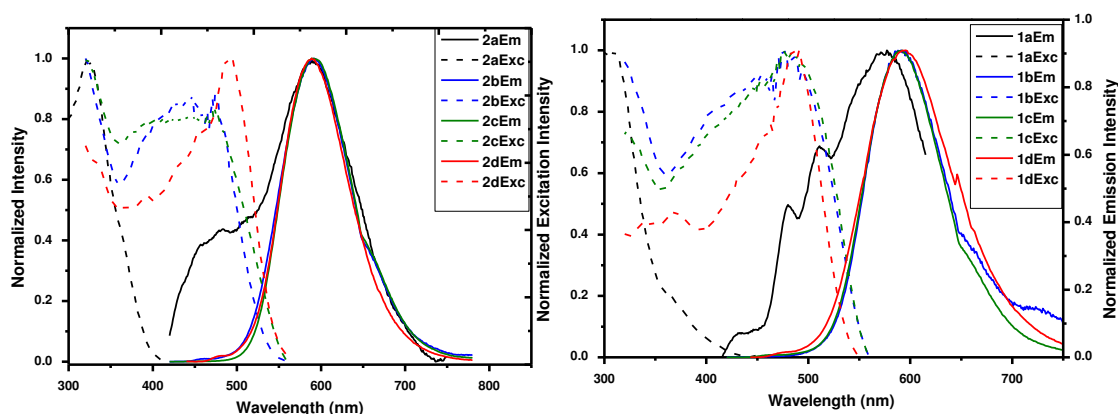


Figure 6. Emission (full line) and excitation (dashed line) of sample **1a-1d** (left) and **2a-2d** (right)

Encouraged by these results, we developed another new silica-type material only based on our surfactant, without CTAB. In order to do so, we decided to use the same procedure as mentioned here above, by using complex **1** (C14) and **2** (C11) with a concentration of 6mM. The SEM picture and the emission-excitation spectrum of the resulting material are shown in **Figure 7**. The obtained spherical silica (**1e** and **2e**, respectively) is very big (5 μm) and we can observe the high emission of the assembled form. (**Figure 8**).

Table 2 shows a recap chart of all the photophysical properties of **1a-1e** and **2a-2e**. As we can see from these tables, the PLQY are higher, but even more interestingly, the ESLT are much longer. We can therefore conclude an improvement of the luminescence of this class of Pt(II) complexes by encapsulation in mesoporous silica matrixes.

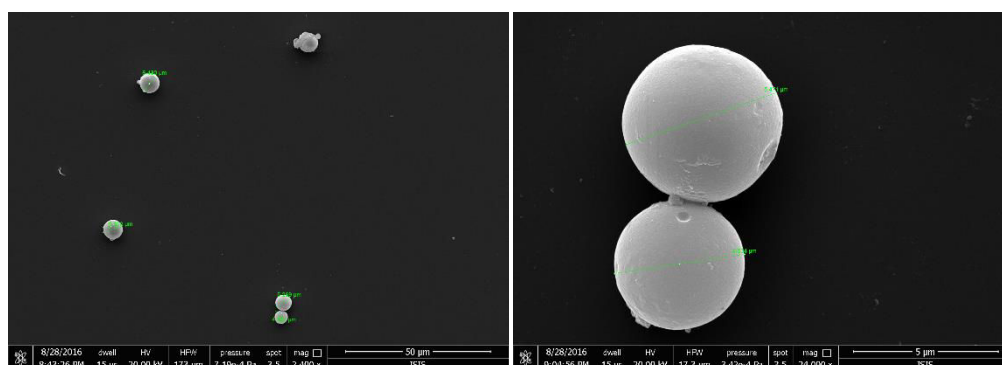


Figure 7. SEM images of **2e**

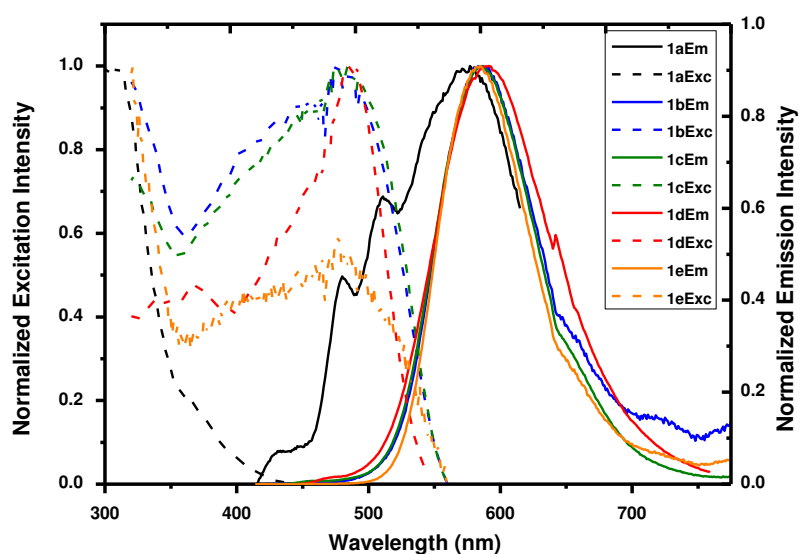


Figure 8. Emission (full line) and excitation (dashed line) of sample **1a-1e**.

Table 2. recap chart of all the photophysical properties of **1a-1e**

Material	$\lambda_{em}(nm, \lambda_{exc}=400nm)$	$\Phi(\%)$	$\tau(\mu s)$
1a	481-510-576	-	0.171(39%) 0.010(61%)
1b	587	28	0.911 (42%) 0.405 (58%)
1c	587	37	0.936(34%) 0.386(66%)
1d	589	41	0.961(40%) 0.363(60%)
1e	592	28	0.662(26%) 0.281(74%)
2a	476-590	-	0.160(31%) 0.008(69%)
2b	590	44	1.247 (19%) 0.706 (81%)
2c	590	45	1.325 (19%) 0.754 (81%)
2d	590	39	0.991(63%) 0.218(37%)
2e	590	28	0.744(30%) 0.331(70%)

The fourth chapter of this thesis is about the study of self-assembly of Pt(II) on gold nanoparticles (AuNPs) and the consequent effect on the photoluminescence properties.¹⁷ To achieve our purpose, a new series of complexes have been synthesized, with the same terdentate ligand but a difference on the ancillary ligand. Indeed, the very well-known affinity of gold for thiols groups, and more general for sulphur brought us to use thiols groups on the ancillary ligand, as shown in **Figure 8**.

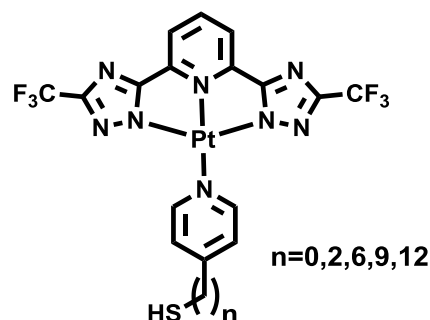
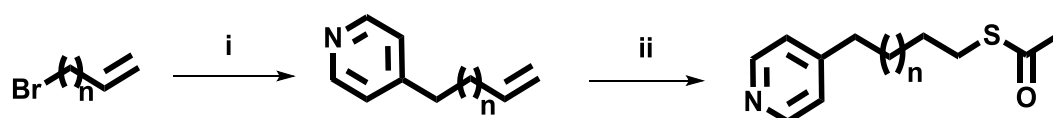


Figure 8. Structure of the studied Pt(II) complexes in chapter 4

As the synthesis of the terdentate ligand and the complexation process have been previously described, only the synthesis of the monodentate ligand is presented here below (**Scheme 3**).¹⁸



- i) 4-picoline, lithium diisopropylamide, Et₂O, -78°C then r.t., overnight
- ii) thioacetic acid, 4,4'-Azobis(4-cyanovaleric acid), THF, UV light, r.t., 96h

Scheme 3. Synthetic pathway for the synthesis of the ancillary ligand

After the characterization of the molecules by NMR and ESI-MS, the photophysical properties have been investigated (**Figure 9**). In dichloromethane at $c = 10^{-4}$ M, the complexes display the emission of the monomeric species, while in solid state we observe a strong emission for the aggregate form due to the ³MMLCT transition. The PLQY of these complexes in solution are very low (1%). However, in solid state, they are strongly emissive thanks to the formation of the aggregates (59%). The emission of complexes decays bi-exponentially in both solution (CH₂Cl₂, $c = 10^{-4}$ M) and in solid state. For instance, for C6 complex: $\tau_1 = 6$ ns (92%) and $\tau_2 = 187$ ns (8%) in solution, whereas $\tau_1 = 753$ ns (90%) and $\tau_2 = 317$ ns (10%) in solid state.

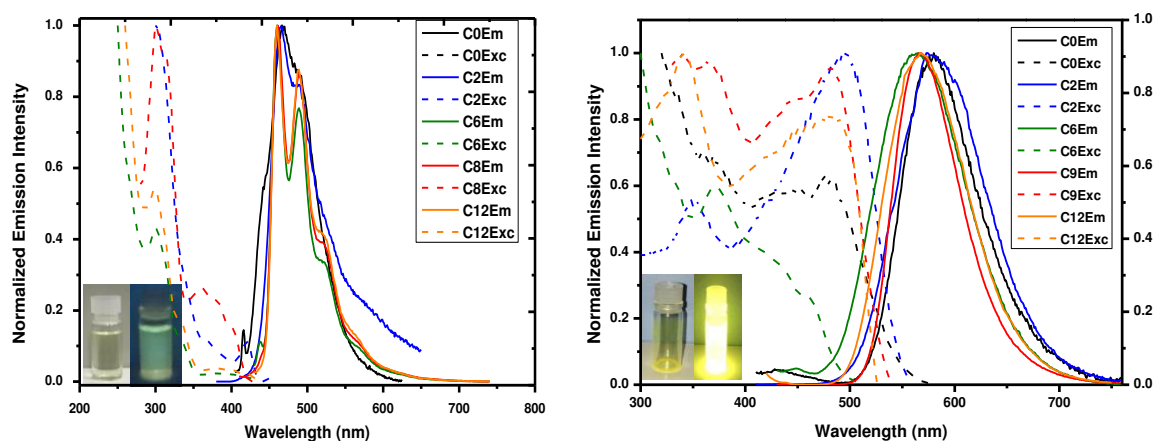


Figure 9. Emission and Excitation spectra of the complexes that are studied in chapter 4.

After deprotection of the thiol group in acidic conditions (HCl 4M),¹⁸ the complexes have been linked to the nanoparticle. XPS and STEM characterization have been performed (Figure 10 as an example for C6 complex). From the S scan in XPS, we can observe both the peaks at 164eV (free S) and at 168 eV (bonded S). STEM image displays the AuNP (around 100nm) surrounded by a layer of the aggregated complex. Regarding the PLQY, we can observe a huge improvement, from 1% without the AuNP to 10% with the latter.

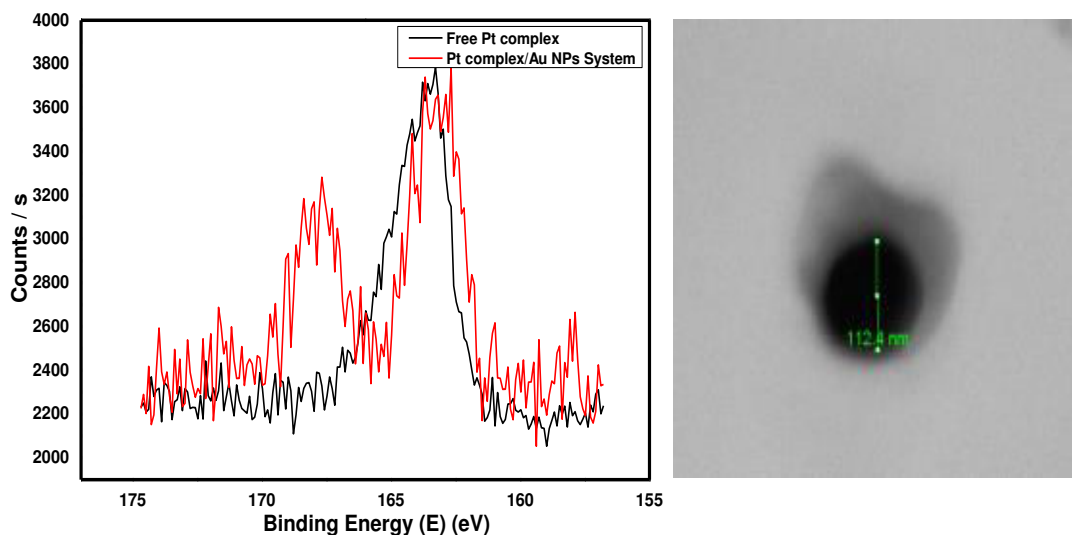
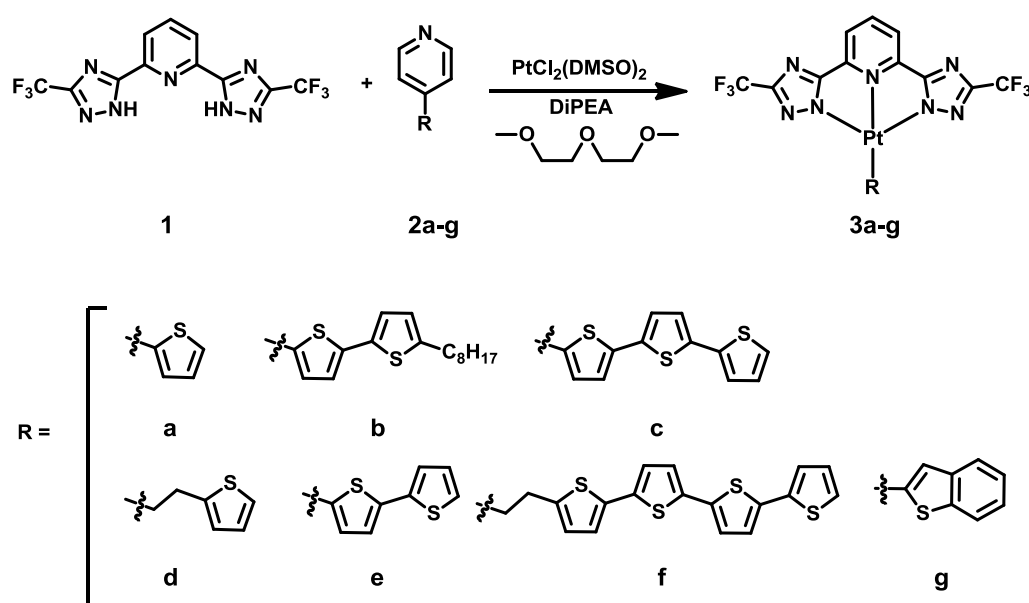


Figure 10. S-scan from XPS spectrum of C6 complex on AUNPs (left), STEM image of C6 complex on AUNP (right)

In chapter 5, a series of square planar platinum (II) complexes containing oligothiophene substituents has been synthesized and characterized. The complexes contain the same dianionic N⁺N⁺N⁺ terdentate ligand and thiophene-functionalized pyridine derivatives as ancillary ligands (**Scheme 4**). Their charge transport properties were studied and the results were correlated to their film morphology, their photophysical properties and the structure of the self-assembly. The establishment of intermolecular Pt-Pt and/or π - π stacking interactions resulted in differences in hole mobility values among the molecules are shown.



Scheme 4. Synthetic pathway towards complexes **3a-g**.

After the synthesis of these complexes, according to the results observed, the complexes showing the best mobility values were further studied, namely complexes **3a**, **3c**, **3f** and **3g**. The emission spectra of the films for **3a**, **3c**, **3f**, **3g** are shown in **Figure 11**.

We simulated the molecular packing of the self-assembled complexes and correlated it with the electron mobility. For this purpose, we selected the assembled of complex **3a**, **3c**, **3f** and **3g** having the best mobility features and measured the PXRD pattern. The geometrical structure was optimized with the program Gaussian.¹⁹ Using the state-of-the-art software Total Pattern Analysis Solution (TOPAS, Bruker AXS),²⁰ the XRD pattern was indexed on 20 peaks within a 2θ value between 5° and 40° , and the investigation was performed for all the crystal systems. Thanks to the same software, a refinement was performed for each structure and then we could obtain the lattice parameters of the studied structures, with Rietveld weighted profiles (Rwp) going from

19% down to 11% (Table SX). An example of PXRD measured and refined pattern is shown in **Figure 12**.

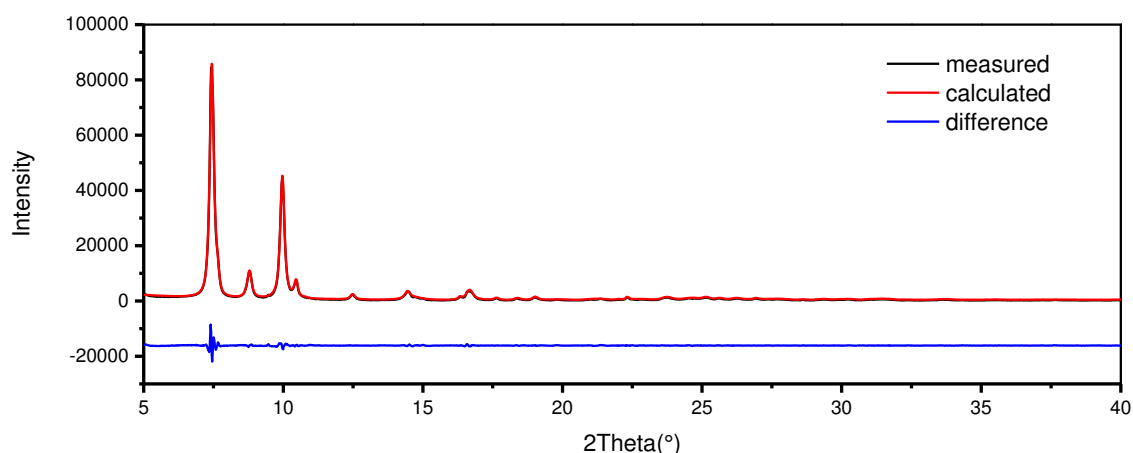


Figure 12. Measured (black trace) and calculated (red trace) PXRD patterns, and difference (blue trace) of **3f**

The simulated molecular packing of each complex has been determined by the Material Studio program, Reflex Module; from the obtained lattice parameters and the structure of the monomeric species. For complexes **3c** and **3f**, which relatively feature a moderate mobility, we don't observe any Pt-Pt interaction. Indeed, the distance is far longer than the required 3.5 Å to have this interaction (6.71 Å). Probably it's due to the tilted conformation of the oligo thiophene which hinders the close packing of the molecules. In particular, **3f** has one ethyl group as a linker between the pyridine and the oligothiophene moieties, inducing free rotation and therefore a slightly distorted geometry. The emission spectra of film **3c** is in agreement with this fact by showing the monomeric emission of the molecules at 440nm, proving the presence of monomers which prevent the formation of close molecular packing.

Complex **3g** features the best hole mobility among all the investigated complexes. This result has been correlated on the one hand from the emission spectrum of the film which shows a very low energy emission; and on the other hand with the intermolecular Pt-Pt distance of 3.2 Å (**Figure 13**)

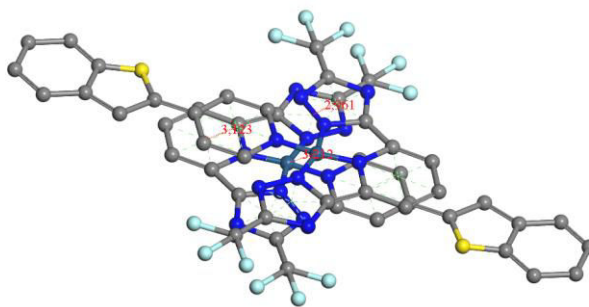


Figure 13. Simulated structure of the self-assembly of **3g**, showing clearly the presence of Pt-Pt interaction

In chapter 6, we show the preparation of new emissive materials based on the inclusion of platinum(II) and iridium(III) complexes inside Al(OH)(bipyridinedicarboxylate) metal organic framework (MOF-253)²¹ (**Figure 14**).

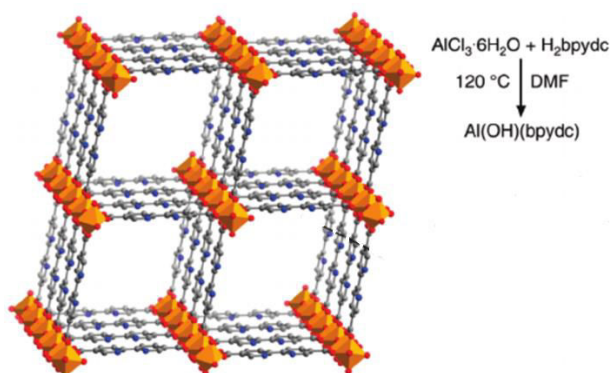
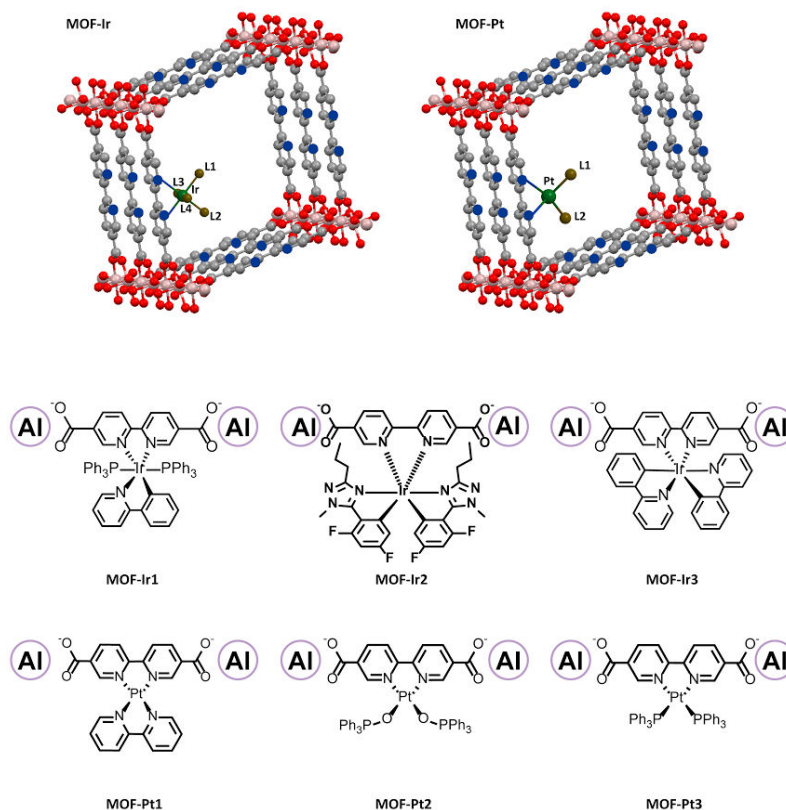


Figure 14. Structure and synthetic pathway of **MOF-253**, the MOF used in this chapter



Scheme 5. Studied MOF-transition metal complexes systems

Firstly, **MOF-253** has been synthesized according to Yaghi's work.²² The further Soxhlet extraction in methanol allows the removal of DMF molecules in order to get a material with pores that are completely empty. The yielded materials have been characterized by TGA, N₂ adsorption-desorption, TEM and PXRD. The photophysical properties of **MOF-253** have been investigated as well, the material being yellow emissive ($\lambda_{\text{max}}=555\text{nm}$), with a very low emission quantum yield (1%) and a very short excited state lifetime, 6ns (87%), 3ns (13%). The inclusion is performed by a ligand substitution leading to the formation of a coordination bond, proven by X-ray photoelectron spectroscopy study, which provides robustness to the system.

In order to prove the creation of this coordination bond, XPS experiments have been performed, using the N1s scan. From this, we could take an interesting point since the difference of binding energy of coordinated and non-coordinated nitrogen in the bipy ligand are different. **Figure 15** shows XPS N 1s high resolution spectra of MOF-253 (A) and MOF-Pt3 (B)

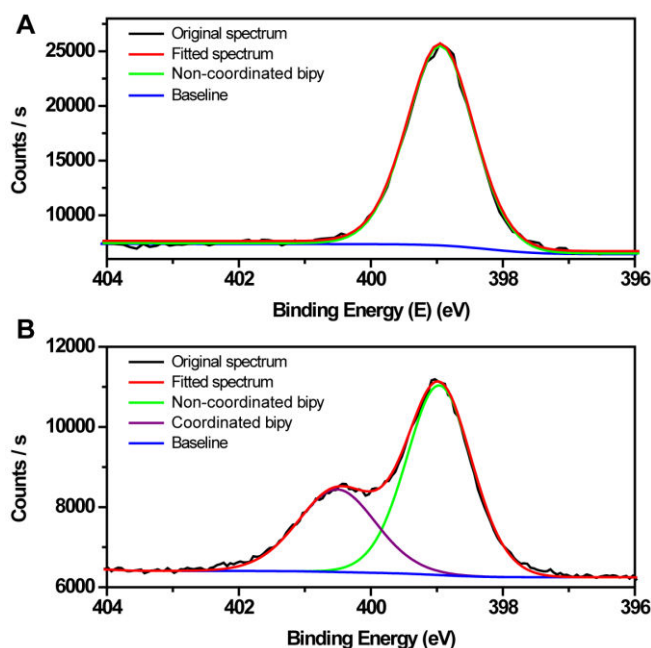


Figure 15. XPS N 1s high resolution spectra of MOF-253 (top) and MOF-Pt3 (bottom).

Apart from XPS, PXRD analysis highlights the high crystallinity of the materials, with a complete change of the lattice parameters before and after each metal complex insertion. Moreover, the photophysical properties of the resulted materials were thoroughly characterized. Using this technique, we are able to tune the emission properties of the materials from the blue to the red, passing by green and yellow. (**Figure 16**). However, we did not observe very significant PLQY after TMC inclusion, the most emissive materials having 5% PLQY.

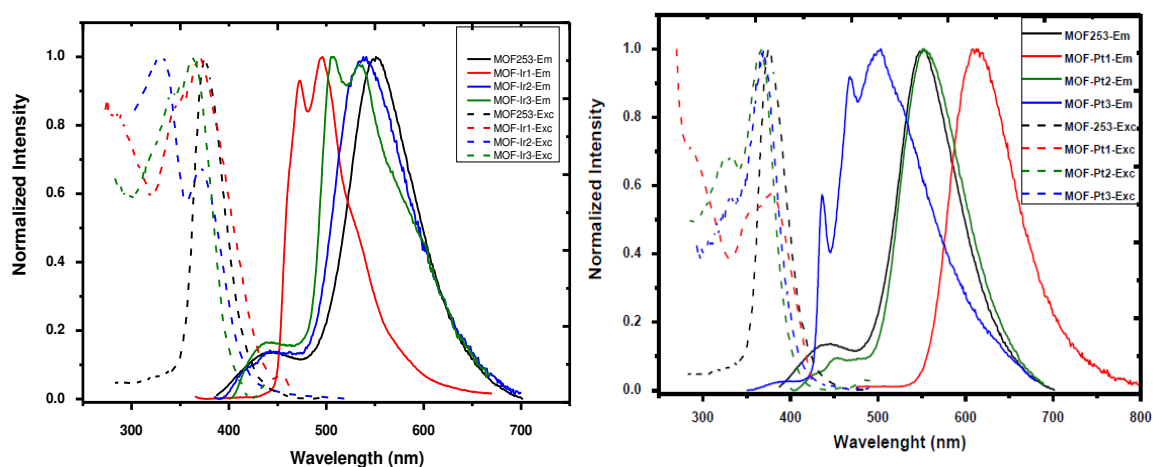


Figure 16. Emission (full line) and excitation (dashed line) of MOF-Ir materials (left) and MOF-Pt (right)

In order to successfully complete all the studies, experimental chemistry requires a lot of physical characterization techniques. According to the yielded product (single molecule, self-assembly, nanomaterial,) and to the information one wants to get, the chosen analytic method, and thus the analytic instrument is different. In the 7th and last chapter of this thesis we describe the different characterization principles, as well as the instruments used to perform these analytical experiments.

4. Conclusion

In this thesis, we successfully synthesized and characterized platinum(II) complexes with a dianionic N⁻N⁻ terdentate ligand. According to the design of the ancillary ligand, we were able to apply the complex for different applications, in order to stabilize the self-assemble aggregates, to improve the photoluminescence properties or even to tune the molecular packing. The incorporation of Pt(II) and Ir(III) complexes by a coordination bond in order to tune the emission color are also investigated

5. References

1. A. J. Lees *Chem. Rev.* **1987**, 87, 711
2. M. Mauro, A. Aliprandi, D. Septiadi, N. S. Kehr, L. De Cola *Chem. Soc. Rev.* **2014**, **43**, 4144
3. C. Cebrian, M. Mauro, D. Kourkoulos, P. Mercandelli, D. Hertel, K. Meerholz, C. A. Strassert, L. De Cola *Adv. Mater.* **2013**, 25, 437
4. Miskowski, V. M.; Houlding V. H. *Inorg. Chem.* **1989**, 28, 1529
5. W. Lu , M. C. W. Chan, N. Zhu, C.-M. Che, C. Li, Z. Hui *J. Am. Chem. Soc.* **2004**, 12, 7639
6. M. Mauro, A. Aliprandi, C. Cebrián, D. Wang, C. Kübel, L. De Cola *Chem. Commun.* **2014**, 50, 7269
7. A. Aliprandi, M. Mauro, L. De Cola, *Nature Chemistry* **2016**, 8, 10
8. B. Ma, J. Li, P. I. Djurovich, M. Yousufuddin, R. Bau, and M. E. Thompson *J. Am. Chem. Soc.* **2005**, 127, 29
9. J.-P. Collin, J. Frey, V. Heitz, J.-P. Sauvage, C. Tock, L. Allouche *J. Am. Chem. Soc.* **2009**, 131, 5609
10. B. J. Coe, S. P. Foxon, E. C. Harper, M. Helliwell, J. Raftery, C.A. Swanson, B. S. Brunshawig, K. Clays, E. Franz, J. Garín, J. Orduna, P. N. Horton, Michael B. Hursthouse *J. Am. Chem. Soc.* **2010**, 132, 1706
11. H. J. Pownall, L. C. Smith *Biochem.* 1974, 13, 2590
12. M. M. Velázquez and Silvia M. B. Costa *J. Chem. Soc., Faraday Trans.* **1990**, **86**, 404313. C. T. Kresge, M. E. Leonowicz, W. J. Roth, J. C. Vartuli, J. S. Beck *Nature* **1992**, 359, 710

14. A. Bertucci, E. A. Prasetyanto, D. Septiadi, A. Manicardi, E. Brognara, R. Gambari, R. Corradini, and L. De Cola *Small* **2015**, 11, 5687
15. M. B. Silva Botelho, J. M. Fernandez Hernandez, T. B. de Queiroz, H. Eckert, L. De Cola Andrea Simone Stucchi de Camargo *J. Mater. Chem.* **2011**, 21, 8829
16. J. S. Beck, J. C. Vart Uli, W. J. Roth, M. E. Leonowicz, C. T. Kresge, K. D. Schmitt, C. T-W. Chu D. H. Olson E. W. Sheppard, S. B. McCullen, J. B. Higgins, and J. L. Schlenkert *J. Am. Chem. Soc.* **1992** 27, 10834
17. S. A. M. Osborne Z. Pikramenou *Faraday Discuss.* **2015**, **185**, 219
18. J. Poppenberg, S. Richter, E. Darlatt, C. H.-H. T, Hyegeun Min, W. E.S. Unger C. A. Schalley *Surf. Sci.* **2012**, 606 367.
19. Gaussian, Inc., Wallingford CT, 2004
20. A. A. Coelho *J. Appl. Cryst.* **2003**, 36, 86
21. J. L.C. Rowsell, O. M. Yaghi *Microporous and Mesoporous Materials* **2004**, 73, 3
22. E. D. Bloch, D. Britt, C. Lee, C. J. Doonan, F. J. Uribe-Romo, H. Furukawa, J. R. Long, O. M. Yaghi, *J. Am. Chem. Soc.* **2010**, 132, 14382

CHAPTER 1:

General Introduction

Abstract

As its name suggests, my thesis deals with the synthesis and the investigation of new emissive hybrid materials based on the encapsulation, adsorption and insertion of transition metal complexes in/on inorganic structures. The first chapter of my thesis is a general introduction explaining the basic principles of luminescence, transition metal complexes and supramolecular chemistry. It also illustrates the state of the art of the different topics discussed in the thesis. In particular, an introduction on mesoporous silica nanoparticles, gold nanoparticles and metal organic frameworks is given. Finally, the scope of the thesis is discussed.

1.1. Introduction on photophysics and photochemistry

Light is a physical phenomenon consisting of electromagnetic waves which are synchronized oscillations of electric and magnetic fields. In general, light can be studied by the frequency or wavelength of their oscillations, which implies the energy according to the following formula:

$$E = h\nu = h\frac{c}{\lambda} \quad (1.1)$$

E: energy of the wave (J)

H: Planck constant $\approx 6.63 \cdot 10^{-34} \text{ J.s}$

ν : frequency of the wave (s^{-1})

λ : wavelength (m or nm)

Although the term “light” refers in the daily life to visible light, it is in reality extended to the entire electromagnetic spectrum (**Figure 1.1**); most particularly the infrared (IR), the visible and the ultraviolet (UV) regions.

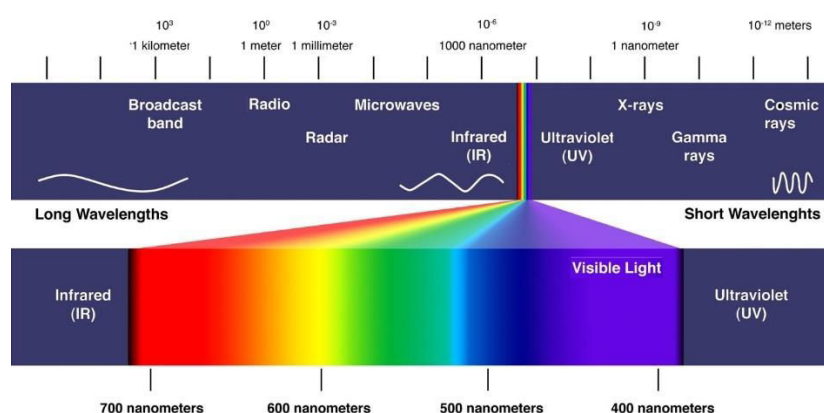


Figure 1.1. Electromagnetic spectrum, with the IR, visible and UV regions brought out. As the wavelength increases, the frequency and the energy decreases

The field of physics which studies light and electromagnetic radiations properties, as well as systems using and emitting light is called wave optics. Due to the wave-particle duality, electromagnetic waves can be modelled in two ways that are complementary. On the one hand, the electromagnetic wave and on the other hand, the photon: corpuscle featuring a null mass and a spin of 1.

The history of electromagnetism discoveries is described as follows. In ancient times, Greeks discover static electricity by rubbing two different materials, amber and fur. It

is only in 1747 that Benjamin Franklin discovered that there are two kinds of charges: positive and negative, and that like charges repel and unlike charges attract. 40 years later, Charles-Augustin Coulomb published Coulomb's law: the force F between two charges q_1 and q_2 is proportional to their product divided by the separation distance r squared:

$$F = \frac{q_1 q_2}{r^2} \quad (1.2)$$

The end of the eighteenth century and the beginning of the nineteenth century showed a big improvement in the field, since Alessandro Volta found chemistry acting on two dissimilar metals generates electricity in 1790. In 1820, Hans Christian Oersted and Michael Faraday discovered that current can induce magnetism, and magnets can have an effect on electricity. In the same year, André Marie Ampère showed that wires carrying current produce forces on each other. In 1860, James Clerk Maxwell summarized the works of Coulomb, Oersted, Ampère, Faraday in the so called Maxwell equations. They are currently studied as the bases of electromagnetic theory. In 1885, Heinrich Hertz proved Maxwell was correct and was able to generate and to detect electromagnetic waves.

The interaction wave-matter can be observed at the molecular scale. In this purpose, luminescence is the physical phenomenon of light emission corresponding to a certain stimulus, that may be electrical, chemical, or photonic.¹⁻⁴ The latter is due to photon absorption by a molecule, which is therefore passing to a state called excited state and emitting light as a result. In this case, we can talk about photoluminescence.

In detail, certain molecules (mostly if they contain π -conjugated systems) are able to absorb a photon at a given range of energy. This molecule A is then in an electronically excited state, according to:



The resulting excited molecule A^* has a different behaviour than the ground state molecule A. The excited molecule has a relatively short lifetime (from less than 1 ns to several ms, according to the nature of the molecule).

The various transitions involving electronic states of similar or different spin multiplicities, as well as vibrations associated with electronic states, are represented

in the so-called Perrin-Jablonski diagram (from Francis Perrin and Alexandre Jablonski, who stated this diagram around 1930) (**Figure 1.2**).

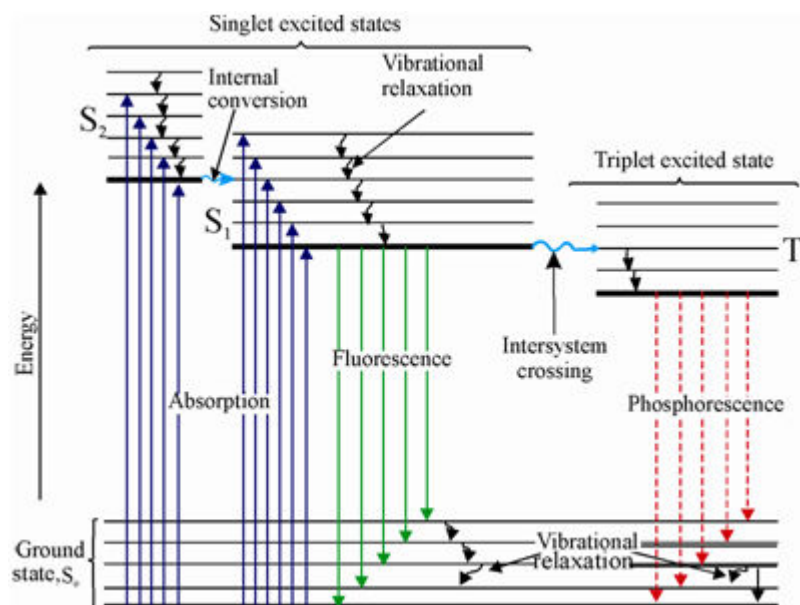


Figure 1.2. Perrin-Jablonski diagram

This diagram is explained here below:

When a molecule absorbs light, it gets excited. Depending on the molecular rigidity, radiative and non-radiative deactivation can take place. However, the internal conversion (IC) decreases exponentially with the increase of the energy gap between states (energy gap law). The radiative deactivation between singlet excited state and ground state is called fluorescence if it occurs with conservation of electronic spin. This process, coming exclusively from the singlet state, is relatively fast (ns range) because it does not need any spin change. It is important to mention that the emitted light possesses lower energy compared to the absorbed light (Stokes shift) due to the loss of heat and reorganization of energy. The resulting outcome is a shift between the absorption or excitation wavelength and the emission wavelength. Nevertheless, intersystem crossing (ISC) between singlet and triplet state can occur in the case of molecules where heavy atoms are involved, and the excited state features a longer lifetime due to its spin-forbidden nature (μs to several ms range). The spin orbit coupling (SOC) is responsible for this process, allowing the flip of the electronic spin and therefore, the ISC to be identified with the so called phenomenon of phosphorescence. This process is obviously induced by the triplet state. The ISC is favoured by heavy atoms, for instance, by collision (external heavy atom effect). The

effect is much more pronounced if they are part of the molecule and involved in the electronic transitions.

For instance, the SOC can be induced by transition metals ions such as Cu(I), Ru(III), Ir(III), Pt(II) and Au(I), but also lanthanides ions or iodide.

Singlet and triplet states can be mixed, leading to excited states with partial singlet and triplet character. Thus, the otherwise strictly forbidden radiative transition from the lowest triplet state can be partially allowed. As the rigidity of the molecule hinders the non-radiative deactivation of the lowest triplet state, a phosphor is obtained (phosphorescence). The deactivation of the excited states follows first order kinetics and the lifetime of the excited states (S1 or T1) can be represented with the equations shown below.

$$\tau_f = \frac{1}{k_r^S + k_{nr}^S} = \frac{1}{k_r^S + k_{ic}^S + k_{isc}} \quad (1.3)$$

$$\tau_p = \frac{1}{k_r^T + k_{nr}^T} \quad (1.4)$$

Due to the spin selection rules, the excited state has the same spin multiplicity as the initial state. Moreover, the excitation process takes about 10 fs, which is a very short time in respect to the characteristic time of molecular vibrations (100 to 1 ps). According to Born–Oppenheimer approximation, the external electrons can move much faster upon external perturbation than the heavier nucleus, the latter being considered as stationary. This results in the Frank-Condon principle, where an electronic transition occurs without change of nuclei positions in the molecular environment. Furthermore, after the absorption of a photon by a molecule in the ground state and the resulting formation of the excited state, the subsequent radiative emission is done from the excited state of lowest energy (S1 or T1); and the emission wavelength is independent on the excitation wavelength. This rule, so-called Kasha rule, is based on the fact that the energy absorbed in the relaxation process from the excited states is much faster (10 fs) than the photon emission (10 ns)

The three main parameters that have to be taken into account for luminescent molecules or materials are: the excited state lifetime (ESLT, τ , s), the emission quantum yield or photoluminescence quantum yield (PLQY, ϕ) and the emission wavelength (λ , nm). They all depend on the material itself, but also on the environment (e.g. solvent, temperature, pressure).

The first parameter, ESLT, is the required time, for a luminescent molecule after excitation, to go back to the ground state. If we take the example of fluorescence phenomenon, upon light excitation, a certain percentage of A molecules are converted to A*. These excited molecules then go back to the ground state, either radiative, or non-radiative, or passing by ISC. As in classical chemical kinetics, the A*rate loss is expressed by the following equation:

$$-\frac{d[{}^1A^*]}{dt} = (k_{nr}^S + k_{nr}^S)[{}^1A^*] \quad (1.5)$$

By integrating this equation, we can obtain the following equation:

$$[{}^1A^*] = [{}^1A^*] \exp\left(\frac{-t}{\tau_s}\right) \quad (1.6)$$

Where $[{}^1A^*]$ is the concentration of excited molecules and τ_s is the excited state lifetime, according to equation (3).

The PLQY can be defined as the ratio between emitted photons over absorbed photons. It is given by the following equations, Φ_F being the fluorescence quantum yield (singlet state), Φ_{ISC} the intersystem crossing quantum yield (passage from the singlet to the triplet state) and Φ_P the phosphorescence quantum yield (triplet state):

=====

$$\Phi_F = \frac{k_r^S}{k_r^S + k_{nr}^S} = k_r^S \tau_s \quad (1.7)$$

$$\Phi_{ISC} = \frac{k_{ISC}}{k_r^S + k_{nr}^S} = k_{ISC} \tau_s \quad (1.8)$$

$$\Phi_P = \frac{k_r^T}{k_r^T + k_{nr}^T} \Phi_{ISC} \quad (1.9)$$

It can never be above 1 or 100%.

1.2. Introduction to transition metal complexes

This thesis is mainly based on the photoluminescence properties of a particular class of molecules, known as transition metal complexes (TMCs).

Transition metals have been deeply studied in many fields, such as bio-medicine,⁵⁻⁷ biomimetic⁸⁻⁹, catalysis and green chemistry,¹⁰⁻¹² magnetism and spin crossover materials,¹³ bio-imaging¹⁴⁻¹⁶, diagnostics,¹⁷ activation of small molecules¹⁸⁻¹⁹, energy conversion²⁰, nanoscience,²¹ supramolecular chemistry,²²⁻²⁴ molecular electronics,²⁵⁻²⁶ or optics and photoluminescence; as active materials in organic light emitting diodes (OLEDs),²⁷⁻²⁸ light emitting electrochemical cells (LEECs)²⁹ or dye sensitized solar cells (DSSCs).³⁰⁻³³ In comparison to their luminescent organic counterparts, most of the TMCs feature long ESLTs, high PLQY, large Stokes shifts, and stability for most of them. In particular, second and third row transition metal ions such as Ru(II), Os(II), Ir(III), Re(I), Pt(II) and Au(I) are investigated for their luminescence properties. They present different coordination number (from 2 to 6), different geometry (linear, trigonal planar, square planar, tetrahedral, trigonal bipyramidal, square pyramidal, octahedral) and different number of valence electrons (6,8,10). This is explained by the molecular orbital theory (MOT), the crystal field theory (CFT) and the ligand field theory (LFT). MOT was first stated and developed by Friedrich Hund, Robert Mulliken, John C. Slater, and John Lennard-Jones during the 30s. It can be defined as a model used for molecular structure determination, in which the electrons are not assigned to chemical bonds between atoms, but they rather can be localized anywhere in the molecule, under the influence of the molecule nucleus. In MOT, each molecule has molecular orbitals, that can be defined as the zone in which the probability to find electrons is the highest. If the probability to find electrons between the nuclei is higher, the orbital is bonding and this makes the bond stronger. If the probability to find electrons somewhere else is higher, the orbital is considered as anti-bonding and weakens the bond. If the probability to find electrons between the nuclei and elsewhere is similar, the orbital is considered as non-bonding. These electrons have no particular effects on the bonding strength.

CFT is a model developed by Hans Bethe and John Hasbrouck van Vleck in 1930 that represents the electronical configuration of TMCs only by considering the electrons in the d orbital. This theory is a combination between electrostatic theory and quantum theory. In CFT, there is repulsion between d orbitals electrons of the metal ion and π electrons of the ligand. The ligand is visualized as charges whereas the metal ion by the d orbitals energy levels and the electrons that they contain.

There are 5 d orbitals, and are called d_{xy} , d_{xz} , d_{yz} , $d_{x^2-y^2}$ and d_z^2 , according to the three directions in the space (**Figure 1.3**) or d_{-2} , d_{-1} , d_0 , d_1 and d_2 if we refer to the magnetic quantum number m ($m=-2, -1, 0, +1, +2$).

By the combination of the two previous theories was established the LFT by John Stanley Griffith and Leslie Eleazer Orgel in 1957.³⁴ It describes the molecular orbitals of a d-metal complex as polyatomic molecules. In this case, the metal and ligand valence orbitals are used to form symmetry-adapted linear combinations and to estimate the relative energies of the molecular orbitals taking into account empirical energy and overlap considerations.

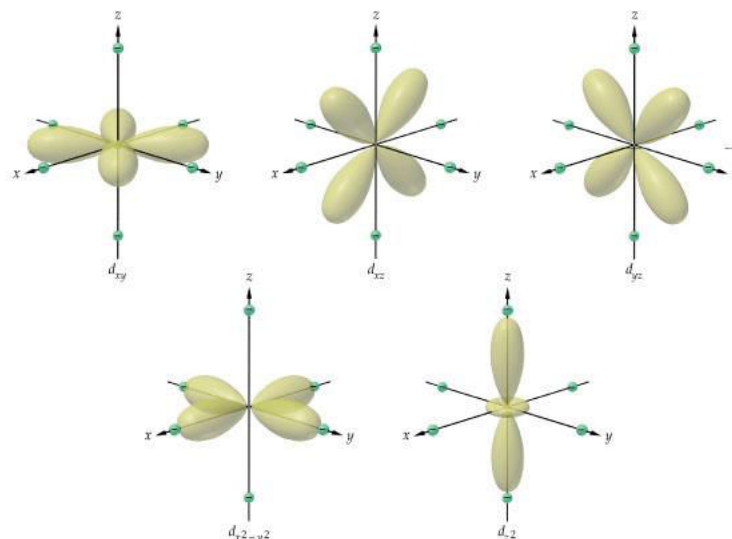


Figure 1.3. Representation of the d orbitals in a transition metal ion

As previously mentioned, molecular electronic transitions happen when outer electrons are excited from an energy level towards a higher one. The energy gap of this transition gives us several information about the molecule, for instance the colour. The relation between the energy level and the radiation frequency is given by equation (1). Electronic transitions of organic compounds can be determined par UV-Vis spectroscopy, as long as the transition takes place in the UV-Vis region of the electromagnetic spectrum. The different molecular electronic transition in an organic molecule occur from the HOMO to the LUMO, and can be described as following (c.f. **Figure 1.4**) : $\sigma \rightarrow \sigma^*$, $\pi \rightarrow \pi^*$, $n \rightarrow \sigma^*$, $n \rightarrow \pi^*$.

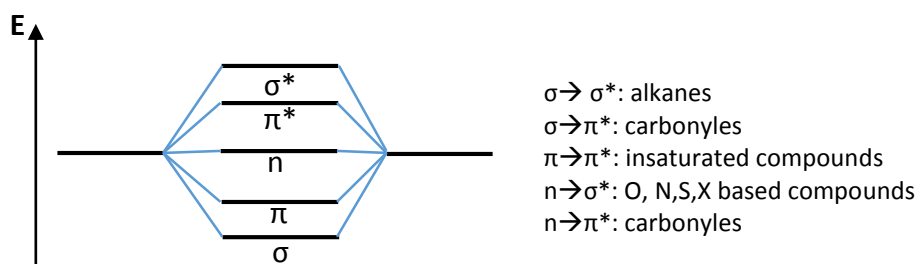


Figure 1.4. Simplified energy diagram showing level energy and some possible transitions

For a sample in solution, the efficiency of such transition are given by the molar extinction coefficient (ϵ , $\text{L}\cdot\text{mol}^{-1}\cdot\text{cm}^{-1}$). The relation between ϵ and the absorbance A (without unit) is given by the following equation, the so-called Beer-Lambert law:

$$A = \epsilon \cdot c \cdot l. \quad (1.10)$$

In which c is the concentration (mol) of the sample, and l is the length (cm) of the optic path of the cell containing the sample, also called cuvette. These phenomena can be solvent dependent, with sometimes additional bathochromic or hypsochromic shifts.

1.3. Introduction on platinum complexes and their assemblies

In particular, this thesis involves the supramolecular self-assembly of platinum (Pt) (II) complexes. Platinum belongs to the third row of TMCs, its electronic configuration is: $[\text{Xe}].4f^{14}.5d^9.6s^1$. The more stable oxidation state of Pt is Pt(II), having the following electronic configuration $[\text{Xe}].4f^{14}.5d^8$, which allows a coordination number of 4 and a square planar geometry. However, under strong oxidative medium, it can be Pt(IV) ($[\text{Xe}].4f^{14}.5d^6$, oxidation number of 6 and octahedral geometry).³⁵

The discovery of cisplatin,³⁶⁻³⁷ and later carboplatin³⁸⁻³⁹ was an important breakthrough in anti-cancer research. More recently, several systems using cisplatin derivative where used, not as a drug but as a prodrug bearing vectors in order to reach the target tumor tissues with minimal loss in the blood circulation and to be released in the correct dosage necessary to kill tumor cells. In this case, the oxidation state of Pt is 4 (c.f. **Figure 1.5.**).⁴⁰

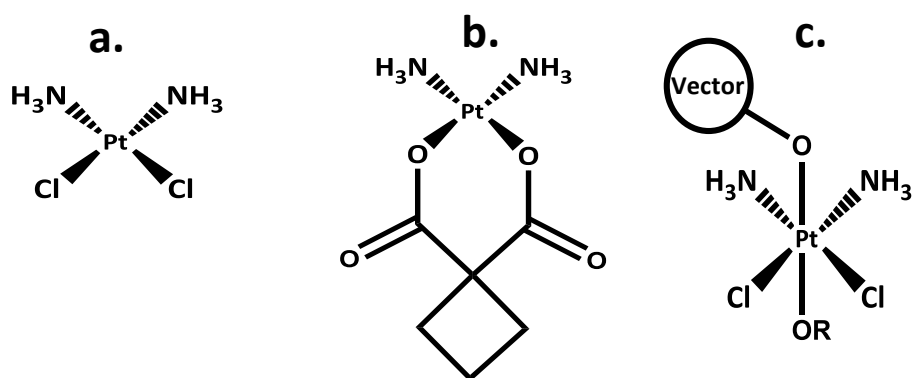


Figure 1.5. Structures of **a.** cisplatin **b** carboplatin **c** cisplatin attached to a vector

Platinum(II) complexes are also used for catalysis purposes, for instance olefin hydrosilylation⁴¹ or cycloadditions⁴². However, they are much less explored than their palladium(II) counterparts.

The pioneer of luminescent Pt(II) complexes is Pt(octaethylporphyrine),⁴³ still currently used as an oxygen sensor.⁴⁴ Since this time, thanks to their enthralling luminescent properties, Pt(II) complexes are intensively studied for applications in OLED,^{28, 45}. In 2014, the group of Li designed WOLED made by excimers of Pt(II) complexes⁴⁶. In Pt(II) complexes, the absorption, excitation and emission wavelengths, as well as the PLQY and ESLT are dependent on the aggregation state, i.e. the supramolecular self-assembly. Thanks to this particular geometry, Pt(II) complexes, while bearing aromatic rings as ligands, have the tendency to self-assemble through π - π stacking (between the ligands). Consequently, when the distance between two species reaches 3.5 Å (because the van der Waals diameter of Pt is 3.5 Å), metal to metal interactions (also called metallophilic interactions), occur due to the overlap of the 5d^{z²} orbitals, resulting in supramolecular polymeric structures. The 3.5 Å distance has been found in both, theoretical and experimental studies, particularly with density functional theory (DFT) calculations and X-ray diffraction crystallography, being the latter one of the main characterization tools in supramolecular chemistry.⁴⁷⁻⁴⁸ In fact, according to LFT, in a square planar TMC, the d^{z²} orbitals are perpendicular to the molecule plane, and contain electrons that do not interact with the ligands coordination sphere. A new electronic transition is hence formed, so-called metal-metal to ligand charge transfer (MMLCT) (**Figure 1.7**).⁴⁹⁻⁵⁰ Because the metal to metal interaction is repulsive, the highest occupied molecular orbital (HOMO) is destabilized, while its lowest unoccupied molecular orbital (LUMO) gets stabilized. The energy gap becomes much shorter, resulting in a bathochromic shift on the absorption (thus excitation) and the emission, yielding dramatic changes in their luminescent properties.⁵¹⁻⁵² The strength of such metal-metal interactions has been compared to that of hydrogen bonding (ca. 30–50 kJ mol⁻¹),⁵³ which is sufficient to form supramolecular structures.

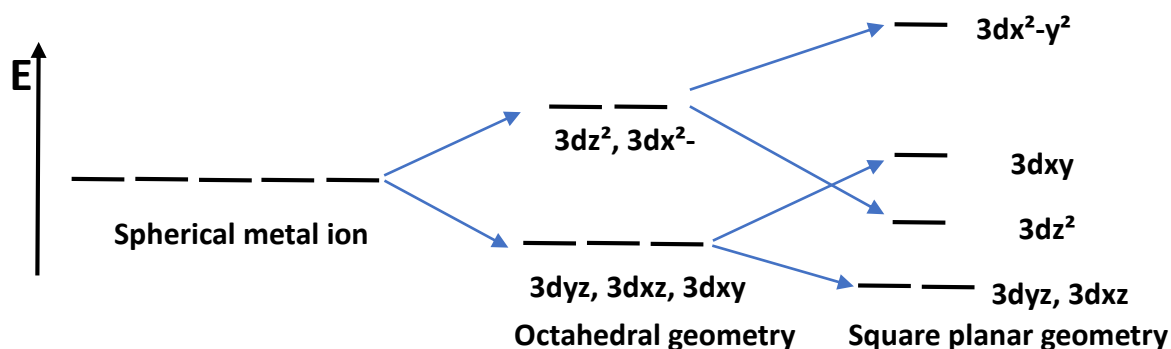


Figure 1.6. Crystal field stabilization energy for octahedral symmetry and square planar symmetry

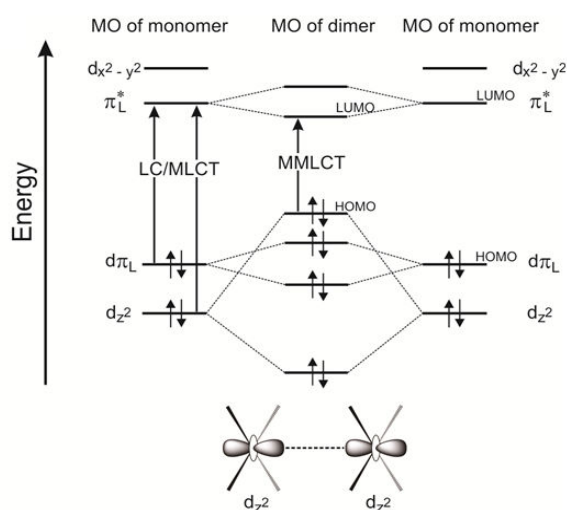


Figure 1.7. Frontier molecular orbital diagram showing the effect of intermolecular interactions and d_{z^2} orbital overlap⁵⁰

Several examples related to self-assembly of Pt(II) complexes were reported in the literature. Since the discovery of Magnus green salt $[\text{Pt}(\text{NH}_3)_4][\text{PtCl}_4]$ and up to now, it is the most studied metal ion for demonstrating metal---metal interactions. Various works involving several ligands were published. For instance, cyanides and isocyanides derivative were deeply studied.^{35, 54-55} Pt(II) complexes aromatic ligands showed a more interesting behaviour, since π - π stacking interactions are also involved in the self-assembly process bearing bidentates ligands were widely described by Yersin,⁵⁶ Gray,⁵⁷ Che⁵⁸ or McMillin, among others. The distance between two platinum cations is solvent and temperature dependent. Che and coworkers showed the existence of excimer formation of $[\text{Pt}(\text{ditert-butyl pyridine})(\text{CN})_2]$ induced by the non-covalent interactions previously mentioned⁵⁹. Vapochromism phenomenon were also found as an interesting feature of Pt(II) complexes, when different organic solvent vapor has an

effect of the emission color of [Pt(phenantroline)(CN)₂].⁶⁰ Vapochromism was then used as efficient sensor by Che, using a cyclometalated carbene ligand.⁶¹ A huge library of other ligands were investigated, such as terpyridines,^{52, 62} or pyridine bistriazoles^{14, 51, 63} as sensors, bio-imaging agents or in order to control the self-assembly process.

1.4. Introduction to self-assembly

Self-assembly is a discipline of chemistry first defined by Prof. Jean-Marie Lehn, 1987 Nobel prize laureate in chemistry⁶⁴ with Charles John Pedersen⁶⁵ and Donald James Cram⁶⁶ for their contribution to the development and use of molecules with structure-specific interactions of high selectivity. He defined it as: «Beyond molecular chemistry, based on covalent bond, *is extended a domain that one can call supramolecular: chemistry of molecular interactions, of the association between two or several chemical species, and of intermolecular bonds*». It involves the selective recognition of molecules through non-covalent interactions⁶⁷⁻⁶⁸ such as hydrogen bonding,⁶⁹⁻⁷¹ van der Waals interactions, hydrophobic interactions,⁷²⁻⁷³ metal-metal interactions, π - π stacking,⁷⁴⁻⁷⁷ electrostatic interactions,⁷⁸⁻⁷⁹ halogen bonding⁸⁰⁻⁸¹ and coordination bonding⁸²⁻⁸³ in order to yield macroscopic organized structures. Although non-covalent interactions are weaker than their covalent counterparts, their combination can form robust structures. Moreover, supramolecular chemistry helped scientists to understand several aspects of science, in particular the behavior and the working of biological systems.⁸⁴

Because supramolecular systems are created from building blocks linked by noncovalent interactions, they can show stimuli-responsive behaviour. Nowadays, approximately supramolecular chemistry and self-assembles structures have been widely explored in templated synthesis, host-guest supramolecular systems, molecular machines,⁸⁵ sensors, gas absorption, catalysis, and drug delivery.

For instance, several works were reviewed on assembled structures of carbon nanotubes, graphene, and fullerenes, and their superstructured assemblies;⁸⁶ or on drug delivery systems based on supramolecular systems.⁸⁷ Zhang's work is more focused on supramolecular polymers prepared from self-assembly of small molecules.⁸⁸ Liu showed the importance of chiral supramolecular entities assemblies.⁸⁹ Catenanes and rotaxanes-type materials, pioneers of molecular rotors,⁸⁵ were mainly developed by Jean-Pierre Sauvage, Nobel Prize laureate in 2016.

Table 1.1. Recap chart of the main non-covalent interactions, with the distance, the strength and the directionality.

Interaction	Consist on:	Distance (Å)	Strength (Energy, kJ. mol ⁻¹)	Directionality
Covalent	Sharing of electron bonding pairs between atoms	0.7-3	100-400	Yes
Hydrogen bonding	Hydrogen shared between electronegative atoms	1.2-3.2	5-45	Yes
Van der Waals	Fluctuations in electron clouds around molecules oppositely polarized between neighboring atoms	Van der Waals radius of each atom	≤5	No
Hydrophobic	Hydrophobic groups interact with water and tend to pack together to exclude water molecules	≤10	1-10	No
Metal-metal	Overlap between two d orbitals of two metals	≤3.5	≤50	Yes
π-π stacking	π orbital overlap in π conjugated systems	≤4	≤10	No
Electrostatic	Attraction between opposite charges and	Dependant on energy (Coulomb law)	1-20	No
Cation- π	Interaction between a positive charge and a π-system of a conjugated molecule	6	1-80	No
Halogen	Overlap between two d orbitals of metal ions	1-4	5-100	Yes
Coordination	Lewis Acid-base type attraction between a metal ion and the lone pair of a ligand	1.5-3	20-300	Yes
Dipole-dipole	Attraction between the positive end of one molecule and the negative end of another	1.5-6	1-30	No

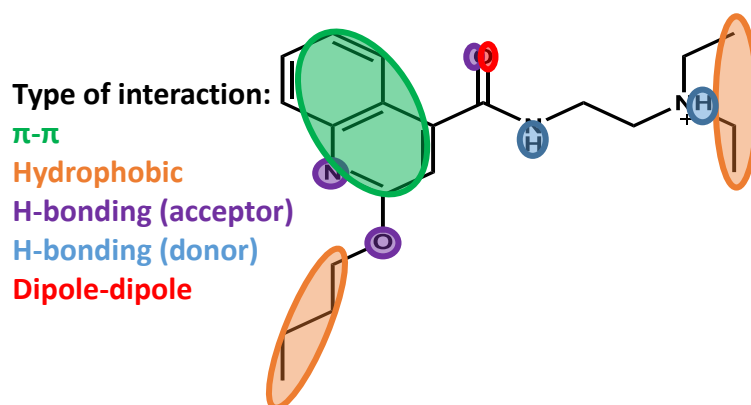


Figure 1.8. Structure of lidocaine showing different type of non-covalent interaction that can be involved

As this thesis is more focused on luminescence of TMCs, self-assembled systems of TMCs were deeply studied⁹⁰. As examples, d^8 Rh(I) complexes take a square planar geometry while coordinated to four different ligands, and their packing was investigated, mainly with isocyanates derivatives.⁹¹⁻⁹² Balch et. al reported red emissive monomeric, dimeric and trimeric species with Rh---Rh bonds between 3.05 and 3.3 Å.⁹³ Ir(I) complexes were less investigated. However, Geoffroy and co-workers reported oligomeric Ir(I) characterized by UV-Vis absorption.⁹⁴ More recently, Gray determined the Ir---Ir distance in such structures, going down to 3.6 Å.⁹⁴

Luminescent supramolecular structures of TMCs has been also developed with Pd(II)⁹⁵, Cu(I),⁹⁶⁻⁹⁷ Ag(I),⁹⁸ Au(I)⁹⁹⁻¹⁰² and Pt(II). The latter was discussed in part 1.3.

Table 1.1 is a recap chart of the main non-covalent interactions, with the distance, the strength and the directionality. **Figure 1.8** shows an example of a molecule featuring many non-covalent interaction sites: Lidocaine, a drug used for anaesthesia.

1.5. Introduction on mesoporous silica nanoparticles

Porous materials represent a class of novel and applicable materials. They can be inorganic, organic or hybrid and are classified as microporous (pore size up to 2 nm), mesoporous (pore size between 2 and 50 nm) and macroporous (pore size above 50 nm). The presence of pores allows a wide range of properties and applications. Typical examples are zeolites and zeolite-like materials, pillared materials, clathrates, molecular sieves, porous hybrid materials, or porous metal oxides.

Among them, mesoporous silica nanoparticles (MSNs) represent a class of porous inorganic materials more and more used in nanotechnology. There were first reported

by the oil company Mobil in 1992¹⁰³ and compared to “zeolite-like materials”. The proposed mechanism of their formation is showed in **Figure 1.9**. During the two last decades, several type of mesoporous silica were synthesized and applied in different fields, such as catalysis,¹⁰⁴⁻¹⁰⁶ adsorption,¹⁰⁷⁻¹⁰⁸ separation,¹⁰⁹⁻¹¹⁰ sensing,¹¹¹⁻¹¹³ and drug delivery.¹¹⁴⁻¹¹⁶ MSNs have been strongly investigated due to their stability, their tunable shape and tunable pore size, their narrow pore distribution, the fact that they are FDA approved, and their high pore size to material size ratio. MSNs are made according to a sol-gel method, in which micelles formed by surfactants act as a template for pores. The condensation of a silica source all around the micelles by a modified Stöber synthesis¹¹⁷ in acidic or basic media enables the formation of silica. The further removal of the surfactants allows the formation of pores. Surfactants arrangement plays a crucial role in the pore ordering. They are also called “*structure directing agents*”, and the use of different surfactants and/or silica sources has as a consequence a change in the pore size, pore ordering, particle size or morphology. For instance, if Na_2SiO_3 is used as silica source, MSNs have larger pores and higher specific surface area than the one with tetraethylorthosilicate (TEOS).¹¹⁸ This is due to the fact that the presence of inorganic salts increases the number of aggregates of the surfactant micelles. In more recent works, by simply adjusting the concentration and the molar ratio of the surfactant and the basic catalyst, it is possible to control the shape, from spherical to rods.¹¹⁹ This result can be explained by the concept of critical micellar concentration (CMC).¹²⁰ CMC can be defined as the concentration needed for a given surfactant in a given solvent and a given temperature to form micelles. As examples, the CMC of cetyltrimethylammonium bromide (CTAB) in water at 25°C is 0.8mM while for sodium dodecyl sulphate (SDS), it is 7mM. A part of these parameters, the CMC also depends on the pH of the medium, the ionic strength (if the surfactant is charged), or geometrical parameters, such as the length of the hydrophobic tail and the volume of the hydrophilic head. It is important to note that several techniques are used to determine CMCs. The most known and used types of MSNs are MCM (Mobil Composition of Matter)-41,^{103, 121} MCM-48,¹²² SBA (Santa Barbara Amorphous)-15.¹²³ **Table 1.2** shows the different characteristics of these three porous nanomaterials. Therefore, as shown in **Figure 1.10**, when the concentration is above the CMC, the surfactant would self-assemble into micelles. According to Philips,¹²⁰ when $(d^3F/dC_t^3)=0$, $C=CMC$; with $F = a[\text{micelle}] + b[\text{monomer}]$, C_t = total concentration, **a** and **b**= constants.

As previously mentioned, according to the geometry and the environment of the surfactant, it is possible to reach a second and a third CMC. At “CMC 2”, the aggregation would have an elongated cylinder shape, and at “CMC 3”, it would take a lamellar structure (**Figure 1.10.**).

Table 1.2. Different characteristics of MCM-41, MCM-48, SBA-15. In MCM-41 synthesis, the concentration of CTAB and of the base is lower than in MCM-48¹²⁴

Type of MSN	Surfactant	Pore size	Structure morphology	Surface area
MCM-41	CTAB	2-3nm	hexagonal	1000m ² /g
MCM-48	CTAB	2-4nm	cubic	1600m ² /g
SBA-15	P123	8nm	hexagonal	500m ² /g

Typically, MSNs are characterized by small angle X-ray scattering (SAXS) for the pores arrangement, electronic microscopy or dynamic light scattering for the particle size and if possible the pore size, together with nitrogen adsorption-desorption analysis for the pore size. If the yielded material is hybrid, thermogravimetric analysis is also required.

MCM-41 is the most extensively studied type of MSNs in our research group, and only MCM-41-like materials are synthesized in this thesis.

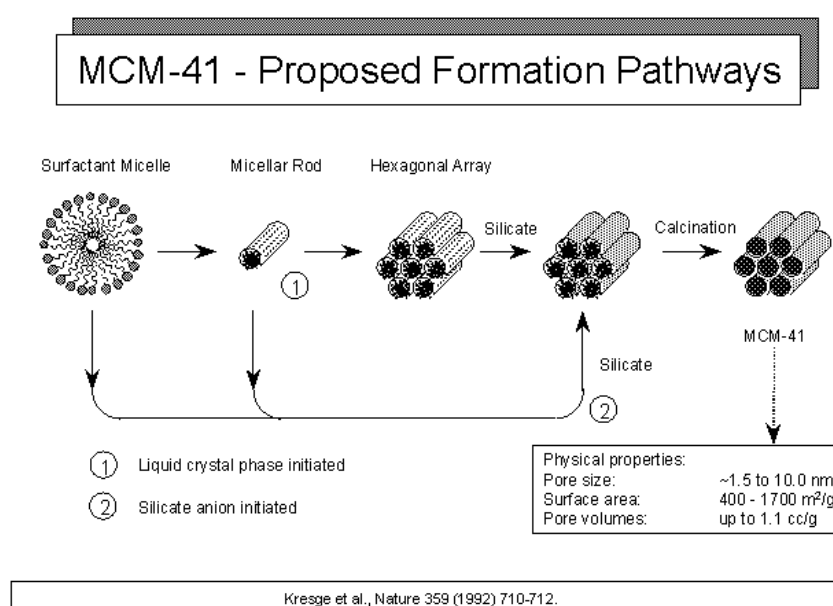


Figure 1.9. Proposed mechanism for the formation of MSNs

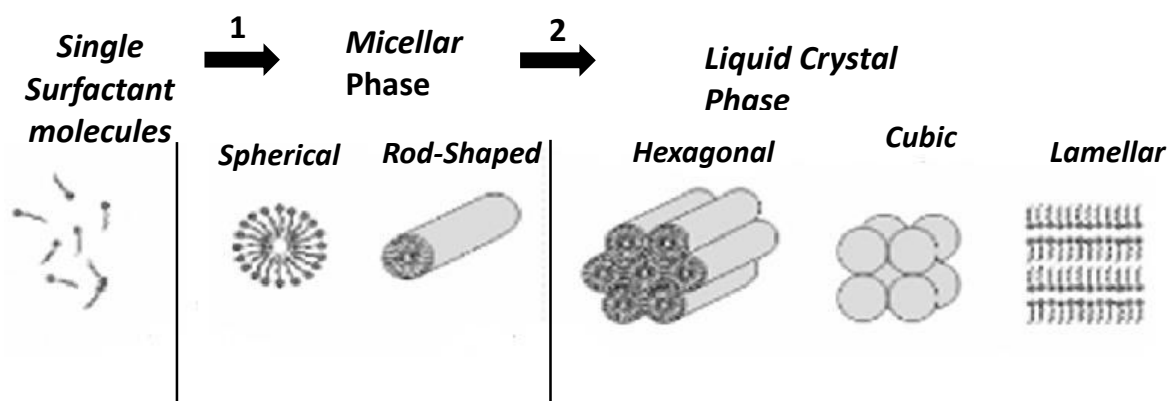


Figure 1.10. Evolution in the organization of surfactant molecules according to their concentration. The final hexagonal material is commonly called MCM-41, while the lamellar and the cubic ones are called MCM-50 and MCM-48, respectively.

1.6. Introduction to gold nanoparticles

Gold nanoparticles (AuNPs) represent a field that is exponentially increasing and taking more and more space in nanoscience and nanotechnology using surface science and self-assembled monolayers. They feature a wide scope in several areas of chemistry and are used for optical,¹²⁵⁻¹²⁷ electronic,¹²⁸⁻¹²⁹ magnetic,¹³⁰⁻¹³¹ catalytic,¹³²⁻¹³⁶ and biomedical applications.¹³⁷⁻¹⁴⁰

Although humans had to deal with gold for several centuries, it is only from the 18th century that people started to be more interested in the scientific aspect of AuNPs. Indeed, in 1718, Hans Heinrich Helcher showed that starch can stabilize AuNPs.

In 1818, Jeremias Benjamin Richters provided an explanation for the differences in colour shown by various preparations of AuNPs. In fact, pink or purple solutions contain single AuNPs, whereas yellow solutions are found when the particles were aggregated.

In 1857, Faraday reported the optical properties of thin films prepared from dried colloidal solutions and observed reversible colour changes of the films upon mechanical stimulus.¹⁴¹ In the 20th century, several methods for the preparation of gold colloids were reported.¹⁴²⁻¹⁴⁴ In the past two decades, the number of reports on AuNPs have been exponentially increased.¹⁴⁵⁻¹⁴⁸

AuNPs can be synthesized in several ways. Among them, the reduction of gold trichloride using citrate as a stabilizing agent.¹⁴⁹ Playing with the ratio citrate/gold precursor has great effects on the size of the particles. Another method for the

synthesis of AuNPs is the so called Brust-Schiffrin method.¹⁵⁰ It requires a biphasic reaction media and stabilization from a thiol derivative. The resulting particles are less sensitive to air or to temperature changes. The seeding-growth procedure is also common.¹⁵¹ The size of the resulting particles is controlled by modifying the ratio of seed to gold salt. Gold nanorods, for instance, have been intensively fabricated using the seeding-growth method. Finally, AuNPs were already synthesized using UV¹⁵² or near IR¹⁵³ irradiation, but also sonochemistry or thermolysis¹⁵⁴⁻¹⁵⁵

AuNPs are mainly characterized by transmission electron microscopy (TEM) for the size and the shape, SAXS and XRD for the arrangement of the capping stabilizing agents forming lattices.

Especially, AuNPs are famous for their surface plasmon resonance (SPR) properties and therefore, can be characterized by UV spectroscopy. Surface plasmon resonance is a physical phenomenon known as a tool to determine the adsorption of molecules on a metal surface. It is explained as follows: when a polarized monochromatic beam light hits an electron rich metal surface (generally gold or silver), a part from the reflected light, a non-radiative electromagnetic wave is spread in a direction perpendicular to the metal interface. The zone crossed by the wave is called oscillating field. The incident field is photon rich, and these photons can enter in resonance with the metal electron cloud (plasmon), this resonance being the actual SPR.

One of the interesting features of SPR is the release of energy in the reflected beam that can be easily detected. Hence, the decrease of the reflected beam intensity can be measured through resonance angle change. The latter is very sensitive to the medium density and therefore, to the refractive index. The resulting oscillations are affected to any change of this boundary, such as the adsorption of molecules to the metal surface. The molecules on the metal surface will induce a mass change and consequently the refractive index will change, and this can be used to determine the resonance angle. Consequently, one can determine the different interactions by studying the change of angle. Conversely, a SPR detection system measures the change of the medium refractive index around the surface after molecules coating. **Figure 1.11** explains in a simple way the principle described above.

This particularity of transition metal nanoparticles in general, and of AuNPs has led researchers to intensively studying the surface enhanced Raman scattering (SERS).

Raman scattering is an optical phenomenon discovered in 1928 by Chandrashekhara Venkata Raman (Nobel Prize laureate 1930) and Leonid Mandelstam. It consists on the inelastic scattering of a photon, meaning the fact that the medium can modify the

frequency of the spread light. This modification corresponds to an energy change between light and the medium.

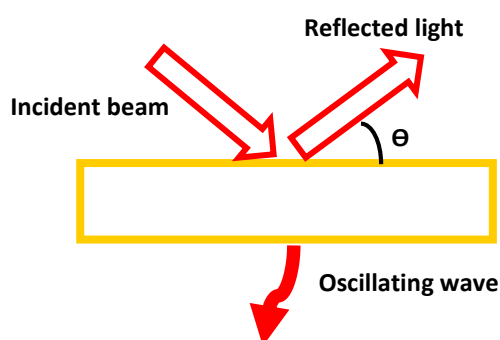


Figure 1.11. Simplified SPR Principle

Raman spectroscopy is the science allowing the studies and the measurements of this energy discrepancy. Contrary to this phenomenon, the Rayleigh scattering is the elastic scattering of photons, meaning there is no energy change between light and the medium. There are two kinds of energy shifts, that do not depend on the excitation wavelength:

- *Stokes shift* (**cf. part 1.1**): the shift is towards higher wavelength, i.e. lower energy, with vibrational excitation or phonon emission.
- *Anti-Stokes shift*: the shift is towards lower wavelength, i.e. higher energy, with vibrational relaxation or phonon absorption.

As previously mentioned, when there is no energy shift, we refer to Rayleigh scattering. with Raman spectroscopy, it is possible to identify the chemical composition of a sample from the way it scatters light.

The intensity of Raman bands is directly dependent on the number of molecules in their vibrational modes. When these vibrational modes are more numerous in lower energy, Stokes shift bands feature a higher intensity than anti-Stokes shift bands. Incident photons can be scattered but also modify the molecular vibrations. Raman bands are proper to the chemical composition of a molecule or a material, to its crystal structure and to its electronic properties. Raman spectroscopy features several advantages: the measurement does not damage the sample, it requires only a very small amount of sample, and in some cases can be quantitative. However, its main drawback is the low intensity of the bands. To increase this intensity, the so called surface-enhanced Raman spectroscopy technique has been thoroughly developed during the past decades.¹⁵⁶⁻¹⁵⁸ It requires the deposition of molecules on a metal

surface (mainly gold or silver, in our case AuNPs), and the enhancement factor can be up to 10^{10} to 10^{11} ,¹⁵⁹⁻¹⁶⁰ which means the technique may detect single molecules.¹⁶¹⁻¹⁶² Depending on the nature of the molecule-AuNPs, the involved mechanism can be different.¹⁶³⁻¹⁶⁴ According to the same principle, the surface enhanced photoluminescence (SEPL) has also been investigated, but to a lesser extent (from Scifinder, SEPL is 30 times less studied than SERS).

1.7. Introduction to metal organic frameworks

Metal–organic frameworks (MOFs, also known as porous coordination polymers or PCPs) are a new class of materials constructed from metal and organic linkers. **Figure 1.12** presents the structure of two of kinds of MOFs.¹⁶⁵⁻¹⁶⁶

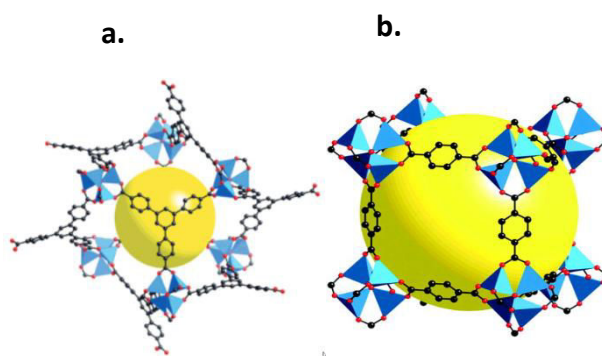


Figure 1.12. Structural representations of MOF-177 (a.) and MOF-5 (b.)

Due to their structural and functional tunability, the area of MOFs has become one of the fastest growing fields in chemistry, in particular since the improvement in structure determination through X-ray diffraction and gas sorption.

First reported by Yaghi *et. al*,¹⁶⁷ MOFs have recently been greatly reviewed over the past decade.¹⁶⁸⁻¹⁷⁰ MOFs feature straightforward synthesis, nanoscale process ability, predictable structures and network geometry, possibility of post-synthetic modification, and in most cases a relatively tunable porosity (with the exception of 0D and 1D MOFs). All these characteristics have allowed this class of materials to be used for several purposes. MOFs are mainly studied in the following areas: synthetic work focusing on metal-containing nodes or coordination bonds, ligand design and post-synthetic modification on linkers, symmetry-guided synthesis and structural characterization of MOFs from micro-, meso-, to macro-scale, MOF interdisciplinary research, and potential applications of MOFs. The latter provides a wide range of possibilities such as gas separation,¹⁷¹⁻¹⁷⁴ gas storage,¹⁷⁵⁻¹⁷⁷ catalysis (alcohol

oxidations,¹⁷⁸ arylations¹⁷⁹ or couplings¹⁸⁰),¹⁸¹⁻¹⁸⁴, medicine¹⁸⁵⁻¹⁸⁷ (especially with the emerging sub class of bio-MOFs) and opto-electronics.¹⁸⁸⁻¹⁸⁹ The first reported MOFs were made from single metal-ion nodes. The incorporation of metal clusters into MOFs has led to significant improvements in porosity and stability.¹⁹⁰⁻¹⁹¹ Moreover, the metal-containing building units and coordination bonds are normally formed *in situ*, almost exclusively from a one-pot procedure. Regarding the ligands, they are pre-designed and generally keep their integrity during MOF formation. Although initial MOF researchers are predominantly inorganic chemists, ironically, MOFs have been more studied by organic chemists, for ligand design and post-synthetic modification of the linker.¹⁹²⁻¹⁹³

The great improvement in structures determination by X-ray has been a critical breakthrough for MOFs characterization. In addition, as for all the other porous and hybrid materials, nitrogen adsorption-desorption and thermogravimetric analysis are required.

MOFs display a wide range of luminescent properties, resulting from LC, MLCT, LMCT transitions, antennae effects, excimer and exciplex emission. Additionally, guest insertion in MOFs pores can have very interesting effects on the luminescence. **Figure 1.13.** shows some possible luminescence sources in porous MOFs.¹⁹⁴ They are described as follows:

- *Linker-based emission*: luminescent conjugated organic molecules that absorb in the UV and visible region. The resulted emission can come from the linker itself, or from a charge transfer with the coordinated metal ions or clusters.
- *Framework metal ions*: Transition-metal ions with unpaired electrons can be efficient quenchers. Moreover, proximity to an organic fluorophore, either within the framework or within the pore, can induce an antenna effect and an increase in the emission intensity.
- *Luminescent guest insertion*: MOFs porosity gives a possibility to entrap luminescent molecules in an otherwise non-emissive (or less emissive) MOF.
- *Exciplex formation*: π - π interactions between conjugated linkers or between a linker and a guest molecule can induce an excited complex, which displays broad, featureless emission.

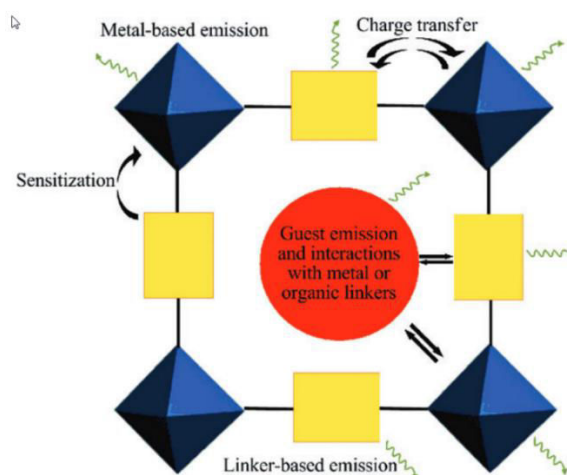


Figure 1.13. Presentation of some possible luminescence sources in porous MOFs, showing the effect of host-guest interaction on the luminescent properties. ¹⁹⁴

1.8. Aim of the thesis

The aim of my PhD is the synthesis, the characterization and the investigation of the photoluminescence properties of new hybrid organic-inorganic materials mainly based on the self-assembly properties of Pt(II) complexes.

In the second chapter of this thesis a series of positively charged amphiphilic Pt(II) complexes bearing a dianionic N⁺N⁺N⁺ terdentate ligand and a pyridine based ancillary ligand was developed. Their photophysical properties were thoroughly investigated and the formation of micellar systems in water was studied.

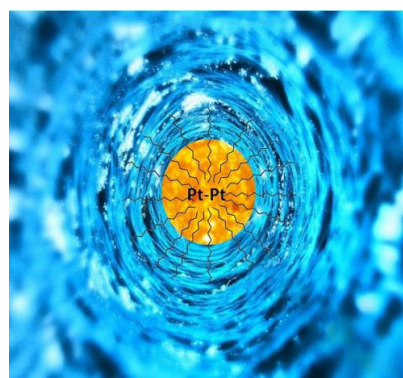


Figure 1.14 Representation of the system studied in *chapter 2*

In the third chapter, the complexes yielded in chapter 2 were applied as templates for the synthesis of MSNs in order to stabilize the aggregates and to enhance their luminescence properties.

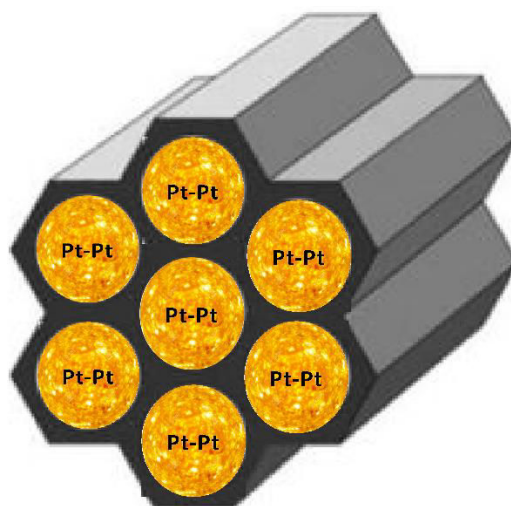


Figure 1.15. Representation of the system studied in *chapter 3*

The fourth chapter explores the effect on the photoluminescence properties of neutral Pt(II) complexes self-assembly on the surface of AuNPs. To achieve this purpose, a series of complexes bearing the same terdentate ligand and alkyl mercaptan-functionalized pyridine derivatives as ancillary ligands was synthesized and characterized.

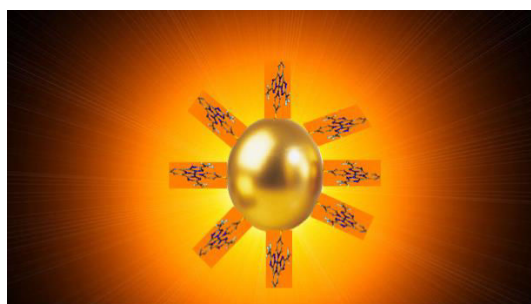


Figure 1.16. Representation of the system studied in *chapter 4*

The fifth chapter deals with the synthesis and the characterization of a series of neutral Pt(II) complexes containing the same type of dianionic N^4N^4N terdentate ligand and oligothiophene-functionalized pyridine derivatives as ancillary ligands. Their film morphology structure and the photophysical properties were studied and correlated to their charge transport properties. Powder X-ray diffraction studies were performed in order to determine the crystal packing of each complex.

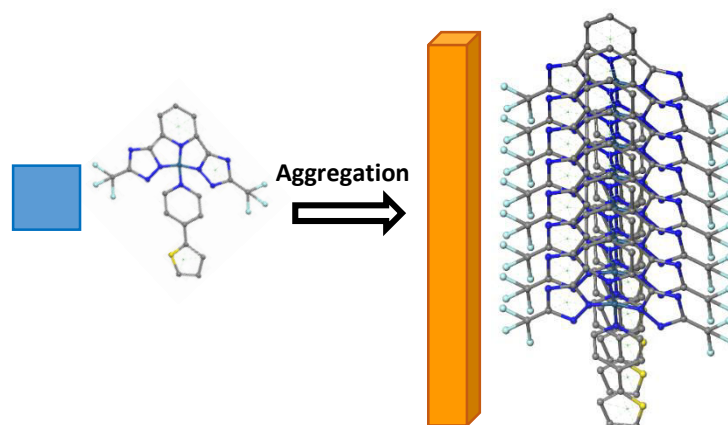


Figure 1.17. Representation of the system studied in *chapter 5*

In chapter 6, we report the preparation of new emissive materials based on the insertion of platinum(II) and iridium(III) complexes inside Al(OH)(bipyridine dicarboxylate) metal organic framework (**MOF-253**). The guest incorporation is performed by coordination of a metal complex precursor, providing increased robustness to the system compared to guest inclusion by its physical diffusion or by non-covalent interactions. The photophysical properties of the resulting materials were investigated.

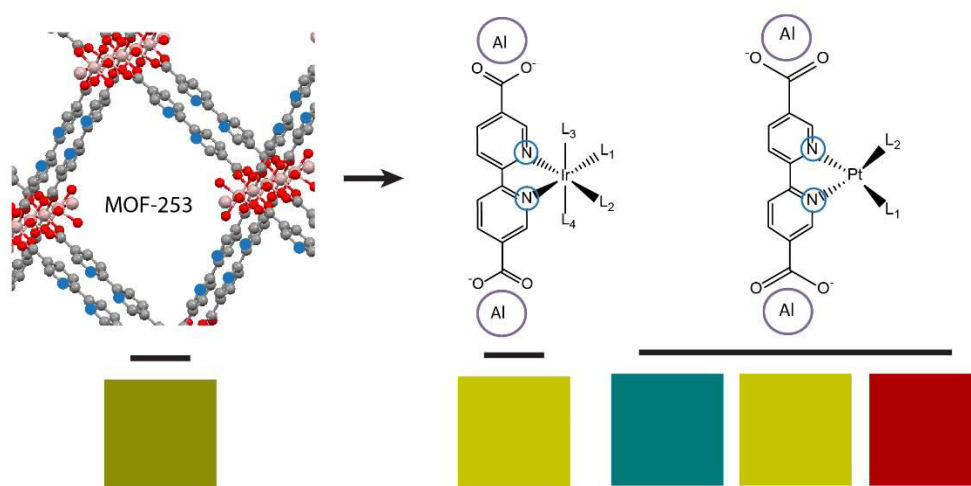


Figure 1.18. Representation of the TMCs in **MOF-253** pores after post synthetic modification

This PhD was funded by Self-Assembly in Confined Space (SACS) project, provided by the European Union FP7-SACS Project (Grant agreement no. 2012-310651). All the already published schemes and figures were taken with copyright permission.

1.9. References

1. Noyes, W. A.; Kassel, L. S., *Chem. Rev.* **1926**, 3 (2), 199.
2. Liu, Z.; Qi, W.; Xu, G., *Chem. Soc. Rev.* **2015**, 44 (10), 3117.
3. Ha, T.; Tinnefeld, P., *Annu. Rev. Phys. Chem.* **2012**, 63 (1), 595.
4. Yi, S. J.; Kim, K. C., *J. Vis.* **2014**, 17 (4), 253.
5. Apps, M. G.; Choi, E. H. Y.; Wheate, N. J., *Endocr. Relat. Cancer* **2015**, 22 (4), R219.
6. Che, C.-M.; Siu, F.-M., *Curr. Opin. Chem. Biol.* **2010**, 14 (2), 255.
7. Williams, R. J. P., *R. Inst. Chem., Rev.* **1968**, 1 (1), 13.
8. Joshi, T.; Graham, B.; Spiccia, L., *Acc. Chem. Res.* **2015**, 48 (8), 2366.
9. Hong, S.; Lee, Y.-M.; Ray, K.; Nam, W., *Coord. Chem. Rev.*
10. Johansson Seechurn, C. C. C.; Kitching, M. O.; Colacot, T. J.; Snieckus, V., *Angew. Chem. Int. Ed.* **2012**, 51 (21), 5062.
11. Li, C.-J.; Trost, B. M., *Proc. Natl. Acad. Sci. U.S.A.* **2008**, 105 (36), 13197.
12. Zhang, T.; Lin, W., *Chem. Soc. Rev.* **2014**, 43 (16), 5982.
13. Krüger, H.-J., *Coord. Chem. Rev.* **2009**, 253 (19–20), 2450.
14. Septiadi, D.; Aliprandi, A.; Mauro, M.; De Cola, L., *RSC Advances* **2014**, 4 (49), 25709.
15. Colombo, A.; Fiorini, F.; Septiadi, D.; Dragonetti, C.; Nisic, F.; Valore, A.; Roberto, D.; Mauro, M.; De Cola, L., *Dalton Trans.* **2015**, 44 (18), 8478.
16. Baggaley, E.; Weinstein, J. A.; Williams, J. A. G., *Coord. Chem. Rev.* **2012**, 256 (15–16), 1762.
17. Reichert, D. E.; Lewis, J. S.; Anderson, C. J., *Coord. Chem. Rev.* **1999**, 184 (1), 3.
18. Arockiam, P. B.; Bruneau, C.; Dixneuf, P. H., *Chem. Rev.* **2012**, 112 (11), 5879.
19. Ackermann, L., *Chem. Rev.* **2011**, 111 (3), 1315.
20. Lehn, J.-M.; Ziessel, R., *Proc. Natl. Acad. Sci. U.S.A.* **1982**, 79 (2), 701.
21. Kaur, R.; Mehta, S. K., *Coord. Chem. Rev.* **2014**, 262, 37.
22. Wang, L.; Han, Y.; Feng, X.; Zhou, J.; Qi, P.; Wang, B., *Coord. Chem. Rev.* **2016**, 307, Part 2, 361.
23. Cook, T. R.; Zheng, Y.-R.; Stang, P. J., *Chem. Rev.* **2013**, 113 (1), 734.
24. Soldati, R.; Aliprandi, A.; Mauro, M.; De Cola, L.; Giacomini, D., *Eur. J. Org. Chem.* **2014**, 2014 (32), 7113.
25. Tuccitto, N.; Ferri, V.; Cavazzini, M.; Quici, S.; Zhavnerko, G.; Licciardello, A.; Rampi, M. A., *Nat Mater* **2009**, 8 (1), 41.
26. Rigaut, S., *Dalton Trans.* **2013**, 42 (45), 15859.
27. Cebrián, C.; Mauro, M.; Kourkoulos, D.; Mercandelli, P.; Hertel, D.; Meerholz, K.; Strassert, C. A.; De Cola, L., *Adv. Mater.* **2013**, 25 (3), 437.
28. Xu, H.; Chen, R.; Sun, Q.; Lai, W.; Su, Q.; Huang, W.; Liu, X., *Chem. Soc. Rev.* **2014**, 43 (10), 3259.

29. Costa, R. D.; Ortí, E.; Bolink, H. J.; Monti, F.; Accorsi, G.; Armaroli, N., *Angew. Chem. Int. Ed.* **2012**, 51 (33), 8178.
30. Polo, A. S.; Itokazu, M. K.; Murakami Iha, N. Y., *Coord. Chem. Rev.* **2004**, 248 (13–14), 1343.
31. Hagfeldt, A.; Boschloo, G.; Sun, L.; Kloo, L.; Pettersson, H., *Chem. Rev.* **2010**, 110 (11), 6595.
32. Kuang, D.; Ito, S.; Wenger, B.; Klein, C.; Moser, J.-E.; Humphry-Baker, R.; Zakeeruddin, S. M.; Grätzel, M., *J. Am. Chem. Soc.* **2006**, 128 (12), 4146.
33. Graetzel, M., *Bull. Jpn. Soc. Coord. Chem.* **2008**, 51, 3.
34. Griffith, J. S.; Orgel, L. E., *Q. Rev. Chem. Soc.* **1957**, 11, 381.
35. Martellaro, P. J.; Hurst, S. K.; Larson, R.; Abbott, E. H.; Peterson, E. S., *Inorg. Chim. Acta* **2005**, 358 (12), 3377.
36. Roberts, D.; O'Dwyer, P. J.; Johnson, S. W., Platinum Complexes for the Treatment of Cancer. In *Cancer Management in Man: Chemotherapy, Biological Therapy, Hyperthermia and Supporting Measures*, Mineev, B. R., Ed. Springer Netherlands: Dordrecht, 2011; pp 145.
37. Siddik, Z. H., *Oncogene* **2003**, 22 (47), 7265.
38. Chu, G.; Martin, R.; Shen, Y.-M.; Baskett, G.; Sussman, H., *Cancer* **1993**, 72 (12), 3707.
39. Yarbrow, C. H., *Semin. Oncol. Nurs.* **1989**, 5 (2), 63.
40. Ravera, M.; Gabano, E.; Zanellato, I.; Perin, E.; Arrais, A.; Osella, D., *Dalton Trans.* **2016**.
41. Meister, T. K.; Riener, K.; Gigler, P.; Stohrer, J.; Herrmann, W. A.; Kühn, F. E., *ACS Catal.* **2016**, 6 (2), 1274.
42. Furstner, A., *Chem. Soc. Rev.* **2009**, 38 (11), 3208.
43. Eastwood, D.; Gouterman, M., *J. Mol. Spectrosc.* **1970**, 35 (3), 359.
44. Mills, A.; Lepre, A., *Anal. Chem.* **1997**, 69 (22), 4653.
45. Wong, W.-Y.; He, Z.; So, S.-K.; Tong, K.-L.; Lin, Z., *Organometallics* **2005**, 24 (16), 4079.
46. Fleetham, T.; Huang, L.; Li, J., *Adv. Funct. Mater.* **2014**, 24 (38), 6066.
47. Enright, G. D.; Takeya, S.; Ripmeester, J. A., X-Ray Diffraction: Addressing Structural Complexity in Supramolecular Chemistry. In *Supramol. Chem.*, John Wiley & Sons, Ltd: 2012.
48. Zhang, J.-P.; Liao, P.-Q.; Zhou, H.-L.; Lin, R.-B.; Chen, X.-M., *Chem. Soc. Rev.* **2014**, 43 (16), 5789.
49. Houlding, V. H.; Frank, A. J., *Inorg. Chem.* **1985**, 24 (22), 3664.
50. Vincent M. Miskowski, V. H. H., *Inorg. Chem. Commun.* **1989**, 28, 4.
51. Aliprandi, A.; Mauro, M.; De Cola, L., *Nat. Chem.* **2016**, 8 (1), 10.
52. Yam, V. W.-W.; Wong, K. M.-C.; Zhu, N., *J. Am. Chem. Soc.* **2002**, 124 (23), 6506.
53. Sculfort, S.; Braunstein, P., *Chem. Soc. Rev.* **2011**, 40 (5), 2741.

54. Hunter, B. M.; Villahermosa, R. M.; Exstrom, C. L.; Hill, M. G.; Mann, K. R.; Gray, H. B., *Inorg. Chem.* **2012**, 51 (12), 6898.
55. Dylla, A. G.; Janzen, D. E.; Pomije, M. K.; Mann, K. R., *Organometallics* **2007**, 26 (25), 6243.
56. Yersin, H.; Donges, D., Low-Lying Electronic States and Photophysical Properties of Organometallic Pd(II) and Pt(II) Compounds. Modern Research Trends Presented in Detailed Case Studies. In *Transition Metal and Rare Earth Compounds: Excited States, Transitions, Interactions II*, Yersin, H., Ed. Springer Berlin Heidelberg: Berlin, Heidelberg, 2001; pp 81.
57. Connick, W. B.; Henling, L. M.; Marsh, R. E.; Gray, H. B., *Inorg. Chem.* **1996**, 35 (21), 6261.
58. Lai, S.-W.; Che, C.-M., Luminescent Cyclometalated Diimine Platinum(II) Complexes: Photophysical Studies and Applications. In *Transition Metal and Rare Earth Compounds: Excited States, Transitions, Interactions III*, Springer Berlin Heidelberg: Berlin, Heidelberg, 2004; pp 27.
59. Wan, K.-T.; Che, C.-M.; Cho, K.-C., *J. Chem. Soc., Dalton Trans.* **1991**, (4), 1077.
60. Bielli, E.; Gidney, P. M.; Gillard, R. D.; Heaton, B. T., *J. Chem. Soc., Dalton Trans.* **1974**, (20), 2133.
61. Li, K.; Chen, Y.; Lu, W.; Zhu, N.; Che, C.-M., *Chem. Eur. J.* **2011**, 17 (15), 4109.
62. Yam, V. W.-W.; Chan, K. H.-Y.; Wong, K. M.-C.; Zhu, N., *Chem. Eur. J.* **2005**, 11 (15), 4535.
63. Mauro, M.; Aliprandi, A.; Cebrian, C.; Wang, D.; Kubel, C.; De Cola, L., *Chem. Commun.* **2014**, 50 (55), 7269.
64. Lehn, J.-M., *Angew. Chem. Int. Ed.* **1988**, 27 (1), 89.
65. Pedersen, C. J., *Angew. Chem. Int. Ed.* **1988**, 27 (8), 1021.
66. Cram, D. J., *Angew. Chem. Int. Ed.* **1988**, 27 (8), 1009.
67. Chakrabarty, R.; Mukherjee, P. S.; Stang, P. J., *Chem. Rev.* **2011**, 111 (11), 6810.
68. Mahadevi, A. S.; Sastry, G. N., *Chem. Rev.* **2016**, 116 (5), 2775.
69. Frank, H. S.; Wen, W.-Y., *Discuss. Faraday Soc.* **1957**, 24 (0), 133.
70. Huyskens, P. L., *J. Am. Chem. Soc.* **1977**, 99 (8), 2578.
71. Frey, P. A., *Magn. Reson. Chem.* **2001**, 39 (S1), S190.
72. Tanford, C., *The hydrophobic effect : formation of micellas and biological membranes*. Wiley: New York, 1980.
73. Onofrio, A.; Parisi, G.; Punzi, G.; Todisco, S.; Di Noia, M. A.; Bossis, F.; Turi, A.; De Grassi, A.; Pierri, C. L., *PCCP* **2014**, 16 (35), 18907.
74. Gray, M.; Goodman, A. J.; Carroll, J. B.; Bardón, K.; Markey, M.; Cooke, G.; Rotello, V. M., *Org. Lett.* **2004**, 6 (3), 385.
75. Hesselmann, A.; Jansen, G.; Schütz, M., *J. Am. Chem. Soc.* **2006**, 128 (36), 11730.
76. Eryazici, I.; Moorefield, C. N.; Durmus, S.; Newkome, G. R., *J. Org. Chem.* **2006**, 71 (3), 1009.

77. Martinez, C. R.; Iverson, B. L., *Chem. Sci.* **2012**, 3 (7), 2191.
78. Warshel, A.; Chu, Z. T., Calculations of Solvation Free Energies in Chemistry and Biology. In *Structure and Reactivity in Aqueous Solution*, American Chemical Society: 1994; Vol. 568, pp 71.
79. Gilson, M. K., *Curr. Opin. Struct. Biol.* **1995**, 5 (2), 216.
80. Meyer, F.; Dubois, P., *CrystEngComm* **2013**, 15 (16), 3058.
81. Metrangolo, P.; Neukirch, H.; Pilati, T.; Resnati, G., *Acc. Chem. Res.* **2005**, 38 (5), 386.
82. Kuppuraj, G.; Dudev, M.; Lim, C., *J. Phys. Chem. B* **2009**, 113 (9), 2952.
83. Yaghi, O. M.; O'Keeffe, M.; Ockwig, N. W.; Chae, H. K.; Eddaoudi, M.; Kim, J., *Nature* **2003**, 423 (6941), 705.
85. Sauvage, J.-P., *Chem. Commun.* **2005**, (12), 1507.
86. Li, Z.; Liu, Z.; Sun, H.; Gao, C., *Chem. Rev.* **2015**, 115 (15), 7046.
87. Gheybi, H.; Adeli, M., *Polymer Chemistry* **2015**, 6 (14), 2580.
88. Yang, L.; Tan, X.; Wang, Z.; Zhang, X., *Chem. Rev.* **2015**, 115 (15), 7196.
89. Liu, M.; Zhang, L.; Wang, T., *Chem. Rev.* **2015**, 115 (15), 7304.
90. Yam, V. W.-W.; Au, V. K.-M.; Leung, S. Y.-L., *Chem. Rev.* **2015**, 115 (15), 7589.
91. Mann, K. R.; Lewis, N. S.; Williams, R. M.; Gray, H. B.; Gordon, J. G., *Inorg. Chem.* **1978**, 17 (4), 828.
92. Lo, L. T.-L.; Ng, C.-O.; Feng, H.; Ko, C.-C., *Organometallics* **2009**, 28 (13), 3597.
93. Tran, N. T.; Stork, J. R.; Pham, D.; Olmstead, M. M.; Fettingner, J. C.; Balch, A. L., *Chem. Commun.* **2006**, (10), 1130.
94. Geoffroy, G. L.; Bradley, M. G.; Keeney, M. E., *Inorg. Chem.* **1978**, 17 (3), 777.
95. Ghedini, M.; Aiello, I.; Crispini, A.; Golemme, A.; La Deda, M.; Pucci, D., *Coord. Chem. Rev.* **2006**, 250 (11–12), 1373.
96. Kitagawa, H.; Ozawa, Y.; Toriumi, K., *Chem. Commun.* **2010**, 46 (34), 6302.
97. Benito, Q.; Le Goff, X. F.; Maron, S.; Fargues, A.; Garcia, A.; Martineau, C.; Taulelle, F.; Kahlal, S.; Gacoin, T.; Boilot, J.-P.; Perruchas, S., *J. Am. Chem. Soc.* **2014**, 136 (32), 11311.
98. Zheng, S.-L.; Volkov, A.; Nygren, C. L.; Coppens, P., *Chem. Eur. J.* **2007**, 13 (30), 8583.
99. Zhang, T.; Ji, C.; Wang, K.; Fortin, D.; Harvey, P. D., *Inorg. Chem.* **2010**, 49 (23), 11069.
100. Tang, S. S.; Chang, C.-P.; Lin, I. J. B.; Liou, L.-S.; Wang, J.-C., *Inorg. Chem.* **1997**, 36 (11), 2294.
101. Toronto, D. V.; Weissbart, B.; Tinti, D. S.; Balch, A. L., *Inorg. Chem.* **1996**, 35 (9), 2484.
102. Yu, S.-Y.; Sun, Q.-F.; Lee, T. K.-M.; Cheng, E. C.-C.; Li, Y.-Z.; Yam, V. W.-W., *Angew. Chem. Int. Ed.* **2008**, 47 (24), 4551.
103. Kresge, C. T.; Leonowicz, M. E.; Roth, W. J.; Vartuli, J. C.; Beck, J. S., *Nature* **1992**, 359 (6397), 710.
104. Webb, J. D.; MacQuarrie, S.; McEleney, K.; Crudden, C. M., *J. Catal.* **2007**, 252 (1), 97.

105. Luque, R.; Mariana Balu, A.; Manuel Campelo, J.; Dolores Gracia, M.; Losada, E.; Pineda, A.; Angel Romero, A.; Carlos Serrano-Ruiz, J., Catalytic applications of mesoporous silica-based materials. In *Catalysis: Volume 24*, The Royal Society of Chemistry: 2012; Vol. 24, pp 253.
106. Eedugurala, N.; Wang, Z.; Chaudhary, U.; Nelson, N.; Kandel, K.; Kobayashi, T.; Slowing, I. I.; Pruski, M.; Sadow, A. D., *ACS Catal.* **2015**, 5 (12), 7399.
107. Huang, C.-H.; Chang, K.-P.; Ou, H.-D.; Chiang, Y.-C.; Wang, C.-F., *Microporous Mesoporous Mater.* **2011**, 141 (1–3), 102.
108. Popat, A.; Liu, J.; Hu, Q.; Kennedy, M.; Peters, B.; Lu, G. Q.; Qiao, S. Z., *Nanoscale* **2012**, 4 (3), 970.
109. Jang, K.-S.; Kim, H.-J.; Johnson, J. R.; Kim, W.-g.; Koros, W. J.; Jones, C. W.; Nair, S., *Chem. Mater.* **2011**, 23 (12), 3025.
110. Sinha, A.; Basiruddin, S. K.; Chakraborty, A.; Jana, N. R., *ACS. Appl. Mater. Interfaces* **2015**, 7 (2), 1340.
111. Melde, B.; Johnson, B.; Charles, P., *Sensors* **2008**, 8 (8), 5202.
112. Wang, F.; Yang, J.; Wu, K., *Anal. Chim. Acta* **2009**, 638 (1), 23.
113. Gao, Z.; Burrows, N. D.; Valley, N. A.; Schatz, G. C.; Murphy, C. J.; Haynes, C. L., *Analyst* **2016**, 141 (17), 5088.
114. Wang, Y.; Zhao, Q.; Han, N.; Bai, L.; Li, J.; Liu, J.; Che, E.; Hu, L.; Zhang, Q.; Jiang, T.; Wang, S., *Nanomed. Nanotechnol. Biol. Med.* **2015**, 11 (2), 313.
115. Bharti, C.; Nagaich, U.; Pal, A. K.; Gulati, N., *International Journal of Pharmaceutical Investigation* **2015**, 5 (3), 124.
116. Prasetyanto, E. A.; Bertucci, A.; Septiadi, D.; Corradini, R.; Castro-Hartmann, P.; De Cola, L., *Angew. Chem. Int. Ed.* **2016**, 55 (10), 3323.
117. Stöber, W.; Fink, A.; Bohn, E., *J. Colloid Interface Sci.* **1968**, 26 (1), 62.
118. Retuert, J.; Martínez, Y.; Quijada, R.; Yazdani-Pedram, M., *J. Non-Cryst. Solids* **2004**, 347 (1–3), 273.
119. Huang, X.; Li, L.; Liu, T.; Hao, N.; Liu, H.; Chen, D.; Tang, F., *ACS Nano* **2011**, 5 (7), 5390.
120. Phillips, J. N., *Trans. Faraday Society* **1955**, 51 (0), 561.
121. Beck, J. S.; Vartuli, J. C.; Roth, W. J.; Leonowicz, M. E.; Kresge, C. T.; Schmitt, K. D.; Chu, C. T. W.; Olson, D. H.; Sheppard, E. W.; McCullen, S. B.; Higgins, J. B.; Schlenker, J. L., *J. Am. Chem. Soc.* **1992**, 114 (27), 10834.
122. Vartuli, J. C.; Schmitt, K. D.; Kresge, C. T.; Roth, W. J.; Leonowicz, M. E.; McCullen, S. B.; Hellring, S. D.; Beck, J. S.; Schlenker, J. L., *Chem. Mater.* **1994**, 6 (12), 2317.
123. Zhao, D.; Feng, J.; Huo, Q.; Melosh, N.; Fredrickson, G. H.; Chmelka, B. F.; Stucky, G. D., *Science* **1998**, 279 (5350), 548.
124. Kumar, D.; Schumacher, K.; du Fresne von Hohenesche, C.; Grün, M.; Unger, K. K., *Colloids Surf. Physicochem. Eng. Aspects* **2001**, 187–188, 109.

125. Zheng, J.; Zhou, C.; Yu, M.; Liu, J., *Nanoscale* **2012**, 4 (14), 4073.
126. Eder José, G.; Ana Paula, R.; Oswaldo, B., *Nanotechnology* **2016**, 27 (1), 015503.
127. Stiles, P. L.; Dieringer, J. A.; Shah, N. C.; Van Duyne, R. P., *Annu. Rev. Anal. Chem.* **2008**, 1 (1), 601.
128. Homberger, M.; Simon, U., *Phil. Trans. R. Soc. A* **2010**, 368 (1915), 1405.
129. Teranishi, T., *C. R. Chim.* **2003**, 6 (8–10), 979.
130. Gréget, R.; Nealon, G. L.; Vilen, B.; Turek, P.; Mény, C.; Ott, F.; Derory, A.; Voirin, E.; Rivière, E.; Rogalev, A.; Wilhelm, F.; Joly, L.; Knafo, W.; Ballon, G.; Terazzi, E.; Kappler, J.-P.; Donnio, B.; Gallani, J.-L., *Chemphyschem* **2012**, 13 (13), 3092.
131. Nealon, G. L.; Donnio, B.; Greget, R.; Kappler, J.-P.; Terazzi, E.; Gallani, J.-L., *Nanoscale* **2012**, 4 (17), 5244.
132. Thompson, D. T., *Nano Today* **2007**, 2 (4), 40.
133. Stratakis, M.; Garcia, H., *Chem. Rev.* **2012**, 112 (8), 4469.
134. Mitsudome, T.; Kaneda, K., *Green Chem.* **2013**, 15 (10), 2636.
135. Mikami, Y.; Dhakshinamoorthy, A.; Alvaro, M.; Garcia, H., *Catal. Sci. Tech.* **2013**, 3 (1), 58.
136. Hvolbæk, B.; Janssens, T. V. W.; Clausen, B. S.; Falsig, H.; Christensen, C. H.; Nørskov, J. K., *Nano Today* **2007**, 2 (4), 14.
137. Dykman, L.; Khlebtsov, N., *Chem. Soc. Rev.* **2012**, 41 (6), 2256.
138. Daniela, C.; Andreea, C.; Rebecca, P.; Alexandru Mihai, G., *Curr. Top. Med. Chem.* **2015**, 15 (16), 1605.
139. Zhang, X., *Cell Biochem. Biophys.* **2015**, 72 (3), 771.
140. Huang, X.; El-Sayed, M. A., *J.A.R.* **2010**, 1 (1), 13.
141. Faraday, M., *Philos. Trans. R. Soc. London* **1857**, 147, 145.
142. Turkevich, J.; Stevenson, P. C.; Hillier, J., *Discuss. Faraday Soc.* **1951**, 11 (0), 55.
143. Frens, G., *Nature Phys Sci* **1973**, 241, 20.
144. Robenek, H., *Scanning* **1990**, 12 (4), 244.
145. Schmid, G., *Chem. Rev.* **1992**, 92 (8), 1709.
146. Schmid, G.; Baumle, M.; Geerkens, M.; Heim, I.; Osemann, C.; Sawitowski, T., *Chem. Soc. Rev.* **1999**, 28 (3), 179.
147. Quinn, B. M.; Liljeroth, P.; Ruiz, V.; Laaksonen, T.; Kontturi, K., *J. Am. Chem. Soc.* **2003**, 125 (22), 6644.
148. Schierhorn, M.; Liz-Marzán, L. M., *Nano Lett.* **2002**, 2 (1), 13.
149. Yonezawa, T.; Kunitake, T., *Colloids Surf. Physicochem. Eng. Aspects* **1999**, 149 (1–3), 193.
150. Schmid, G.; Pfeil, R.; Boese, R.; Banderhmann, F.; Meyer, S.; Calis, G. H. M.; van der Velden, J. W. A., *Chem. Ber.* **1981**, 114 (11), 3634.

151. Meltzer, S.; Resch, R.; Koel, B. E.; Thompson, M. E.; Madhukar, A.; Requicha, A. A. G.; Will, P., *Langmuir* **2001**, 17 (5), 1713.
152. Zhou, Y.; Wang, C. Y.; Zhu, Y. R.; Chen, Z. Y., *Chem. Mater.* **1999**, 11 (9), 2310.
153. Niidome, Y.; Hori, A.; Sato, T.; Yamada, S., *Chem. Lett.* **2000**, 2000 (4), 310.
154. Chen, W.; Cai, W.; Zhang, L.; Wang, G.; Zhang, L., *J. Colloid Interface Sci.* **2001**, 238 (2), 291.
155. Nakamoto, M.; Yamamoto, M.; Fukusumi, M., *Chem. Commun.* **2002**, (15), 1622.
156. Schlücker, S., *Angew. Chem. Int. Ed.* **2014**, 53 (19), 4756.
157. Stiles, P. L.; Dieringer, J. A.; Shah, N. C.; Duyne, R. P. V., *Annu. Rev. Anal. Chem.* **2008**, 1 (1), 601.
158. Graham, D.; Goodacre, R., *Chem. Soc. Rev.* **2008**, 37 (5), 883.
159. Le Ru, E. C.; Blackie, E.; Meyer, M.; Etchegoin, P. G., *The Journal of Physical Chemistry C* **2007**, 111 (37), 13794.
160. Blackie, E. J.; Ru, E. C. L.; Etchegoin, P. G., *J. Am. Chem. Soc.* **2009**, 131 (40), 14466.
161. Nie, S.; Emory, S. R., *Science* **1997**, 275 (5303), 1102.
162. Le Ru, E. C.; Meyer, M.; Etchegoin, P. G., *J. Phys. Chem. B* **2006**, 110 (4), 1944.
163. Lombardi, J. R.; Birke, R. L.; Lu, T.; Xu, J., *The Journal of Chemical Physics* **1986**, 84 (8), 4174.
164. Lombardi, J. R.; Birke, R. L., *The Journal of Physical Chemistry C* **2008**, 112 (14), 5605.
165. J. L. C. Rowsell, O. M. Y., *J. Am. Chem. Soc.* **2006**, 128.
166. Nathaniel L. Rosi, J. E., Mohamed Eddaoudi, David T. Vodak, Jaheon Kim, Michael O'Keeffe, Omar M. Yaghi, *Science* **2003**, 5622, 3.
167. Rowsell, J. L. C.; Yaghi, O. M., *Microporous Mesoporous Mater.* **2004**, 73 (1-2), 3.
168. Eddaoudi, M.; Sava, D. F.; Eubank, J. F.; Adil, K.; Guillerm, V., *Chem. Soc. Rev.* **2015**, 44 (1), 228.
169. O'Keeffe, M.; Yaghi, O. M., *Chem. Rev.* **2012**, 112 (2), 675.
170. Lee, Y.-R.; Kim, J.; Ahn, W.-S., *Korean J. Chem. Eng.* **2013**, 30 (9), 1667.
171. Mason, J. A.; Veenstra, M.; Long, J. R., *Chem. Sci.* **2014**, 5 (1), 32.
172. Li, J.-R.; Kuppler, R. J.; Zhou, H.-C., *Chem. Soc. Rev.* **2009**, 38 (5), 1477.
173. Li, B.; Wang, H.; Chen, B., *Chem. Asian J.* **2014**, 9 (6), 1474.
174. Li, J.-R.; Sculley, J.; Zhou, H.-C., *Chem. Rev.* **2012**, 112 (2), 869.
175. Li, Y.; Yang, R. T., *Langmuir* **2007**, 23 (26), 12937.
176. Zhao, Z.; Ma, X.; Kasik, A.; Li, Z.; Lin, Y. S., *Ind. Eng. Chem. Res.* **2012**, 52 (3), 1102.
177. Getman, R. B.; Bae, Y.-S.; Wilmer, C. E.; Snurr, R. Q., *Chem. Rev.* **2012**, 112 (2), 703.
178. Man Wang, B. Y., Tongmei Ma, Huanfeng Jiang Yingwei Li, *RSC Advances* **2012**, 2, 3.
179. Liu, H.; Yin, B.; Gao, Z.; Li, Y.; Jiang, H., *Chem. Commun. (Camb.)* **2012**, 48 (14), 2033.
180. Carson, F.; Agrawal, S.; Gustafsson, M.; Bartoszewicz, A.; Moraga, F.; Zou, X.; Martin-Matute, B., *Chemistry (Easton)* **2012**, 18 (48), 15337.

181. Wang, C.; Wang, J. L.; Lin, W., *J. Am. Chem. Soc.* **2012**, *134* (48), 19895.
182. Wang, C.; Wang, J.-L.; Lin, W., *J. Am. Chem. Soc.* **2012**, *134* (48), 19895.
183. Liu, J.; Chen, L.; Cui, H.; Zhang, J.; Zhang, L.; Su, C.-Y., *Chem. Soc. Rev.* **2014**, *43* (16), 6011.
184. Yoon, M.; Srirambalaji, R.; Kim, K., *Chem. Rev.* **2012**, *112* (2), 1196.
185. Rowe, M. D.; Thamm, D. H.; Kraft, S. L.; Boyes, S. G., *Biomacromolecules* **2009**, *10* (4), 983.
186. Liu, R.; Yu, T.; Shi, Z.; Wang, Z., *Int J. Nanomedicine* **2016**, *11*, 1187.
187. Horcajada, P.; Gref, R.; Baati, T.; Allan, P. K.; Maurin, G.; Couvreur, P.; Férey, G.; Morris, R. E.; Serre, C., *Chem. Rev.* **2012**, *112* (2), 1232.
188. Cui, Y.; Yue, Y.; Qian, G.; Chen, B., *Chem. Rev.* **2012**, *112* (2), 1126.
189. Allendorf, M. D.; Schwartzberg, A.; Stavila, V.; Talin, A. A., *Chemistry – A European Journal* **2011**, *17* (41), 11372.
190. Férey, G.; Mellot-Draznieks, C.; Serre, C.; Millange, F.; Dutour, J.; Surblé, S.; Margiolaki, I., *Science* **2005**, *309* (5743), 2040.
191. Zhang, X.; Zhang, X.; Johnson, J. A.; Chen, Y.-S.; Zhang, J., *J. Am. Chem. Soc.* **2016**, *138* (27), 8380.
192. Cohen, S. M., *Chem. Rev.* **2012**, *112* (2), 970.
193. Evans, J. D.; Sumby, C. J.; Doonan, C. J., *Chem. Soc. Rev.* **2014**, *43* (16), 5933.
194. Allendorf, M. D.; Bauer, C. A.; Bhakta, R. K.; Houk, R. J. T., *Chem. Soc. Rev.* **2009**, *38* (5), 1330.

CHAPTER 2:

Cationic Pt(II) Complexes and their Assemblies

Abstract

In this chapter, we focus on the synthesis, characterization and luminescence properties of a new type of cationic platinum(II) complexes. The addition of relatively long hydrophobic moiety chain and the hydrophilic functional group at the extremity of the ancillary ligand, allows the formation of particular aggregates. This molecular design allows us to have high luminescence water soluble supramolecular entity, even at very low concentration.

Keywords

Pt(II) complexes, Luminescent properties, Surfactants, Micelles

2.1. Introduction

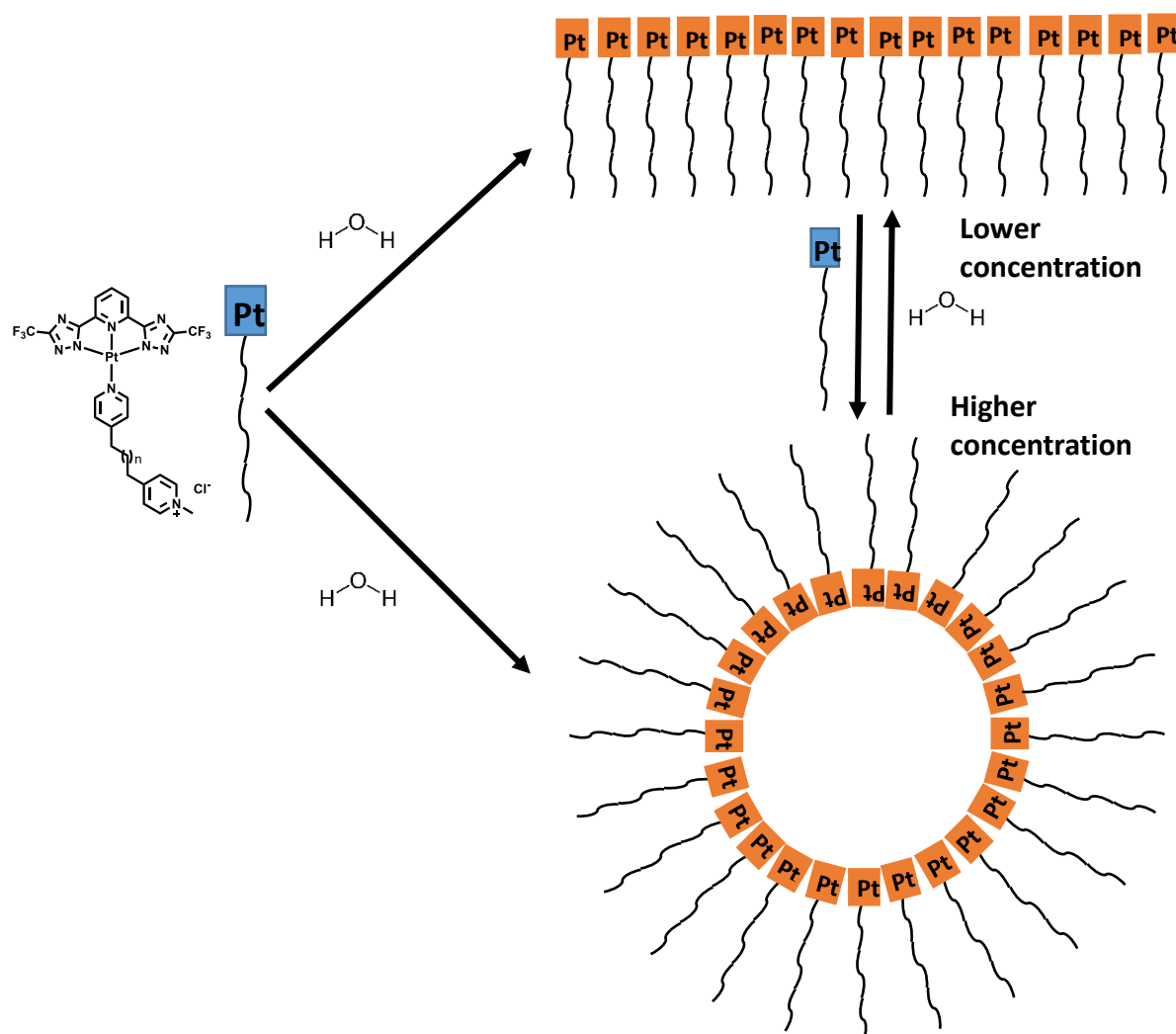
The design of amphiphilic molecules have been an active field of research in the past decades, yielding different structures,¹⁻³ even though luminescent transition metal complexes (TMCs) have been less explored.⁴⁻⁸ The main advantage of amphiphilic TMCs is that they combine the features of regular amphiphilic molecules with the one of TMCs. Indeed, they can form new supramolecular structures due to their dual hydrophilic-hydrophobic moieties, which in some cases possess interesting emerging properties, not present in the simple single component. Amphiphilic TMCs have been studied for their magnetic,⁹ catalytic,^{10, 8} or luminescence properties.¹¹ For instance, Liao and co-workers show the design of new catalysts based on amphiphilic TMCs for biphasic catalysis reactions.¹⁰ Spin crossover amphiphilic Mn(II) complexes were reported by Albrecht and co-workers.⁹ Also, Ru(II) complexes containing 2,6-bis(1-octadecylbenzimidazolyl)-pyridine as a ligand,¹² and charged Cu(II) complexes used and resulting in two dimensional self-assembled structures were reported.¹³ Closer to our research field, charged Re(I) complexes showed a great enhancement of the photoluminescence quantum yield (PLQY) and excited state lifetime ESIT after functionalized by a long aliphatic chain leading to aggregation.¹⁴ In our research group, works on amphiphilic Ru(II)¹⁵ and Ir(III) complexes also used as a mesoporous silica nanoparticles synthesis template, for enhancement of luminescent properties or for controlling the emission colour, were achieved.^{16-17, 11}

Amphiphilic Pt(II) complexes, seem to be even less reported than their TMCs counterparts. Indeed, only a few reports are found in the literature for applications in catalysis,¹⁸⁻¹⁹ or for studying the resulting structures and properties.²⁰⁻²¹ Kunitake et al. reported a mixed valence Pt(II) complex that shows a formation of supramolecular structures upon introduction of anionic lipid molecules as counter anions to obtain molecular wires.²² Optical properties of the micellar systems made by Pt(II) complexes has also been reported. For instance, photo-switchable amphiphilic units were attached to Pt(II) complexes in order to demonstrate the photochromic effect of such molecule.²³

The aim of the work presented in this chapter is to develop luminescent supramolecular self-assembled structures and to study the effect of the self-assembly on the luminescent properties. To achieve our purpose, we decided to synthesized a series of amphiphilic positively charged Pt(II) complexes with a terdentate N⁺N⁺N⁺ dianionic ligand as the hydrophobic moiety being coordinating the metal cation, and a

para position substituted pyridine as an ancillary ligand. On the other hand, the hydrophilic moiety is a pyridinium salt grafted at the end of the ancillary ligand with a long alkyl chain (**Scheme 2.1**).

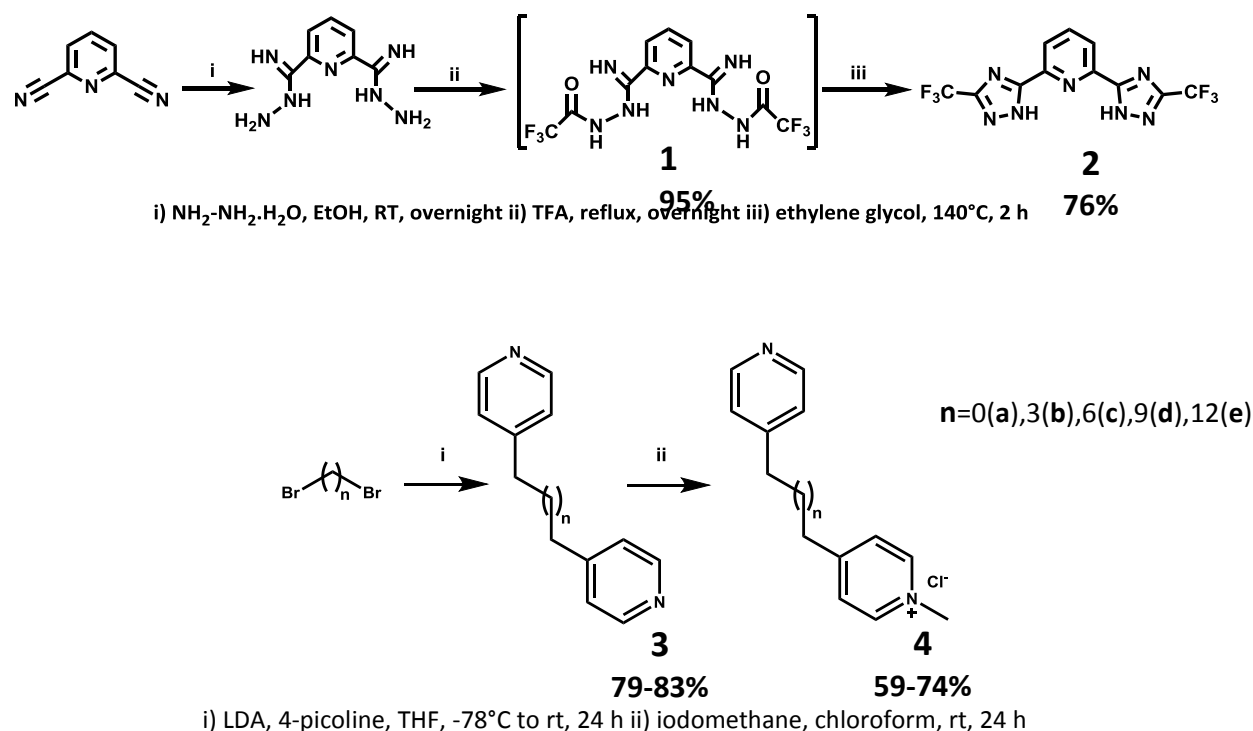
The terdentate ligand, 2,6-bis(3-(trifluoromethyl)-1H-1,2,4-triazol-5-yl)pyridine (pyC₅CF₃-tzH₂, molecule **2**) has been chosen because terdentate ligands provide a chelating unit with high rigidity, due to the presence of the triazole bearing a bis-negative charge upon complexation, and a strong ligand field. The CF₃ groups on the triazole rings enhance the solubility, and, by inductive electron-withdrawing effect, stabilize the highest occupied molecular orbital (HOMO), increasing the energy gap between the HOMO and the lowest unoccupied molecular orbital (LUMO). Moreover, the hydrophobicity of the CF₃ groups increase the self-assembly tendency of the complexes in water.



Scheme 2.1. Representation of the final system in this chapter

2.2. Results and discussion

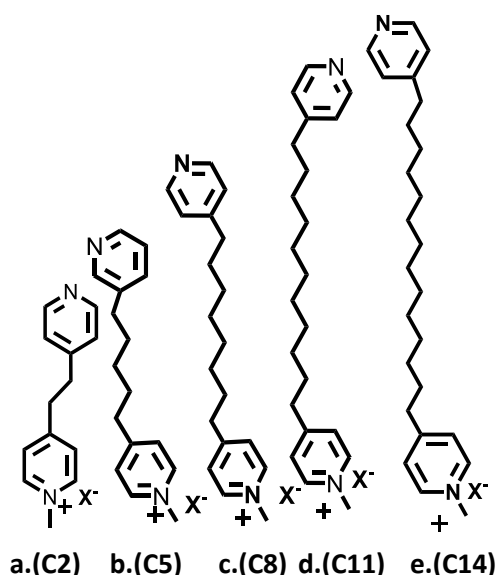
The synthesis of the ligands and the complexes is shown in **scheme 2.2**.²⁴⁻²⁶



Scheme 2.2. Synthetic pathways of **2** (top) and **4** (bottom)

The ancillary ligands were obtained in 2 steps reaction starting from the commercially available dibromoalkanes with different carbon chain lengths (**Scheme 2.2**, bottom; **Scheme 2.3**), as following: the 4-picoline first deprotonates ($\text{pK}_a \approx 32$) using lithium diisopropyl amide (LDA), a strong base ($\text{pK}_a \approx 35$) which has the particularity not to be nucleophilic due to its steric hindrance, to obtain the carbanion, stabilized by mesomeric effect. After adding the di-brominated derivative to the media, it reacts with the deprotonated 4-picoline as a double nucleophilic substitution from the carbanion, which is more reactive than the nitrogen. The yielded di(pyridin-4-yl) **3** alkane is then purified over column chromatography using silica before reacting with iodomethane. One equivalent of iodomethane is used to yield the monoadduct **4**, isolated and purified over column chromatography. The latter was performed over alumina, because the high polarity of silica didn't allow a successful purification. The mechanism is explained in **scheme 2.4** taking as example 1,3,-dibromopropane (**b.**). It is important to mention that for these two steps reaction, an inert atmosphere is

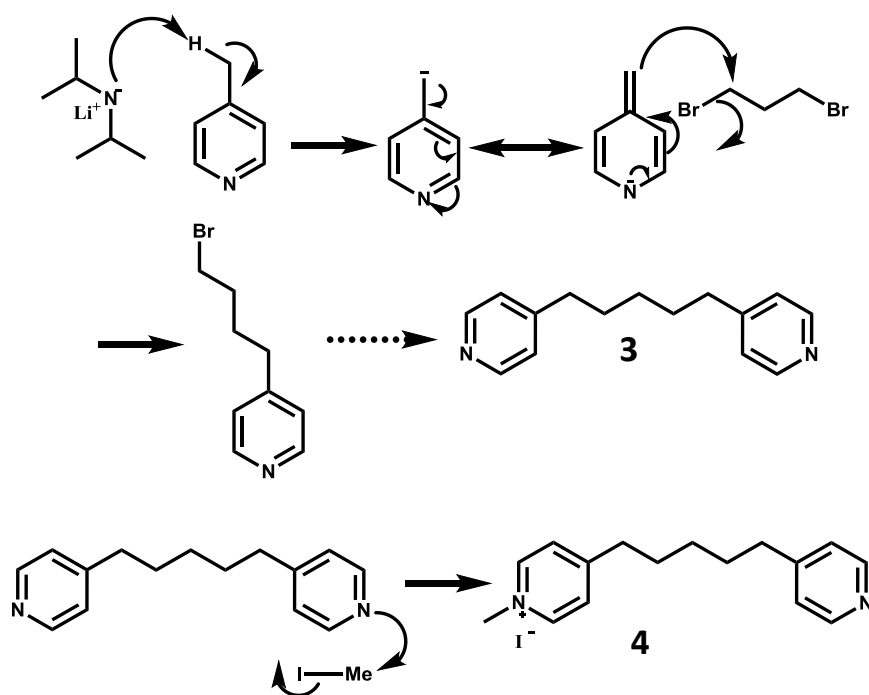
required, because strong bases are very sensitive to water molecules, and iodomethane is very unstable molecule, reacting with water. The use of different carbon chain lengths is dictated by the fact that we intend to investigate the effect of the pyridinium salt on the luminescence properties of the TMC, and on the ability to form vesicles or micelles. It is known that pyridinium salts are very efficient phosphorescence quenchers, due to their very strong electron withdrawing behaviour.²⁷⁻²⁸ Therefore, the distance between the complex and the quencher could affect the emission properties. Secondly, we wanted to study supramolecular assembly of the molecules forming micellar systems and investigate the correlation between the assembly and the luminescence properties of the system. Consequently, a long carbon chain should lead to different stability of the assembly and even different morphology than the short hydrophobic chain.



Scheme 2.3. Structure of the different pyridine alkylpyridinium ligands **4** studied in this work

The mechanism for the synthesis of the terdentate ligand **2** is drawn in **scheme 2.5**. The reaction started with two compounds that are commercially available. The hydrazine first reacts according to a nucleophilic addition over the nitrile group of 2,6-pyridine dicarbonitrile. The obtained adduct, **3**, subsequently reacts with one equivalent of activated trifluoroacetic acid (TFA), which here acts as a reagent, as a solvent and a Brønsted acid co-reagent. After the removal of one water molecule, the TFA is removed by distillation, and the triazole was formed, thanks to the high temperature reaction of the in ethylene glycol. Indeed, a lot of energy is needed to reach the thermodynamic compound.

On the other hand, the Pt(II) precursor has been synthesized by a reaction between potassium platinum tetrachloride (K_2PtCl_4) with dimethylsulfoxide (DMSO) in water, to get $Pt(II)(Cl)_2(DMSO)_2$. The latter is involved in the complexation reaction with the terdentate and the different monodentate ancillary ligands **2** and **4** in basic media in order to deprotonate the two triazoles moieties and thus to allow the coordination of the terdentate ligand as shown in **scheme 2.6**.



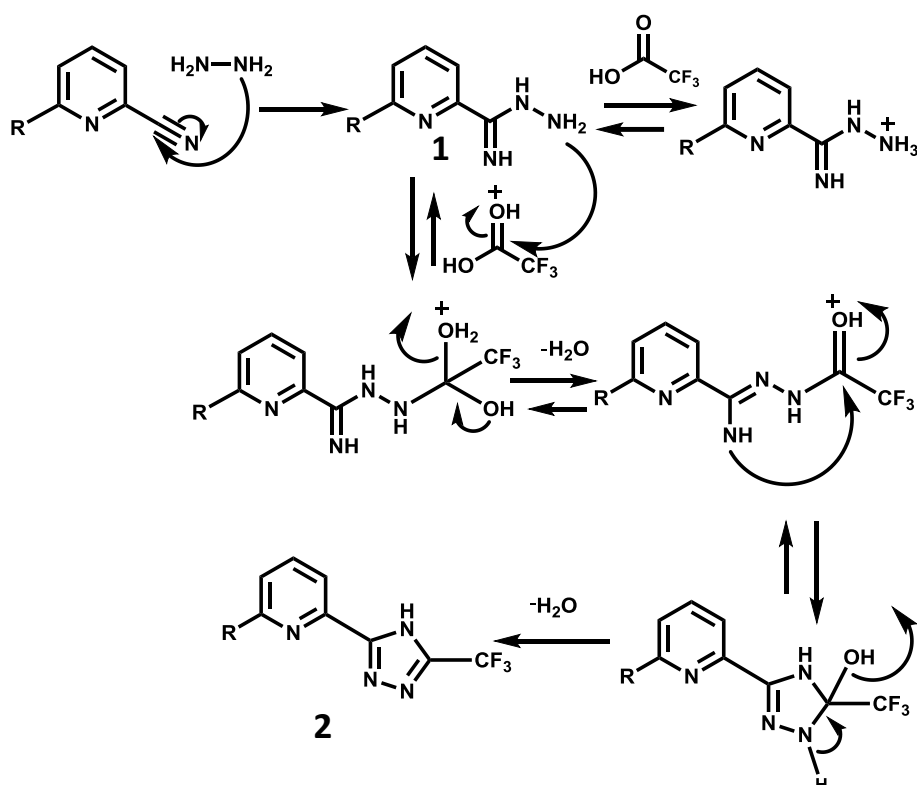
Scheme 2.4. Proposed mechanism for the formation of **3** and **4**

For the complexation step, solvent selection is not very important, nor the aerated atmosphere. In fact, the yields are good in acetonitrile as well as in methanol or 2-ethoxyethanol, in both aerated and de-aerated conditions. Nonetheless, we need to select the right base: it needs to be strong enough to allow the deprotonation process, and it needs to provide enough steric hindrance, not to coordinate the metal. Therefore, a good candidate is diisopropylethylamine (DIPEA), strong ($pK_a \approx 13$) and bulky enough for our requirements. The choice of a too strong base could force us to use inert conditions, which is much less convenient.

The ligands and complexes have been characterized using 1H , ^{13}C , ^{19}F NMR spectroscopy and mass spectrometry, using the electrospray ionization method (ESI-MS for the ligands, HR ESI-MS for the complexes). The characterization data of ligands and complex is shown in the experimental section (**Figures 2.11-2.24**). 1H NMR spectra of **1** displays 3 signals at 7.8 ppm (2H, 2 equivalents protons on pyridine the moiety),

7.6 ppm (1H, proton at para position of the pyridine's moiety) and 6 ppm, that could be attributed to the protons bonded to the nitrogen. Ligand **2** shows 2 signals in the ^1H NMR spectrum, both at 8.1 ppm, integrating for 2 protons and 1 proton and attributed to the protons at meta position and para position of the pyridine's nitrogen. Protons of the triazole rings are not shown.

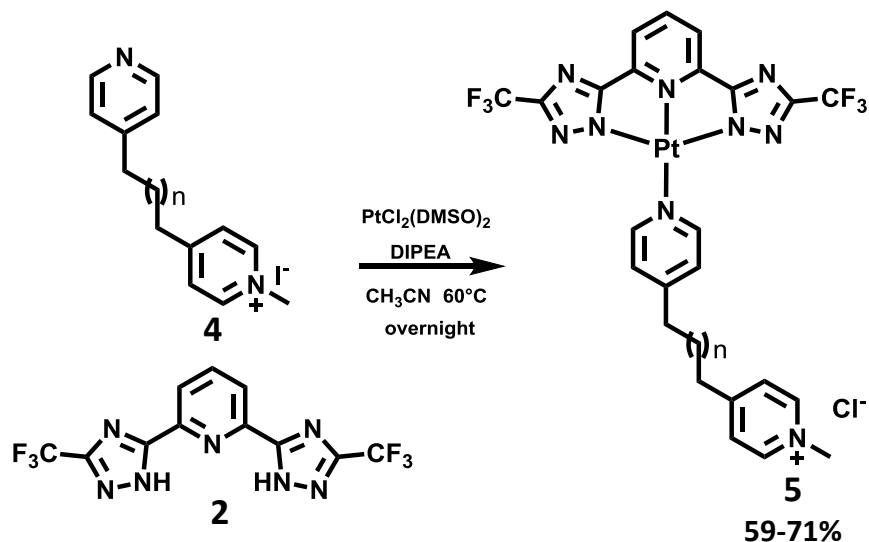
Molecules **3** show two multiplets at 6.9 and 8.3 ppm, respectively referring to the 4 protons at ortho and 4 protons meta position of the pyridine's nitrogen. Being symmetrical molecules, the protons on the two pyridine moieties are equivalent, 4 by 4. The quasi triplet at 2.4 ppm and integrating for 4 protons is attributed to the protons on the carbon adjacent to the aromatic rings. The two other signals in the aliphatic region have a multiplet character, they are attributed to the protons on the middle of the carbon chain.



Scheme 2.5. Proposed mechanism for the formation of **2**. As “-R” represent another nitrile group, the same reaction occurs on this moiety.

Because the molecules lose their symmetric character upon mono-addition of iodomethane, ligands **4** have a ^1H NMR spectra showing more signals. Indeed, we observe now four peaks in the aromatic region, each one integrating for 2 protons, with the adducted pyridine having signals that are more deshielded. Moreover, a singlet at 4.6 ppm and integrating for 3 protons is observed, and attributed to methyl

group of the pyridinium moiety. It is important to mention that the bis-adduct product was yielded as a side product, and therefore the spectra, not shown here, only show two signals in the aromatic region. All the ^{13}C NMR spectra could be correlated with the ^1H ones.



Scheme 2.6. Synthetic procedure for the preparation of complexes 5

The absorption spectra of the compounds, in water at a concentration of 5.10^{-5}M at room temperature, are shown in **Figure 2.1**. They all present the same profile, with a sharp band at 224nm (ϵ between 30000 and 25000 $\text{L.mol}^{-1}.\text{cm}^{-1}$) and two other bands at lower energy (255 nm, ϵ between 12000 and 9000 $\text{L.mol}^{-1}.\text{cm}^{-1}$); additionally, with one shoulder at 295 nm, (ϵ between 5000 and 3000 $\text{L.mol}^{-1}.\text{cm}^{-1}$) These transitions are mainly referred to ligand centered (^1LC) and metal-perturbed ligand centered states. Moreover, we can observe a broad, less intense bands between 350nm and 500nm (ϵ between 1500 and 1000 $\text{L.mol}^{-1}.\text{cm}^{-1}$), and this is attributed to metal to ligand charge transfer ($^1\text{MLCT}$) transitions.

The emission and excitation spectra of all the complexes in water (10^{-4}M) and in the solid state are depicted in **Figures 2.2** and **2.3**. Strikingly, they display the same excitation and emission profiles independently on the state (solid or solution). All the excitation spectra have a band at 500 nm referring to a MMLCT transition induced by Pt---Pt interactions, and other bands at higher energy attributed to MLCT or LC transition as already discussed for the absorption spectra. The emission spectra present a broad, featureless band at 585 nm, typical for Pt(II) complexes in their aggregated state and attributed to a $^3\text{MMLCT}$ transition as already reported for similar compounds.²⁹⁻³¹ This result proves that the length of the carbon chain of the ancillary ligands does not have any effect on the emission energy. However, we see an effect on

the emission quantum yields which mirrors the increase of the chain length with the intensity of the luminescence (**Table 2.1**). The effect of the increase in the emission can have two different reasons: i) the pyridinium quenching effect can play a role that relates to the distance between the donor and acceptor; ii) different complexes can pack in a variety of morphologies which can affect the emission intensity, due to rigidity or shielding of dioxygen (**Figure 2.4**).

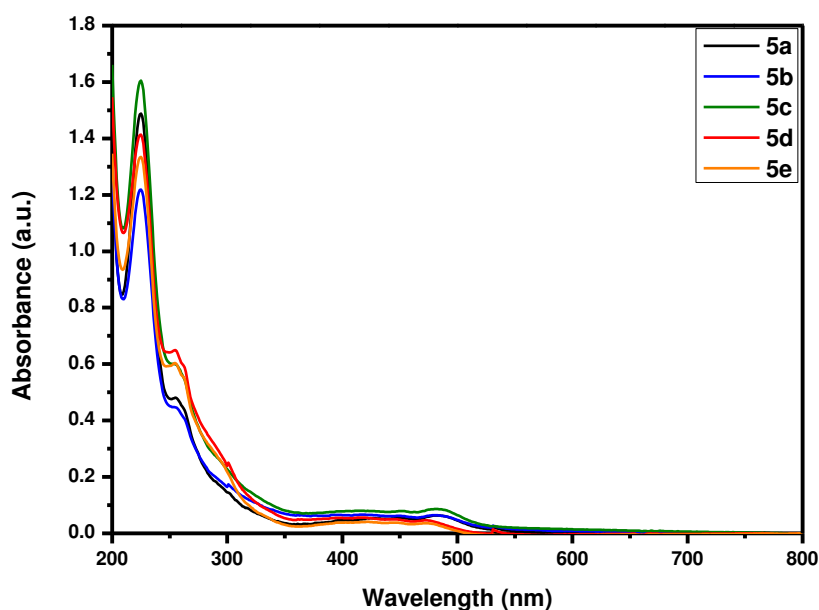


Figure 2.1. Absorption spectra of complexes **5a** (C2-black trace), **5b** (C5-blue trace), **5c** (C8-green trace), **5d** (C11-red trace) and **5e** (C14-orange trace) in water at 5.10^{-5} M.

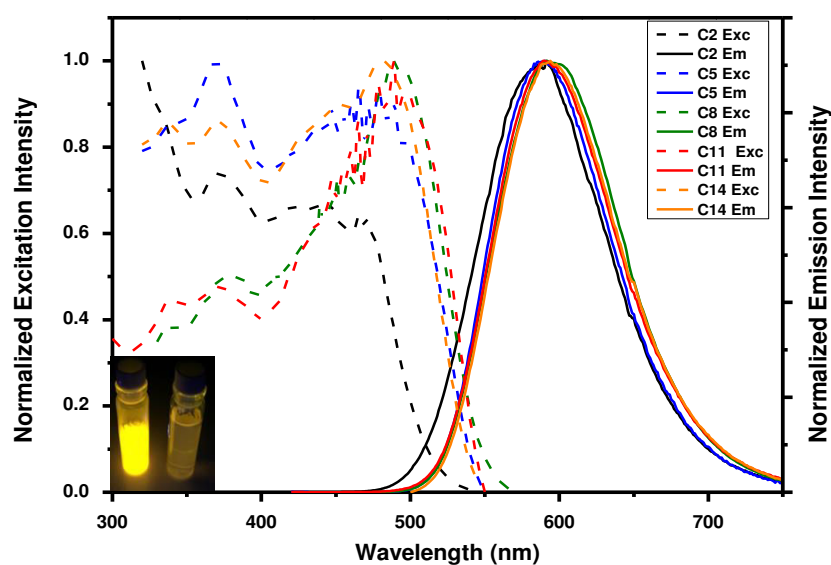


Figure 2.2. Excitation ($\lambda_{em}=600\text{nm}$) and Emission ($\lambda_{exc}=400\text{nm}$) spectra of complexes **5a** (C2-black trace), **5b** (C5-blue trace), **5c** (C8-green trace), **5d** (C11-red trace) and **5e** (C14-orange trace) in water at 10^{-4}M . Inset, images of sample **5a** under UV light (366 nm, water, 10^{-2}M , left; water, 10^{-4}M , right).

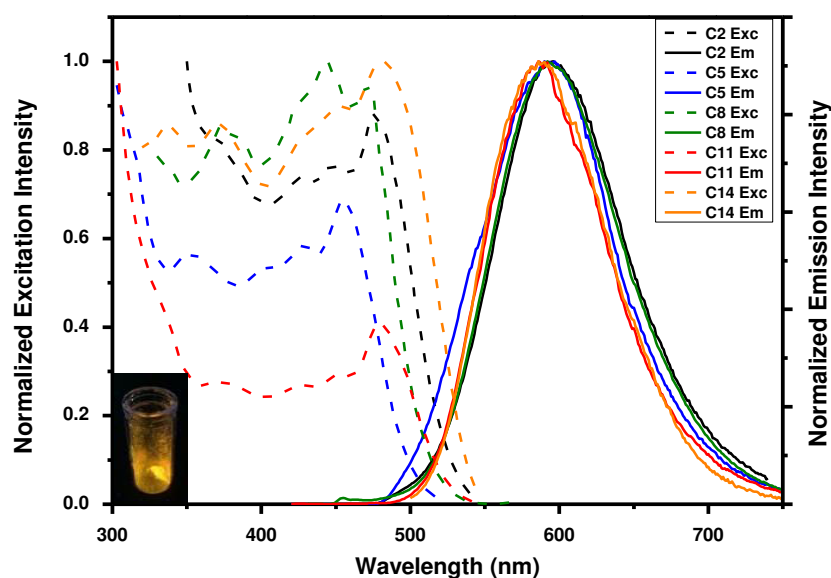


Figure 2.3. Excitation ($\lambda_{em}=600\text{ nm}$) and Emission ($\lambda_{exc}=400\text{ nm}$) spectra of complexes **5a** (C2-complex, black trace), **5b** (C5- complex, blue trace), **5c** (C8- complex, green trace), **5d** (C11- complex, red trace) and **5e** (C14- complex, orange trace) in solid state. Inset: image of sample **5a** in solid state.

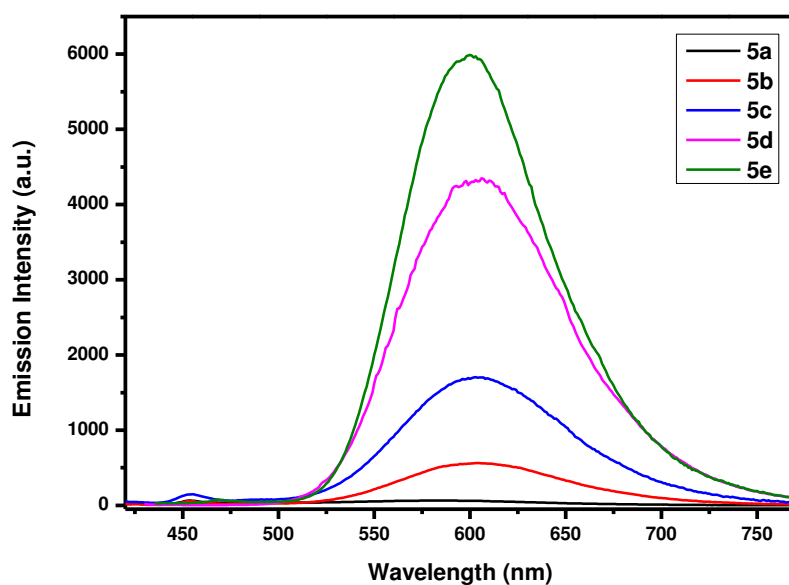


Figure 2.4. Emission spectra of complexes **5a-e**. in water at 10^{-4}M

To estimate the effect of the pyridinium unit, known as a good electron acceptor, we should measure the quenching of the emission depending on the distance between the emitter (platinum complex) and the quencher. In order to discriminate between the effect of the packing and the effect of the quencher we need to measure the emission spectra of the complexes in their monomeric form, meaning without aggregation. To avoid the aggregation, and the consequent Pt---Pt interactions, we have to change the solubility from water to organic solvents, in which the apolar platinum moiety is solvated.

The presence of the positive charge on the pyridine implies a counter ion that can modulate the solubility of the system. It is very well known that a halide as counter anion, often increase solubility in water while hexafluorophosphates (PF_6^-) or tetrafluoroborates (BF_4^-) as counter anions facilitate the dissolution in organic solvents. For this purpose, a counter anion exchange from halide to PF_6^- was performed. The counter anion exchange was achieved by dissolving the complexes in water and precipitation with a large excess of tetrabutylammonium hexafluorophosphate (NH_4PF_6) led to the PF_6^- salts. The yielded compounds become soluble in dichloromethane, and the resulting emission spectra measured with the same parameters used for the water solutions (concentration, temperature, excitation wavelength, excitation and emission slits), are shown in **Figure 2.5**.

The solutions in dichloromethane at 10^{-4} M, were isoabsorptive at the excitation wavelength at 375 nm. Excitation of all the complexes at the mentioned lambda display predominantly a profile attributed to the emission of the complex in its non-aggregated state with structured bands at 461 nm, 489 nm and 525 nm as observed in similar complexes.³²⁻³³ In addition they show emission intensity which reflects the quenching process due to the different distance between the pyridinium and the emitter. We can therefore conclude that in water, where the self-assembly process is present for all the complexes, the difference in emission quantum yields is indeed higher emission intensity with related to the quencher but we cannot rule out the different packing morphology that can also contribute to the enhancement of the emission. In the two extreme cases, in water at 10^{-4} M, complex **5a** has a PLQY of only 1%, and complex **5e** has a PLQY of 14% (**Table 2.1**). For similar platinum complexes to see the emission of the monomeric form high dilution is necessary $<10^{-4}$ M^{32, 34}, and the Pt(II) complex self-assembles to form green-yellow emissive fibers (**Figure 2.6**).³²

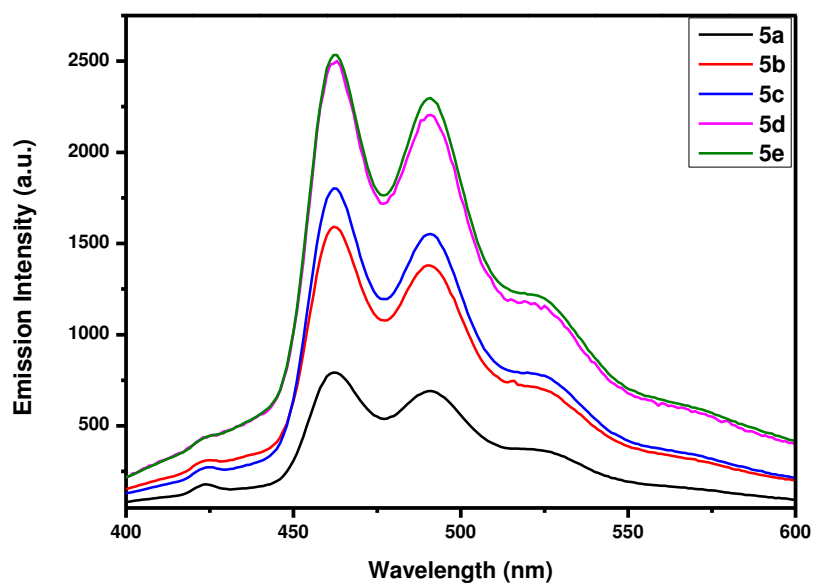


Figure 2.5. Emission spectra ($\lambda_{\text{exc}}=375$ nm) of complexes **5a-e** after anion exchange in dichloromethane at 10^{-4}M .

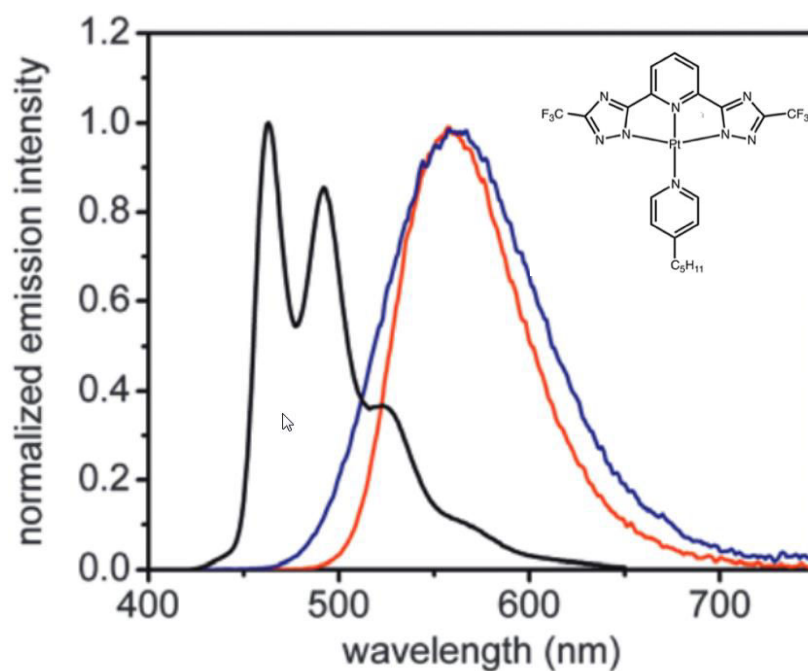


Figure 2.6. Emission spectra of Pt(II) complex, from a previous report of our research group, in solution in chloroform ($5 \cdot 10^{-5}\text{M}$, black trace), fibers obtained from acetone (red trace), and from dichloromethane (blue trace). Inset: molecular structure of the studied complex. ($\lambda_{\text{exc}}=400$ nm)

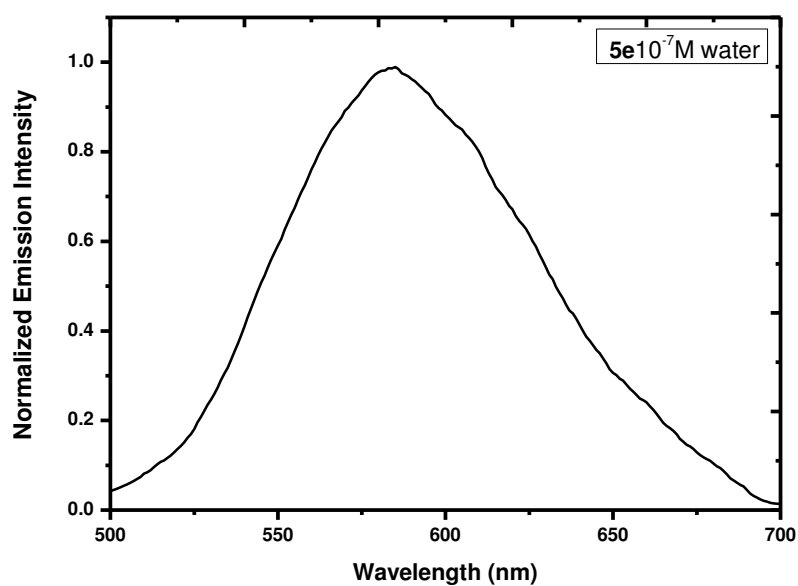


Figure 2.7. Emission spectrum ($\lambda_{\text{exc}}=400$ nm) of complex **5e** in water at 10^{-7} M

Table 2.1. Photophysical properties of complexes **5a.-e.** in water at 10^{-4} M

Complex	λ_{em} (nm, $\lambda_{\text{exc}}=400\text{nm}$)	$\Phi(\%)$	τ (μs)
5a	593	1	0.304 (71%) 0.063 (29%)
5b	590	1	0.308(47%) 0.094(53%)
5c	590	6	0.367 (73%) 0.108 (26%)
5d	587	11	0.302 (35%) 0.115 (65%)
5e	587	14	0.442 (56%) 0.141 (44 %)

Table 2.2. Photophysical properties of complexes **5a.-e.** in solid state

Complex	λ_{em} (nm, $\lambda_{\text{exc}}=400\text{nm}$)	$\Phi(\%)$	τ (μs)
5a	593	4	0.546 (47%) 0.180 (53%)
5b	590	7	0.260 (48%) 0.112 (52%)
5c	590	7	0.332 (43%) 0.186 (57%)
5d	589	11	0.396(51%) 0.146(49%)
5e	593	14	0.452 (57%) 0.140 (43%)

Interestingly for our complexes the platinum center is so hydrophobic, that they have an extremely high tendency to aggregate, leading to the yellow-orange luminescence characteristic of a short distance (<3.5 Å) between two adjacent platinum complexes. To illustrate this behavior, the emission spectrum of complex **5e** in water at 10^{-7} M was acquired (**Figure 2.7**) showing the emission of the aggregated form.

Deeper studies on this phenomenon were performed by dynamic light scattering (DLS) experiments on complex **5e**, (**Figure 2.8**) with concentrations going from 10^{-6} (spot **1**) to $8 \cdot 10^{-4}$ M (spot **2**). From this experiments, as the scattering intensity starts to increase from the spot **1** we can conclude that the aggregates are already formed at such a low concentration. Dynamic light scattering experiments were also performed at different concentrations (1 µM, 10 µM, 100 µM, 500 µM). **Figure 2.9.a** shows the field correlation function versus the diffusion time. From this and using an inverse Laplace transformation, we can determine relaxation rate (ms^{-1}) according to the scattering vector q (**Figure 2.9.a**, inset):

$$q = \frac{4\pi\eta}{\lambda} \sin \frac{\theta}{2} \quad (2.1)$$

In which η is the refractive index of water (1.331) λ is the wavelength of the light source (639 nm) and θ is the scattering angle (°).

Subsequently, the diffusion coefficient was calculated from the relaxation rate of the structures, and the hydrodynamic radius R was given by the following formula:

$$R = \frac{kT}{6\pi\eta d} \quad (2.2)$$

In which d refers to the diffusion coefficient ($\text{m}^2 \cdot \text{s}^{-1}$), k is the Boltzmann's constant ($1.38064852 \cdot 10^{-23} \text{ J} \cdot \text{K}^{-1}$), T stands for the temperature of the medium (273 K), η is the viscosity of the medium (constant, $\text{kg} \cdot \text{s}^{-1} \cdot \text{m}^{-1}$). All the parameters being known; the radius can be determined (**Figure 2.9.b**).

The results were very interesting, since the most diluted sample as the lower diffusion rate (10ms), and the higher the concentration, the faster the aggregates diffuse. This is in agreement with our assumption, that is to say that at lower concentration, below the CMC, the formed assembly is actually a supramolecular polymer promoted by π - π stacking and Pt---Pt interactions and hence displaying a bigger hydrodynamic radius; and when the concentration increases, the assembly takes spherical micelle shape induced by hydrophobic interactions in water. Obviously, the supramolecular polymer

features a hydrodynamic radius much bigger than the micelles. **Table 2.1** and **2.2** summarize the photophysical properties of complexes **5a-e** in solution (water, 10^{-4} M) and in solid state, respectively. The supramolecular assembly is illustrated in **Figure 2.10**.

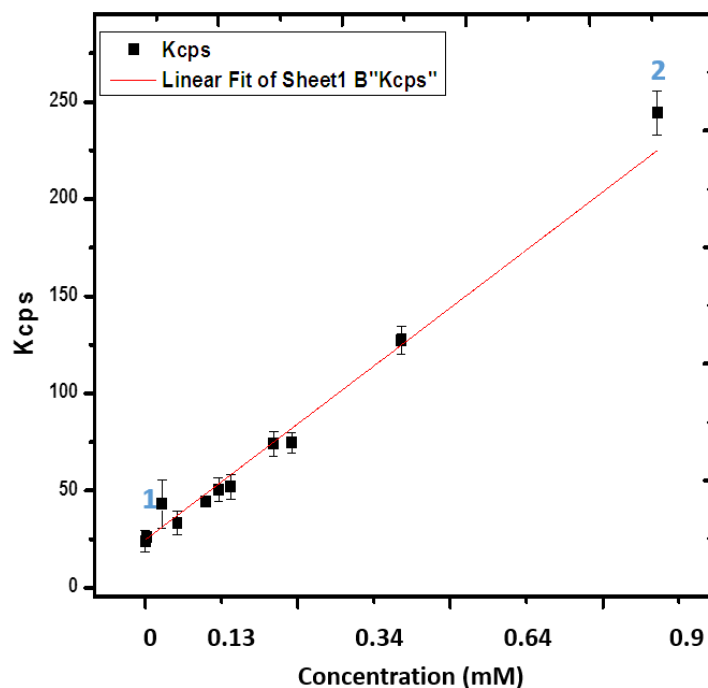


Figure 2.8. Plot of scattering intensity vs. concentration of **5a** in water

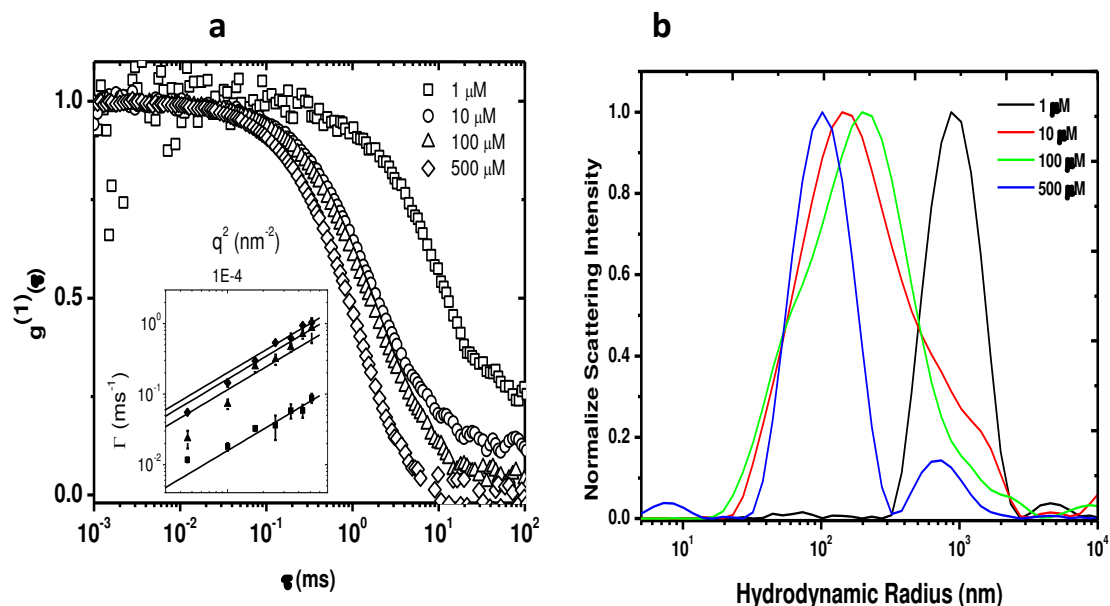


Figure 2.9.a. Field correlation function versus the diffusion time, inset: plot of relaxation rate versus scattering vector **b.** Plot of scattering intensity versus hydrodynamic radius of complex **5e** in water, at 20°C at different concentrations

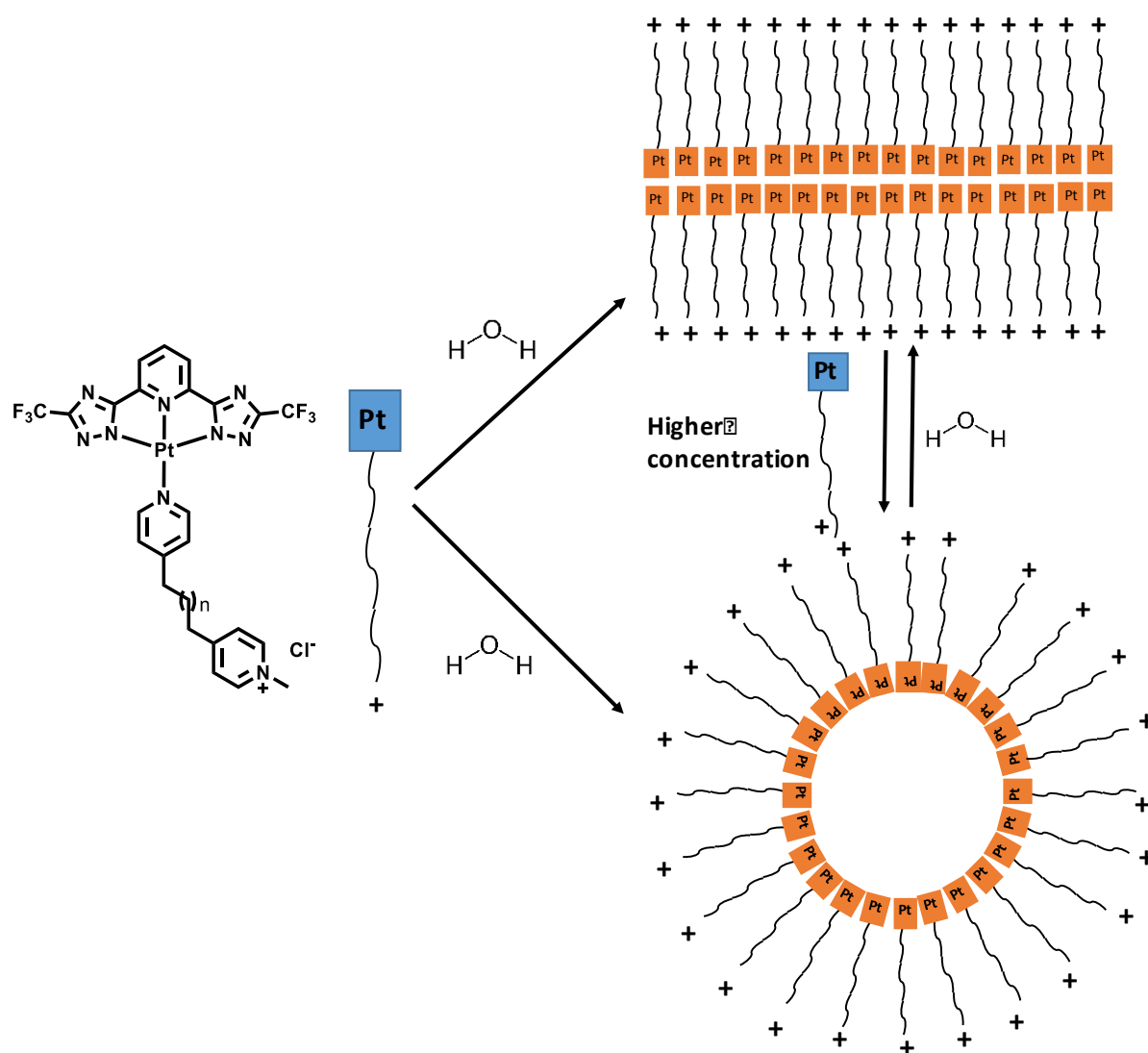


Figure 2.10. Illustration of the formation of self-assembled structures of the studied complexes according to the concentration of the latter

2.3. Conclusion

A series of amphiphilic Pt(II) complexes was synthesized, and their photophysical properties were thoroughly studied in water and in solid state. In water, these complexes tend to aggregate by hydrophobic effect, but also by Pt---Pt interactions. Even at very low concentration, the complexes display the emission of their aggregated form. Subsequently, the study of the self-assemblies was investigated, highlighting the formation of nanostructures.

2.4. Experimental section

2.4.1. Materials and methods

All the solvents and reagents were used as received from Aldrich, Fluka, TCI and VWR without any further purification. K_2PtCl_4 was purchased from Precious Metal Online (PMO). $PtCl_2(DMSO)_2$ was synthesized according to reported procedures. All the synthesis and characterization of the ligands and the complexes are described below. Nuclear Magnetic Resonance (NMR) spectra were acquired on a Bruker Avance 400 spectrometer, the NMR chemical shifts were given in ppm. Electro-Spray ionization Mass Spectrometry (ESI-MS) analysis were performed on a Bruker Daltonics microTOF spectrometer (Bruker Daltonik GmbH, Bremen, Germany) equipped with an orthogonal ESI interface. Calibration was performed using Tuning mix (Agilent Technologies). Sample solutions were introduced into the spectrometer source with a syringe pump (Harvard type 55 1111: Harvard Apparatus Inc., South Natick, MA, USA) with a flow rate of $5 \mu L \cdot min^{-1}$.

DLS measurements were conducted on a Delsa Nano C Particle Analyzer (Beckman Coulter, Brea, CA, USA; operative wavelength 655 nm), and the Contin algorithm was used to supply the hydrodynamic diameters as intensity and volume distributions.

2.4.2 Photophysical measurements

All solvents used for spectroscopic characterization were spectrometric grade and purchased by VWR. Absorption spectra were measured on a Shimadzu UV-3600 spectrophotometer double-beam UV–VIS–NIR spectrometer and baseline corrected. Steady-state emission spectra were recorded on a Horiba Jobin–Yvon IBH FL-322 Fluorolog 3 spectrometer equipped with a 450 W xenon arc lamp, double-grating excitation, and emission monochromators (2.1 nm mm^{-1} of dispersion; $1200 \text{ grooves mm}^{-1}$) and a TBX-04 single photon-counting detector. Emission and excitation spectra were corrected for source intensity (lamp and grating) and emission spectral response (detector and grating) by standard correction curves. Time-resolved measurements were performed using the time-correlated single-photon-counting (TCSPC) PicoHarp300 or the Multi Channel Scaling (MCS) electronics NanoHarp 250 of the PicoQuant FluoroTime 300 (PicoQuant GmbH, Germany), equipped with a PDL 820 laser pulse driver. A pulsed laser diode LDH-P-C-405 ($\lambda_{exc} = 405 \text{ nm}$) was used to excite the sample and mounted directly on the sample chamber at 90° . The photons were collected by a PMA-C-192 photomultiplier(PMT) single-photon-counting detector. The data were acquired by using the commercially available software EasyTau (PicoQuant

GmbH, Germany), while data analysis was performed using the commercially available software FluoFit (PicoQuant GmbH, Germany).

PLQY measurements were performed by using an absolute photoluminescence quantum yield spectrometer Quantaaurus C11347 (Hamamatsu, Japan) exciting the sample at $\lambda_{\text{exc}} = 350$ and 400 nm. All solvents were spectrometric grade.

2.4.3. Synthetic procedures

Synthesis of pyridine-2,6-bis(carboximidhydrazone)(1)

To a solution of pyridine-2,6-dicarbonitrile (20.0 g, 38.75 mmol, 1.0 eq.) in EtOH (125 ml) was slowly added hydrazine monohydrate (38 mL, 775 mmol, 20 eq). The reaction mixture was stirred at room temperature overnight, yielding a pale yellow precipitate in a pale yellow solution. The precipitate was filtered off, washed with twice with cold ethanol and dried to yield a pale yellow solid (7.11 g, 36.82 mmol, 95%) ^1H NMR (400 MHz, d_6 DMSO) δ [ppm]= 7.82 (m, 2H), 7.66 (m, 1H), 6.05 (s, 4H), 5.26 (s, 4H) ^{13}C NMR (100 MHz, d_6 DMSO) δ [ppm]= 151.2, 144.5, 136.8, 118.5.

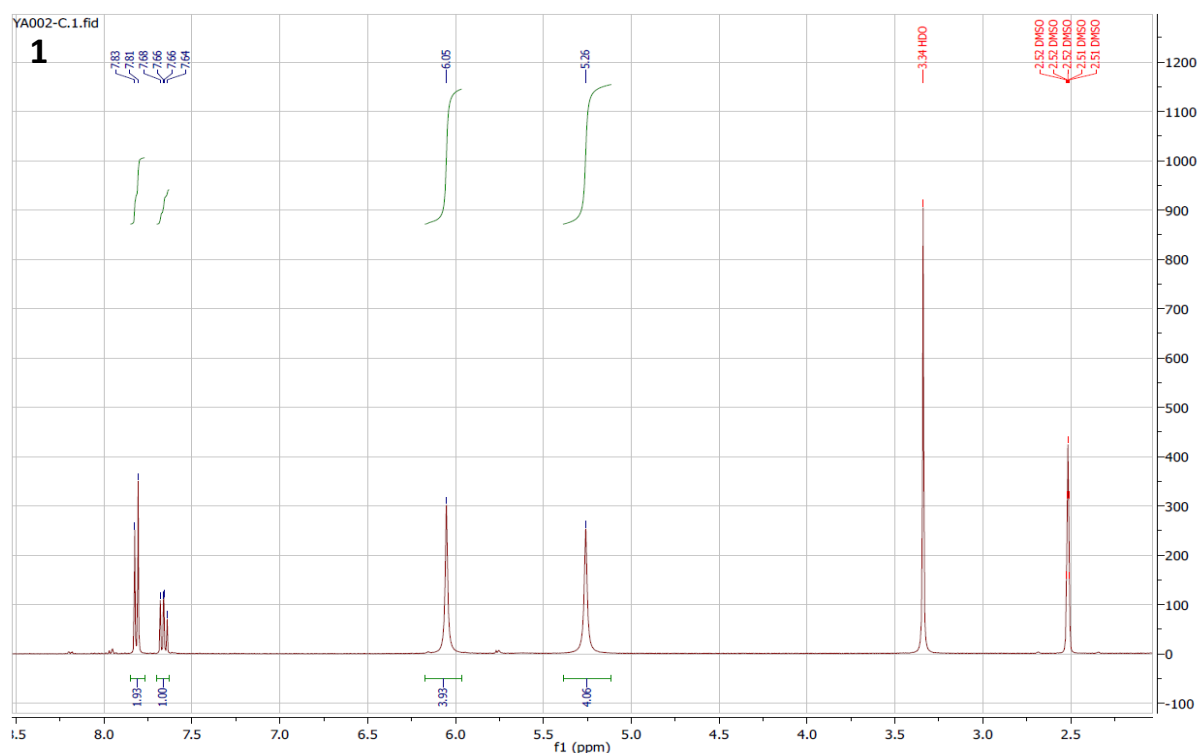


Figure 2.11. ^1H NMR spectrum of **1**

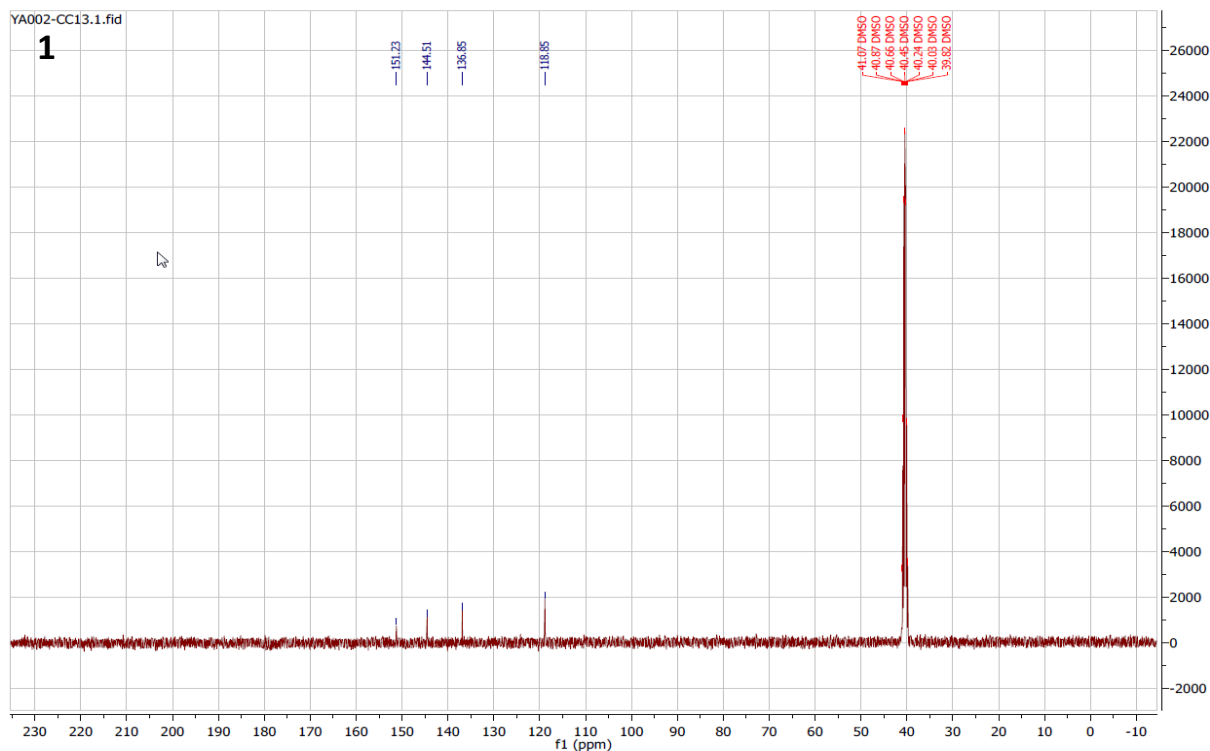
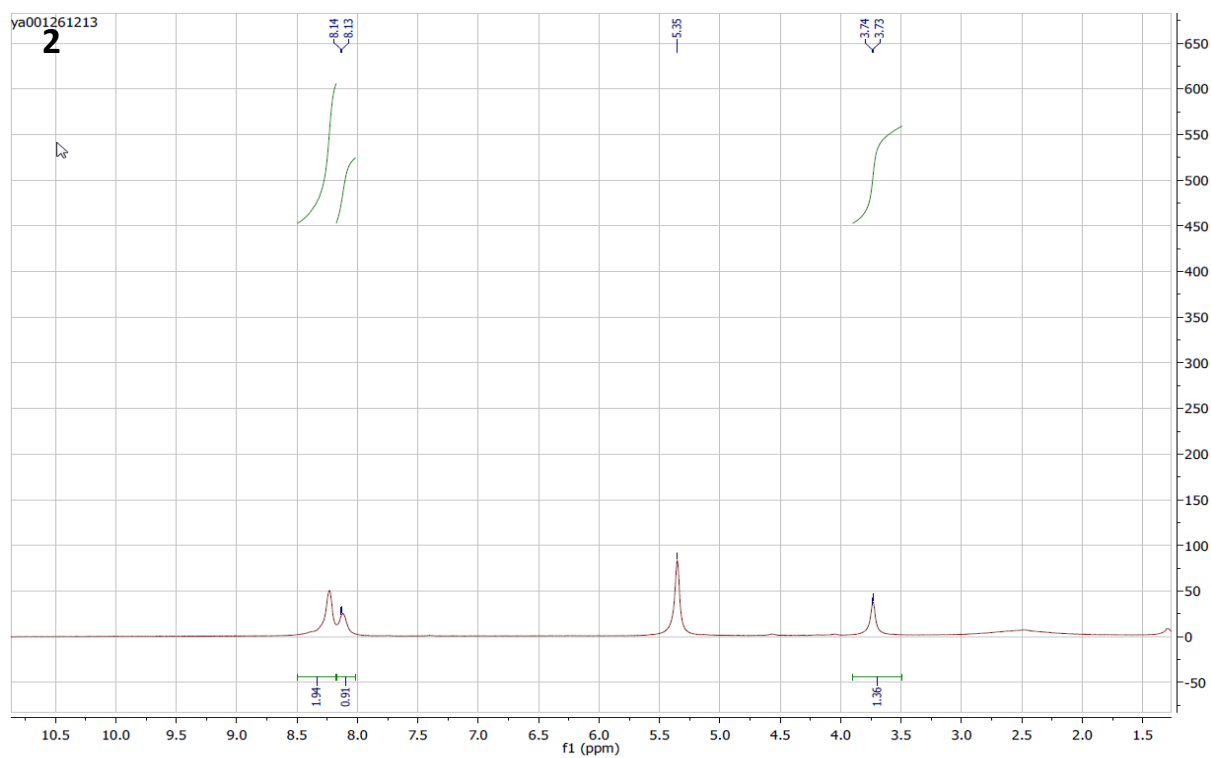
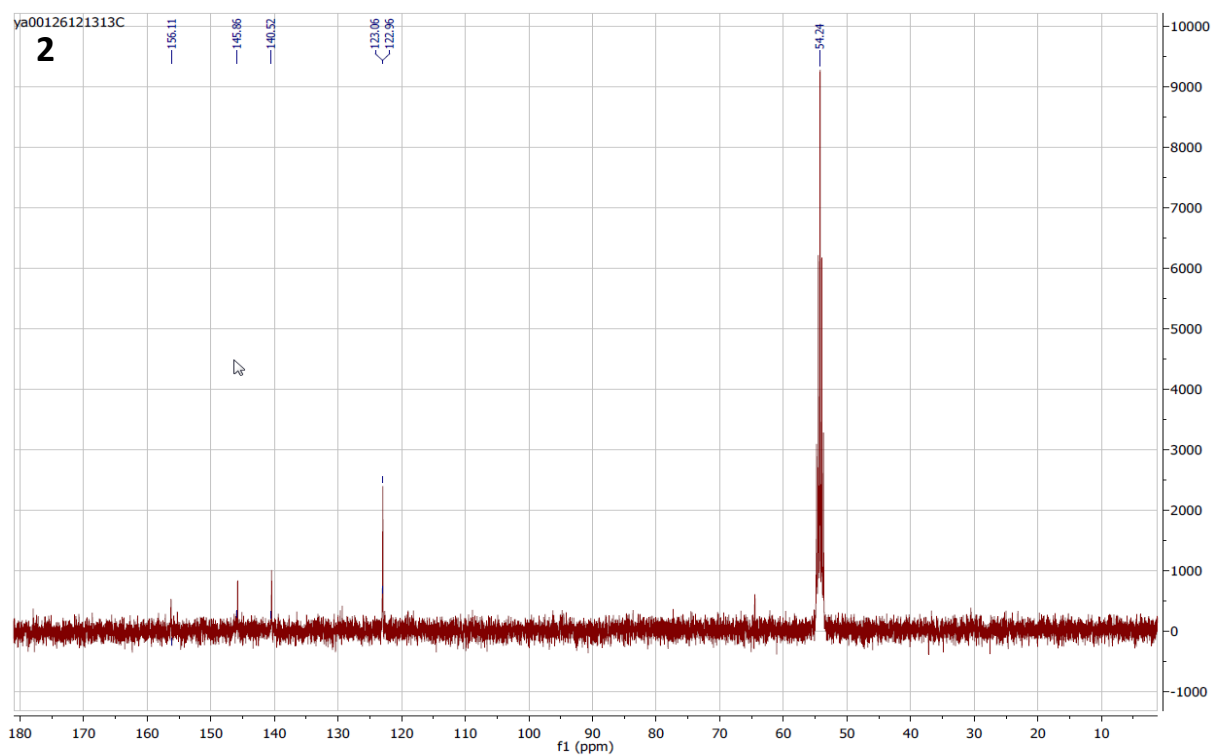


Figure 2.12. ^{13}C NMR spectrum of **1**

Synthesis of 2,6-bis(3-(trifluoromethyl)-1H-1,2,4-triazol-5-yl)pyridine (pyC5-CF3-tzH2,2)

(Pyridine-2,6-bis(carboximidhydrazide) (5g, 25.89 mmol, 1eq) was added to trifluoroacetic acid (TFA) (30mL, large excess) and the mixture was refluxed overnight. TFA was then removed by distillation and ethylene glycol (50 mL) was added. The mixture was heated up at 130°C for 3 hours, and cooled down to room temperature overnight. To the obtained brown solution was added water and the mixture was stirred for 30 minutes to yield, after filtration, washing 3 times with water and 3 times with ethanol, a white powder (6.87g, 19.6mmol, 76%) ^1H NMR (400 MHz, CD_2Cl_2) δ [ppm] = 8.23 (m, 2H), 8.12 (m, 1H); ^{13}C NMR (100 MHz, d_6 DMSO) δ [ppm]= 155.3, 144.4, 140.7, 122.9, 120.7, 118.0. ^{19}F NMR (375 MHz, CD_2Cl_2): -65.61 (1F). HR-ESI-MS (m/z): $[\text{M}+\text{H}]^+$ calculated 350.0583; found 350.0627.

Figure 2.13. ^1H NMR spectrum of **2**Figure 2.14. ^{13}C NMR spectrum of **2**

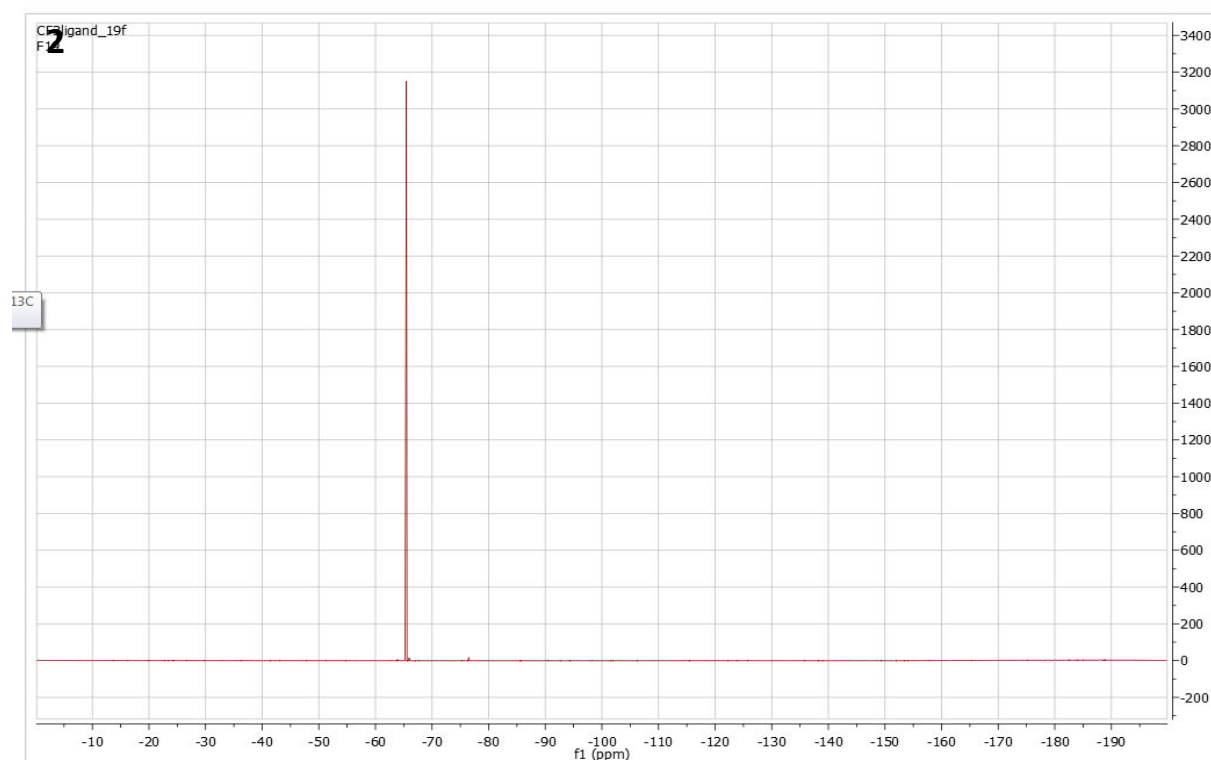


Figure 2.15. ^{19}F NMR spectrum of **2**

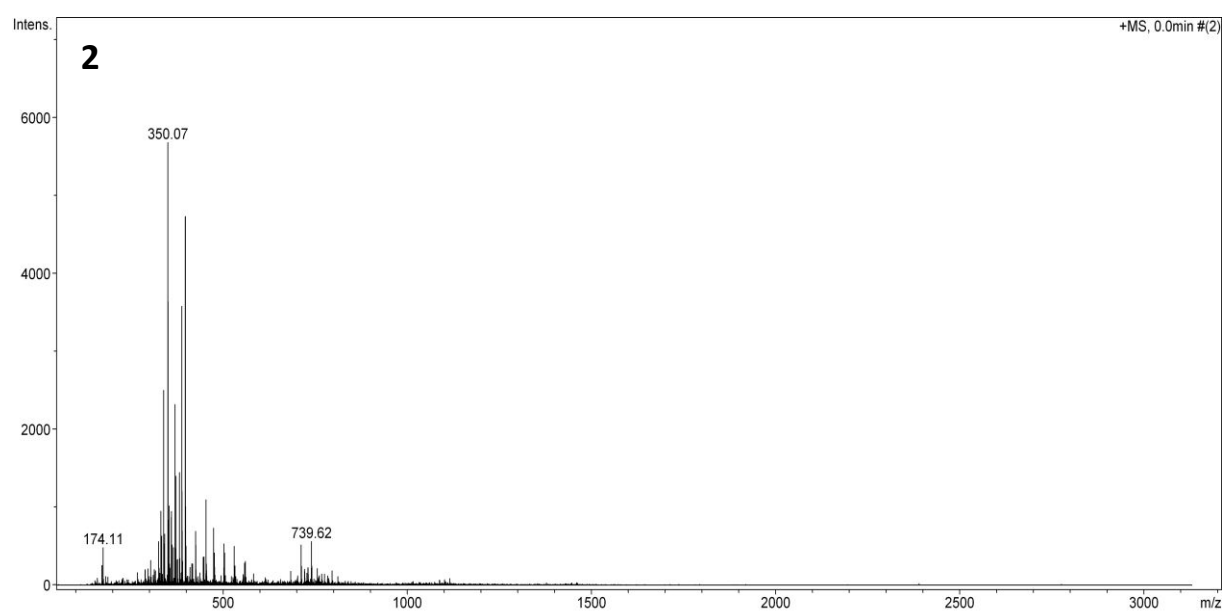


Figure 2.16. ESI-MS spectrum of **2**

Synthesis of 1,*n*-di(pyridin-4-yl)alkane (3b-e)

To a 2.0 M solution of lithium diisopropyl amide in a mixture THF/heptane/ethylbenzene (18.3 mL, 33.52 mmol, 2.2eq) at -78°C was added dropwise 4-picoline (4.28 mL, 33.52 mmol, 2.2 eq) and the reaction medium was stirred

for 1 hours. The corresponding dibromoalkane (15.24 mmol, 1 eq) was then added at -78°C and stirred for 24 h at room temperature. Deionized water (100 mL) was added and the mixture was transferred into an extraction funnel, extracted with 3×100 mL of diethylether and dried over magnesium sulfate. The mixture of solvents was removed under reduced pressure and the product was purified by column chromatography on silica gel (eluent: CH_2Cl_2 97-92: MeOH 3-8) to afford the desired compound (79-83%).

3b ^1H NMR (400 MHz, CDCl_3) δ [ppm]= 8.33 (m, 4H), 6.93 (m, 4H), 2.43 (t, 4H), 1.49 (m, 4H), 1.21 (2H)

3c ^1H NMR (400 MHz, CDCl_3) δ [ppm]= 8.49 (m, 4H), 7.10 (m, 4H), 2.59 (t, 4H), 1.61 (m, 4H), 1.31 (m, 8H)

^{13}C NMR (100 MHz, CDCl_3) δ [ppm]= 151.7, 149.7, 124.0, 35.3, 30.3, 29.3, 29.2

3d ^1H NMR (400 MHz, CDCl_3) δ [ppm]= 8.48 (m, 4H), 7.09 (m, 4H) 2.59 (t, 4H), 1.68 (m, 4H), 1.25 (m, 16H) ^{13}C NMR (100 MHz, CDCl_3) δ [ppm]= 151.9, 149.7, 124.1, 35.4, 30.4, 29.8, 29.7, 29.5, 29.3

3a ^1H NMR (400 MHz, CDCl_3) δ [ppm]= 8.4 (m, 4H), 7.09 (m, 4H) 2.57 (t, 4H), 1.66 (m, 4H), 1.25 (m, 20H) ^{13}C NMR (100 MHz, CDCl_3) δ [ppm]= 152.0, 149.9, 124.2, 35.6, 30.6, 29.9, 29.8, 29.7, 29.5

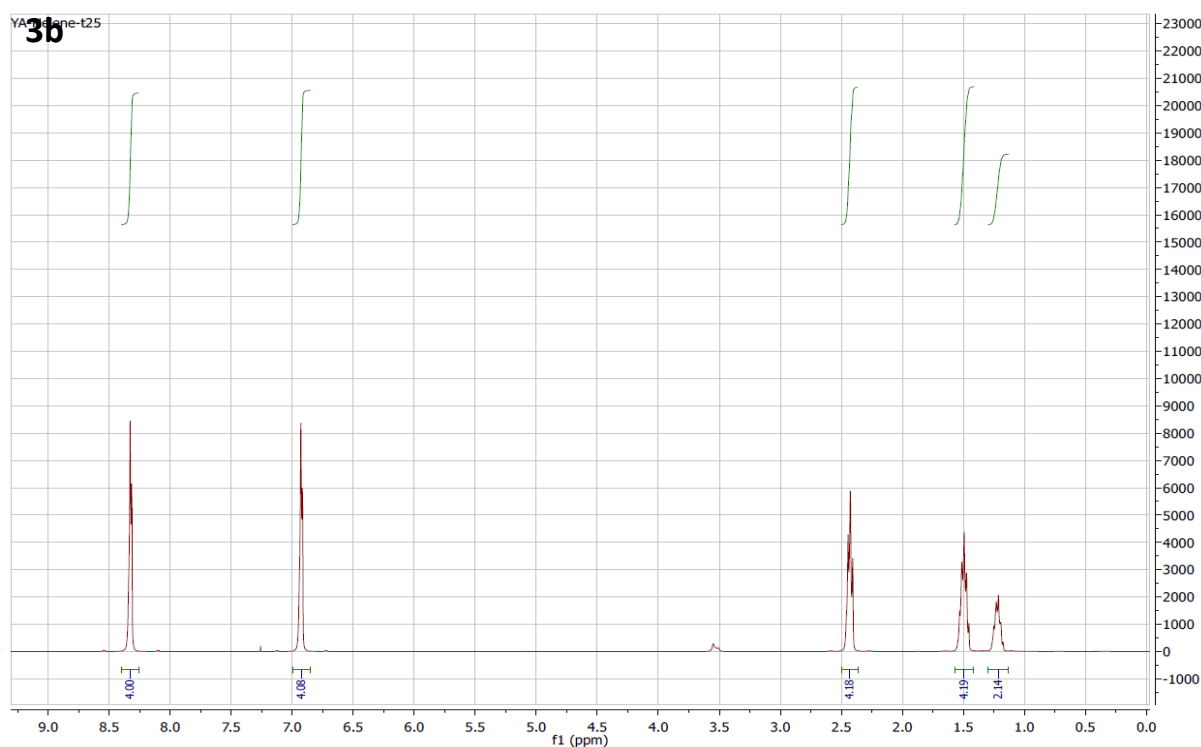


Figure 2.17. ^1H NMR spectrum of **3b**

Synthesis of 1-methyl-4-(n-(pyridin-4-yl)acyl)pyridin-1-ium iodide (4a-e):

To a solution of 1,n-di(pyridin-4-yl)alkane (n=2,5, 8, 11, 14) (15.4mmol, 1eq) in chloroform (50ml) was added slowly iodomethane (96mL, 15.4mmol, 1eq) and the reaction mixture was stirred at room temperature for 24 h. Chloroform was then removed under reduced pressure and the product was purified by chromatography column on silica (eluent: CH₂Cl₂ 96-90: MeOH 4-10) to afford the desired compound (59-74%)

4a ¹H NMR (400 MHz, CDCl₃) δ [ppm]= 9.06 (2H), 8.53 (2H), 7.85 (2H), 7.19 (2H), 4.64 (3H), 2.96 (2H), 2.62 (2H), ¹³C NMR (100 MHz, MeOD) δ [ppm]= 162.6, 151.1, 149.6, 144.9, 127.5, 125.1, 123.1, 48.6, 35.6

4b ¹H NMR (400 MHz, CDCl₃) δ [ppm]= 9.04 (2H), 8.51 (2H), 7.82 (2H), 7.15 (2H), 4.62 (3H), 2.95 (2H), 2.61 (2H), 1.76 (3H), 1.60 (2H) 1.24 (20H) ¹³C NMR (100 MHz, MeOD) δ [ppm]= 162.9, 151.1, 149.7, 149.6, 144.9, 144.7, 127.9, 125.5, 123.9, 48.9, 35.7, 34.9, 29.9, 29.3, 28.5

ESI-MS (m/z): [M+H]⁺ 241.17

4c ¹H NMR (400 MHz, CDCl₃) δ [ppm]= 9.09 (2H), 8.47 (2H), 7.81 (2H), 7.11 (2H), 4.64 (3H), 2.86 (2H), 2.60 (2H), 1.63 (4H), 1.32 (8H) ¹³C NMR (100 MHz, MeOD) δ [ppm]= 163.5, 151.1, 148.8, 145.2, 128.1, 124.2, 49.1, 36.1, 30.4, 29.8, 30.0, 29.5, 29.4, 29.3

4d ¹H NMR (400 MHz, CDCl₃) δ [ppm]= 9.12 (2H), 8.48 (2H), 7.79 (2H), 7.09 (2H), 4.65 (3H), 2.90 (2H), 2.65 (2H), 1.74 (4H), 1.43 (2H) ¹³C NMR (100 MHz, MeOD) δ [ppm]= 162.6, 151.5, 148.8, 144.4, 127.3, 123.4, 48.5, 35.3, 34.6, 30.5, 30.0, 29.0, 28.8, 28.8, 28.7, 28.6, 28.5 ESI-MS (m/z): [M+H]⁺ 351.21

4e ¹H NMR (400 MHz, CDCl₃) δ [ppm]= 9.15 (2H), 8.46 (2H), 7.82 (2H), 4.36 (3H) 2.88 (2H), 2.59 (2H), 1.63 (2H), 1.60 (4H) 1.24 (12H) ¹³C NMR (100 MHz, MeOD) δ [ppm]= 163.5, 152.0, 149.6, 145.4, 127.9, 124.1, 49.0, 36.1, 35.3, 30.4, 27.7, 29.6, 29.5, 29.4, 29.3, 29.2 ESI-MS (m/z): [M+H]⁺ calculated 367.29; found 367.31.

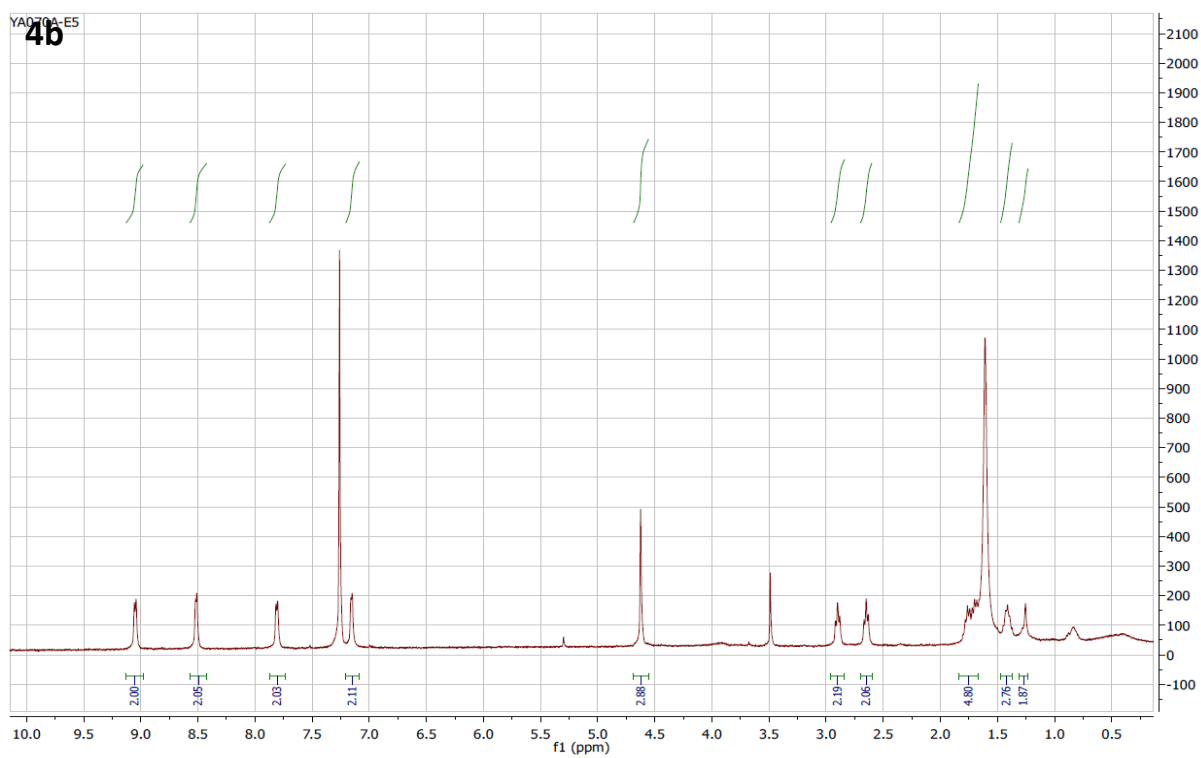


Figure 2.18. ^1H NMR spectrum of **4b**

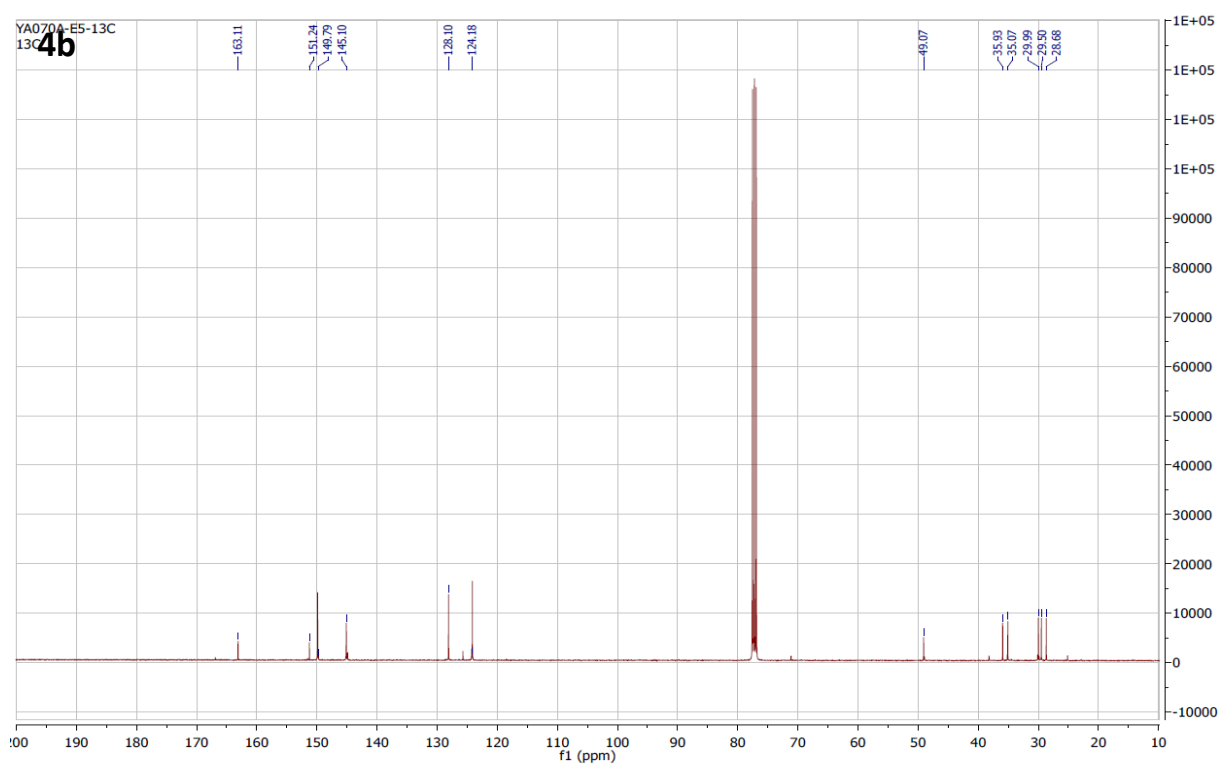


Figure 2.19. ^{13}C NMR spectrum of **4b**

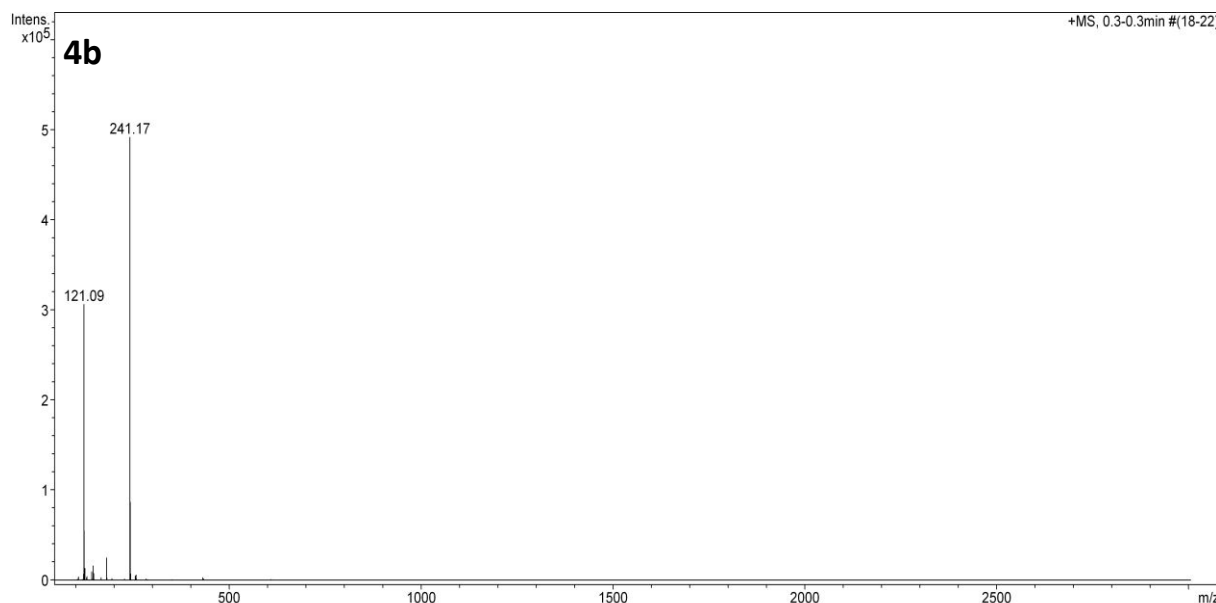


Figure 2.20. ESI-MS spectrum of **4b**

Synthesis of $\text{PtCl}_2(\text{DMSO})_2$

To a suspension of K_2PtCl_4 (10g, 24.1 mmol, 1eq) in water in water (200mL) was slowly added DMSO (3.76 mL, 5.3 mmol, 2.2eq). The reaction mixture was stirred for 2 h to give a pale yellow precipitate. The later was filtered and washed with cold deionized water (2×50mL) and the pale yellow crystals were dried to yield the final product (10.25 g, 24.1 mmol, 100%)

Synthesis of Pt(II) complexes (5a-e):

A solution of 2,6-bis(3-(trifluoromethyl)-1H-1,2,4-triazol-5-yl)pyridine (0.5 g, 1.432 mmol, 1 eq), $\text{PtCl}_2(\text{DMSO})_2$ (0.604 g, 1.432 mmol, 1 eq) and DIPEA (0.5 mL, 3.15 mmol, 2.2 eq) were in acetonitrile was stirred and heated up to 50°C for 10 minutes. The corresponding 1-methyl-4-(n-(pyridin-4-yl)acyl)pyridin-1-ium iodide (1.432 mmol, 1 eq) was then added and the media was stirred at 50°C overnight. The product was dried under reduced pressure and was purified by chromatography column on slightly basic alumina (eluent: CH_2Cl_2 96-90: MeOH 4-10) to afford the desired compound (59-71%)

5a ^1H NMR (400 MHz, MeOD) δ [ppm]= 9.31 (2H), 9.03 (2H), 8.22 (2H), 8.14 (1H), 7.53 (2H), 7.48 (2H), 4.32 (3H), 3.28 (2H) 3.07 (2H) ^{13}C NMR (100 MHz, CD_2Cl_2) δ : 162.9, 160.4, 153.6, 151.5, 147.0, 144.5, 143.3, 127.2, 125.8, 120.4, 117.9, 33.8, 33.4 ^{19}F [^1H] NMR (375 MHz, MeOD) δ [ppm]= -65.55

HR-ESI-MS (m/z): [M+H]⁺ calculated 741.1232; found 741.1323

5b ¹H NMR (400 MHz, MeOD) δ [ppm]= 8.83 (2H), 8.32 (2H), 8.05 (2H), 7.66 (1H), 6.87 (2H), 6.74 (2H), 4.43 (3H), 2.63 (2H), 1.87 (2H), 1.68 (2H), 1.56 (2H) ¹³C NMR (75 MHz, MeOD) δ: 163.2, 162.8, 151.3, 146.9, 144.6, 142.7, 127.6, 126.6, 124.6, 118.1, 35.0, 34.4, 29.3 29.2, 28.4. ¹⁹F [¹H] NMR (375 MHz, MeOD) δ [ppm]= −65.68

HR-ESI-MS (m/z): [M+H]⁺ calculated 783.1703; found 783.1741

5c ¹H NMR (400 MHz, MeOD) δ [ppm]= 8.82 (2H), 8.33 (2H), 8.08 (2H), 7.69 (1H), 6.86 (2H), 6.76 (2H), 4.44 (3H), 2.66 (2H), 1.88 (2H), 1.70 (2H), 1.53 (2H) ¹³C NMR (75 MHz, MeOD) δ [ppm]= 164.9, 164.3 158.0, 152.8, 148.4, 146.0, 144.7, 129.0, 127.2, 126.0, 122.2, 119.5, 36.6, 36.1, 30.9, 30.7, 30.5, .0.4, 30.4, 30.3 ¹⁹F [¹H] NMR (375 MHz, MeOD) δ [ppm]= −65.46

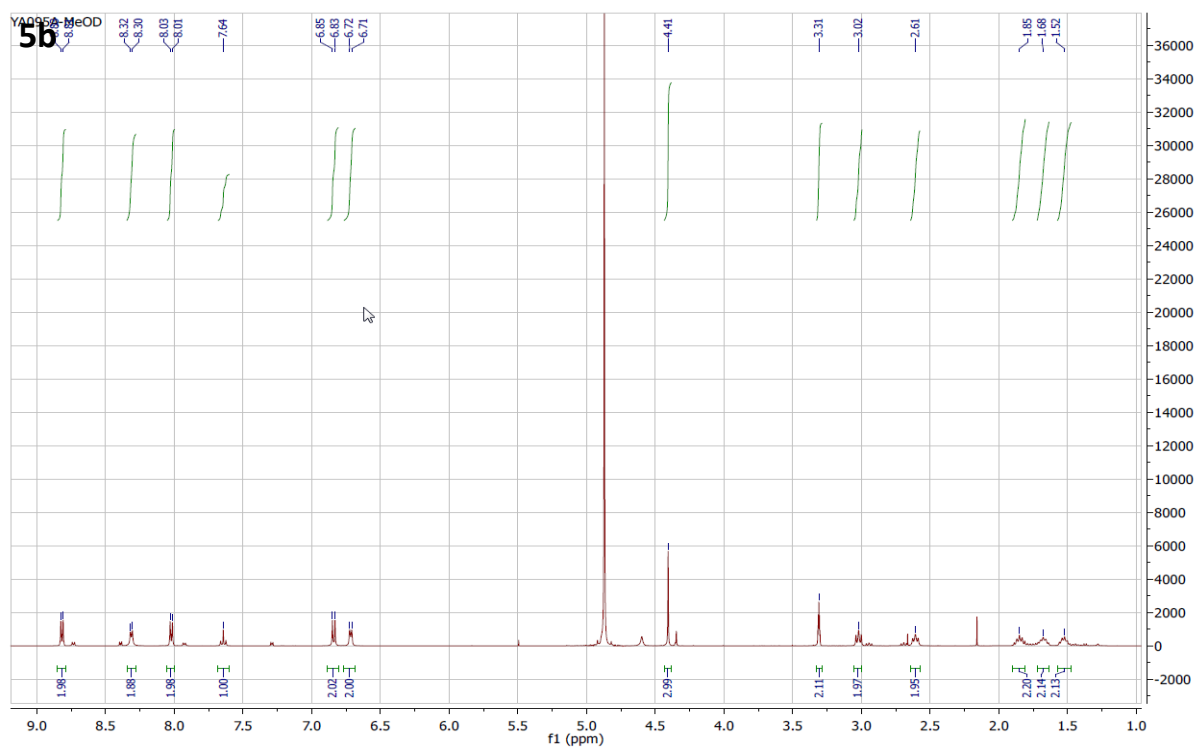
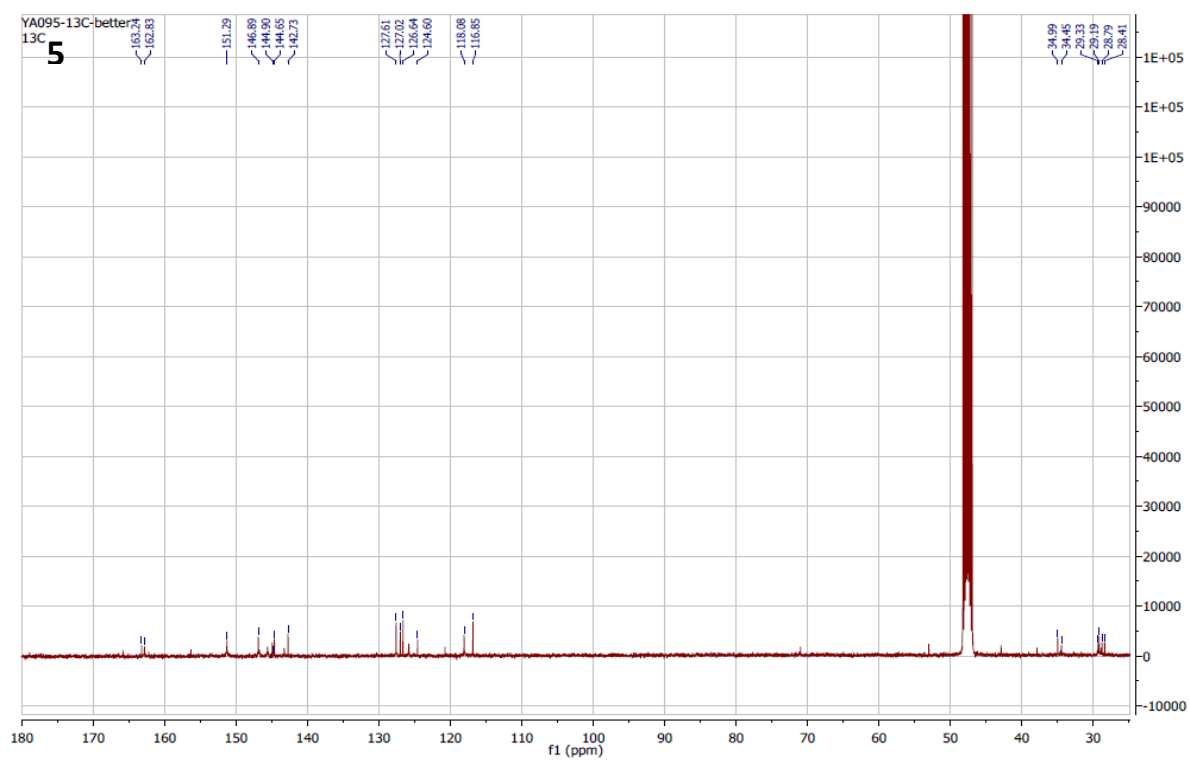
HR-ESI-MS (m/z): [M+H]⁺ calculated 783.1703; found 783.1741

5d ¹H NMR (400 MHz, MeOD) δ [ppm]= 8.80 (2H), 8.45 (2H), 7.95 (2H), 7.72 (1H), 7.00 (2H), 6.75 (2H), 4.38 (3H), 2.98 (2H) 2.60 (2H), 1.79 (2H), 1.64 (2H), 1.42 (14H); ¹³C NMR (75 MHz, MeOD) δ: 164.9, 164.1, 157.9, 152.7, 148.2, 146.0, 128.9, 127.1, 122.1, 119.5, 36.1, 30.9, 30.8, 30.7, 30.6, 30.6, 30.5, 30.4, 30.3, 30.3. ¹⁹F [¹H] NMR (375 MHz, MeOD) δ [ppm]= −65.38

HR-ESI-MS (m/z): [M+H]⁺ calculated 868.2720; found 868.2710

5e ¹H NMR (400 MHz, MeOD) δ [ppm]= 8.77 (2H), 8.54 (2H), 7.94 (2H), 7.74 (1H), 7.05 (2H), 6.80 (2H), 4.36 (3H), 2.95 (2H) 2.61 (2H), 1.76 (2H), 1.63 (2H), 1.35 (20H); ¹³C NMR (75 MHz, MeOD) δ [ppm]= 164.9, 164.1, 157.8, 152.8, 152.6, 152.4, 148.1, 146.0, 144.6, 127.0, 122.1, 119.4, 36.6, 36.11, 31.0, 30.9, 30.8, 30.8, 30.7, 30.7, 30.6, 30.6, 30.5, 30.4, 30.3 ¹⁹F [¹H] NMR (375 MHz, MeOD) δ [ppm]= −65.50

HR-ESI-MS (m/z): [M+H]⁺ calculated 909.3112; found 909.3160

Figure 2.21. ^1H NMR spectrum of **5b**Figure 2.22. ^{13}C NMR spectrum of **5b**

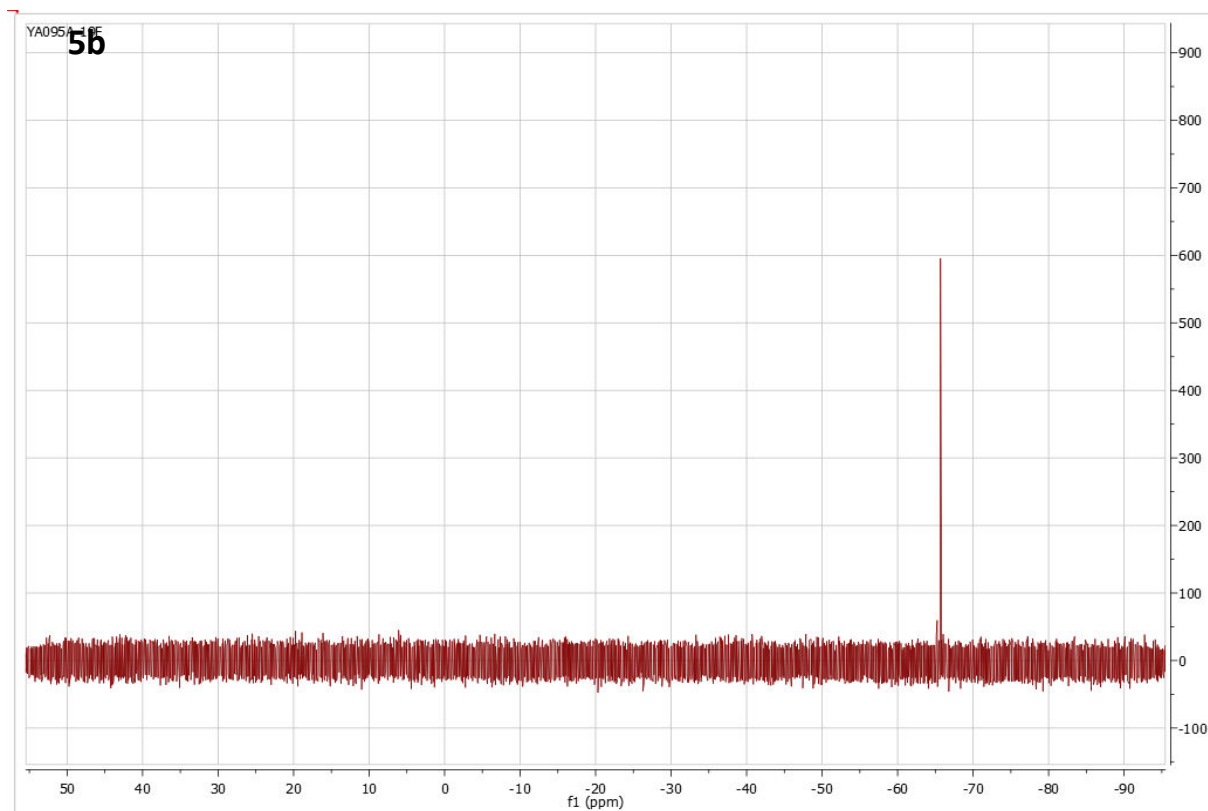


Figure 2.23. ^{19}F NMR spectrum of **5b**

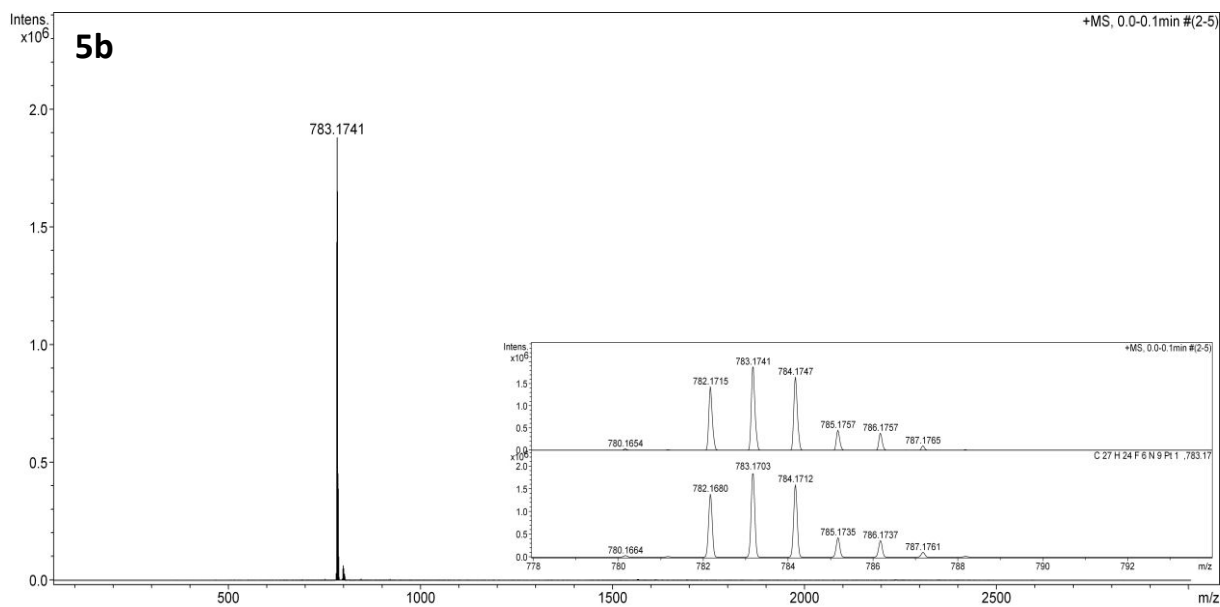


Figure 2.24. ESI-MS spectrum of **5b** Inset: measured (top) and calculated (bottom) HR-MS spectrum of **5b**

2.5. References

1. Shinoda, K. N., T.; Tamamushi, B.; Isemura, T. , *Colloidal Surfactants*. Academic Press:: New York, 1963.
2. Gelbart, W. M. B.-S., A.; Roux D. A. , *Micelles, Membranes, Microemulsions, and Monolayers*. Springer-Verlag: New York, 1997
3. Zieliński, R.; Ikeda, S.; Nomura, H.; Kato, S. *J. Colloid Interface Sci.* **1987**, *119*, 398.
4. De Cola, L. *Inorganic Photochemistry* **2011**, *1*, 47.
5. Coronado, E.; Galan-Mascarós, J.; Miller, J., *Comprehensive Organometallic Chemistry III*, ed. RH Crabtree and DMP Mingos. Elsevier, Amsterdam: 2006.
6. Griffiths, P. C.; Fallis, I. A.; Chuenpratoom, T.; Watanesk, R. *Adv. Colloid Interface Sci.* **2006**, *122*, 107.
7. Shakya, R.; Keyes, P. H.; Heeg, M. J.; Moussawel, A.; Heiney, P. A.; Verani, C. N. *Inorg. Chem.* **2006**, *45*, 7587.
8. Parera, E.; Marín-García, M.; Pons, R.; Comelles, F.; Suades, J.; Barnadas-Rodríguez, R. *Organometallics* **2016**, *35*, 484.
9. Gandolfi, C.; Cotting, T.; Martinho, P. N.; Sereda, O.; Neels, A.; Morgan, G. G.; Albrecht, M. *Dalt. Trans.* **2011**, *40*, 1855.
10. Mao, H.; Yu, H.; Chen, J.; Liao, X. *Sci. Rep.* **2013**, *3*, 2226.
11. de Barros e Silva Botelho, M.; Fernandez-Hernandez, J. M.; de Queiroz, T. B.; Eckert, H.; De Cola, L.; de Camargo, A. S. S. *J. Mater. Chem.* **2011**, *21*, 8829.
12. Haga, M.-a.; Kato, N.; Monjushiro, H.; Wang, K.; Hossain, M. D. *Supramol. Sci.* **1998**, *5*, 337.
13. Li, S.-S.; Yang, Z.-Y.; Yan, C.-J.; Yan, H.-J.; Wan, L.-J.; Guo, P.-Z.; Liu, M.-H. *J. Phys. Chem. C* **2007**, *111*, 4667.
14. Manimaran, B.; Thanasekaran, P.; Rajendran, T.; Lin, R.-J.; Chang, I. J.; Lee, G.-H.; Peng, S.-M.; Rajagopal, S.; Lu, K.-L. *Inorg. Chem.* **2002**, *41*, 5323.
15. Dominguez-Gutierrez, D.; De Paoli, G.; Guerrero-Martinez, A.; Ginocchietti, G.; Ebeling, D.; Eiser, E.; De Cola, L.; Elsevier, C. J. *J. Mater. Chem.* **2008**, *18*, 2762.
16. Guerrero-Martínez, A.; Vida, Y.; Domínguez-Gutiérrez, D.; Albuquerque, R. Q.; De Cola, L. *Inorg. Chem.* **2008**, *47*, 9131.
17. Mauro, M.; De Paoli, G.; Otter, M.; Donghi, D.; D'Alfonso, G.; De Cola, L. *Dalt. Trans.* **2011**, *40*, 12106.
18. Swami, A.; Kumar, A.; Pasricha, R.; Mandale, A. B.; Sastry, M. *J. Colloid Interface Sci.* **2004**, *271*, 381.
19. Karasik, A. A.; Naumov, R. N.; Balueva, A. S.; Spiridonova, Y. S.; Golodkov, O. N.; Novikova, H. V.; Belov, G. P.; Katsyuba, S. A.; Vandyukova, E. E.; Lönnecke, P.; Hey-Hawkins, E.; Sinyashin, O. G. *Heteroat. Chem* **2006**, *17*, 499.
20. Taira, T.; Suzuki, Y.; Osakada, K. *Chem. Asian J.* **2008**, *3*, 895.
21. Castriciano, M.; Romeo, A.; Romeo, R.; Monsu'Scolaro, L. *Eur. J. Inorg. Chem.* **2002**, *2002*, 531.
22. Kimizuka, N.; Oda, N.; Kunitake, T. *Inorg. Chem.* **2000**, *39*, 2684.
23. Einaga, Y.; Mikami, R.; Akitsu, T.; Li, G. *Thin Solid Films* **2005**, *493*, 230.
24. Aliprandi, A.; Mauro, M.; De Cola, L. *Nat. Chem.* **2016**, *8*, 10.
25. Collin, J.-P.; Frey, J.; Heitz, V.; Sauvage, J.-P.; Tock, C.; Allouche, L. *J. Am. Chem. Soc.* **2009**, *131*, 5609.

26. Coe, B. J.; Foxon, S. P.; Harper, E. C.; Helliwell, M.; Raftery, J.; Swanson, C. A.; Brunschwig, B. S.; Clays, K.; Franz, E.; Garín, J.; Orduna, J.; Horton, P. N.; Hursthouse, M. B. *J. Am. Chem. Soc.* **2010**, *132*, 1706.
27. Pownall, H. J.; Smith, L. C. *Biochemistry* **1974**, *13*, 2590.
28. Velazquez, M. M.; Costa, S. M. B. *J. Chem. Soc., Faraday Trans.* **1990**, *86*, 4043.
29. Che, C. M.; He, L. Y.; Poon, C. K.; Mak, T. C. W. *Inorganic Chemistry* **1989**, *28*, 3081.
30. Naziruddin, A. R.; Lee, C.-S.; Lin, W.-J.; Sun, B.-J.; Chao, K.-H.; Chang, A. H. H.; Hwang, W.-S. *Dalt. Trans.* **2016**, *45*, 5848.
31. Imoto, H.; Tanaka, S.; Kato, T.; Watase, S.; Matsukawa, K.; Yumura, T.; Naka, K. *Organometallics* **2016**, *35*, 364.
32. Mauro, M.; Aliprandi, A.; Cebrian, C.; Wang, D.; Kubel, C.; De Cola, L. *Chem. Commun.* **2014**, *50*, 7269.
33. Solomatina, A. I.; Krupenya, D. V.; Gurzhiy, V. V.; Zlatkin, I.; Pushkarev, A. P.; Bochkarev, M. N.; Besley, N. A.; Bichoutskaia, E.; Tunik, S. P. *Dalt. Trans.* **2015**, *44*, 7152.
34. El Garah, M.; Sinn, S.; Dianat, A.; Santana-Bonilla, A.; Gutierrez, R.; De Cola, L.; Cuniberti, G.; Ciesielski, A.; Samori, P. *Chem. Commun.* **2016**, *52*, 11163.

CHAPTER 3:

Hybrid Pt(II) Complexes-Silica Nanoparticles Materials: Synthesis and Properties

Abstract

This chapter, describes the development of new luminescent hybrid systems based on the use of platinum complexes as templates for the construction of porous silica nanoparticles. In particular, the self-assembly of the platinum(II) complexes, studied in Chapter 2, is explored in a sol-gel process, to replace part of the surfactant molecules used in the synthesis of mesoporous silica nanoparticles (MSNs). The properties of these new materials were deeply investigated and a comparison of the photophysical properties of the platinum complexes in solution and in these hybrid materials is made. The emission profile is identical in energy in both cases but, interestingly, the photoluminescence quantum yields of the hybrid systems are higher and the excited state lifetimes are longer than the those of the complexes in solutions.

Keywords

Pt(II) complexes, Luminescent properties, Mesoporous silica nanoparticles, Self-assembly

3.1. Introduction

Among all the methods to stabilize and isolate Pt(II) complexes aggregates (creation of polymeric systems, freezing the medium, ...), encapsulation in porous matrices is definitely an attractive strategy to protect the compounds from dioxygen or media quenching, to increase rigidity, to avoid undesired reactions.

Inorganic porous materials is a class of materials that are more and more used in research.¹ Typical examples are zeolites and zeolite-like materials, pillared materials, clathrates, molecular sieves, porous carbon materials, porous hybrid materials, or porous metal oxides.²⁻⁷ In particular, mesoporous silica nanoparticles, MSNs, have been deeply investigated due to their stability, their tunable size, shape and pore size, their narrow pore distribution, and their high pore volume to material size ratio.⁸ They are hence used in catalysis,⁹⁻¹⁰ chemical sensors,¹¹⁻¹² drug delivery systems,¹³⁻¹⁴ molecular separation¹⁵⁻¹⁷, since different molecules can be encapsulated in MSNs. In comparison with zeolites, MSNs feature bigger pores, and therefore allow a wider range of possible guest molecules.

There are several ways to process the encapsulation of transition metal complexes (TMCs) inside silica. For instance, the creation of covalent bonds between silica and the complex can be performed,¹⁸ but the absence of selective binding site inside the pores, in respect to the surface (both the pores and the surface contain only silanol groups), makes the regioselectivity difficult to control. Another way to load the TMCs into silica pore is by sublimation, but the often metal complexes are heavy or charged making the process rather complicated (high vacuum and often very high temperatures are required).

To overcome these problems, we propose a strategy based on the creation of a surfactant-type complex, that can form nanostructures, e.g. micelles able to act as a template for the silica and therefore remaining inside the pores. The complexes described in *Chapter 2* are therefore very good candidates for this technique. The concept is depicted in **Figure 3.1** that summarize the overall strategy. Such an approach was already followed in our group to encapsulate positively charged Ir(III) complexes. In this case however the Iridium unit acted as hydrophilic head,¹⁹ and the tail was hydrophobic. In our design the situation is reversed since we aim to have Pt complexes as hydrophobic part. We envisage the formation of micellar systems, with the Pt complexes in the core of the nanostructures. The other reason to employ Pt(II) compounds instead of Ir(III) complexes is, as described in *Chapter 1*, that Pt(II)

complexes have the tendency to stack by non-covalent interactions and to even form Pt-Pt bonds.²⁰⁻²² Therefore, the self-assembly process is more interesting with Pt(II) than with Ir(III) complexes, and the aggregation coming from the structural micellar systems is then stabilized by the Pt---Pt interactions.

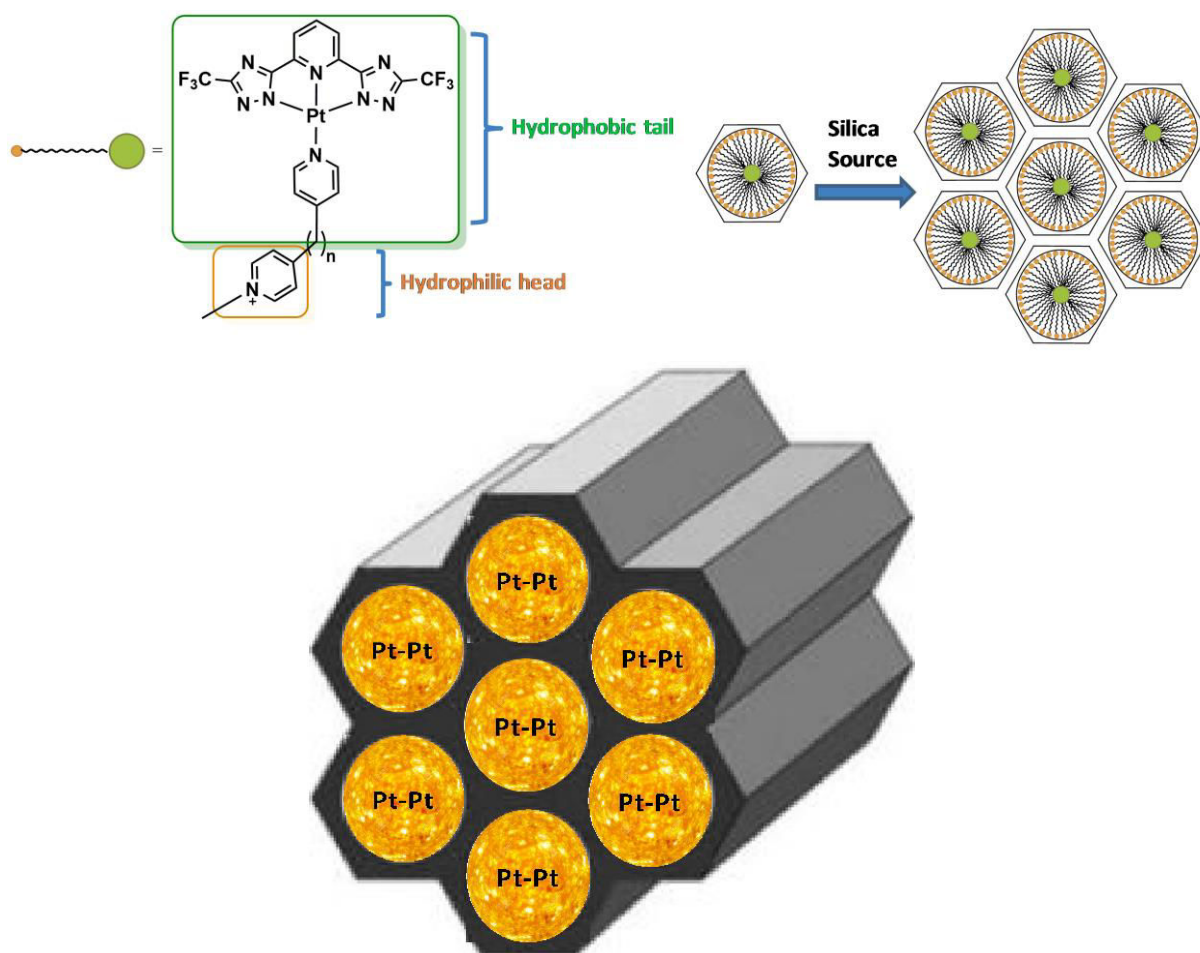


Figure 3.1. Design of the final system

3.2. Results and discussion

In order to understand why the surfactant based on Pt(II) complexes are interesting for the formation of the silica we have to briefly describe the synthesis of porous silica nanoparticles as e.g. MCM-41 (see *chapter 1*). The condensation of a silica precursor occurs indeed around the micelles that are formed with a given surfactant, e.g. hexadecyltrimethylammonium bromide, also called cetyltrimethylammonium bromide or CTAB. Above a certain CMC, these surfactants molecules self-assemble to form micelles (**Figure 3.2**). CTAB micelles act as templates for the silica condensation and therefore determine the pore size in the particles. The bigger are the micelles, the

larger are the pores at the end of the synthesis.²³⁻²⁴ When the micelles concentration increases, hexagonal structures appear.²⁵ Then, the process can go on with the assembly of the hexagonal arrays a lamellar phase, with possibly cubic phase intermediate.²⁶ The CMC of CTAB in water at 25°C is about 0.9 mM, and the shape of the assembly changes upon increasing of the concentration.²⁵ As silica source, the most used precursor is tetraethyl orthosilicate (TEOS), but it can be substituted with different silica source such as tetramethyl orthosilicate (TMOS), tetrapropyl orthosilicate (TPOS), sodium silicate, etc.²⁷⁻²⁹ In basic aqueous media, the silica source will hydrolyze resulting in tetrahydroxy silane and further condenses/polymerizes all around the micellar systems. The basic media (sodium hydroxide or ammonia) regulates the speed of both hydrolysis and condensation of the silica source.²⁹

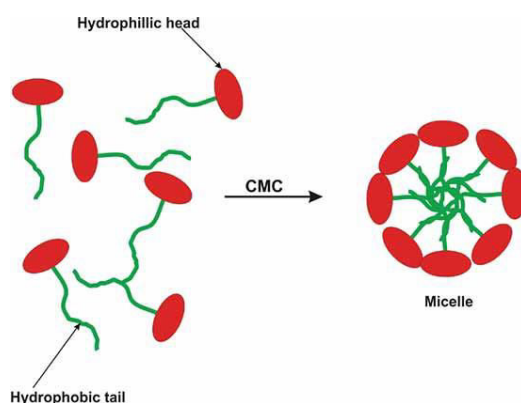


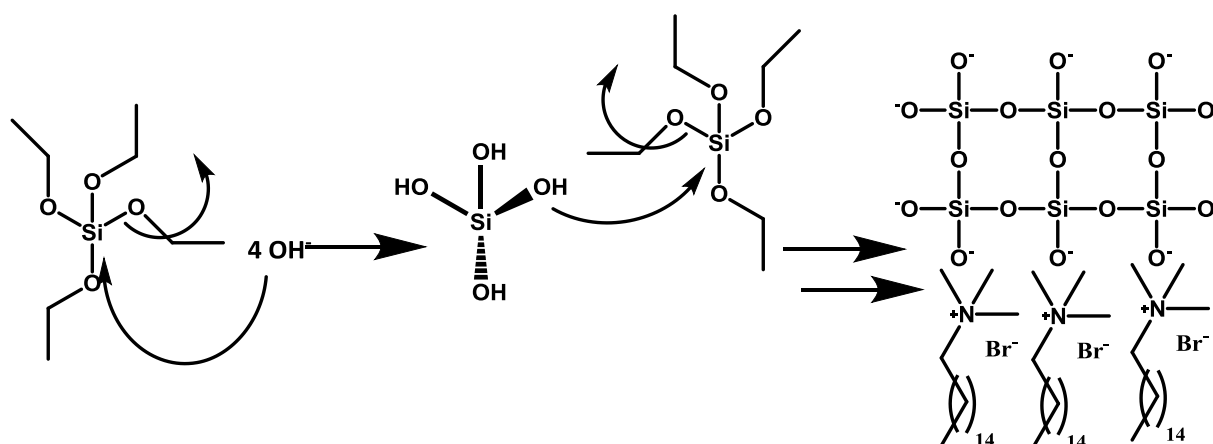
Figure 3.2. Arrangement of surfactants to form micellar systems

Table 3.1. Shape of the aggregated structures formed by CTAB according to its concentration in water at 25°C

CTAB concentration	Shape of the aggregated structure
$0.83\text{M} \leq [\text{CTAB}] \leq 11 \text{ wt } \%$	Spherical
$11 \text{ wt } \% \leq [\text{CTAB}] \leq 25 \text{ wt } \%$	Rod-like
$65 \text{ wt } \% \leq [\text{CTAB}] \leq 65 \text{ wt } \%$	Hexagonal

Based on this mechanism, the encapsulation of the complexes, described in *chapter 2*, has been performed. To match the length of CTAB and to facilitate the formation of hybrid micelle TMCs/CTAB, we only focus on complex **5d** and **5e** (*Chapter 2*) which we called **2** and **1** in this chapter, respectively (**Figure 3.3.**). To study the effect of the TMCs molecules in the formation of the silica nanoparticles and the photophysical properties

of these complexes in the rigid matrix, different ratios complexes/CTAB were studied (**Table 6.2**) while the amount of TEOS was kept constant across the work done for this chapter (45mM).



Scheme 3.1. Proposed mechanism for MCM-41 synthesis

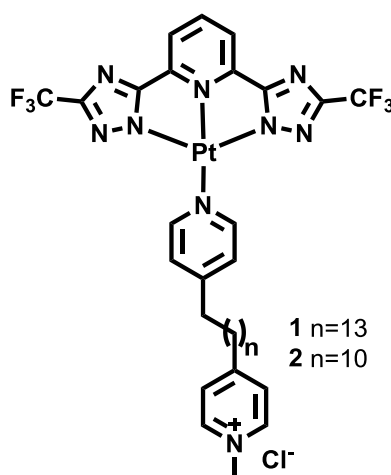


Figure 3.3. Molecular structure of the Pt(II) complexes studied in this chapter

Table 3.2. Studied complexes, “1” represents the C14 complex, while “2” the C11 complex

	[Pt(II) Complex](mM)	[CTAB](mM)
Sample 1a/2a	10^{-3}	2.75
Sample 1b/2b	0.02	2.75
Sample 1c/2c	0.1	2.25
Sample 1d/2d	0.2	2

The yielded materials have been characterized by SEM, TEM, TGA, N₂ sorption, and the photophysical properties of these materials were studied in micellar solutions and solid state. When necessary, the results were compared to MCM-41. SEM pictures (**Figures**

3.5. and **3.6)** show, for all the hybrid materials a spherical shape. Intriguingly, the particles containing the metal complexes are bigger than the regular MCM-41 (**Figure 3.4**). This can be explained by the size of the Pt(II) complex, which takes more space during the synthesis process.

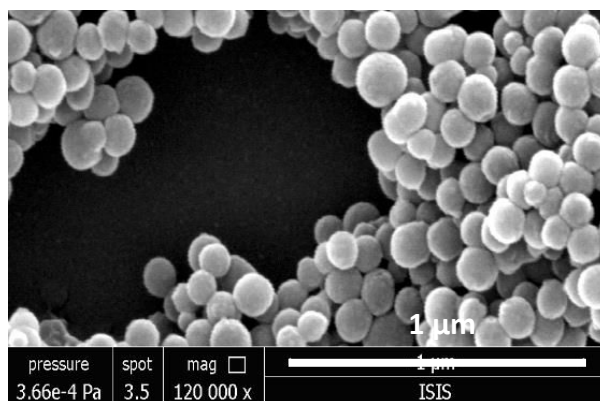


Figure 3.4. SEM image of MCM-41

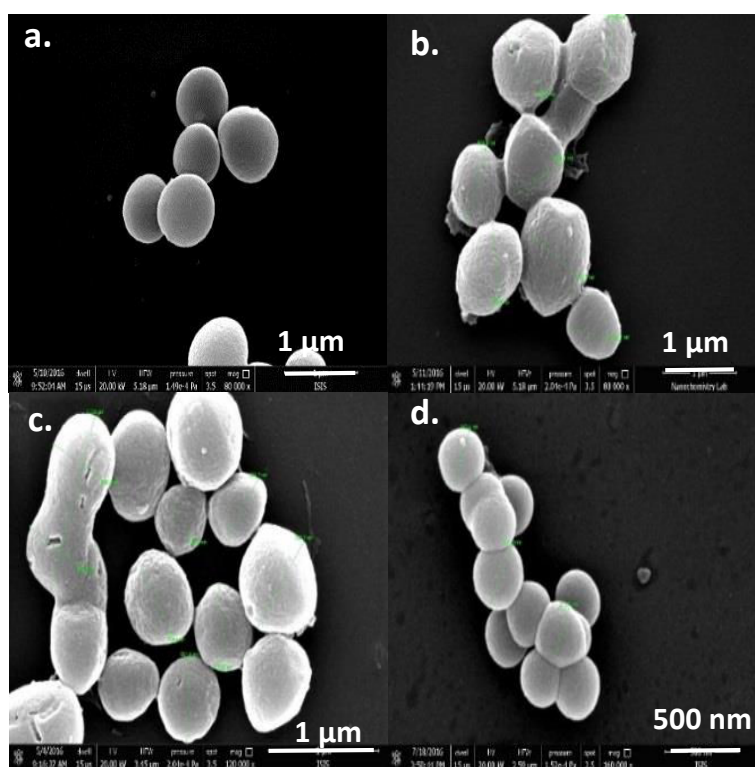


Figure 3.5. SEM pictures of sample **1a** (a.), sample **1b** (b.), sample **1c** (c.), sample **1d** (d.)

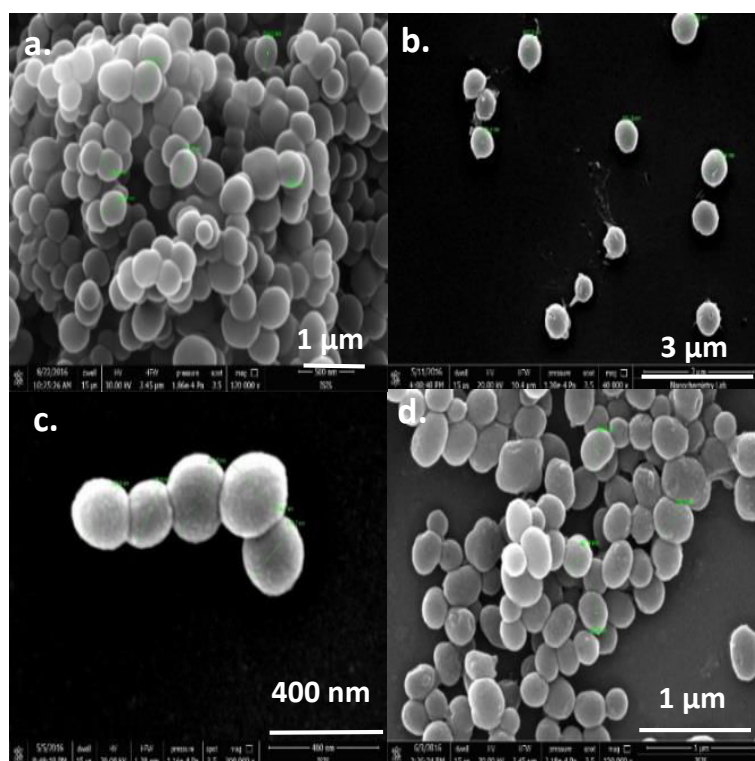


Figure 3.6. SEM picture of sample **2a** (a.), sample **2b** (b.), sample **2c** (c.), sample **2d** (d.)

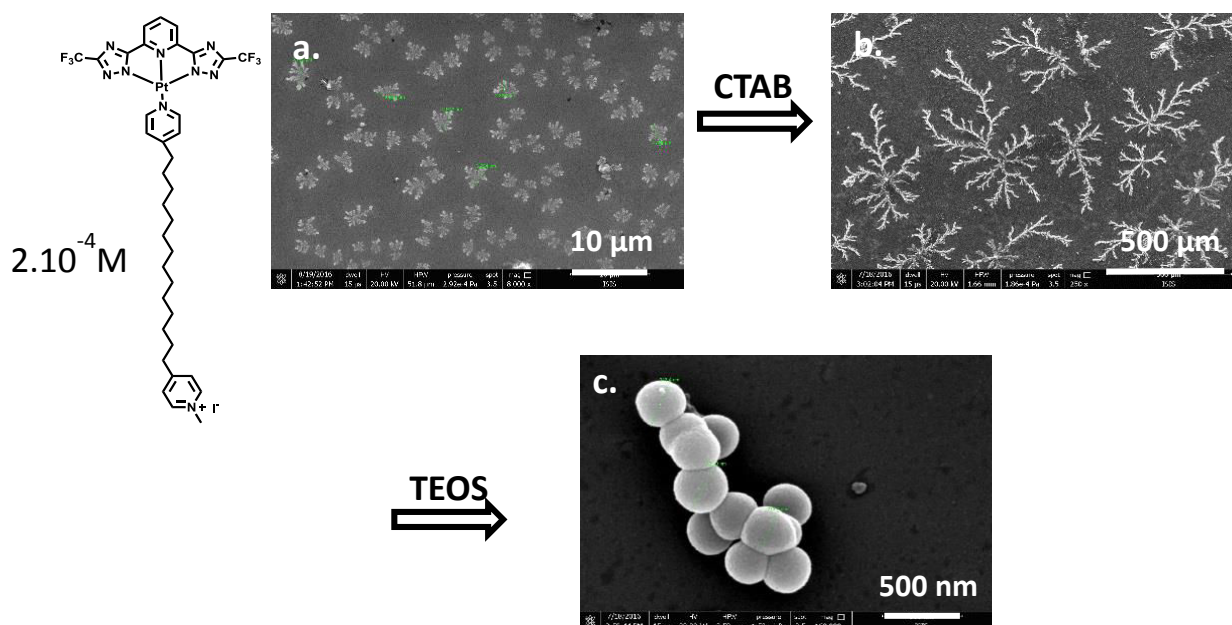


Figure 3.7. SEM images showing the monitoring of **1.d** formation: **a.** complex **1** sample prepared by dropcasting a 0.2mM solution; **b.** sample prepared from dropcasting a solution of 0.2mM of complex/0.2M of CTAB; **c.** sample prepared by adding TEOS to the previous solution

The synthesis of the particles has also been followed by SEM, an example is shown in **Figure 3.7** with material **1d**. Dry sample after drop-casting a 2.10^{-4} M solution of **1** forms

dendrimers-like structures of $2\mu\text{m}$ size (**Figure 3.7.a**). Interestingly, sample from drop-casting a solution of 2.10^{-4}M of **1** with 2mM of CTAB yields to materials having the same type of dendritic shape, but more than 200 times bigger ($500\mu\text{m}$ size, **Figure 3.6.b**). This result implies that CTAB plays an important role on the self-assembly of the complexes, dramatically increasing the resulting size.

Finally, dry sample from drop-casting a solution of 2.10^{-4}M of **1** with 2mM of CTAB and 45mM of TEOS leads to an observation of the final material i.e. spherical particles with a size of around 400nm (**Figure 3.7.c** or **Figure 3.5.d**).

Thermogravimetric analysis (TGA) of the materials were performed between 20 and 1100°C , and the results are shown in **Figure 3.8**. As MCM-41 is purely inorganic, the comparison between the hybrid materials and MCM-41 was not necessary. All the materials already lost around 8% of their weight at 150°C , referring to the remaining traces of water. Between 200°C and 500°C , Complex **1** have a more important weight loss than samples **2**, explained by the higher molecular mass of **1** than **2** (between 40 and 55% for samples **1**, between 25 and 45% for samples **2**). At higher temperature, the profiles display a plateau, and no weight change was observed from 500°C to 1100°C .

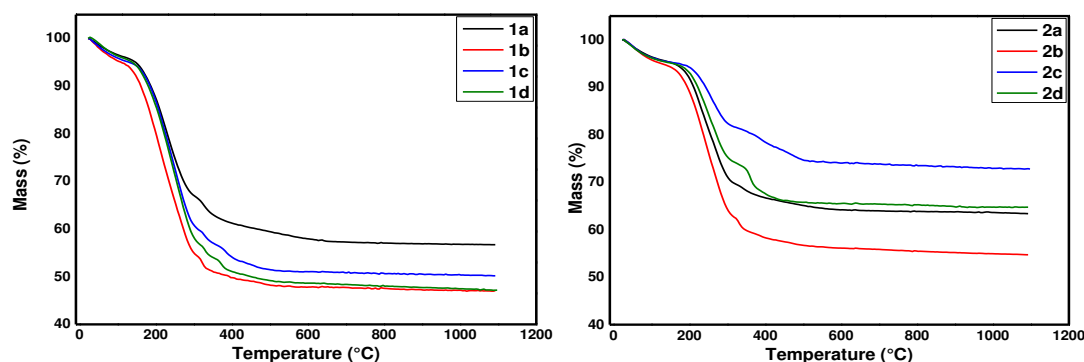


Figure 3.8. TGA profile of materials **1a.-d.** (left) and **2a.-d.** (right)

The calcinated samples from TGA were taken out and subsequently TEM analysis were performed for each samples. The images are shown in **Figures 3.9** and **3.10**. Like for SEM pictures, the first observation is that MSNs made by a complex/CTAB mixture are bigger than particles prepared with pure CTAB as a surfactant. Moreover, we can clearly see the arrangement of pores, having a size of only few nanometers. The addition of TMCs into the system does not disturb the formation of ordered mesopores. From the TEM images, we clearly see the pore arrangement even up to 10% ratio of TMCs compare to the CTAB. Even though the TEM images are clearly

shown a porosity, the pore size and shape cannot be determined by this techniques. Therefore, N₂ adsorption-desorption experiments were performed on each sample, in order to determine the pore size of the materials and to state a correlation between the amount of complex and the pore size (**Figures 3.11-3.12**).

In comparison with MCM-41, which here acts as a reference, MSNs synthesized with a mixture complex/CTAB mixture feature a bigger pore size, around 3.5 nm, while for MCM-41 the pore size is around 2.3 nm. As for the particle size, this result can be explained by the fact that Pt(II) complexes occupy more space than CTAB, increasing the aggregates size and leading to larger pores after calcination of the material. This is in line with other reports, in which changing the surfactant size yields materials with larger pores.²³⁻²⁴

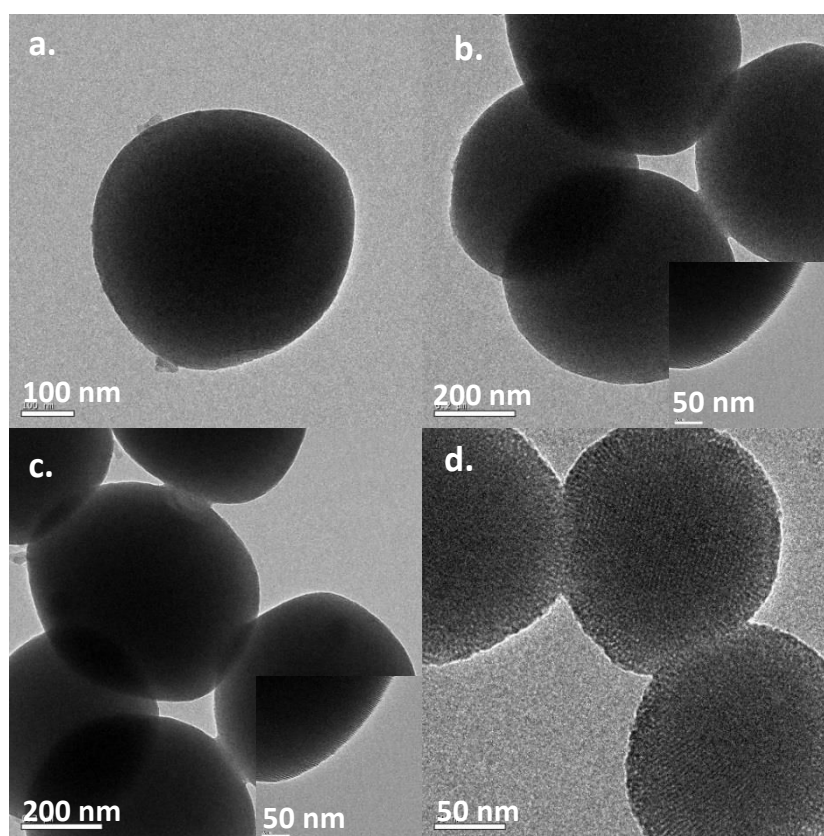


Figure 3.9. TEM pictures of sample **1a** (a.), sample **1b** (b.), sample **1c** (c.), sample **1d** (d.)

Insets: zoom

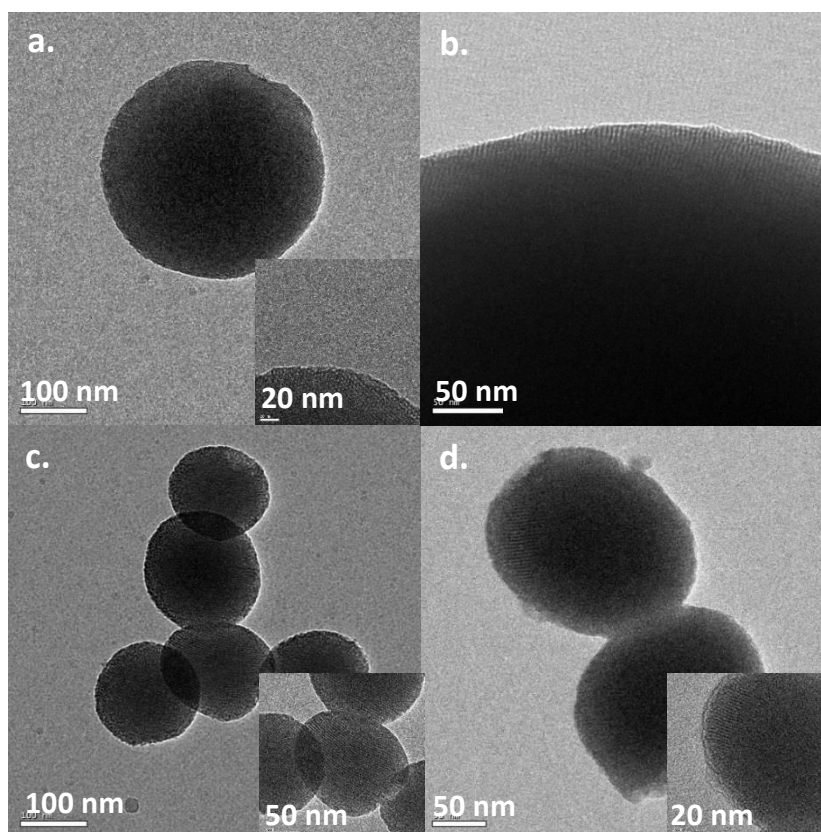


Figure 3.10. TEM pictures of sample **2a** (a.), sample **2b** (b.), sample **2c** (c.), sample **2d** (d.)

Inset: zoom

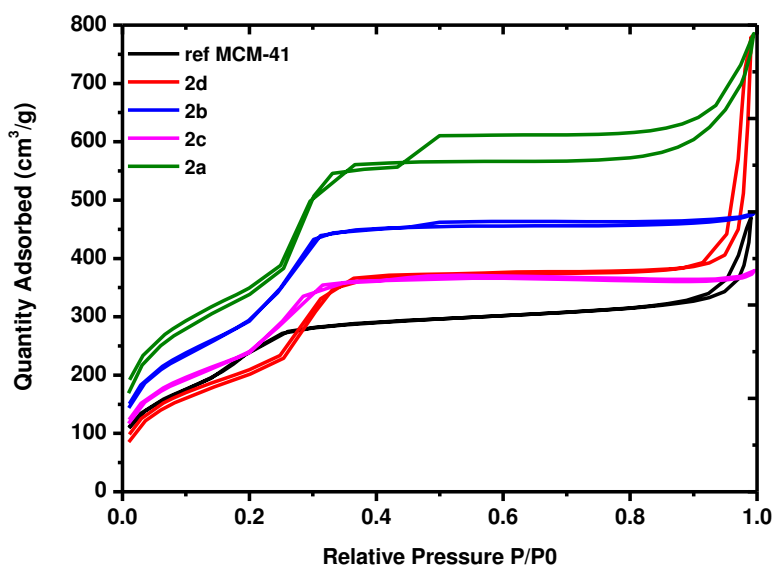


Figure 3.11. Isothermal curves of materials MCM-41 (black trace), **2a.** (green trace), **2b.** (blue trace), **2c.** (magenta trace), **2d.** (red trace)

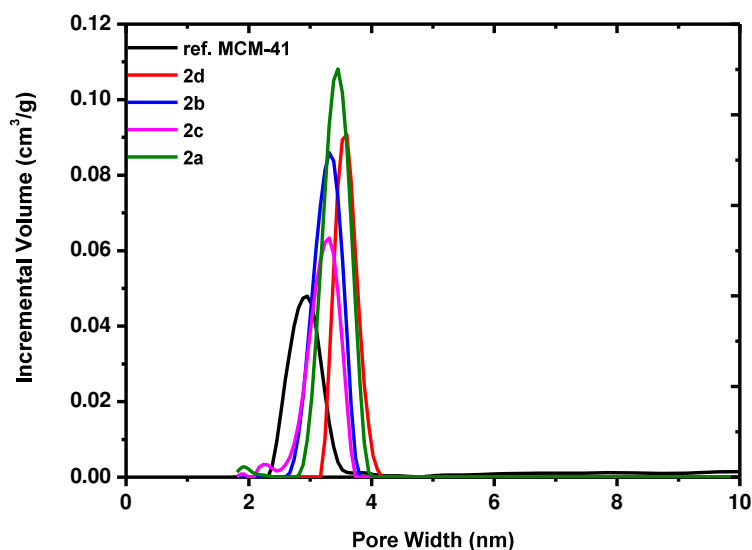


Figure 3.12. Pore size distribution of MCM-41 (black trace), **2a.** (green trace), **2b.** (blue trace), **2c.** (magenta trace), **2d.** (red trace)

Photophysical properties of the materials **1 a.-d.** and **2 a.-d.** were then studied, and the emission and excitation spectra are shown in **figures 3.13** and **3.14**, respectively. Before analyzing the photophysical properties of TMCs inside the mesoporous silica, we investigated TMCs encapsulated inside the CTAB micelle (**Tables 3.3-3.4**). A mixture of each studied Pt(II) complex and CTAB in solution in a mixture water 9:1 ethanol (0.2mM and 2mM, respectively), as referred in **Figure 3.7.b** was prepared and the photoluminescence quantum yields (PLQY) and excited state lifetimes (ESLT) were measured (**1@CTAB**, **2@CTAB**). The complexes inside the micelles possess an emission profile that resembles the complexes in water solution, with a broad, featureless band at 590 nm typical for Pt(II) complexes in their aggregated state. The complexes inside silica show an important enhancement of the luminescence properties, with a PLQY of 26%, from originally 11 to 14 % in water, and an ESLT around 0.6 μ s (~60%) and 0.3 μ s (~40%), solution. The rather rigid shell created by CTAB induces a certain confinement and rigidity to the complex, leading to less non-radiative decay. Moreover, CTAB acts as a shield toward dioxygen diffusion, and therefore protects the emissive state from quenching.

Table 3.3. Photophysical properties of complex **1** in solid state and in water (10^{-4} mM), and of complex **1** in CTAB micelles

Material	$\lambda_{em}(nm, \lambda_{exc}=400nm)$	$\phi(\%)$	$\tau(\mu s)$
Aggregate of 1 in water	587	6	0.442 (56%) 0.142 (44%)
Aggregate of 1 in solid state	593	11	0.452 (57%) 0.140 (53%)
1 @CTAB	590	26	0.592 (57%) 0.317 (43%)

Table 3.4. Photophysical properties of complex **2** in solid state and in water (10^{-4} mM), and of complex **2** in CTAB micelles

Material	$\lambda_{em}(nm, \lambda_{exc}=400nm)$	$\phi(\%)$	$\tau(\mu s)$
Aggregate of 2 in water	587	4	0.302 (35%) 0.115 (65%)
Aggregate of 2 in solid state	589	7	0.393 (56%) 0.148 (44%)
2 @CTAB	590	26	0.553 (61%) 0.303 (39%)

Samples of hard materials (**1**@MSNs, **2**@MSNs) having a relatively high concentration of complex (**b.**, **c.** and **d.**), feature the same emission profile as the complexes in water or in solid state, with a broad, featureless band at 590nm, typical for Pt(II) complexes in their aggregated form, attributed to MMLCT transition and matching the results obtained in *chapter 2*.³⁰ Strikingly, samples **a.**, having the least amount of chromophore complexes (10^{-6} M) display interesting emission profiles, with the same broad, featureless band that have a slight hypsochromic effect (576nm) and also narrow bands at higher energy (481 and 505 nm), also observed in other reported cases and attributed to LC or MLCT transition, i.e. Pt(II) complexes in their monomeric state. At the same concentration of complexes, the latter in water do not show any emission signal at such a high energy, and we can conclude that, in a way, CTAB is able to brake the aggregates, probably by intercalating the complexes.

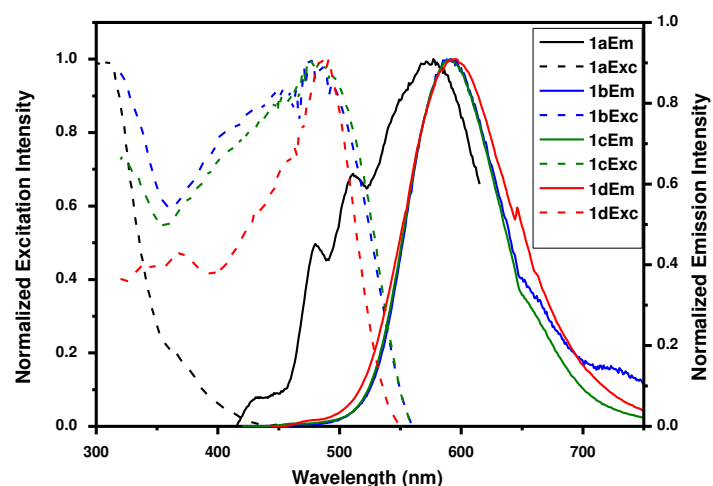


Figure 3.13. Emission (full line, $\lambda_{\text{exc}}=400\text{nm}$) and excitation (dashed line, $\lambda_{\text{em}}=600\text{nm}$) of compounds **1a-d**.

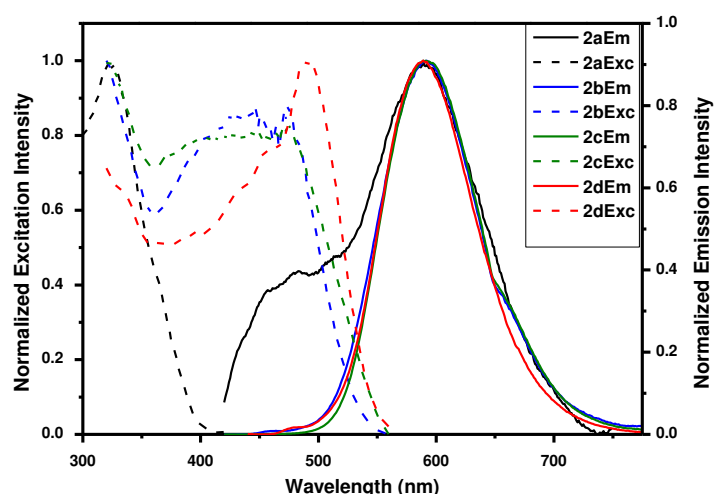


Figure 3.14. Emission (full line, $\lambda_{\text{exc}}=400\text{nm}$) and excitation (dashed line, $\lambda_{\text{em}}=600\text{nm}$) of compounds **2a-d**.

The PLQY and ESLT of materials **1**. and **2**. show a great enhancement in comparison to the aggregates in water, or even to the complexes in solid state (**Table 3.5**) Indeed, upon encapsulation in MSNs, the PLQY of **1** increases up to four times higher and the ESLT are approximatively doubled. Regarding complex **2**, the PLQY increases by a factor of seven and the ESLT are approximatively twice longer. The rigidity provided by the confined space of the MSNs, as well as the protection of oxygen quenching have an undeniable effect on the photophysical properties enhancement. The matrix is a much

better environment vs the micelles most likely due to the lack of the dynamic behavior and the better confinement that can provide.

Table 3.5. Photophysical properties of materials **1a.-d.** and **2a.-d** encapsulated in porous silica.

Material	$\lambda_{em}(nm, \lambda_{exc}=400nm)$ ** $\lambda_{exc}=350nm$	$\phi(\%)$	$\tau(\mu s)$
1a	481-510-576**	n.d.*	0.171(39%)** 0.010(61%)**
1b	587	28	0.911 (42%) 0.405 (58%)
1c	587	37	0.936(34%) 0.386(66%)
1d	589	41	0.961(40%) 0.363(60%)
2a	476-590**	n.d.*	0.160(31%)** 0.008(69%)**
2b	590	44	1.247 (19%) 0.706 (81%)
2c	590	45	1.325 (19%) 0.754 (81%)
2d	590	39	0.991(63%) 0.218(37%)

* The absorbance is too low to have a reliable data

Finally, hybrid materials involving complexes **1** and **2**. in MSNs without CTAB were synthesized. The materials are respectively called **1e** and **2e**. The schematic representation of such system is presented in **Figure 3.15**. For this purpose, the synthesis was first performed using the Pt(II) complexes acting as structure directing agent, and a TEOS solution as a silica source, in a mixture water 9:1 ethanol (18mL), in basic media at 80°C with a final concentration of 0.6mM and 45mM, respectively. From SEM images (**Figure 3.16**), the resulting material has no spherical shape, but only fibers of complexes surrounded by silica are observed. They are around 1 μm long and 50 nm wide. Contrary to soft materials in which the actual structure in solution is not necessarily what we see on SEM analysis, in this case the SEM images of hard materials, coming from a static state, can be relevant of what is happening in solution (or in dispersion), the silica playing the role of “freezing agent”. Subsequently, the same

procedure was used using a 6mM solution of complexes. From SEM images (**Figures 3.17**), we interestingly observe the formation of big particles, around 5 μm diameter. Such big particles are due to the total absence of CTAB and the high concentration of voluminous and bulky complexes. According to these SEM images (**Figure 3.16** and **3.17**) we can conclude that at 80°C, micelles start to form at a concentration between 0.6mM and 6mM.

The photophysical properties of materials **1e** and **2e** were investigated and compared to the complexes without silica, as well as to the materials previously described.

As expected, they exactly display the same emission wavelength as **b**., **c**. and **d**. and the aggregated complexes without silica. Their PLQY and ESLT are shown in **Table 3.6**.

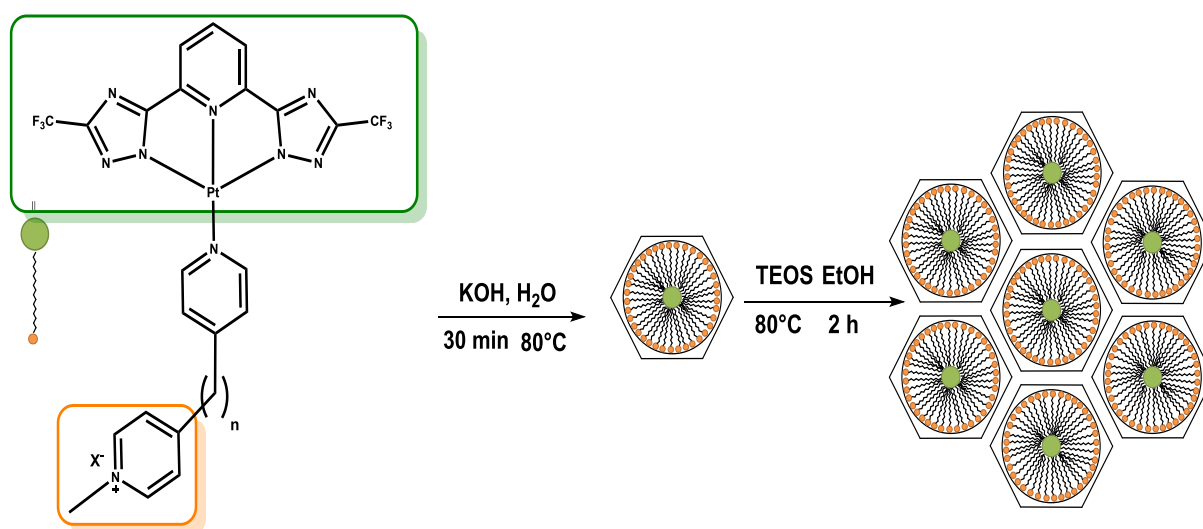


Figure 3.15. Synthetic Scheme for the procedure of MSNs without CTAB

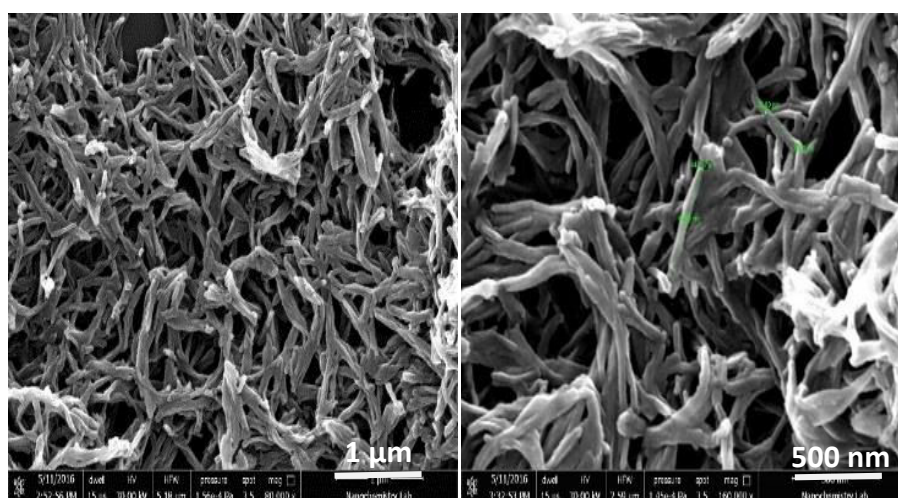
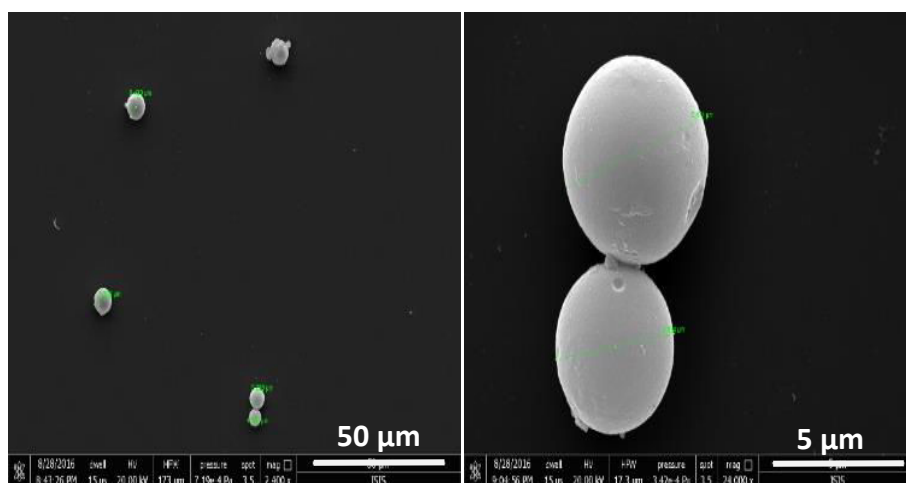
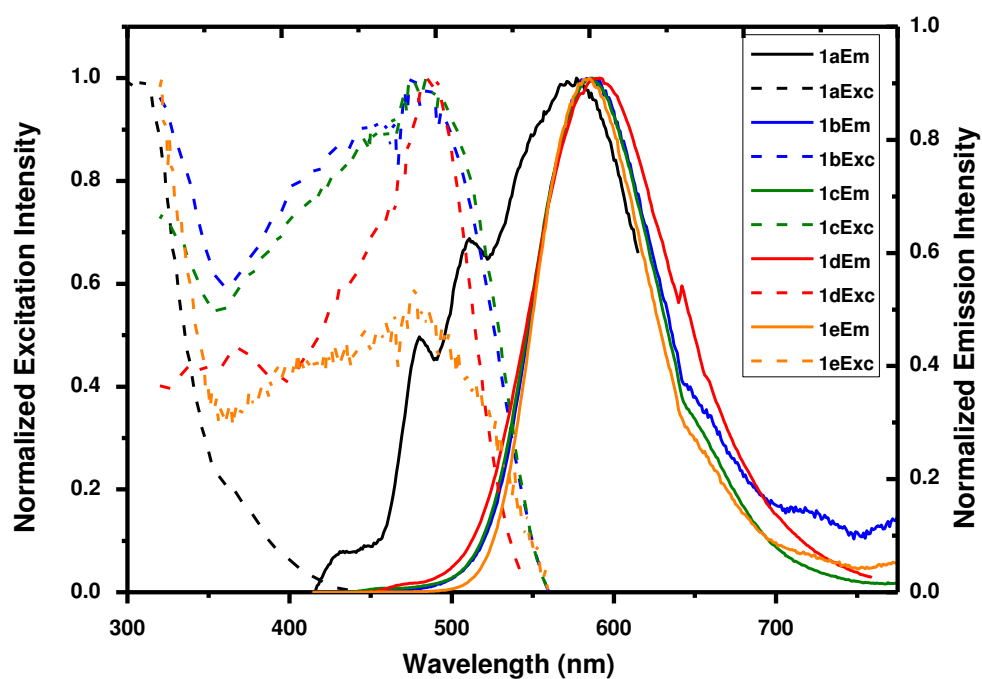


Figure 3.16. SEM images of complex **1** inside MSNs, prepared by a 0.6mM solution of **1****Figure 3.17.** SEM images of complex **1** inside MSNs, prepared by a 6mM solution of **1** (**1e**)**Figure 3.18.** Emission (full line, $\lambda_{\text{exc}}=400\text{nm}$) and excitation (dashed line $\lambda_{\text{em}}=400\text{nm}$), spectra of materials **1a-e****Table 3.6.** Photophysical properties of complex **1.e.** and **2.e.**

Material	$\lambda_{\text{em}}(\text{nm}, \lambda_{\text{exc}}=400\text{nm})$	$\Phi(\%)$	$\tau(\mu\text{s})$
1e	592	28	0.662(26%)
			0.281(74%)

2e	590	28	0.744(30%) 0.331(70%)
-----------	-----	----	--------------------------

The photophysical properties of materials **1e** and **2e** were investigated and compared to the complexes without silica, as well as to the materials previously described. As expected, they exactly display the same emission wavelength as **b.**, **c.** and **d.** and the aggregated complexes without silica. Their PLQY and ESLT are shown in **Table 3.6**. For clarity reasons, emission and excitation spectra of materials made by **1** are shown one more time, with **1e** in order to compare (**Figure 3.18**).

3.3. Conclusion

In this work we demonstrated that upon encapsulation of Pt(II) complexes in MSNs we can achieve better emission properties and stabilize the self-assembled structures. To achieve our purpose, amphiphilic Pt(II) complexes were used as silica pores template for a sol-gel method, either alone or together with CTAB. Even though the shape is spherical, both the particles and the pores are bigger than the regular MCM-41.

The results show that the rigidity provided by the confined space of the MSNs, as well as the protection of oxygen quenching are responsible for the photophysical properties enhancement. Moreover, at very low ratio complex/CTAB the complex shows an emission profile that resembles Pt(II) complexes at their monomeric state, implying that the presence of CTAB can prevent the formation of Pt---Pt interactions acting as a spacer in the micelle structure.

3.4. Experimental procedure

3.4.1. Materials and methods

All the solvents and reagents were used as received from Aldrich, Fluka, TCI and VWR without any further purification.

Scanning Electron Microscopy (SEM) images were recorded with a FEI Quanta FEG 250 instrument (FEI corporate, Hillsboro, Oregon, USA) with an acceleration voltage of 20 kV. The sample is prepared by drop-casting a dispersion of particles in EtOH onto a glass cover slip, subsequently sputter coated with Au (Emitech K575X peltier cooled) for 60 s at 60 mA prior to fixation on an Al support.

Transmission Electron Microscopy (TEM) samples were analysed on a Hitachi 7500 instrument at an acceleration voltage of 80 kV. Ethanolic suspensions of the materials

were drop-casted onto Formvar coated Cu grids (400 mesh) and allowed to dry overnight prior to visualization.

Thermogravimetric Analysis (TGA) were conducted on a Perkin Elmer TGA4000 Instrument machine under nitrogen atmosphere. The samples (0.1 – 2 mg) were kept at 100 °C for 30 minutes for stabilization, then heated from 100 to 750 °C at a speed of 10 °C/min, before being held at this temperature for further 30 minutes before cooling. The analyses were performed under a gas flow of N₂ at 60 mL/min.

Nitrogen Adsorption-Desorption analyses of the samples were performed using a Micromeritics porosimeter (model ASAP-2020). The samples were degassed at 150 °C for 3h and N₂ adsorption/ desorption measurement was done at -196 °C. The surface areas and pore volume were calculated by BET method and the pore size distributions were calculated by DFT methods.

Steady-state emission spectra were recorded on a Horiba Jobin-Yvon IBH FL-322 Fluorolog 3 spectrometer equipped with a 450 W xenon arc lamp, double-grating excitation, and emission monochromators (2.1 nm mm⁻¹ of dispersion; 1200 grooves mm⁻¹) and a TBX-04 single photon-counting detector. Emission and excitation spectra were corrected for source intensity (lamp and grating) and emission spectral response (detector and grating) by standard correction curves. Time-resolved measurements were performed using the time-correlated single-photon-counting (TCSPC) PicoHarp300 or the Multi Channel Scaling (MCS) electronics NanoHarp 250 of the PicoQuant FluoroTime 300 (PicoQuant GmbH, Germany), equipped with a PDL 820 laser pulse driver. A pulsed laser diode LDH-P-C-405 (λ_{exc} = 405 nm) was used to excite the sample and mounted directly on the sample chamber at 90°. The photons were collected by a PMA-C-192 photomultiplier(PMT) single-photon-counting detector. The data were acquired by using the commercially available software EasyTau (PicoQuant GmbH, Germany), while data analysis was performed using the commercially available software FluoFit (PicoQuant GmbH, Germany).

PLQY measurements were performed by using an absolute photoluminescence quantum yield spectrometer Quantaaurus C11347 (Hamamatsu, Japan) exciting the sample at a range λ_{exc} between 350 and 500 nm. All solvents were spectrometric grade.

3.4.2. Synthesis of 1a-d and 2a-d

To a solution of cetyl trimethylammonium bromide (CTAB) and the cationic Pt(II) complex 1 or 2 in water (96 mL) at different concentrations were added 1 mL of NaOH 2M and 10 mL of EtOH. The solution was then heated up to 80°C and stirred vigorously.

Meanwhile, TEOS (1 mL) was dissolved in absolute ethanol (3 mL). The latter was then added to the first solution and the final mixture was vigorously stirred for 2 hours at 80°C. The particles were then recovered by centrifugation and washed 3 times with water and 3 times with EtOH to yield the final material.

3.4.3. Synthesis of **1e** and **2e**

To a solution of **1** or **2** in water (18 mL) at different concentrations were added 1 mL of NaOH 2M and 2 mL of EtOH. The solution was then heated up to 80°C and stirred vigorously. Meanwhile, TEOS (1 mL) was dissolved in absolute ethanol (3 mL). The latter was then added to the first solution and the final mixture was vigorously stirred for 2 hours at 80°C. The particles were then recovered by centrifugation and washed 3 times with water and 3 times with EtOH to yield the final material.

3.5. References

1. Davis, M. E. *Nature* **2002**, 417, 813.
2. Jin, Y.; Konno, Y.; Nagao, J. *Energy & Fuels* **2012**, 26, 2242.
3. Ryoo, R.; Joo, S. H.; Kruk, M.; Jaroniec, M. *Adv. Mater.* **2001**, 13, 677.
4. Bertucci, A.; Lülfi, H.; Septiadi, D.; Manicardi, A.; Corradini, R.; De Cola, L. *Adv. Healthcare Mater.* **2014**, 3, 1812.
5. Li, F.; Yao, X.; Wang, Z.; Xing, W.; Jin, W.; Huang, J.; Wang, Y. *Nano Lett.* **2012**, 12, 5033.
6. Jun, S.; Joo, S. H.; Ryoo, R.; Kruk, M.; Jaroniec, M.; Liu, Z.; Ohsuna, T.; Terasaki, O. *J. Am. Chem. Soc.* **2000**, 122, 10712.
7. Kirumakki, S.; Huang, J.; Subbiah, A.; Yao, J.; Rowland, A.; Smith, B.; Mukherjee, A.; Samarajeewa, S.; Clearfield, A. *J. Mater. Chem.* **2009**, 19, 2593.
8. Tang, F.; Li, L.; Chen, D. *Adv. Mater.* **2012**, 24, 1504.
9. Prasetyanto, E. A.; Khan, N.-u. H.; Seo, H.-U.; Park, S.-E. *Top. Catal.* **2010**, 53, 1381.
10. Laveille, P.; Guillois, K.; Tuel, A.; Petit, C.; Basset, J. M.; Caps, V. *Chem. Commun.* **2016**, 52, 3179.
11. Yasuo Suto, T. U., Hidetoshi Kumata Mikio Tsuzuki, Kitao Fujiwara *Anal. Sci.* **2011**, 27, 2.
12. Xu, P.; Yu, H.; Li, X. *Anal. Chem.* **2011**, 83, 3448.
13. Bertucci, A.; Prasetyanto, E. A.; Septiadi, D.; Manicardi, A.; Brognara, E.; Gambari, R.; Corradini, R.; De Cola, L. *Small* **2015**, 11, 5687.
14. Wang, Y.; Zhao, Q.; Han, N.; Bai, L.; Li, J.; Liu, J.; Che, E.; Hu, L.; Zhang, Q.; Jiang, T.; Wang, S. *Nanomed. Nanotechnol. Biol. Med.* **2015**, 11, 313.
15. Carla Thoelen, K. V. d. W., Ivo F. J. Vankelecom and Pierre A. Jacobs *Chem. Commun.*, **1999**, 2
16. M. Grfin, A. A. K., S. Schacht, F. Schiith, K.K. Unger *J. Chromatogr. A* **1996**, 740, 9.
17. Juère, E.; Florek, J.; Larivière, D.; Kim, K.; Kleitz, F. *New J. Chem.* **2016**, 40, 4325.
18. Kohsuke Mori, K. W., Masayoshi Kawashima, Michel Che, and Hiromi Yamashita *J. Phys. Chem. C* **2011**, 115, 7.

19. Moema de Barros e Silva Botelho, J. M. F.-H., Thiago Branquinho de Queiroz, Hellmut Eckert, Luisa De Cola, Andrea Simone Stucchi de Camargo *J. Mater. Chem.* **2011**, 21, 6.
20. Miskowski, V. M.; Houlding, V. H. *Inorg. Chem.* **1991**, 30, 4446.
21. Lu, W.; Chan, M. C. W.; Zhu, N.; Che, C.-M.; Li, C.; Hui, Z. *J. Am. Chem. Soc.* **2004**, 126, 7639.
22. Mydlak, M.; Mauro, M.; Polo, F.; Felicetti, M.; Leonhardt, J.; Diener, G.; De Cola, L.; Strassert, C. A. *Chem. Mater.* **2011**, 23, 3659.
23. Bagshaw, S. A.; Prouzet, E.; Pinnavaia, T. J. *Science* **1995**, 269, 1242.
24. Yang, P.; Zhao, D.; Chmelka, B. F.; Stucky, G. D. *Chem. Mater.* **1998**, 10, 2033.
25. Cortes, L. S. J. *J. Phys. Chem.* **1985**, 89, 3.
26. B. Jönsson, B. L., K. Holmberg, B. Kronberg, *Surfactants and Polymers in Aqueous Solution*. 2nd ed ed.; John Wiley & Sons: West Sussex, England, 1998.
27. Sierra, L.; Guth, J.-L. *Microporous Mesoporous Mater.* **1999**, 27, 243.
28. Kang, K.-K.; Rhee, H.-K. *Microporous Mesoporous Mater.* **2005**, 84, 34.
29. Bernards, T. N. M.; van Bommel, M. J.; Boonstra, A. H. *J. Non-Cryst. Solids* **1991**, 134, 1.
30. Mauro, M.; Aliprandi, A.; Cebrian, C.; Wang, D.; Kubel, C.; De Cola, L. *Chem. Commun.* **2014**, 50, 7269.

CHAPTER 4:

Self-Assembly of Pt(II) on Gold Nanoparticles for Surface Enhanced Photoluminescence

Abstract

In this chapter, we study the self-assembly of Pt(II) complexes on gold nanoparticles (AuNPs) and its consequent effect on the photoluminescence properties. To achieve our purpose, a new series of complexes comprising the same dianionic N⁻N⁻ terdentate ligand, but differences on the ancillary ligand, was developed but a difference on the ancillary ligand. Indeed, the very well-known affinity of gold for thiol groups, and more in general for sulphur prompted us to use thiol groups on the ancillary ligand.

Keywords

Pt(II) complexes, Luminescent properties, Gold nanoparticles, Surface enhanced photoluminescence

4.1. Introduction

The design of transition metal complexes (TMCs) as sensors and cellular probes has recently caught the attention of researchers,¹ even though nanoscale probes are still more suitable for cells.² Especially, gold and silver nanoparticles (AuNPs, AgNPs) have been used for biologic applications.³ In particular, AuNPs are very interesting due to their surface enhanced Raman scattering (SERS). On the other hand, square planar Pt(II) complexes are widely investigated for their interesting self-assembly properties.⁴⁻⁶ In the frame of this work, these two phenomena were combined, and Pt(II) complexes were coupled to AuNPs and the SERS properties of such systems were investigated. The particles and their studies can provide an understanding of the mechanism involved in quenching of the fluorescence.⁷ The fluorescence signal by plasmonic nanoparticles at short distances has been attributed to energy transfer leading to non-radiative pathways.⁷

TMCs-AuNPs materials were not deeply investigated so far. Pikramenou and co-workers demonstrated the effect of spacers length between Ru(II) complexes and AuNPs, with an obvious improvement of the luminescent properties⁸. However, in general, surface enhanced photoluminescence (SEPL) is more applied to quantum dots,⁹⁻¹¹ lanthanides complexes¹²⁻¹³ or organic dyes.¹⁴⁻¹⁶ For instance, van Hulst and coworkers studied the enhancement of polarized intensity of Cd/Se systems on gold.⁹ More recently, the research group of Lang designed a hybrid based quantum dots semiconductor-AuNP in order to study the plasmon-exciton interaction by luminescence.¹⁰ Regarding rare-earth complexes, Eu(III) complex with ethylene diamine acetate (ETDA) on AgNPs was investigated by Zhou and coworkers. He found out that Eu(III) complex-AgNPs system displays an emission intensity up to 4 times higher than the single Eu(III).¹² About organic dyes, Sun and co-workers demonstrated an emission enhancement of rhodamine 6G by grafting on silver surfaces, showing an enhancement factor of 30.¹⁶

Nevertheless, a limitation of their use has been the quenching of the luminescence when the fluorophore is too close to the gold. Indeed, the latter can strongly reduce the radiative rates of the luminophore.^{7, 17-18} The distance (*d*) between the AuNPs and the luminescent molecule is a very important parameter, as well as the shape or the size of the particle. In 2012, Kang and co-workers reported the effect of the distance between AuNPs and a luminescent modified cryptate on the emission intensity of the

latter (**Figure 4.1.**).¹⁹ This distance was controlled by the incorporation of ethylene glycol based spacers. When the fluorophore is directly linked to a 50 nm particle, the photoluminescence is completely quenched. While increasing the length of the spacer, the emission intensity becomes higher and higher until reaching a maximum of 30 times the emission of the single cryptate ($d=5$ nm); and starts to decrease to reach, with $d=10$ nm, an emission intensity 15 times higher than the single molecule.

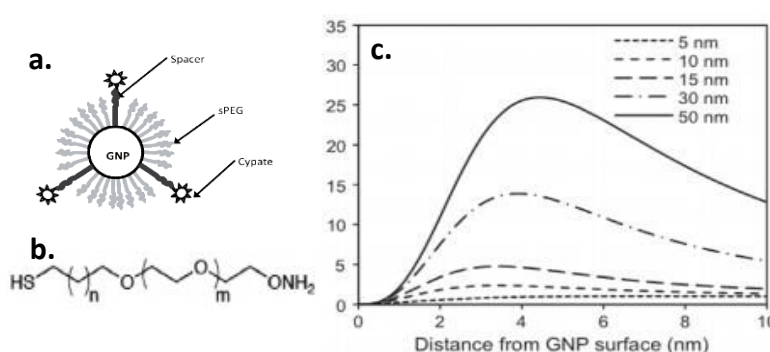
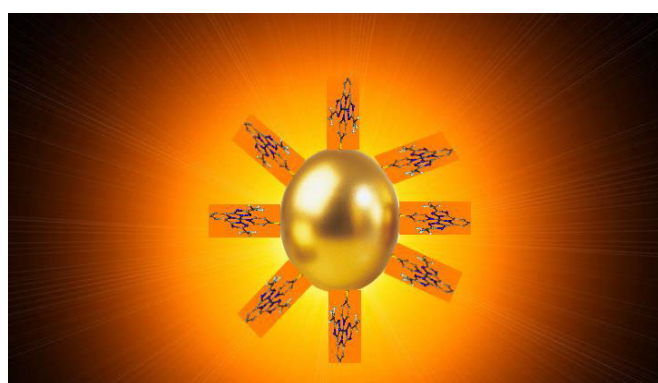


Figure 4.1.a. Schematic representation of the studied cryptate-AuNP system, **b.** Schematic representation of the spacer, **c.** spectrum of the enhancement intensity factor of the luminophore vs. the distance from the AuNP.

By combining these very interesting features, our idea is to design Pt(II) complexes-AuNPs and to study the self-assembly process on 100 nm AuNPs, as well as the SEPL. For this purpose, a series of Pt(II) complexes bearing N⁻N⁻ dianionic terdentate ligand and a thiol functionalized pyridine as ancillary ligand were synthesized and characterized. It is important to note that the reason of using a thiol group, is that it is very well known for being a stabilizing group of AuNPs thanks to the very strong S-Au bond.²⁰⁻²¹



Scheme 4.1. Schematic representation of the studied system

4.2. Results and discussion

The Pt(II) series of Pt(II) complexes studied in this work is shown in **Figure 4.2**.

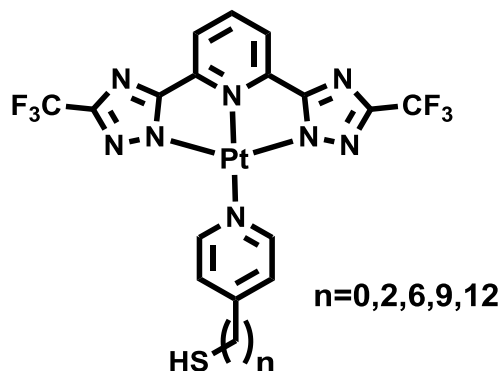
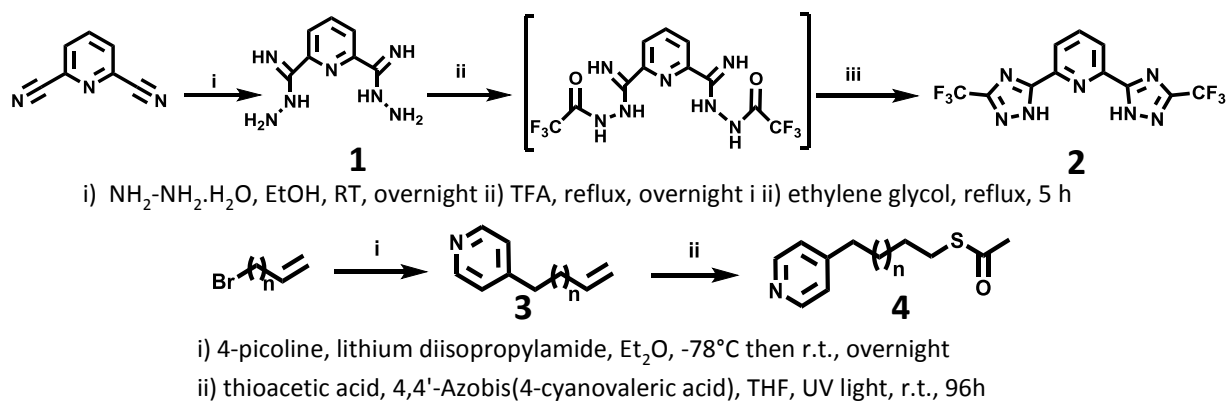


Figure 4.2. Pt(II) complexes used in this chapter

The terdentate N^NN ligand **1** synthesis (**Scheme 4.2, top**) and the complexation (**Scheme 4.3**) process were already explained in *chapter 2*. Therefore, only the synthesis of the ancillary ligand **4** for $n=6, 9, 12$ (**Scheme 4.2, bottom**) is shown following, and the mechanism is explained her below explained (**Scheme 4.4**),²² the ligands with $n=0$ (**4a**) and $n=2$ (**4b**) were purchased:

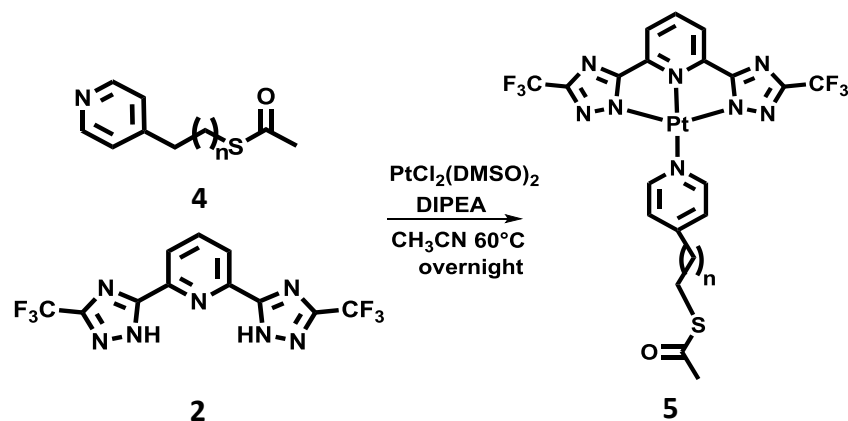
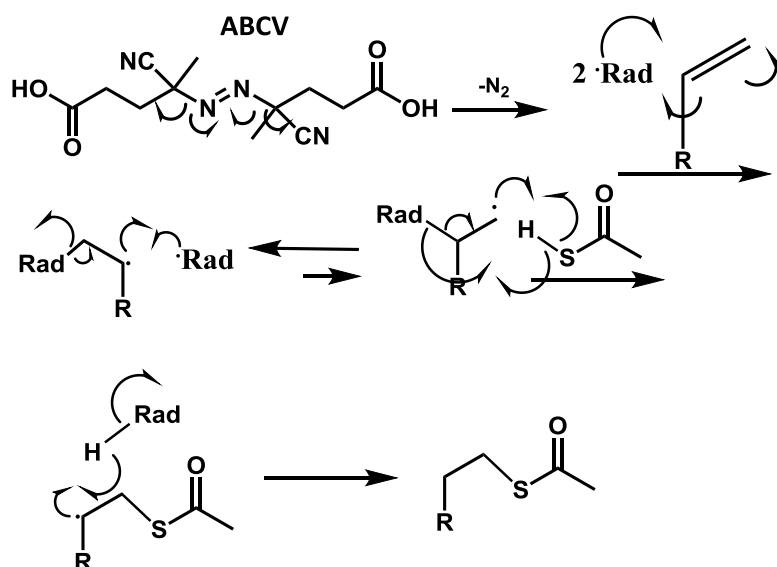


Scheme 4.2. Synthetic pathways of **2** (top) and **4** (bottom)

It is worth to mention that thiol groups are very sensitive to oxygen and, moreover, they are prone to form disulphide bonds.^{23-25 26} Hence, a synthesis with protected thiol was envisaged.

The mechanism of synthesis of the second step (4) in Scheme 4.2 (ii) is described in **Scheme 4.4**. It is a radical reaction, requiring a radical initiator, 4,4'-Azobis(4-

cyanovaleic acid) (ABCV) and UV light. The initiation step is the activation by UV light of ABCV, forming the radical species (Rad^\cdot) and a nitrogen gas release as a driving force. The propagation step starts by Rad^\cdot reacting with the sp^2 carbon at the end of the chain of compound **3**, allowing the formation an intermediate bearing a secondary radical, more stable than its primary counterpart. This intermediate subsequently reacts with another Rad^\cdot to form the primary radical. The latter, much more reactive directly interacts with the thioacetic acid, leading to the thioester radical favoured by the creation of a S-C bond, and a “protonated” radical (H-Rad). The thioester radical finally takes the hydrogen from H-Rad, in order to yield the desired thioester molecule and the radical obtained during the initiation process and another catalytic radical cycle starts. The termination step is the assembly of all the radical species present in the media. The reaction is thus considered as finished.

Scheme 4.3. Synthetic pathway of **5**Scheme 4.4. Proposed mechanism for the synthesis of **4**

Some examples of NMR and ESI-MS spectra of the ligands **3** and **4**, and complexes **5** are shown in the experimental section (characterization of **1** and **2** is shown in *Chapter 2*) (**Figures 4.10-18**) ^1H NMR spectra of ligands **3** show two signals at 8.4 and 7.2 ppm, each one integrating for 2 protons and referred to the protons at *ortho* and *meta* positions to the pyridine's nitrogen, respectively. Two multiplets are displayed at 5.5 ppm (1H) and at 4.9 ppm (2H), attributed to the olefin's protons. The signal at 2.5 ppm integrating for 2 protons corresponds to the protons adjacent to the pyridine ring, while the one at 2 ppm integrating for 2 protons is attributed to the protons adjacent to the double bond. The other peaks, at the aliphatic region, are for the protons in the middle of the carbon chain.

Ligands **4** show the same multiplets for the aromatic protons, and interestingly, we can observe the disappearance of the protons on the C-C double bond, and the appearance of a singlet at 2.3 ppm integrating for 3 protons and corresponding to the methyl of the thioester group. ^{13}C NMR spectra of ligands **4** show, among other, the appearance of a peak at 196 ppm referred to the carbonyl's carbon. Finally, ^1H NMR spectra of complexes **5** show the signals of ligand **1** (see chapter 2) and ligand **4**, with however an obvious shielding of the pyridine's protons signals, due to the effect of the metal ion.

Table 4.1. Crystal parameters of complexes **5a-e**

Complex	Crystal system	Space group	A(Å)	B(Å)	C(Å)	Alpha(°)	Beta(°)	Gamma(°)	Cry (nm)	Rwp
5a	-	-	-	-	-	-	-	-	-	-
5b	Monoclinic	P2	41.45	3.85	15.73	90	57.06	90	21.9	29.0
5c	Cubic	Ia-3	54.3	54.35	54.35	90	90	90	29.7	23.9
5d	Orthorhombic	C222	70.20	14.62	10.89	90	90	90	30.6	12.9
5e	Monoclinic	P21/n	25.01	26.94	32.57	90	90	97.73	47.4	23.1

After the characterization of the molecules by NMR and ESI-MS (c.f. experimental section, **Figures 4.10-18**), the crystallinity of the self-assembled structures made by the complexes was studied. To achieve this investigation, PXRD experiments were performed on thin films prepared from drop-casting a 1mM solution of dichloromethane on a zero background silicon wafer. Complex **5a** did not show any crystallinity, whereas all the other structures showed evidence of crystallinity and after refinement (see *Chapter 5* for more details), we were able to determine the way the

aggregated structures pack (crystal system and space group), as well as the size of one unit cell. The results are shown in **Table 4.1**.

Subsequently, the photophysical properties have been investigated. In dichloromethane at $c = 10^{-4}$ M, all the complexes display the same absorption (**Figure 4.3**), excitation and emission profiles (**Figure 4.4**), typical for the monomeric species of Pt(II) complexes. Regarding the absorption and excitation spectra they display intense bands in the UV region respectively at 253 nm (ϵ between 26000 and 28000 L.mol⁻¹.cm⁻¹) and 302 nm (ϵ between 15000 and 18000 L.mol⁻¹.cm⁻¹). These transitions are mainly attributed to the ligand center (¹LC) and metal-perturbed inter-ligand charge transfer (¹ILCT). At lower energy, a broad band between 350–450 nm ($\epsilon=700$ L.mol⁻¹.cm⁻¹) is observed. It is attributed to the metal-to-ligand charge transfer (¹MLCT) and ¹IL transitions. Similar values are also found in already reported Pt(II) complexes.²⁷ For the emission, we can observe a structured profile with two bands at 460 and 489 nm, and two shoulders at 520 and 567 nm.

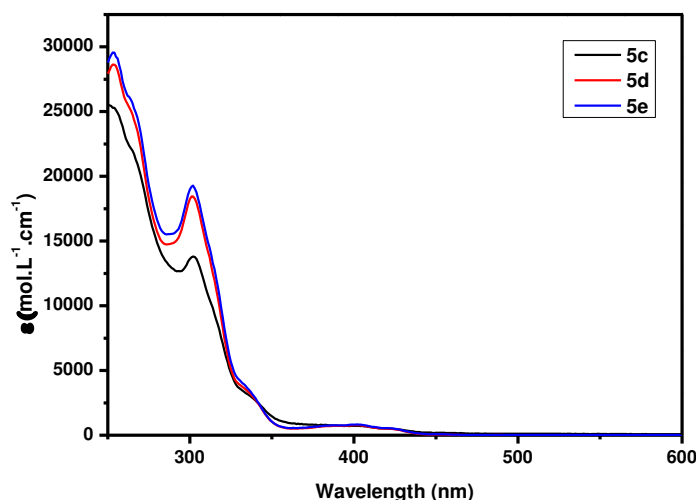


Figure 4.3. Absorption spectra of the Pt(II) complexes studied in this chapter
(Dichloromethane, 10^{-4} M)

The low photoluminescence quantum yield (PLQY) (1%) goes along with the relatively short excited state lifetime (ESLT) (~200 ns). Interestingly, the complex exhibits very different photophysical behaviour in the solid state. It is well known that the square planar geometry of such complexes induces aggregates formation leading through Pt--Pt interaction. Thus, the lowest electronic transition has an MMLCT character. This phenomenon is first observed from the excitation spectra, with a new band at lower

energy (460 nm) standing for MMLCT transition. The emission of the complexes is also lower in energy with a broad, featureless band between 565 and 570 nm and a PLQY of 60%. The emission decays according to a bi-exponential process ($\tau_1=750$ ns (90%) $\tau_2= 320$ ns (10%)).

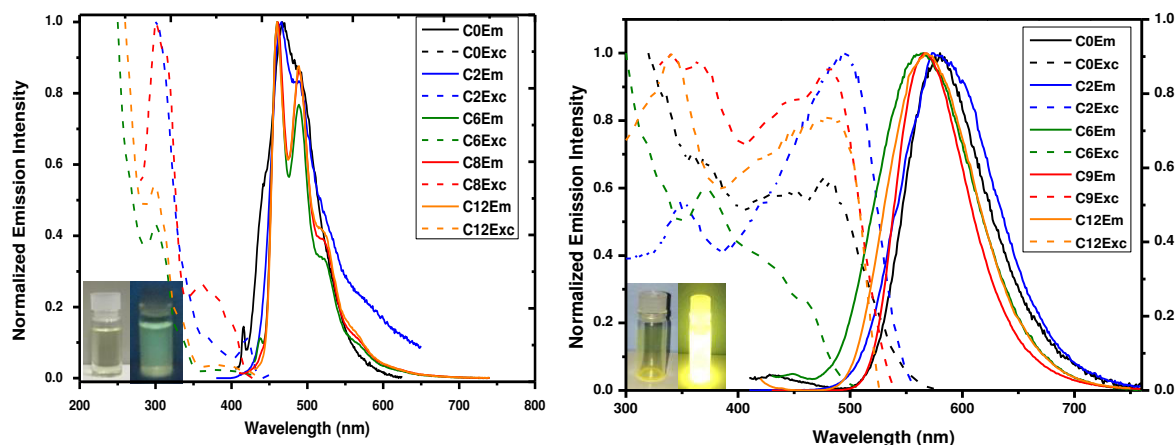


Figure 4.4. Excitation (dashed line) and emission (full line) spectra of the Pt(II) complexes studied in this chapter in solution (left, dichloromethane, 10^{-4} M) and in solid state (right).

Inset: picture of one sample under ambient light (left) and visible light (right)

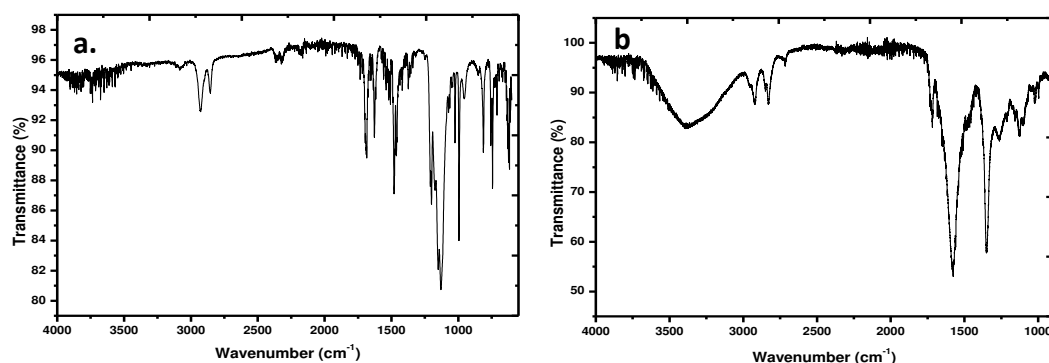
After deprotection of the thiol group in basic conditions using sodium methoxide, the complexes have been linked to 100 nm spherical AuNPs. The deprotection was proved by infrared (IR) spectroscopy, by observing the disappearance of the band for the stretching of the carbonyl bond at 1690 cm^{-1} . An example is shown in **Figure 4.5**, with complex **5d**.

Table 4.2. Recap chart of the photophysical properties of the studied Pt(II) complexes in solution state (dichloromethane, 10^{-4} M)

Complex	Em	PLQY (%)	ESLT (ns)
5a (C0)	461, 490	1	193
5b (C2)	461, 490	1	220
5c (C6)	460, 488	1	175
5d (C9)	460, 489	1	170
5e (C12)	460, 488	1	200

Table 4.3. Recap chart of the photophysical properties of the studied Pt(II) complexes in solid state

Complex	Em	PLQY (%)	ESLT (ns)
5a (C0)	579	42	581 (71%) 277 (29%)
5b (C2)	579	49	532 (56%) 230 (44%)
5c (C6)	569	58	759 (90%) 319 (10%)
5d (C9)	569	52	632 (70%) 314 (30%)
5e (C12)	569	58	759 (90%) 317 (10%)

**Figure 4.5.** Infrared spectra of complex **5d** before (a.) and after (b.) deprotection

In order to know if the complex is linked to the particle by the S-Au bond, X-ray photoelectron spectroscopy (XPS) were performed (**Figure 4.6**) as an example for C6 complex. From the S2p scan in XPS, we can observe both the peaks at 164eV, standing the free sulphur and at 168 eV, signal for the bonded sulphur. This result gives us information about the way the complexes surround the particle. Indeed, the first assumption is that there is a first layer of complexes on the AuNP surface, and other complexes aggregated to this layer without coordinating the AuNP. This assumption is confirmed by scanning transmission electron microscopy (STEM, **Figure 4.7**) and transmission electron microscopy (TEM, **Figure 4.8**). Due to a lack of time and facilities, only one example of TEM image was recorded (complex **5a** coating AuNP, **Figure 4.8**).

It displays the spherical AuNP (around 100nm) surrounded by a cloud of the aggregated complex.

After characterization of the system, the difference of photophysical properties was studied between the complexes, and the complexes attached to the AuNPs.

Interestingly, the luminescence of complex **5a** was completely quenched after linking to the AuNPs. This is due to the strong luminescence quenching effect of AuNPs when the luminescent center is too close to the particle and can be correlated to other works in the literature.^{3, 28} Complex **5b** presents the same behaviour as **5a**, showing a quenching effect of the AuNPs. Indeed, the short distance between the complex and the particle suggests an efficient energy transfer between the two parts of the system. When linked to the AuNPs, complex **5c** feature a PLQY of 10% and this is explained by the fact that the particle is far enough from the complex not to disturb the luminescence. Regarding complex **5d**, once attached to the AuNPs, the PLQY is slightly higher than for **5c**@AuNPs(14%), following thus the tendency previously described. Finally, complex **5e** show a great improvement while linked to the AuNPs (PLQY: 25%) the Plasmon resonance effect likely playing an important role on such improvement. All the results are illustrated in **Figure 4.9** and shown in table **4.4**.

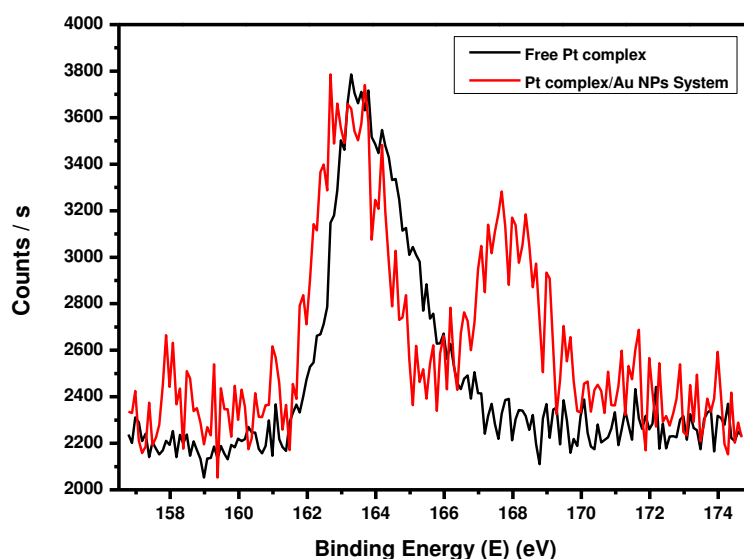


Figure 4.6. XPS spectra of complex **5e** (black trace) and complex **5e**, deprotected and linked to AuNPs (red trace)

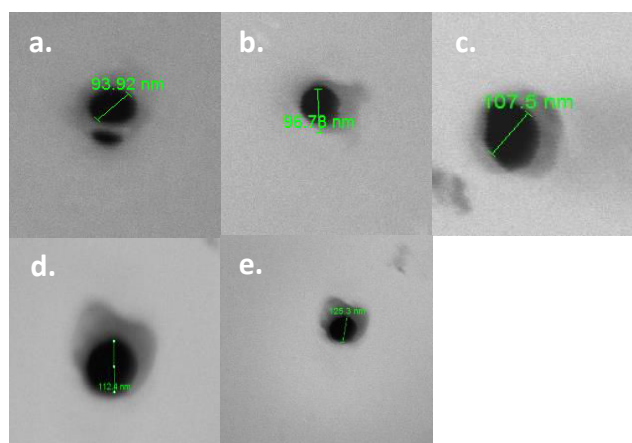


Figure 4.7. STEM images of **5a-e** coating AuNP

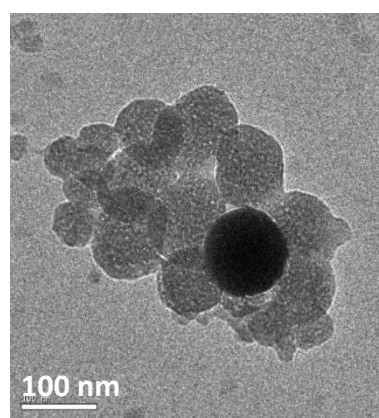


Figure 4.8. TEM image of **5a** coating AuNP

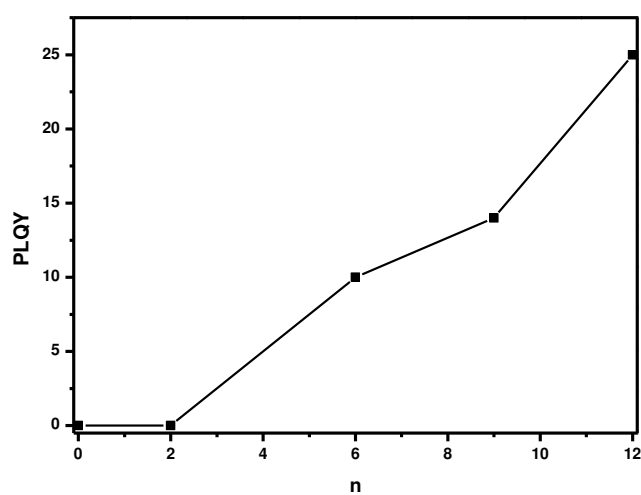


Figure 4.9. Plot of the PLQY of the final systems, **5a-e**. coating AuNP versus the number of $-CH_2$ groups between the complex and the AuNPs n

Table 4.4. PLQY of the final systems, **5a.-e.** coating AuNPs

Material	PLQY
5a coating AuNPs	-
5b coating AuNPs	-
5c coating AuNPs	10%
5d coating AuNPs	14%
5e coating AuNPs	25%

4.3. Conclusion

In this work, a new series of luminescent neutral Pt(II) complexes functionalized by a thiol group, **5a.-e.** were synthesized. Their crystallinity was studied, as well as their photophysical properties in dichloromethane solution and in solid state. Their further attachment to AuNPs was performed and characterized by XPS and electron microscopy. The effect of AuNPs on the luminescent properties of the complexes was investigated, and a correlation between the distance separating the AuNPs from the complexes and the PLQY was established. Thus, at shorter distances, quenching is observed while larger ones led to the enhancement of the latter. Interesting perspectives would be to change the shape and/or the size of the AuNPs in order to study the consequent effect of the luminescent properties. The use of AgNPs instead of AuNPs would also be a possible interesting future investigation.

4.4. Experimental section

4.4.1. Materials and methods

All the reactions were carried out under inert atmosphere (Schlenk technique). All the solvents were used as received from Aldrich or Fluka without any further purification. All the chemicals were purchased from Aldrich or TCI Europe and used as received. The compounds were purified by column chromatography by using silica gel 60 (230–400 mesh) or slightly basic alumina (pH of 10% suspension in water: 9–10) as stationary phase. ^1H , ^{13}C and ^{19}F NMR spectra were recorded on a Bruker Avance 400 spectrometer. The ^1H NMR chemical shifts (δ) are given in ppm and referred to residual protons on the corresponding deuterated solvent. All deuterated solvents were used as received without any further purification. ESI-MS experiments were performed on a Bruker Daltonics microTOF spectrometer (Bruker Daltonik GmbH, Bremen, Germany) equipped with an orthogonal electrospray (ESI) interface.

Calibration was performed using Tunning mix (Agilent Technologies). Sample solutions were introduced into the spectrometer source with a syringe pump (Harvard type 55 1111: Harvard Apparatus Inc., South Natick, MA, USA) with a flow rate of 5 $\mu\text{L}\cdot\text{min}^{-1}$.

PXRD data were acquired using a Bruker D2-PHASER diffractometer using $\text{CuK}\alpha$ radiation ($\lambda = 1.5418 \text{ \AA}$) at 300W (30kV, 10mA) power with Ni $\text{K}\beta$ -filter and equipped by a 0.1mm divergence slit and 1mm air scatter screen. The samples were prepared by dropcasting the corresponding solution on a zero background silicon sample holder. All the measurements were performed in the Bragg-Brentano geometry, with 2θ values ranging from 5 to 40° with an exposure time of several seconds per step. All samples were measured at room temperature and room pressure. The crystal parameters were determined using TOtal Pattern Analysis Solution program (TOPAS) after refinement using the indexing method.

All solvents used for spectroscopic characterization were spectrometric grade and purchased by VWR. Absorption spectra were measured on a Shimadzu UV-3600 spectrophotometer double-beam UV–VIS–NIR spectrometer and baseline corrected. Steady-state emission spectra were recorded on a Horiba Jobin–Yvon IBH FL-322 Fluorolog 3 spectrometer equipped with a 450 W xenon arc lamp, double-grating excitation, and emission monochromators (2.1 nm mm^{-1} of dispersion; $1200 \text{ grooves mm}^{-1}$) and a TBX-04 single photon-counting detector. Emission and excitation spectra were corrected for source intensity (lamp and grating) and emission spectral response (detector and grating) by standard correction curves. Time-resolved measurements were performed using the time-correlated single-photon-counting (TCSPC) PicoHarp300 or the Multi Channel Scaling (MCS) electronics NanoHarp 250 of the PicoQuant FluoroTime 300 (PicoQuant GmbH, Germany), equipped with a PDL 820 laser pulse driver. A pulsed laser diode LDH-P-C-405 ($\lambda_{\text{exc}} = 405 \text{ nm}$) was used to excite the sample and mounted directly on the sample chamber at 90° . The photons were collected by a PMA-C-192 photomultiplier(PMT) single-photon-counting detector. The data were acquired by using the commercially available software EasyTau (PicoQuant GmbH, Germany), while data analysis was performed using the commercially available software FluoFit (PicoQuant GmbH, Germany).

PLQY measurements were performed by using an absolute photoluminescence quantum yield spectrometer Quantaaurus C11347 (Hamamatsu, Japan) exciting the sample at $\lambda_{\text{exc}} = 350$ and 400 nm . All solvents were spectrometric grade.

4.4.2. Synthetic procedures

Synthesis of pyridine-2,6-bis(carboximidhydrazide) 1

To a solution of pyridine-2,6-dicarbonitrile (20.0 g, 38.75 mmol, 1.0 eq.) in EtOH (125 ml) was slowly added hydrazine monohydrate (38 mL, 775 mmol, 20 eq). The reaction mixture was stirred at room temperature overnight, yielding a pale yellow precipitate in a pale yellow solution. The precipitate was filtered off, washed with twice with cold ethanol and dried to yield a pale yellow solid (7.11 g, 36.82 mmol, 95%) ^1H NMR (400 MHz, d_6 DMSO) δ [ppm]= 7.82 (m, 2H), 7.66 (m, 1H), 6.05 (s, 4H), 5.26 (s, 4H) ^{13}C NMR (100 MHz, d_6 DMSO) δ [ppm]= 151.2, 144.5, 136.8, 118.5.

Synthesis of 2,6-bis(3-(trifluoromethyl)-1H-1,2,4-triazol-5-yl)pyridine (pyC₅-CF₃-tzH₂, 2):

Pyridine-2,6-bis(carboximidhydrazide) **1** (5g, 25.89 mmol, 1eq) was added to trifluoroacetic acid (TFA) (30mL, large excess) and the mixture was refluxed overnight. TFA was then removed by distillation and ethylene glycol (50 mL) was added. The mixture was heated up at 130°C for 3 hours, and cooled down to room temperature overnight. To the obtained brown solution was added water and the mixture was stirred for 30 minutes to yield, after filtration, washing 3 times with water and 3 times with ethanol, a white powder (6.87g, 19.6mmol, 76%) ^1H NMR (400 MHz, CD_2Cl_2) δ [ppm] = 8.23 (m, 2H), 8.12 (m, 1H); ^{13}C NMR (100 MHz, d_6 DMSO) δ [ppm]= 155.3, 144.4, 140.7, 122.9, 120.7, 118.0. ^{19}F NMR (375 MHz, CD_2Cl_2): -65.61 (1F). HR-ESI-MS (m/z): [M⁺] calculated. 350.0583; found 350.0627.

Synthesis of Alkenyl pyridine 3

To a 2.0 M solution of lithium diisopropyl amide in a mixture THF/heptane/ethylbenzene (20 mL, 36.63 mmol, 2.2eq) at -78°C was added dropwise 4-picoline (4.68 mL, 36.63 mmol, 2.2 eq) and the reaction medium was stirred for 1 hour. The corresponding bromoalcene (16.65 mmol, 1 eq) was then added at -78°C and stirred for 24 h at room temperature. Deionized water (100 mL) was added and the mixture was transferred into an extraction funnel, extracted with 3×100 mL of diethylether and dried over magnesium sulfate. The mixture of solvents was removed under reduced pressure and the product was purified by column chromatography on silica gel (eluent: CH_2Cl_2 98-96 MeOH 2-4) to afford the desired compound (82-86%).

3c ^1H NMR (400 MHz, CDCl_3) δ [ppm] = 8.46 (m, 2H), 7.08 (m, 2H), 5.75 (m, 1H), 4.95 (m, 2H), 2.60 (m, 2H), 2.04 (q, 2H) 1.66 (m, 2H), 1.43 (m, 2H); ^{13}C NMR (100 MHz, CDCl_3) δ [ppm]= 151.7, 149.9, 138.7, 124.1, 115.0, 35.3, 33.7, 30.0, 28.6

3d ^1H NMR (400 MHz, CDCl_3) δ [ppm] = 8.47 (m, 2H), 7.09 (m, 2H), 5.78 (m, 1H), 4.96 (m, 2H), 2.59 (m, 2H), 2.05 (q, 2H) 1.62 (m, 2H), 1.36 (m, 8H); ^{13}C NMR (100 MHz, CDCl_3) δ [ppm]= 151.7, 149.6, 139.0, 124.0, 114.2, 35.1, 33.3, 30.0, 29.7, 29.3, 29.0, 28.6

3e ^1H NMR (400 MHz, CDCl_3) δ [ppm] = 8.46 (m, 2H), 7.05 (m, 2H), 5.77 (m, 1H), 4.93 (m, 2H), 2.55 (m, 2H), 2.00 (m, 2H) 1.59 (m, 2H), 1.38 (m, 18H); ^{13}C NMR (100 MHz, CDCl_3) δ [ppm]= 151.9, 149.8, 139.3, 124.1, 114.3, 35.4, 34.0, 30.5, 29.8, 29.7, 29.7, 29.6, 29.6, 29.4, 29.3, 29.2

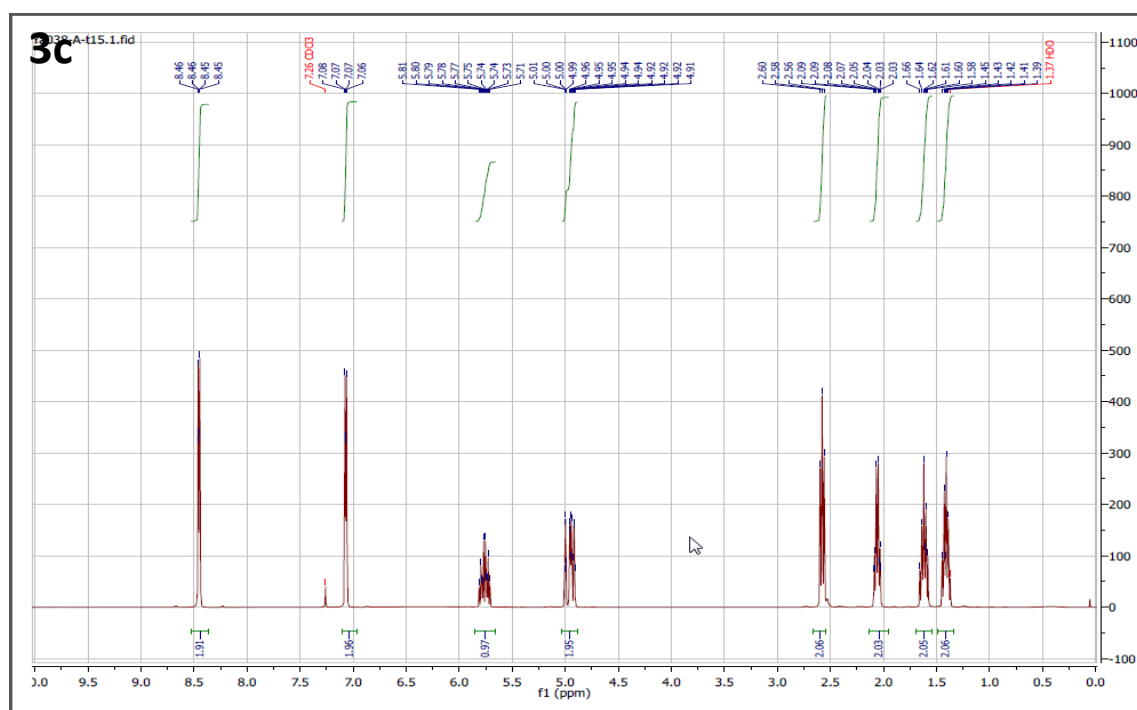


Figure 4.10. ^1H NMR spectrum of **3c**

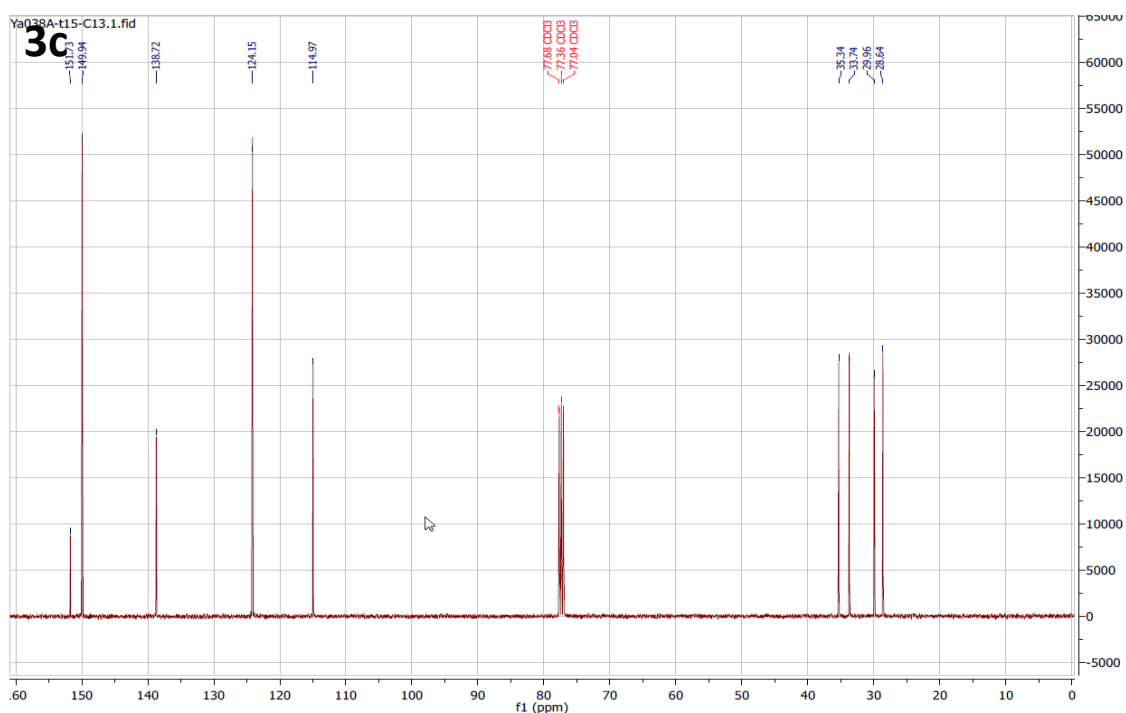


Figure 4.11. ^{13}C NMR spectrum of **3c**

Synthesis of pyridinalkyl ethanethioate **4**

Thioacetic acid (27.9 mL, 40.5 mmol, 10 eq) and 4,4'-azobis(4-cyanovaleric acid) (230 mg, 0.81 mmol, 0.2 eq) were added to Alkenyl pyridine (**1g**, 4.05 mmol) dissolved in 100 mL of THF. The mixture was stirred at r.t. and irradiated by UV-light for 24 h. After another addition of 4,4'-azobis(4-cyanovaleric acid) (250 mg, 0.875 mmol), the irradiation was continued for 72 h. Afterwards, thioacetic acid and THF were removed under reduced pressure and the product was purified by column chromatography on silica gel with (eluent: Cyclohexane 2-1 EtOAc) to yield the final product (46-50%).

4c ^1H NMR (400 MHz, CDCl_3) δ [ppm] = 8.46 (m, 2H), 7.08 (m, 2H), 2.84 (t, 1H), 2.58 (t, 2H), 2.31 (s, 3H), 1.55 (m, 4H), 1.48 (m, 4H) ^{13}C NMR (100 MHz, CDCl_3) δ [ppm] = 196.1, 151.6, 149.8, 124.0, 35.2, 30.7, 30.2, 29.5, 28.6, 29.12, 28.7, 28.6

4d ^1H NMR (400 MHz, CDCl_3) δ [ppm] = 8.52 (m, 2H), 7.20 (m, 2H), 2.85 (t, 2H), 2.63 (t, 2H), 2.31 (s, 3H), 1.58 (m, 4H), 1.31 (m, 10H) ^{13}C NMR (100 MHz, CDCl_3) δ [ppm] = 196.2, 154.3, 148.0, 124.6, 35.6, 30.8, 30.3, 29.6, 29.4, 29.2, 29.1, 28.9

4e ^1H NMR (400 MHz, CDCl_3) δ [ppm] = 8.47 (m, 2H), 7.09 (m, 2H), 2.85 (m, 2H), 2.61 (m, 2H), 2.30 (s, 3H) 1.57 (m, 4H), 1.27 (m, 18H); ^{13}C NMR (100 MHz, CDCl_3) δ [ppm] =

196.1, 152.1, 149.4, 124.0, 35.3, 30.7, 30.3, 29.6, 29.5, 29.4, 29.4, 29.3, 29.2, 29.1, 28.9
ESI-MS (m/z): [M⁺] calculated 322.22; found 322.22

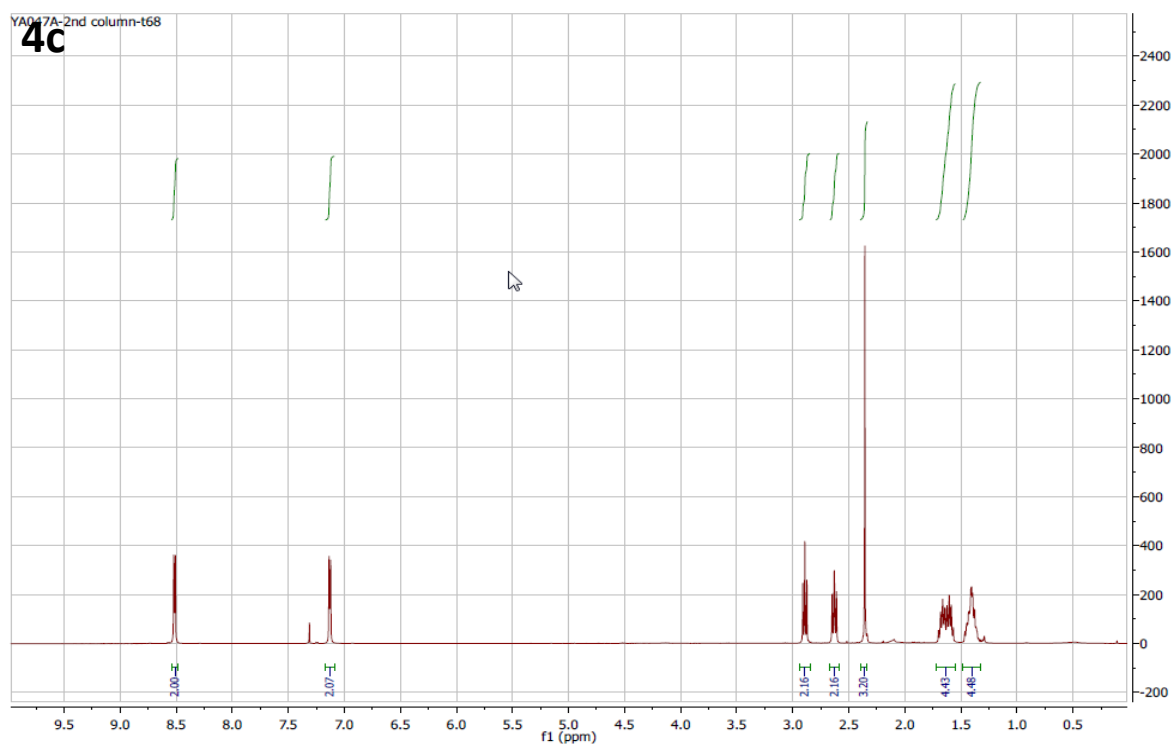


Figure 4.12. ¹H NMR spectrum of **4c**

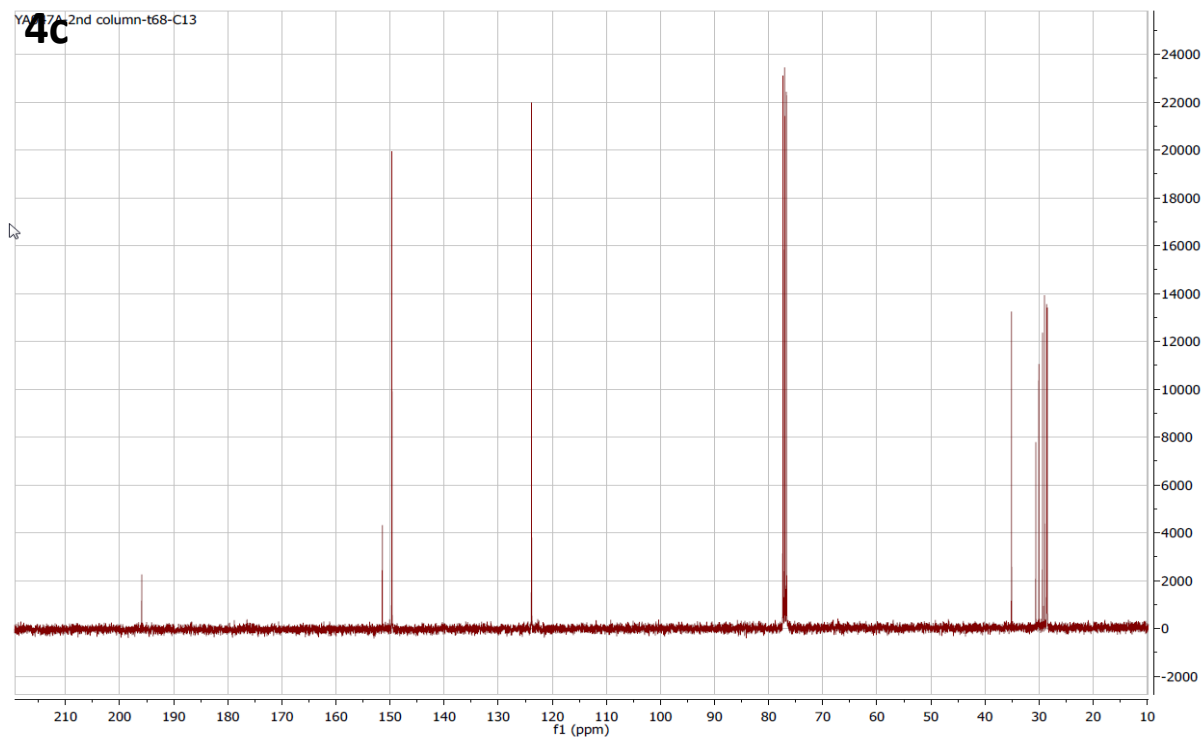
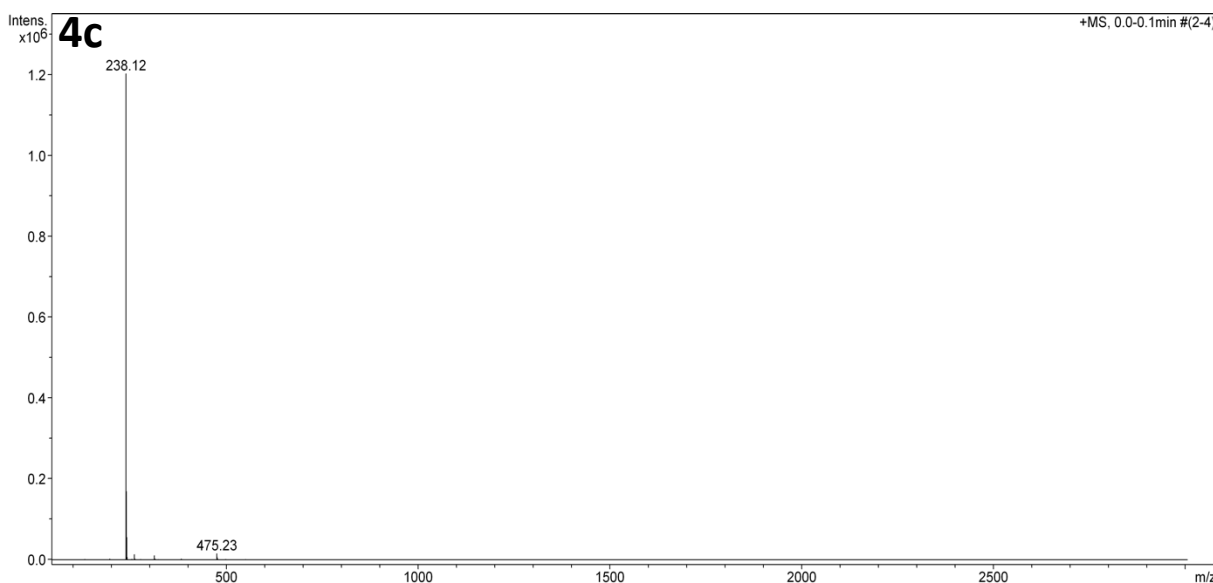


Figure 4.13. ¹³C NMR spectrum of **4c**

Figure 4.14. MS spectrum of **4c****Synthesis of Pt(II) complexes (5a-e):**

A solution of 2,6-bis(3-(trifluoromethyl)-1H-1,2,4-triazol-5-yl)pyridine (0.5 g, 1.432 mmol, 1 eq), PtCl₂(DMSO)₂ (0.604 g, 1.432 mmol, 1 eq) and DIPEA (0.5 mL, 3.15 mmol, 2.2 eq) were in acetonitrile was stirred and heated up to 50°C for 10 minutes. The corresponding pyridinalkyl ethanethioate **4** (1.432 mmol, 1 eq) was then added and the media was stirred at 50°C overnight. The product was dried under reduced pressure and was purified by chromatography column on silica (eluent: CH₂Cl₂ 96-92: MeOH 4-8) to afford the desired compound (64-82%).

5a ¹H NMR (400 MHz, MeOD) δ [ppm] = 9.40 (m, 2H), 7.90 (m, 1H), 7.66 (m, 2H), 7.31 (m, 2H) ¹³C NMR (100 MHz, MeOD) δ[ppm]= 150.7, 150.5, 150.4, 128.8, 126.3, 121.8, 121.7, 121.6, 120.5, 119.8, ¹⁹F NMR (375 MHz, MeOD) δ [ppm]= -64.78

5b ¹H NMR (400 MHz, MeOD) δ [ppm] = 9.27 (m, 2H), 7.91 (m, 1H), 7.70 (m, 2H), 7.35 (m, 2H) 2.89 (t, 2H), = 2.45 (s, 2H) ¹³C NMR (100 MHz, CDCl₃) δ[ppm]= 196.2, 164.0, 156.0, 153.4, 149.4, 142.1, 126.1, 121.4, 119.3, 118.4, 35.6, 31.0, ¹⁹F NMR (375 MHz, CDCl₃) δ [ppm]= -64.18

5c ¹H NMR (400 MHz, CDCl₃) δ [ppm] = 9.41 (m, 2H), 7.94 (m, 1H), 7.70 (m, 2H), 7.35 (m, 2H) 2.89 (t, 2H), 2.58 (t, 2H), 2.33 (s, 3H), 1.73 (m, 4H), 1.63 (m, 4H), 1.44 (m, 4H) ¹³C NMR (100 MHz, CDCl₃) δ[ppm]= 196.2, 164.0, 156.8, 152.9, 149.0, 143.2, 126.7,

121.4, 118.7, 118.4, 35.6, 31.0, 29.7, 29.3, 29.0, 28.8 ^{19}F NMR (375 MHz, CDCl_3) δ [ppm] = -64.18

HR-ESI-MS (m/z): $[\text{M}+\text{H}]^+$ calculated 780.1263; found 783.1272

5d ^1H NMR (400 MHz, CDCl_3) δ [ppm] = 9.44 (m, 2H), 8.00 (m, 1H), 7.78 (m, 2H), 7.35 (m, 2H) 7.39 (t, 2H), 2.86 (t, 2H), 2.75 (t, 1H), 2.32 (s, 3H), 1.72 (m, 2H), 1.36 (m, 12H)

^{13}C NMR (100 MHz, CDCl_3) δ [ppm] = 196.2, 163.8, 156.9, 152.7, 148.8, 143.0, 126.5, 121.2, 118.5, 118.2, 35.5, 30.8, 29.7, 29.6, 29.4, 29.3, 29.2, 29.1, 28.9 ^{19}F NMR (375 MHz, MeOD) δ [ppm] = -64.38

HR-ESI-MS (m/z): $[\text{M}+\text{H}]^+$ calculated 822.1733; found 822.1751

5e ^1H NMR (400 MHz, CDCl_3) δ [ppm] = 9.18 (m, 2H), 7.78 (m, 1H), 7.48 (m, 2H), 7.18 (m, 2H) 2.86 (t, 2H), 2.70 (t, 2H), 2.32 (s, 3H), 1.69 (m, 2H), 1.56 (m, 2H), 1.29 (m, 16H)

^{13}C NMR (100 MHz, CDCl_3) δ [ppm] = 196.4, 163.7, 156.9, 152.5, 148.5, 143.0, 126.4,

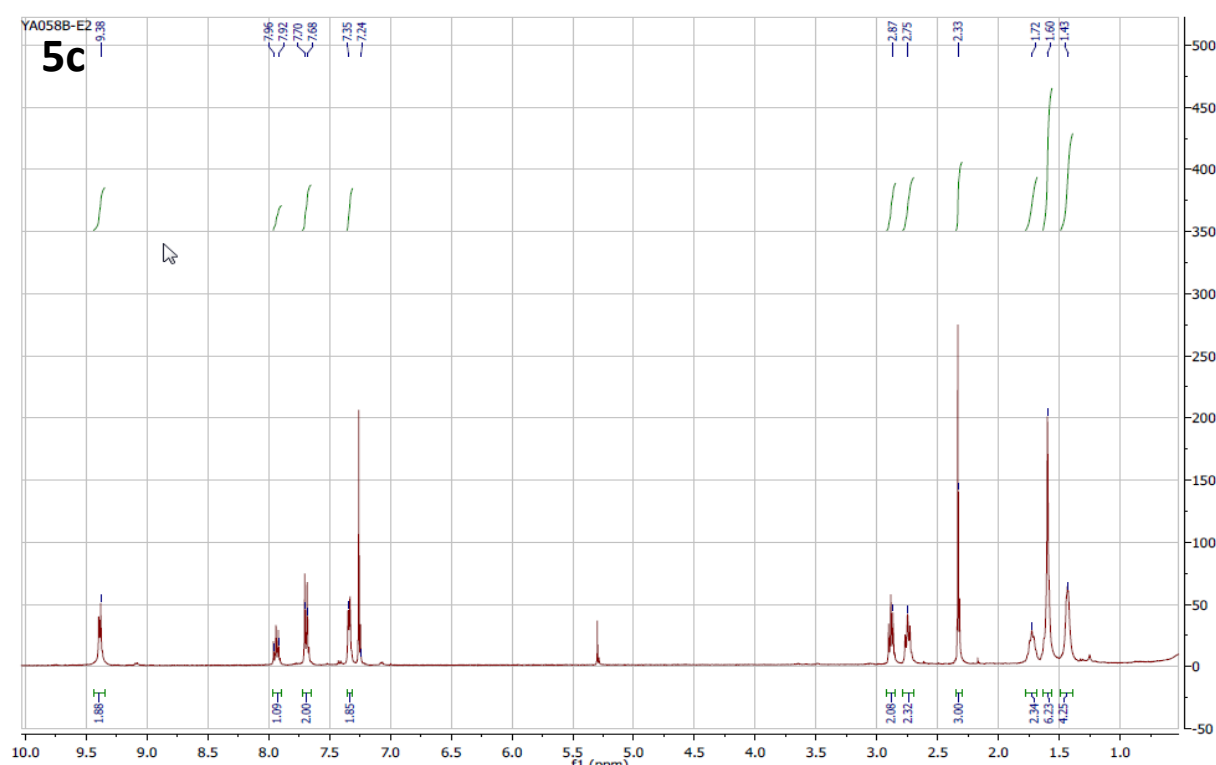
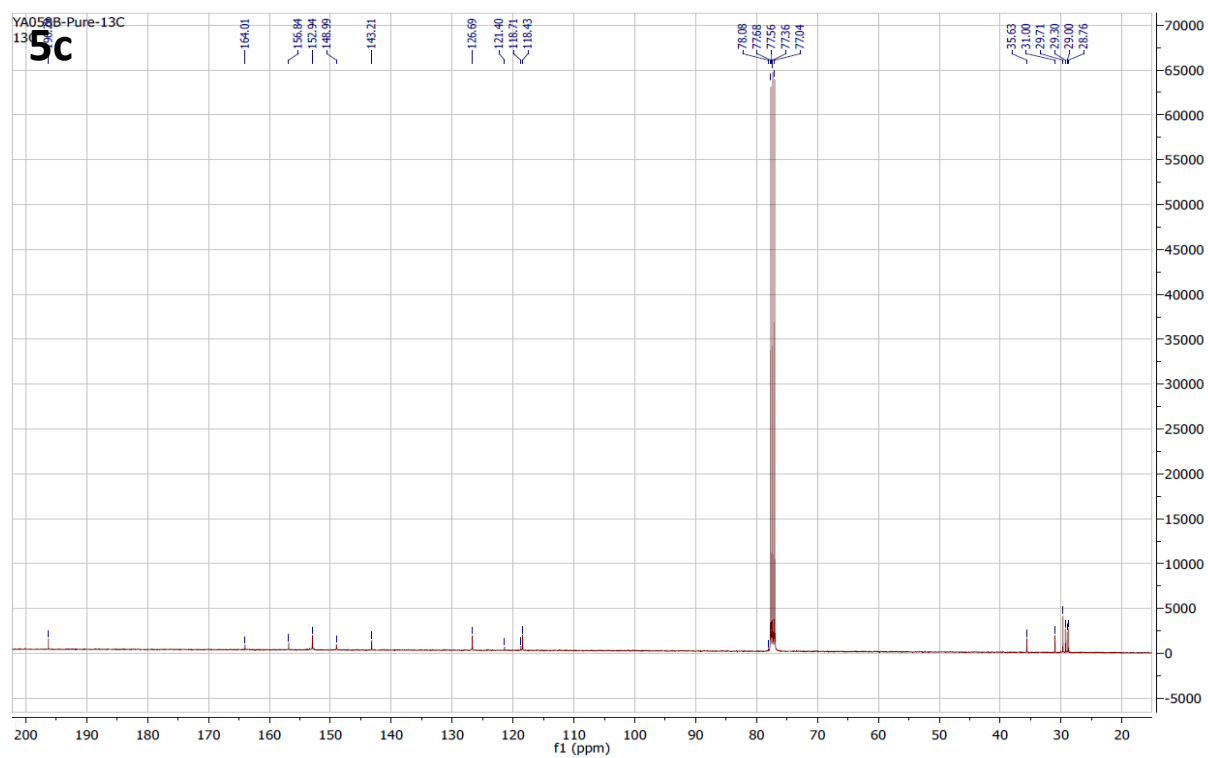
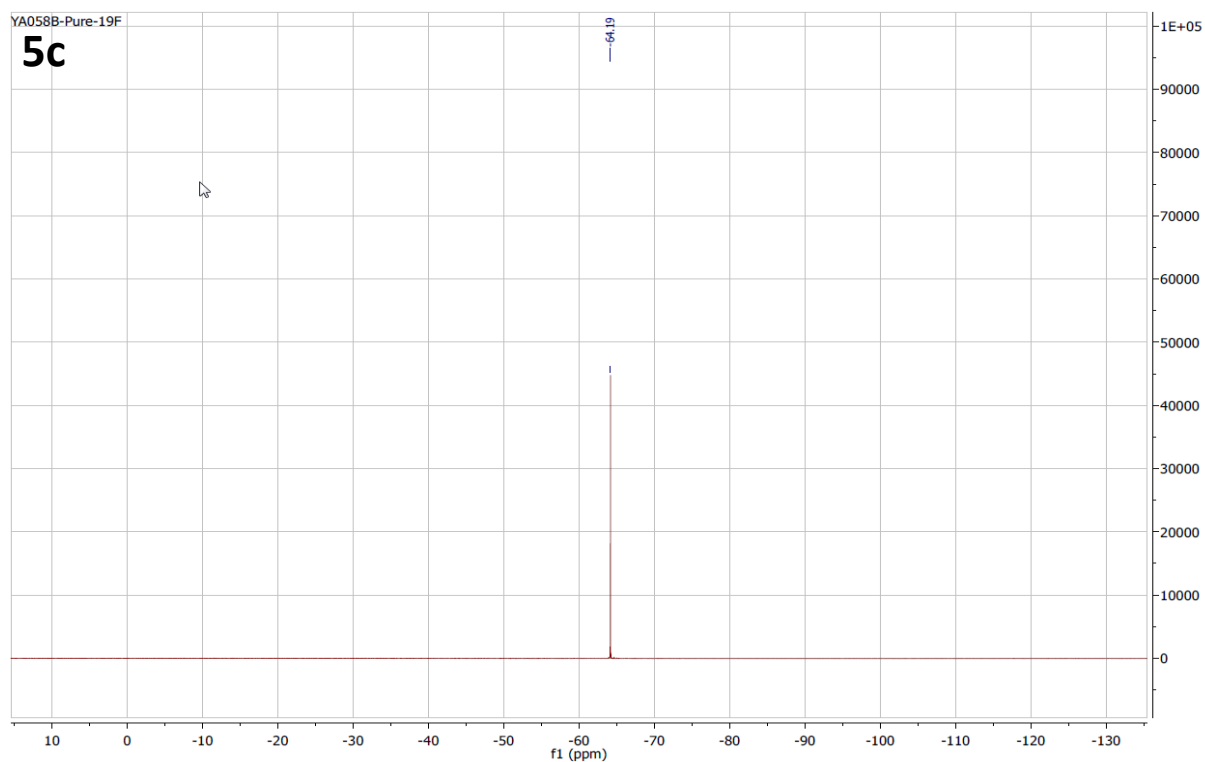


Figure 4.15. ^1H NMR spectrum of **5c**

Figure 4.16. ^{13}C NMR spectrum of 5cFigure 4.17. ^{19}F NMR spectrum of 5c

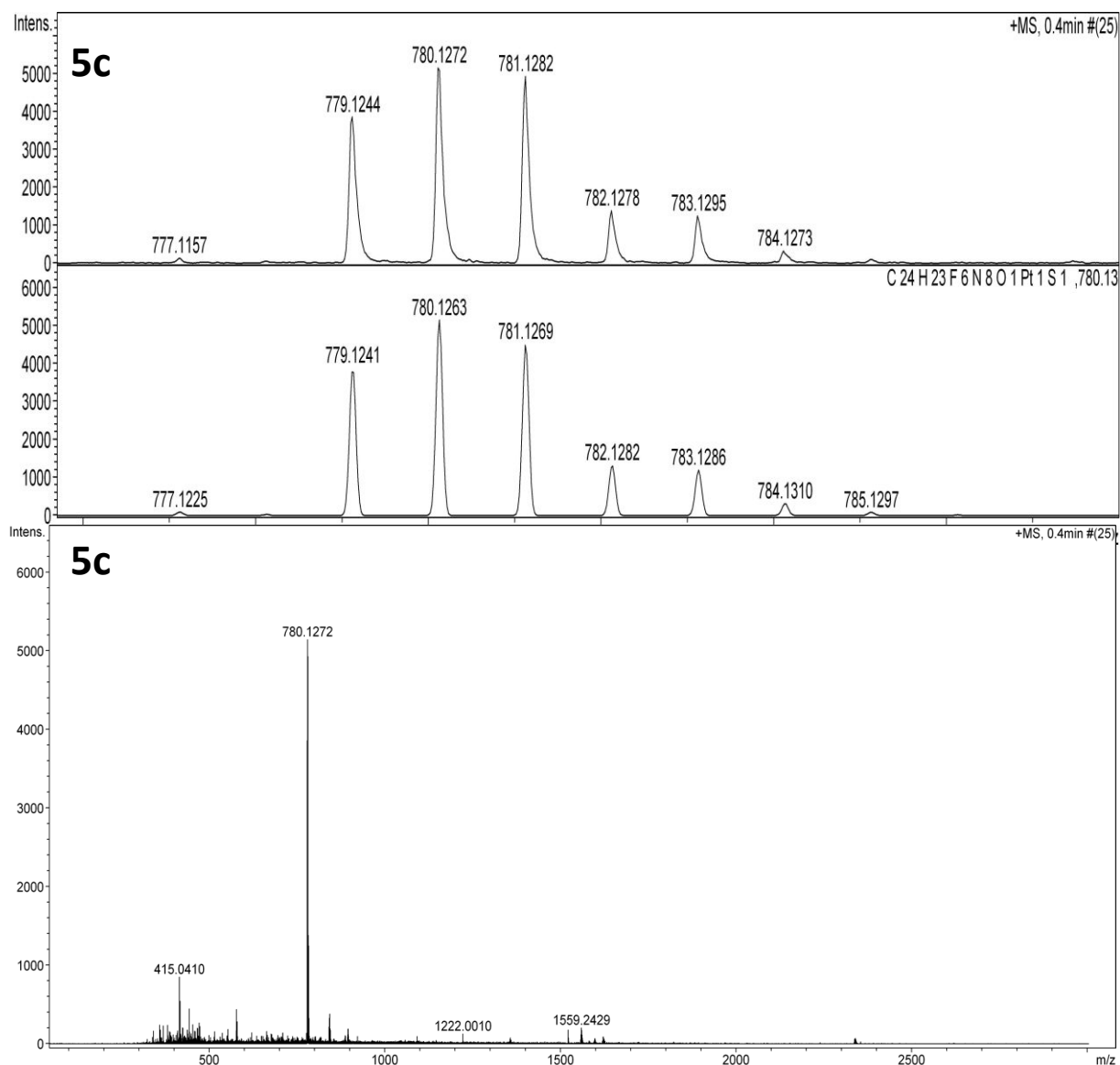


Figure 4.18. HR ESI-MS spectrum of **5c** (top), ESI-MS spectrum of **5c** (bottom)

4.5. References

1. Eustis, S.; El-Sayed, M. A., *Chem. Soc. Rev.* **2006**, 35 (3), 209.
2. Glomm, W. R.; Moses, S. J.; Brennaman, M. K.; Papanikolas, J. M.; Franzen, S., *J. Phys. Chem. B* **2005**, 109 (2), 804.
3. Zhang, P.; Wang, J.; Huang, H.; Chen, H.; Guan, R.; Chen, Y.; Ji, L.; Chao, H., *Biomaterials* **2014**, 35 (32), 9003.
4. Tsai, J. L.-L.; Zou, T.; Liu, J.; Chen, T.; Chan, A. O.-Y.; Yang, C.; Lok, C.-N.; Che, C.-M., *Chem. Sci.* **2015**, 6 (7), 3823.
5. Aliprandi, A.; Mauro, M.; De Cola, L., *Nat. Chem.* **2016**, 8 (1), 10.

6. Allampally, N. K.; Mayoral, M. J.; Chansai, S.; Lagunas, M. C.; Hardacre, C.; Stepanenko, V.; Albuquerque, R. Q.; Fernández, G., *Chem. Eur. J.* **2016**, 22 (23), 7810.
7. Dulkeith, E.; Morteau, A. C.; Niedereichholz, T.; Klar, T. A.; Feldmann, J.; Levi, S. A.; van Veggel, F. C. J. M.; Reinhoudt, D. N.; Möller, M.; Gittins, D. I., *Phys. Rev. Lett.* **2002**, 89 (20), 203002.
8. Osborne, S. A. M.; Pikramenou, Z., *Faraday Discuss.* **2015**, 185 (0), 219.
9. Curto, A. G.; Volpe, G.; Taminiau, T. H.; Kreuzer, M. P.; Quidant, R.; van Hulst, N. F., *Science* **2010**, 329 (5994), 930.
10. Strelow, C.; Theuerholz, T. S.; Schmidtke, C.; Richter, M.; Merkl, J.-P.; Kloust, H.; Ye, Z.; Weller, H.; Heinz, T. F.; Knorr, A.; Lange, H., *Nano Lett.* **2016**, 16 (8), 4811.
11. Munechika, K.; Chen, Y.; Tillack, A. F.; Kulkarni, A. P.; Plante, I. J.-L.; Munro, A. M.; Ginger, D. S., *Nano Lett.* **2010**, 10 (7), 2598.
12. Wang, Y.; Zhou, J.; Wang, T., *Mater. Lett.* **2008**, 62 (12–13), 1937.
13. Nabika, H.; Deki, S., *Eur. Phys. J. D* **2003**, 24 (1), 369.
14. Wertz, E. A.; Isaacoff, B. P.; Biteen, J. S., *ACS Photonics* **2016**, 3 (10), 1733.
15. Tseng, M. L.; Leu, B.-H.; Li, P.-Y.; Chung, K. S.; Chiang, H.-P., *Plasmonics* **2015**, 10 (6), 1301.
16. Jiang, Y.; Wang, H.-Y.; Wang, H.; Gao, B.-R.; Hao, Y.-w.; Jin, Y.; Chen, Q.-D.; Sun, H.-B., *J. Phys. Chem. C* **2011**, 115 (25), 12636.
17. Nikoobakht, B.; Burda, C.; Braun, M.; Hun, M.; El-Sayed, M. A., *Photochem. Photobiol.* **2002**, 75 (6), 591.
18. Raikar, U. S.; Tangod, V. B.; Mastiholi, B. M.; Fulari, V. J., *Opt. Commun.* **2011**, 284 (19), 4761.
19. Jianting, W.; Joseph, M.; Sebastien, L.; Michael, N.; Samuel, A.; Kyung, A. K., *Nanotechnology* **2012**, 23 (9), 095501.
20. Pensa, E.; Cortés, E.; Corthey, G.; Carro, P.; Vericat, C.; Fonticelli, M. H.; Benítez, G.; Rubert, A. A.; Salvarezza, R. C., *Acc. Chem. Res.* **2012**, 45 (8), 1183.
21. Xue, Y.; Li, X.; Li, H.; Zhang, W., *Nat. Commun.* **2014**, 5, 4348.
22. Poppenberg, J.; Richter, S.; Darlatt, E.; Traulsen, C. H. H.; Min, H.; Unger, W. E. S.; Schalley, C. A., *Surf. Sci.* **2012**, 606 (3–4), 367.
23. Winther, J. R.; Thorpe, C., *Biochim. Biophys. Acta* **2014**, 1840 (2), 10.1016/j.bbagen.2013.03.031.
24. Houk, J.; Whitesides, G. M., *J. Am. Chem. Soc.* **1987**, 109 (22), 6825.
25. Bach, R. D.; Dmitrenko, O.; Thorpe, C., *J. Org. Chem.* **2008**, 73 (1), 12.
26. Iversen, R.; Andersen, P. A.; Jensen, K. S.; Winther, J. R.; Sigurskjold, B. W., *Biochemistry* **2010**, 49 (4), 810.
27. Mauro, M.; Aliprandi, A.; Cebrian, C.; Wang, D.; Kubel, C.; De Cola, L., *Chem. Commun.* **2014**, 50 (55), 7269.
28. Jebb, M.; Sudeep, P. K.; Pramod, P.; Thomas, K. G.; Kamat, P. V., *J. Phys. Chem. B* **2007**, 111 (24), 6839.

CHAPTER 5:

Pt(II) Complexes: Photophysical Properties, Packing mode and Electronic Mobility

Abstract

A series of square planar platinum (II) neutral complexes containing oligothiophene substituents has been synthesized and characterized. The complexes contain the same N^+N^+ dianionic terdentate ligand and thiophene-functionalized pyridine derivatives as ancillary ligands. Their film morphology structure and the photophysical properties were studied and correlated to their charge transport properties. The establishment of intermolecular Pt---Pt and/or π - π stacking interactions resulted in differences in hole mobility values among the molecules here shown. The influence on the packing of the number of thiophene rings on the ancillary ligand has been explored, as well as the presence of fused aromatic systems.

Keywords

Pt(II) complexes, Luminescent properties, Morphology, Packing mode, Electronic mobility

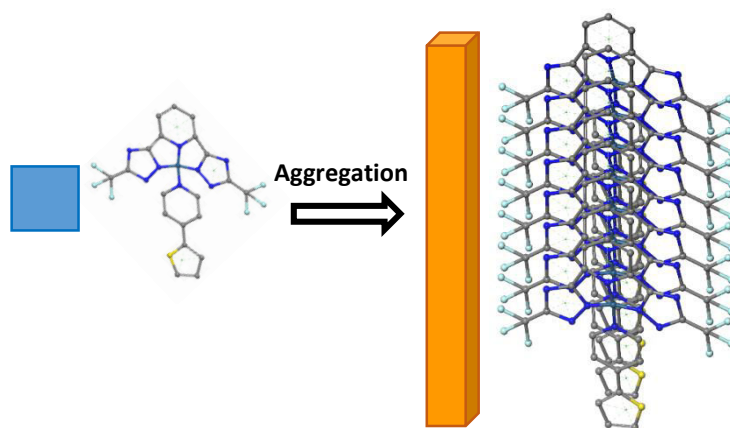
5.1. Introduction

Self-assembled structures have inspired much research interest due to the exciting properties that can arise from the architectures formed. Many non-covalent interactions can be employed to build such assemblies, as for example π - π stacking,¹ hydrogen bonds,²⁻³ halogen bonds⁴ and metallophilic interactions.⁵⁻⁶ In particular, d⁸ metal ions, and especially Pt(II), have been recognized as interesting building blocks for supramolecular structure, since their square planar geometry results in a high stacking tendency. If the distance between the two adjacent metal complexes is below 3.5 Å the dz² orbitals can electronically interact leading to the formation of a metal-metal bond. Such interaction can also lead to the formation of anisotropic nanostructures.⁷ Furthermore, the Pt---Pt interactions⁸⁻¹² results to the formation of new excited states, namely metal-metal-to-ligand charge transfer (MMLCT) transitions, that can be conveniently used to enhance the emission properties and to induce a large bathochromic shift of both, emission and excitation.¹³⁻¹⁵

Such metallophilic interactions are weaker than covalent bonds but they can reach binding strengths similar to hydrogen bonds. They are usually present together with other non-covalent forces,¹⁶ yielding supramolecular architectures where the interplay of all the coexisting interactions drive the assembly formation.^{17, 5, 14-15} Several cases of the combination of Pt---Pt with other non-covalent interactions have been reported, finding examples for the construction of liquid crystals,¹⁸ nanotubes,⁸ nanosheets,⁹ metallo-gelators^{19-20, 12} and nanowires²¹ with interesting optical and semiconducting properties.^{22, 21, 23} Our group has recently shown the difference in photophysical properties and nanostructure morphology depending on the interplay between π - π stacking and Pt---Pt interactions.¹⁷ Weakly blue emitting fibres were observed in solution in the absence of metal-metal interactions, while green to orange emissive aggregates were observed when Pt---Pt and even π - π stacking were involved in the formation of the assemblies. Differences in electronic properties have also been explored by studying the interplay of other non-covalent interactions. Che *et al.* for example reported cationic cyclometalated/terpyridyl Pt(II) complexes containing arylisocyanide and arylacetylide ligands. They demonstrated that depending on the stacking arrangement of the complexes in the crystal structure, the charge carriers could be ambipolar or electron-based.^{22, 21}

The focus of the work described in this chapter is the synthesis, the optical and the electrochemical properties of a library of oligothiophene containing Pt(II) complexes.

The spectroscopic behaviour was investigated for all the complexes as isolated species and in their self-assembled structures. The aim is to study the effect of the ancillary ligand, the series of complexes was designed maintaining the same N⁴N⁴N⁴ terdentate ligand previously used, and varying the ancillary ligand based on thiophene containing pyridine rings.

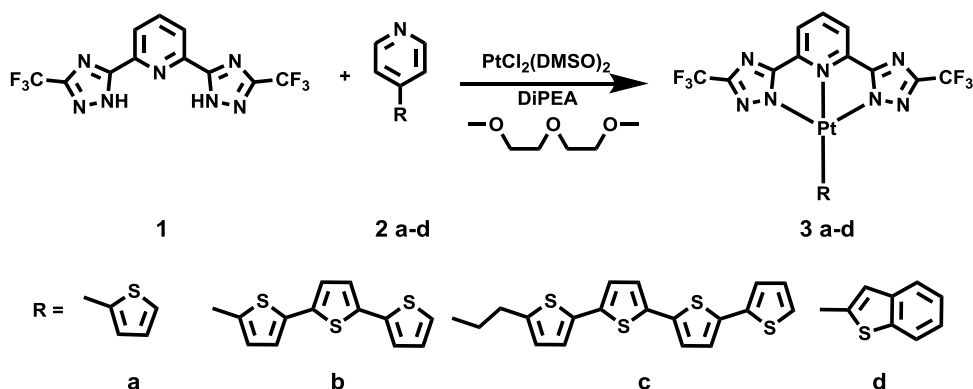


Scheme 5.1. Schematic representation of the studied process

5.2. Results and discussion

The functionalization of the pyridine moiety used as the ancillary ligand with different oligothiophene derivatives was performed using Stille coupling reactions. The ligands were prepared in the group of Prof. Farinola at the University of Bari.

The thiophene-containing platinum (II) complexes have been obtained using a one-pot synthesis, as shown in **Scheme 5.2**.



Scheme 5.2. Synthetic approach for complexes **3a-d**

Complexes **3a**, **3b** and **3c** containing one and up to four thiophene units covalently attached to the pyridine ring employed as ancillary ligand, and complex **3d** with a benzothiophene unit were prepared using $\text{PtCl}_2(\text{DMSO})$ as precursor and diethylene glycol dimethyl ether as a solvent. As mentioned in *chapter 2* the choice of the solvent is not crucial, since the same reaction also works with high yields using acetonitrile or methanol. Moreover, the complexation step was performed in basic media, and the base needs to be strong enough to allow the deprotonation process, and also to provide enough steric hindrance, not to coordinate the metal. Therefore, a good candidate is to be diisopropylethylamine (DIPEA), strong ($\text{pK}_a \approx 13$) and bulky enough for our requirements. The choose of a too strong base could force us to use inert conditions, which is much less convenient. The thiophene rings were directly attached to the pyridine ring in complexes **3a** and **3b** but a short ethyl group linker was needed in the case of complex **3c** because of solubility issues. The compounds were purified by filtration and washings with water and dichloromethane and characterized by ^1H -NMR, ^{13}C -NMR, ^{19}F -NMR, and high resolution mass spectrometry.

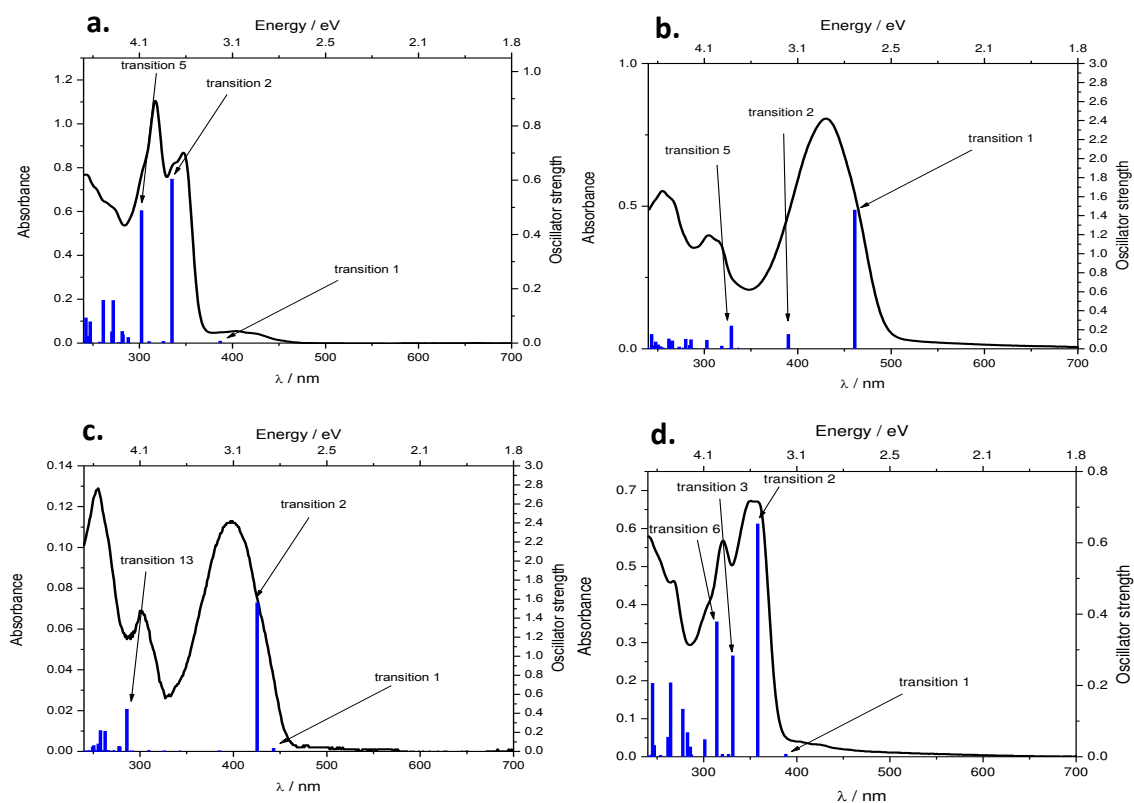


Figure 5.1. Calculated (blue trace) and measured (black trace) absorption spectra of complexes **3a(a.)**, **3b(b.)** **3c(c.)** **3d(d.)**

The absorption spectra of complexes **3a-d** are shown in **figure 5.1**. All complexes display characteristic absorption bands in the UV region related to π - π^* ligand-centered transitions (275 to 350 nm) and intraligand charge transfer bands. At lower energy, we observe broad bands attributed to singlet and triplet metal-to-ligand charge transfer transitions (350 to 500) in the case of complexes **3a** and **3d**. For complexes **3b** and **3c**, we observe also transitions involving the oligothiophene units, as characteristic broad bands centered at 430 nm and 400 nm for **3b** and **3c** respectively. Time-dependant density functional theory (TD-DFT) calculations have been performed to estimate all the transitions and all the electronic singlet transitions for all complexes are listed on **tables 5.1, 5.3, 5.5 and 5.7** together with the electron-density-difference maps in **tables 5.2, 5.4, 5.6 and 5.8**.

The electron-density-difference maps (EDDM) show that the Pt centers are not involved in the transitions happening at lower energies in complexes **3b** and **3c**, being the opposite in the case of **3a** and **3d**, where the metal center is directly involved. When comparing to the excitation (**Figure 5.2.**) spectra it is observed that complexes **3a** and **3d** show additional bands with maxima at 438 nm and 521 nm respectively, that are not observed in the absorption spectra, indicating excimer formation where the Pt centers are involved, as reported elsewhere.^[23,24] On the other hand, complexes **3b** and **3c** show excitation spectra that are similar to absorption spectra, demonstrating the absence of excimers.

The photophysical properties in solution and in solid state are summarized in **Table 5.9** and **Table 5.10**, respectively. Complexes **3a-d** are weakly emissive in dilute solution (dichloromethane, 10^{-5} M) at room temperature, with the exception of complex **3c** that exhibit a good photoluminescence quantum yield (PLQY) of 12%. Emission spectra of the complexes **3a-d** in dichloromethane at 10^{-5} M are shown in **Figure 5.3**.

Table 5.1. Main electronic singlet transitions for compound **3a**, based on TD-DFT

No.	λ (nm)	f	Major contributions	Minor contributions
1	386	0.0085	HOMO->LUMO (91%)	HOMO->L+1 (8%)
2	335	0.605	H-1->LUMO (90%)	H-4->LUMO (5%)
3	325	0.008	H-2->LUMO (93%)	H-2->L+1 (7%)
4	310	0.0069	HOMO->L+1 (90%)	HOMO->LUMO (8%)
5	302	0.4889	H-2->L+4 (11%), H-1->L+1 (35%), HOMO->L+2 (41%)	H-4->LUMO (7%)

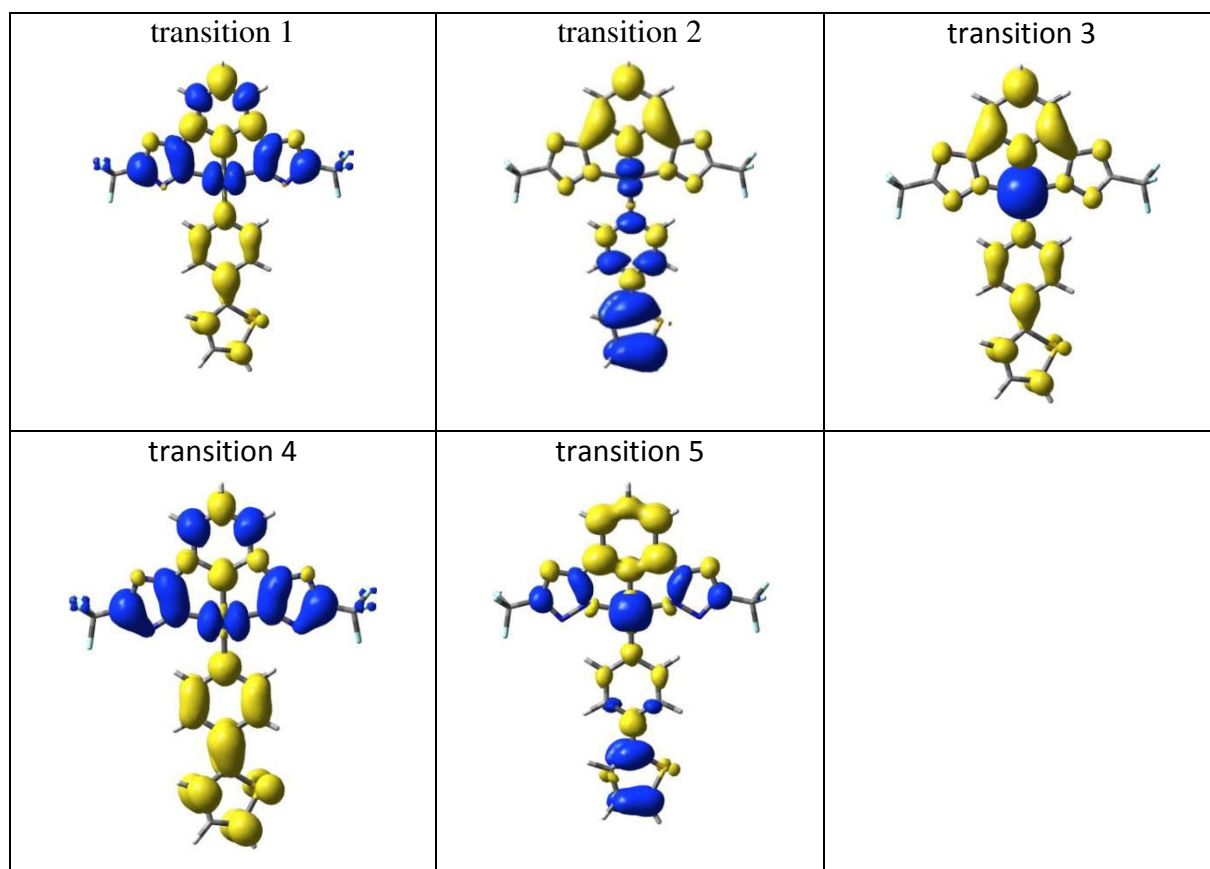
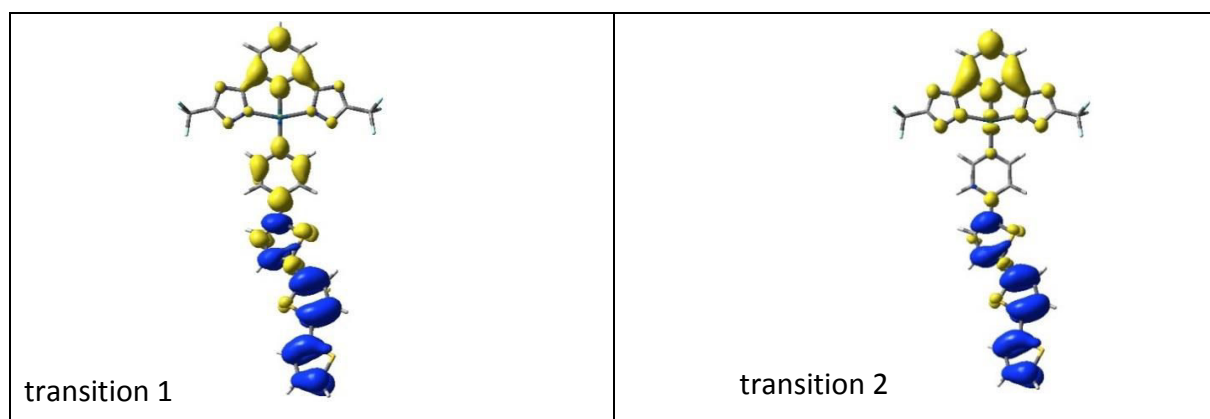
Table 5.2. Electron-density-difference maps representing the singlet transitions calculated for compound **3a**. The blue isosurfaces represent the depletion of electron density and the yellow isosurfaces represent the accumulation of electron density during an electronic transition.

Table 5.3. Main electronic singlet transitions for compound **3b**, based on TD-DFT

No.	λ (nm)	f	Major contribs	Minor contribs
1	461	1.4612	HOMO->LUMO (94%)	HOMO->L+1 (5%)
2	390	0.1553	HOMO->L+1 (94%)	HOMO->LUMO (5%)
3	388	0.0072	H-1->LUMO (66%), H-1->L+1 (32%)	
4	336	0.0005	HOMO->L+2 (99%)	
5	329	0.2432	H-2->LUMO (37%), HOMO->L+3 (56%)	

Table 5.4. Electron-density-difference maps representing the singlet transitions calculated for compound **3b**. The blue isosurfaces represent the depletion of electron density and the yellow isosurfaces represent the accumulation of electron density during an electronic transition.**Table 5.5.** Main electronic singlet transitions for compound **3c**, based on TD-DFT

No.	λ (nm)	f	Major contribs
1	443	0.0364	HOMO->LUMO (98%)
2	425	1.5651	HOMO->L+1 (98%)
3	385	0.0095	H-2->LUMO (98%)
4	360	0	HOMO->L+2 (100%)

Table 5.6. Electron-density-difference maps representing the singlet transitions calculated for compound **3c**. The blue isosurfaces represent the depletion of electron density and the yellow isosurfaces represent the accumulation of electron density during an electronic transition.

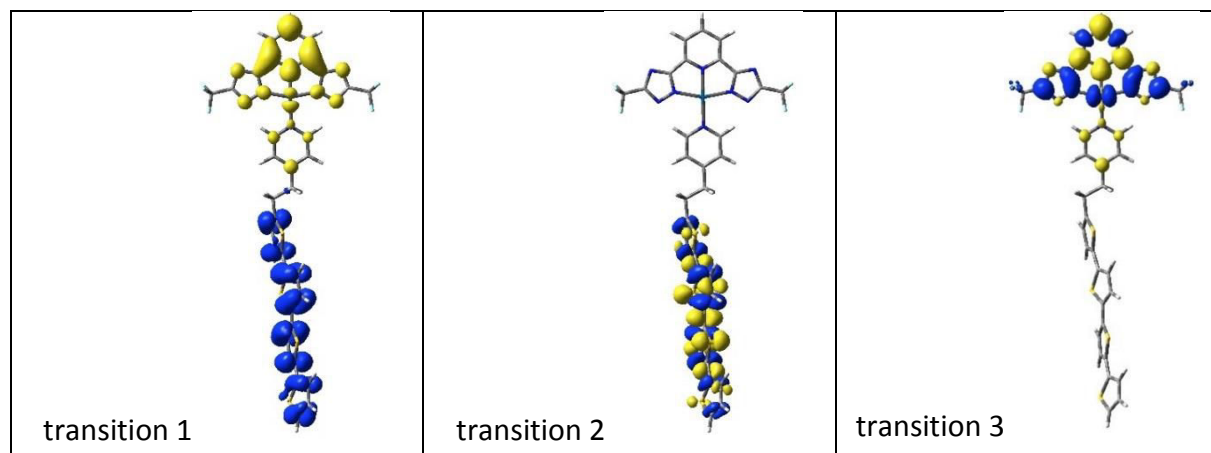
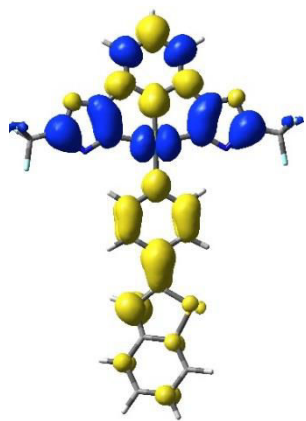
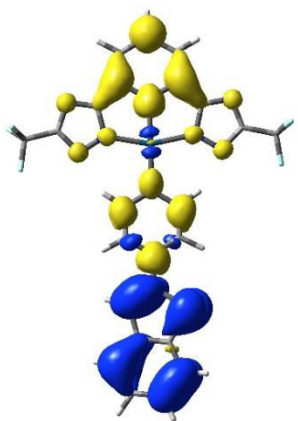
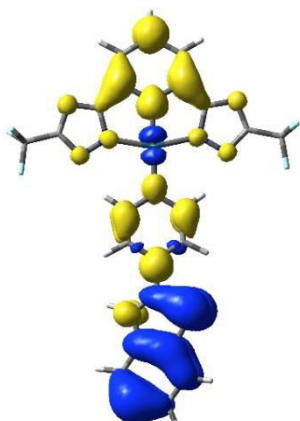
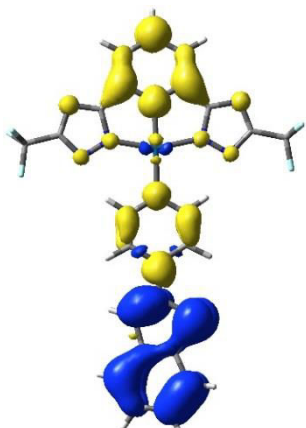
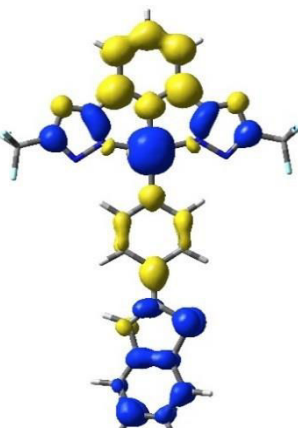


Table 5.7. Main electronic singlet transitions for compound **3d**, based on TD-DFT

No.	λ (nm)	f	Major contribs	Minor contribs
1	388	0.008	H-1->LUMO (84%), H-1->L+1 (14%)	
2	358	0.654	HOMO->LUMO (92%)	HOMO->L+1 (5%)
3	331	0.284	H-2->LUMO (79%)	H-4->LUMO (3%), H-2->L+1 (9%), HOMO->L+1 (6%)
4	327	0.008	H-3->LUMO (87%), H-3->L+1 (13%)	
5	320	0.008	H-1->LUMO (14%), H-1->L+1 (83%)	
6	314	0.379	HOMO->L+1 (77%)	H-2->LUMO (5%), H-2->L+1 (4%), H-1->L+2 (6%), HOMO->LUMO (3%)
7	301	0.049	H-4->LUMO (22%), H-2->L+1 (14%), H-1->L+2 (36%), HOMO->L+1 (11%)	H-4->L+1 (3%), H-3->L+4 (8%), HOMO->LUMO (3%)

Table 5.8. Electron-density-difference maps representing the singlet transitions calculated for compound **3d**. The blue isosurfaces represent the depletion of electron density and the yellow isosurfaces represent the accumulation of electron density during an electronic transition.

<p>transition 1</p> 	<p>transition 2</p> 	<p>transition 3</p> 
<p>transition 6</p> 	<p>transition 7</p> 	

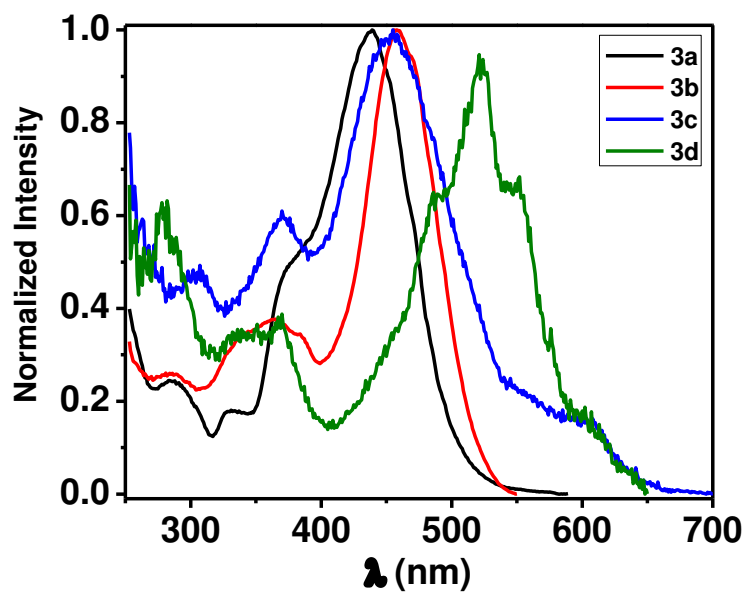


Figure 5.2. Excitation spectra of complexes **3a-d** in CH_2Cl_2 5.10^{-5} M.

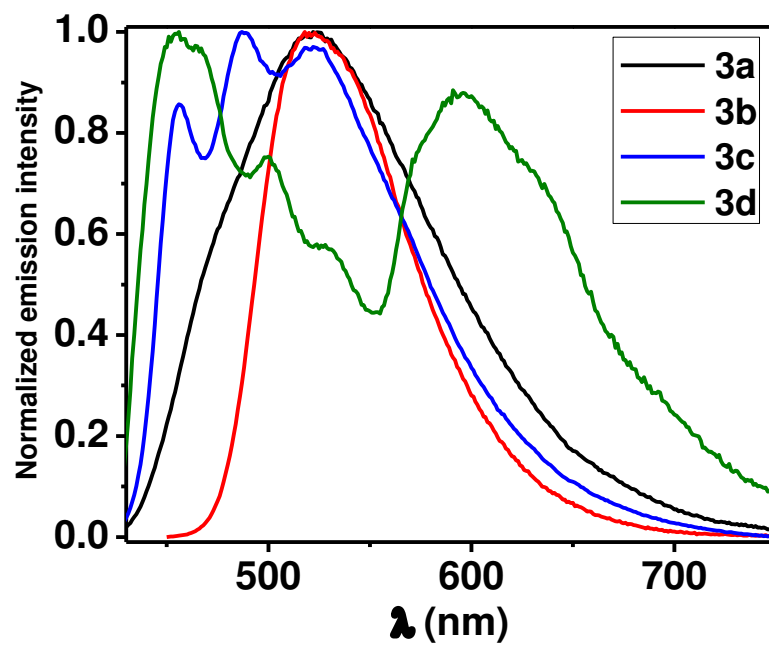


Figure 5.3. Emission spectra of complexes **3a-d** in dichloromethane at 10^{-5} M.

Table 5.9. Photophysical properties of complexes **3a-d** in solution (CH₂Cl₂, 5.10⁻⁵M)

Complex	λ_{abs} (nm), (ϵ . 10 ⁻⁴ , L.M ⁻¹ . cm ⁻¹)	λ_{max} [nm]	τ [ns]	PLQY (%)
3a	246(1.51), 317(2.21), 347(1.73), 403(0.11)	525	0.18(23%), 0.8(67%), 2.6(10%),	1
3b	256(1.11), 304(0.79) 430 (1.62)	518	6.9(52%), 22(38%), 1.2(9%)	12
3c	254(0.26), 302(0.14), 397(0.23)	457, 487, 522	3(78%), 1.19(22%)	1.5
3d	267(0.92), 320(1.13), 354(1.34), 418(0.07)	559(s), 594, 671	7(61%), 0.82(7%), 3.8(32%)	1

Complexes **3a** and **3b**, show a broad, featureless bands with emission λ_{max} at 525 and 520 nm. Such emission bands can be attributed to the MMLCT transition involving intermolecular Pt---Pt interactions. However, complex **3a** displays a shoulder at high energy that can be attributed to a residual emission from the monomeric species. Complex **3c** shows emission maxima at 455 nm, 488 nm and 521 nm. In this case, the emission spectrum is more structured than the spectra of complexes **3a** and **3b**, possibly due to the presence of a short alkyl spacer between the quaterthiophene segment and the pyridine ring that makes the complex able to rotate around the sp³ carbons, disturbing the aggregate and therefore showing the typical emission profile of complexes in their monomeric form. However, the shape of the emission and the fact that the last vibrational band is rather intense point out to a small aggregation. We attributed the emission to a triplet ligand centre state with some charge transfer character. (³LC/³ILCT). Complex **3d** shows a very complicated emission constituted by some featureless bands centred at 595 nm that can be attributed to the formation of aggregates and therefore to metal-metal to ligand charge transfer, ³MMLCT transitions. In addition, the emission of the complex in its non-aggregated state is

observed at higher energy with maxima at 466 nm, 498 nm and 530 nm, as observed in similar complexes.^{6, 24}

The excited state lifetimes of complexes **3a-d** in solution at room temperature present multiexponential kinetics, showing values of just a few nanoseconds (**Table 5.9**). reaching hundreds of nanoseconds in the solid state (powder) (**Table 5.10**).

Table 5.10. Photophysical properties of complexes **3a-d** in solid state

Complex	λ_{em} [nm]	τ [ns]	PLQY (%)
3a	598	463(41%), 182(59%),	3
3b	578	930(88%), 136(12%)	12
3c	569, 611	495(80%), 147(20%)	1
3d	461, 491, 557	955(78%), 156(22%),	1.5

To understand the self-assembly properties, the complexes morphology was investigated in their thin films state. The samples were prepared by dropcasting the corresponding solutions by varying the solvent, the solution concentrations, the thermal treatments, the aging of the samples. Together with scanning electron microscopy (SEM), powder X-ray diffraction (PXRD) studies on such films were also performed to understand the role of the packing mode and the interplay of the non-covalent interactions coexisting in the assemblies formed by the complexes.

Together with chloroform (CHCl_3), 1,2, -dichlorobenzene (ODCB or Cl_2Bz) was used in order to highlight the role of a high boiling point solvent where complexes **3a-d** presented good solubility at high temperature. Other solvents such as toluene, acetonitrile and tetrahydrofurane were discarded due to the low solubility of the complexes. Thin films were prepared by drop-casting solutions at different concentrations, ranging from $5 \cdot 10^{-3}$ M to 0.1 M. Freshly prepared solutions were used and solutions stirred at high temperature (55 °C for CHCl_3 and 120 °C for Cl_2Bz) for several hours before gradually cooling down. Some of the studied films were prepared by aging the solution for several days before drop casting. Taking into account these preparation methods, the most optimal conditions for each complex were chosen by studying the morphology by SEM. Subsequently, the emission properties of the complexes on thin films were studied and the results were correlated with the packing mode of the complexes on thin films studied by PXRD and their charge transport properties.

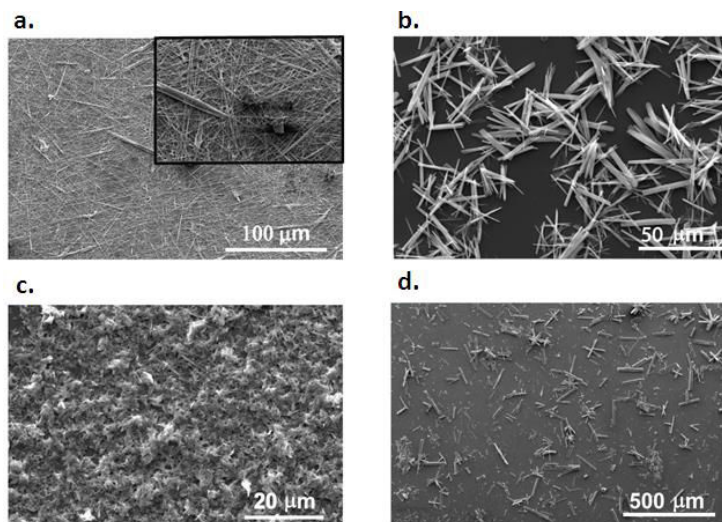


Figure 5.4. SEM images of optimized films made with complexes **3a-d**.

Thin films of complex **3a** were prepared by drop casting a 72 hours aged, 0.01 M Cl_2Bz solution. Well-defined fiber-like structures of hundreds of μm in length were observed (**Figure 5.4.a**). They are monodispersed and a very good coverage of the surface was found.

After 24 hours (**Figure 5.5**) we could see that the fibers are already formed, even though they are slightly shorter and displaying a lower surface coverage. However, in chloroform, (**Figure 5.6**) the result was much less promising

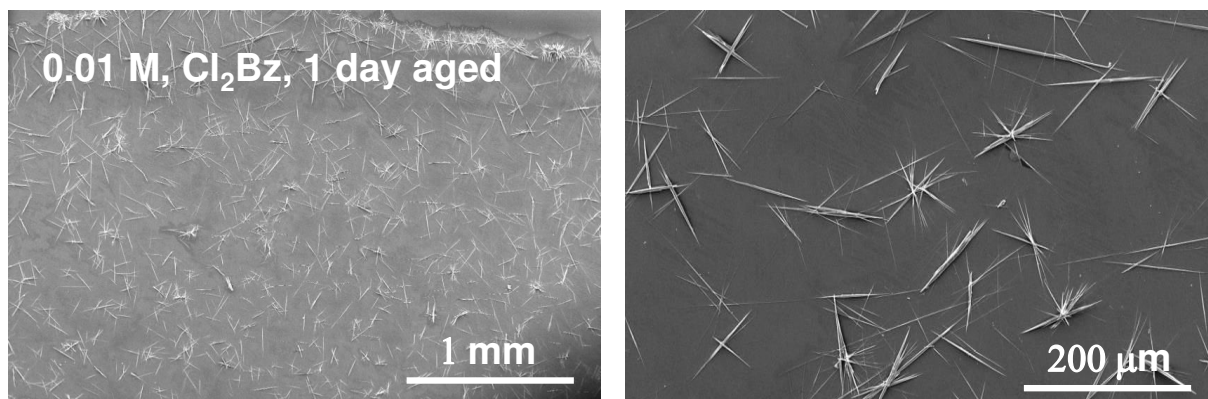


Figure 5.5. SEM images of complex **3a** thin film dropcasting from a solution of 0.01M in ortho-dichlorobenzene, after 24 h aged

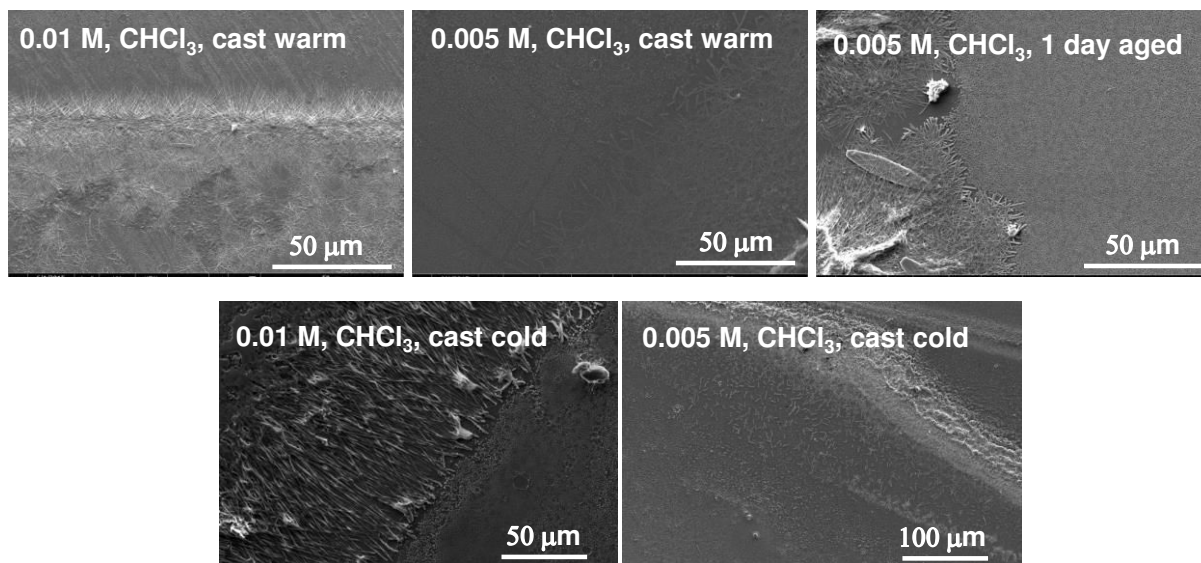


Figure 5.6. SEM images of complex **3a** thin film dropcasting from a chloroform solution

Complex **3b** thin films were prepared by drop casting a 0.01 M, Cl_2Bz solution that was previously heated at 120 °C with stirring until complete dissolution of the complex and then cooled down to room temperature. Needle-like structures of approximately 50 μm in length were observed (**Figure 5.4.b**).

Similarly to complex **3a**, CHCl_3 solutions at different concentrations and aging times did not form good films, with the exception of dropcasting from a 0.01M solution aged of 72 hours (**Figure 5.7**).

Thin films of complexes **3c** and **3d** were prepared by the same way as complex **3a**. Flake-like structures of tens of μm in length were found for complex **3c** (**Figure 5.4.c**) with total surface coverage and fibers structures of approximately 100 μm in length were found for **3d** (**Figure 5.4.d**). As in the previous cases, chloroform as the solvent, different concentrations and aging times did not yield good morphology films. **Table 5.11** is a summary of the optimized conditions used for the thin film preparation of each complex.

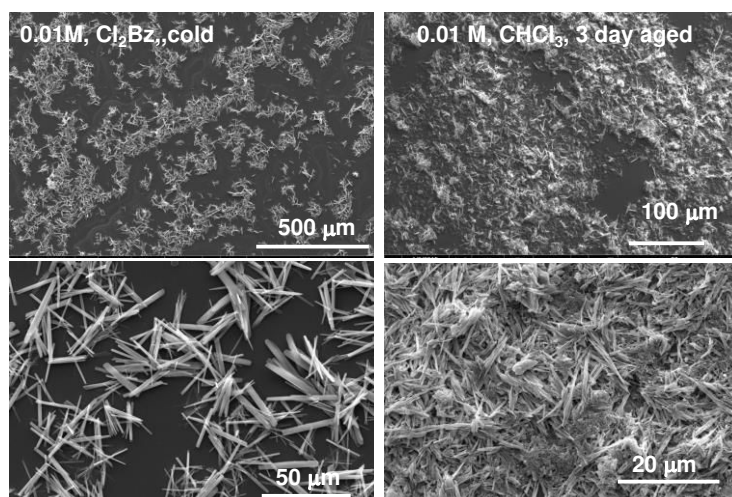


Figure 5.7. SEM images of complex **3b** thin film dropcasting from a solution of 0.01M in ortho-dichlorobenzene, after cooling down the solution (right), and from a solution of 0.01M in CHCl_3 aged of 72 hours.

Table 5.11. Recap chart of the optimized conditions used for the thin film preparation of each complex.

Complex	Solvent	Concentration	Temperature	Aging
3a	o-DCB	0.01 M	120°C	72h
3b	o-DCB	0.01 M	120°C	After cooling down
3c	o-DCB	0.01 M	120°C	72h
3d	o-DCB	0.01 M	120°C	72h

The emission properties of the films prepared by the protocols previously mentioned were also measured, and showed in **Figure 5.8**. Complex **3a** shows a featureless, broad emission band with λ_{max} at 687 nm with a shoulder at 615 nm assigned to aggregation mode in a face-to-face manner.²⁵ Compared to the emission in dichloromethane solution, a dramatic bathochromic shift can be observed. Complex **3b** displays a broad band centered at 592 nm and a more structured signal at higher energy attributable to the ligand emission. Complex **3c** shows a broad, featureless band centered at 612 nm, additionally a shoulder at 576 nm is also observed. The latter was also observed as in the case of complex **3a** but much less intense. Finally, complex **3d** presents a different spectrum compared to the other complexes in the series. A main band at 608 nm can be observed together with a shoulder at 659 nm and another shoulder at higher energy at 557 nm. Interestingly, complex exhibits the most red-shifted emission signal as a sign of the enhanced stacking ability of this complex, even compared to complex **3b** containing a terthiophene segment conjugated to the pyridine ring. In all cases the

spectra are red-shifted compared to the ones in solution as a sign of further aggregation in the solid state. We also simulated the molecular packing of the self-assembled complexes. For this purpose, the geometrical structures of the monomeric species were first optimized with the program Gaussian. The powder XRD pattern of complexes **3a-d** were then measured. They are shown in **Figures 5.9-5.12**. Subsequently, using the state-of-the-art software Total Pattern Analysis Solution (TOPAS, Bruker AXS),²⁶ the XRD patterns were indexed on maximum 20 peaks, and the investigation was performed for all the crystal systems. Using the same software, a refinement²⁷ was performed for each structure and then we could obtain the lattice parameters of the studied structures with Rietveld weighted profiles (R_{wp}) going from 19% to 11% (**Table 5.10**). The simulated molecular packing of each complex has been determined by the Materials Studio program, Reflex Module, from the lattice parameters and the structure of the monomeric species.²⁸⁻²⁹ The images of the polymeric structures (shown as dimers or tetramer for clarity reasons) are displayed in **Figure 5.13**.

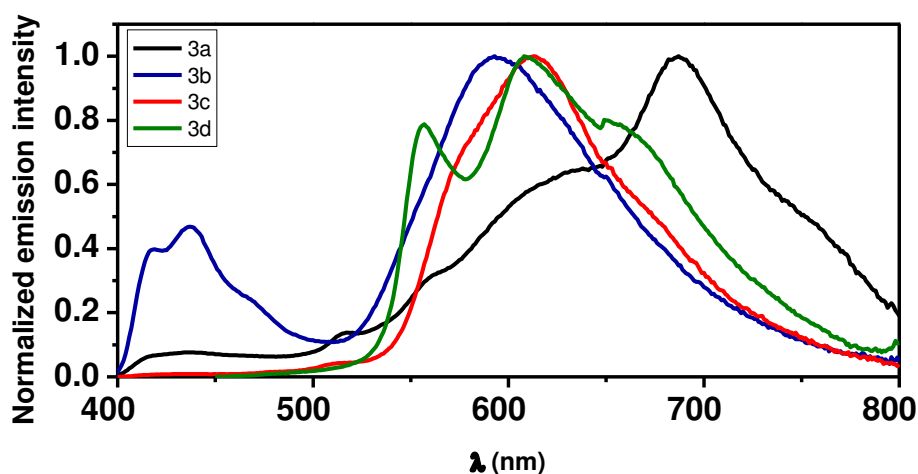


Figure 5.8. Thin film emission spectra of complexes **3a-d**

Complex **3a** shows Pt---Pt distance of 3.79 Å and π - π interactions in a parallel, face-to-face fashion between the rings of the terdentate ligand of one complex and the pyridine-thiophene moiety of another one (**Figure 5.13.a**), finding a distance of 3.79 Å for each interaction. Regarding complex **3d** a Pt---Pt distance of 3.21 Å was observed, being the complex that places the Pt centers in closer proximity. π - π interactions of 3.1 Å and 2.9 Å between the tridentate ligands of two neighbouring complexes are found (**Figure 5.13.d**). Such results are in agreement with the emission properties observed

in the thin films since no monomeric species emission signal was observed for complexes **3a** and **3d**. Complex **3a** has particularly red-shifted emission in comparison to the other complexes and indicating that small, rigid ligands promote packing. Complexes **3b** and **3c** do not show any Pt---Pt interaction, exhibiting a distance calculated from the simulation of 6.71 Å and 11.41 Å respectively, which is much larger distance than the required to have such kind of Pt---Pt interaction (3.5 Å) (**Figures 5.13.b** and **5.13.c**, respectively). We believe it is due to the tilted conformation of the oligothiophene segments which hinders the packing of the molecules to place the metal centers in close proximity. Particularly, the quarterthiophene segment could induce free rotation and render a slightly distorted geometry. Complex **3b** places neighbouring complexes in an antiparallel manner showing distances of 4.9 Å between the pyridine ring of the tridentate ligand and one of the pyrazole rings of the tridentate ligand of a neighboring complex. All the values of Pt—Pt and π - π stacking interactions are shown in **Table 5.10**.

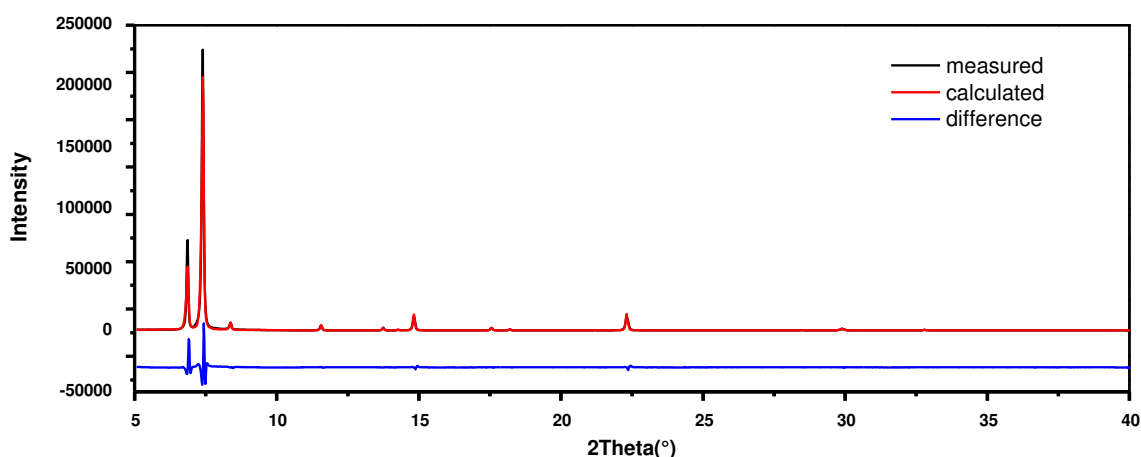


Figure 5.9. The result of quantitative Rietveld analyses made with commercial TOPAS program for complex **3a**.

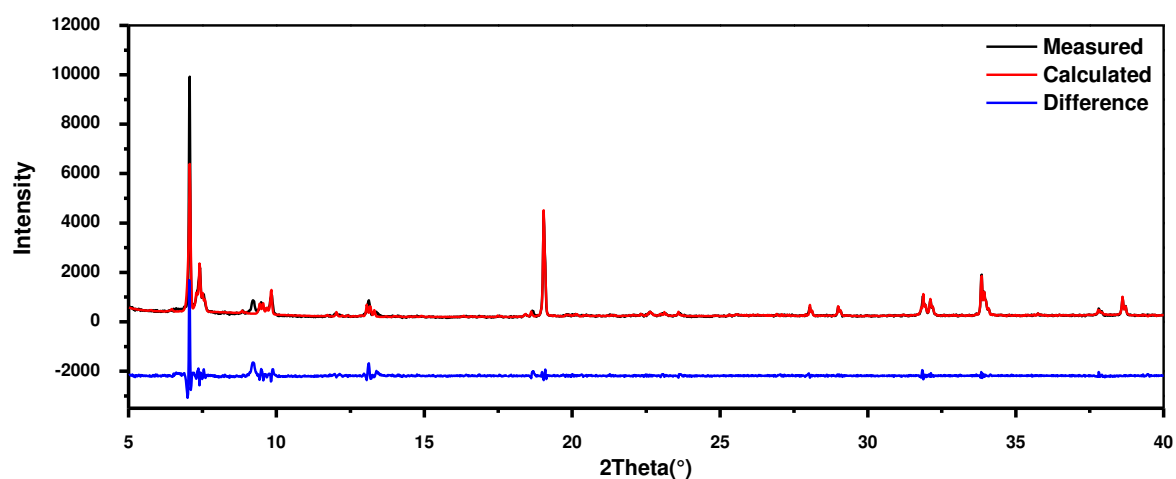


Figure 5.10. The result of quantitative Rietveld analyses made with commercial TOPAS program for the complex **3b**. The large difference at 7 degrees is due to preferential orientation of the sample.

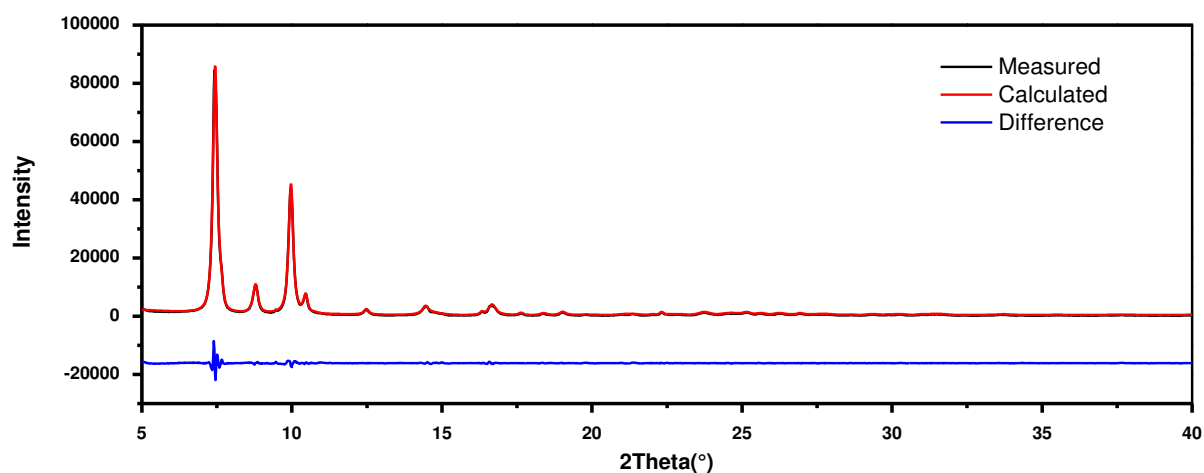


Figure 5.11. The result of quantitative Rietveld analyses made with commercial TOPAS program for the sample **3c**.

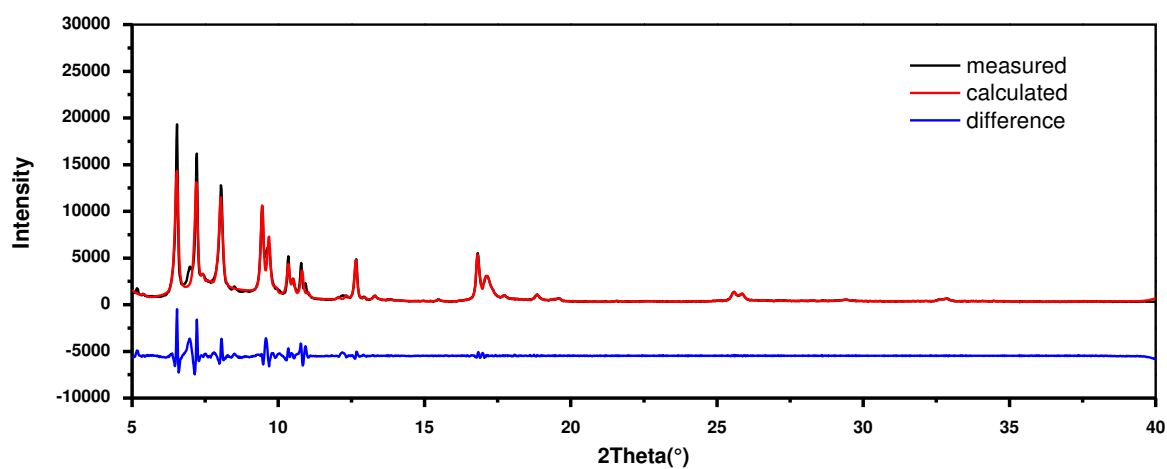
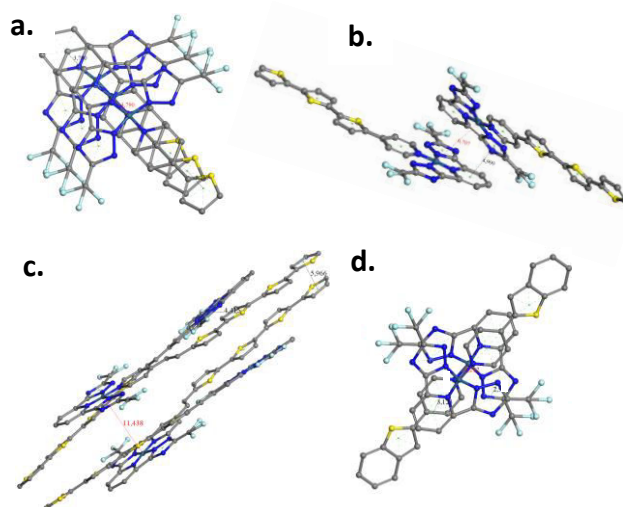


Figure 5.12. The result of quantitative Rietveld analyses made with commercial TOPAS program for the sample **3d**.

Table 5.12. PXRD parameters for complexes **3a-3d**.

Complex	Crystal system	Space group	A(Å)	B(Å)	C(Å)	Alpha(°)	Beta(°)	Gamma(°)	Cry (nm)	Rwp
3a	Monoclinic	P21(4)	15.353	3.790	13.567	90	128.770	90	333	18.1
3b	Triclinic	P-1(2)	2.999	24.897	40.0052	89.653	90.129	90.078	366	14.9
3c	Orthorhombic	P222(16)	35.4967	12.1729	5.0067654	90	90	90	156	10.2
3d	Triclinic	P-1(2)	13.5495	22.4959	27.0455	83.99	87.85	90.7	60	11.5

**Figure 5.13.** Simulated structures of self-assembled complexes **3a(a.)**, **3b(b.)**, **3c(c.)**, **3d(d.)**

Complex **3c** does not evidence Pt centers of neighbouring complexes in close proximity. Distances of 4.4 Å and 5.4 Å between a pyrazole ring in the tridentate ligand and a thiophene ring of the ancillary ligand of a neighbouring complex and between thiophene rings from two different complexes, respectively.

To continue studying the assembly properties of the complexes, charge transport measurements were performed by fabricating space-charged-limited current (SCLC) devices. For this purpose, two terminal devices were built using the thin films previously described. Interestingly, not only the electronic properties of the single molecule can explain the results and the packing of the complexes plays an important role. Even with moderate values ($1.2 \cdot 10^{-7} \text{ cm}^2 \cdot \text{V}^{-1} \cdot \text{s}^{-1}$), complex **3a** with only one thiophene ring shows higher current and better transport than complex **3b** containing a terthiophene segment. Interestingly, the HOMO level for **3a** falls at -6.15 V, making the injection process very difficult. However, we believe **3a** presents better mobility

than **3b** and **3c** due to the enhanced packing ability of **3a** as demonstrated by its thin film emission properties and the PXRD data. Complexes **3b** and **3c** present similar mobility values ($0.4 \times 10^{-7} \text{ cm}^2 \cdot \text{V}^{-1} \cdot \text{S}^{-1}$) despite the difference in HOMO energy values.

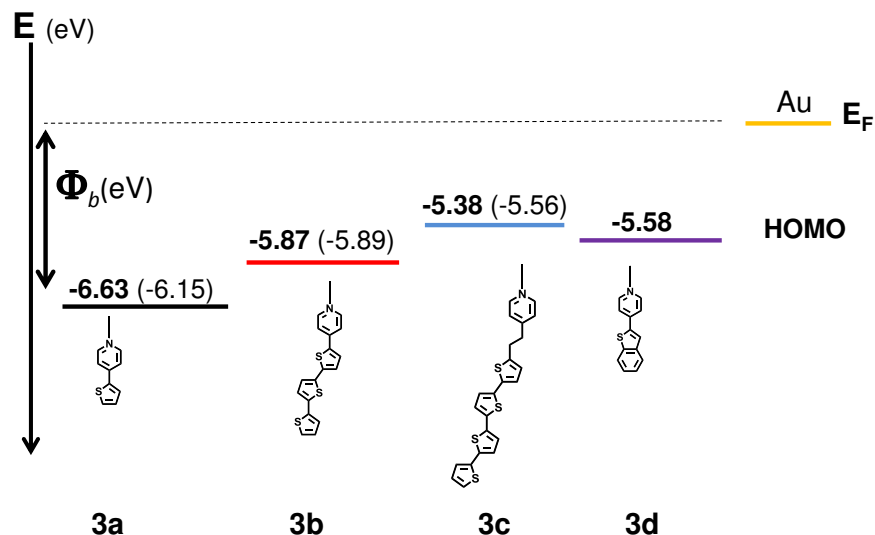


Figure 5.14. HOMO levels of complexes **3a-3d**. Φ_b represents the injection barrier for holes.

This result correlates the PXRD patterns and the simulated aggregation form, since no Pt---Pt interaction was found for complexes **3b** and **3c**. In particular, the presence of the ethylene linker in complex **3c** can make the packing of the complex less efficient for transporting charges than in complex **3b** where the direct attachment of the terthiophene segment to the pyridine can make the entire structure more rigid. This can explain the higher mobility value for complex **3b** than **3c**.

Complex **3d** showed the highest mobility ($2.6 \times 10^{-6} \text{ cm}^2 \cdot \text{V}^{-1} \cdot \text{S}^{-1}$) of the series, presenting mobility values one order of magnitude higher. It can be explained by both, electronic and packing properties. The HOMO level at -5.58 V makes the injection barrier more favourable than for complexes **3a** and **3b** but not for **3c**. However, the mobility value found for **3d** is one order of magnitude higher most likely because the Pt---Pt and π - π interactions in this complex are stronger and make the complexes packing in a more efficient way to transport charges. The fact that complex **3d** places Pt centers in closer proximity than the rest of the complexes, gives an idea about how important this interaction is to enhance packing and therefore the charge transport.

5.3. Conclusions

We have shown the synthesis of a series of oligothiophene-substituted neutral Pt(II) complexes. Their photophysical properties have been studied in solution and on thin films. Their self-assembly properties have been studied on thin films using microscopy techniques and PXRD. The results have been correlated to their charge transport properties to demonstrate that the molecular packing plays a crucial role when devices are fabricated. Interestingly, we have observed that the complex that places Pt centers in closer proximity (**3d**) is the one presenting higher mobility values, not only thanks to its HOMO level but also because it gives the best intermolecular packing.

5.4. Powder X-ray diffraction: basics and data treatment

This chapter involves deep PXRD characterizations. Thus, a short explanation of such phenomenon is required. X-ray diffraction is an important tool to identify the structure of a crystal, in which the atoms are arranged in a specific way. Because the interatomic distance is in the Angstrom range, the wavelength used to probe the atomic arrangement of a crystal must be in the same order of magnitude. Such values are characteristics of X-rays (**Figure 5.15**).

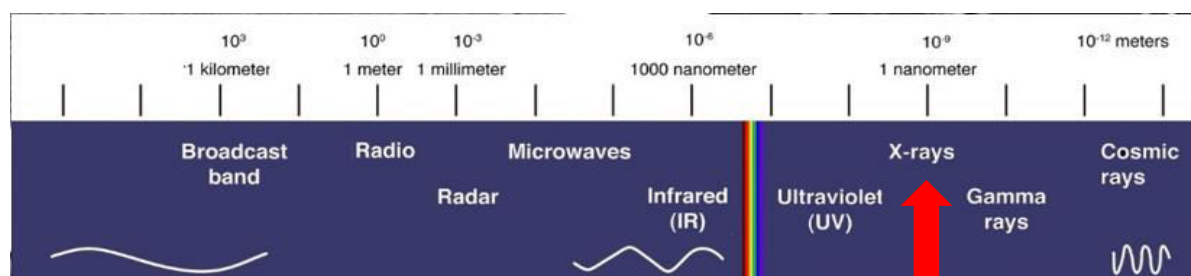


Figure 5.15. Electromagnetic spectrum highlighting the X-rays region by the red arrow.

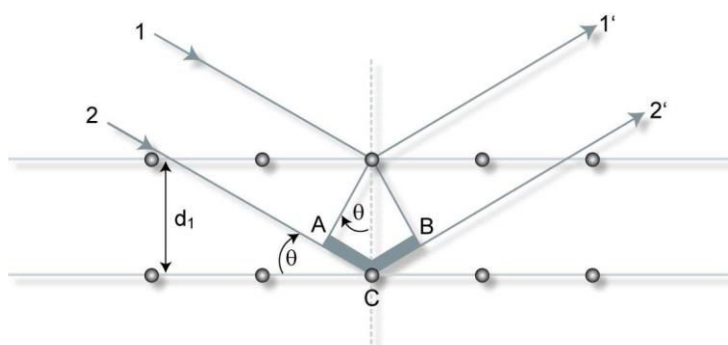


Figure 5.16. Schematic representation of X-rays (1 and 2) shining a structure with well-arranged atoms (grey circles) d is the distance separating two lattice plans, θ is the diffraction angle.

Like for UV radiations, explained in chapter 1, X-rays are electromagnetic radiation featuring a dual character: they have the properties of waves and particles, so they will show typical characteristics like diffraction, and are able to collide with other particles and in order to interact with them. X-ray diffraction of a solid and periodic structure reveals the atomic position inside the structure. When a crystal is shined by a by an x-ray beam, diffraction happened only for a specific atomic position, meaning at specific angles (Figure 5.16). This method was studied by William Henry Bragg (father) and William Lawrence Bragg (son), 1915 Nobel Prize Laureates for their works on x-ray diffraction and the development of a simple relation for scattering angles, now referred to as Bragg's law:

$$n.\lambda = 2d.\sin\theta \quad (5.1)$$

In which n is refractive index of the medium, typically 1, λ is the X-ray beam wavelength (constant) d is the distance separating two lattice plans, and θ represent the diffraction angle. Two main techniques for structure determination are used: Single crystal XRD (SCXRD) and PXRD. Their difference is illustrated in **Figure 5.17**.

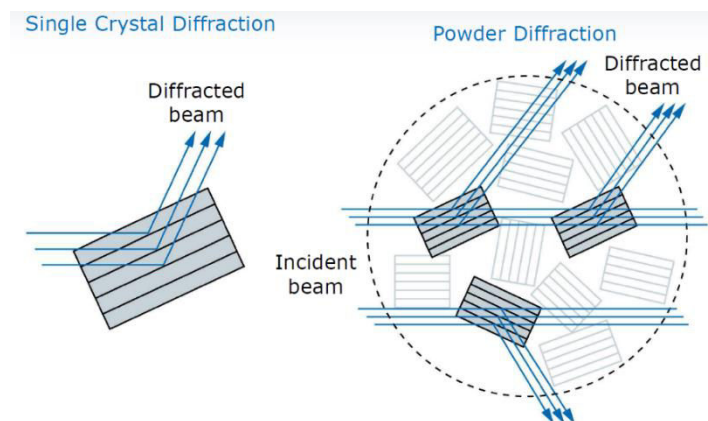


Figure 5.17. Difference between SCXRD (left) an PXRD (right)

On the one hand, SCXRD occurs when the crystal is oriented toward one direction. The obtained data is a three dimension well defined pattern (**Figure 5.18**, left.), and the information treatment is relatively straightforward but the sample is more difficult to obtain. On the other hand, PXRD occurs when several crystals are oriented toward various (random) directions. The resulted data is a mono dimensional pattern (**Figure**

5.18, right) and even though the sample obtaining is less difficult than for SCXRD, the data treatment is longer and less trivial.

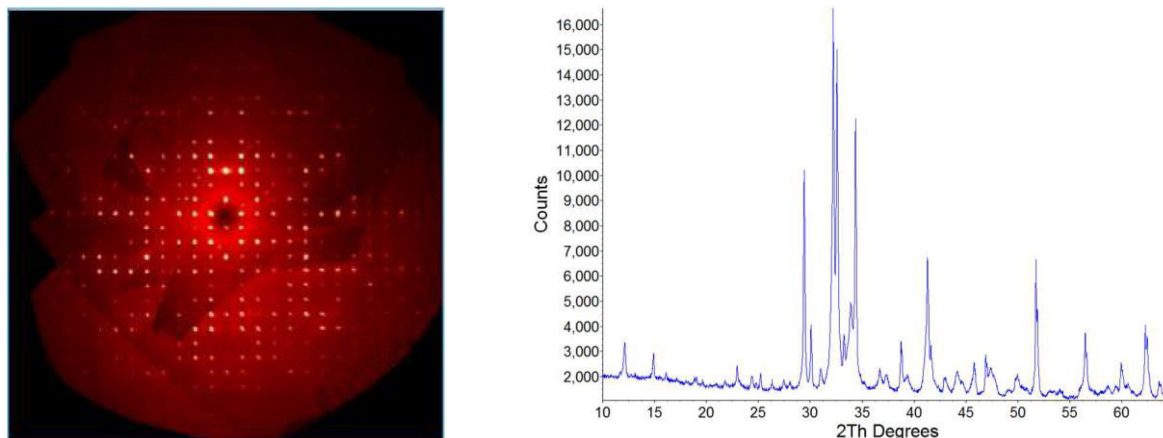


Figure 5.18. SCXRD (left) and PXRD (right) patterns

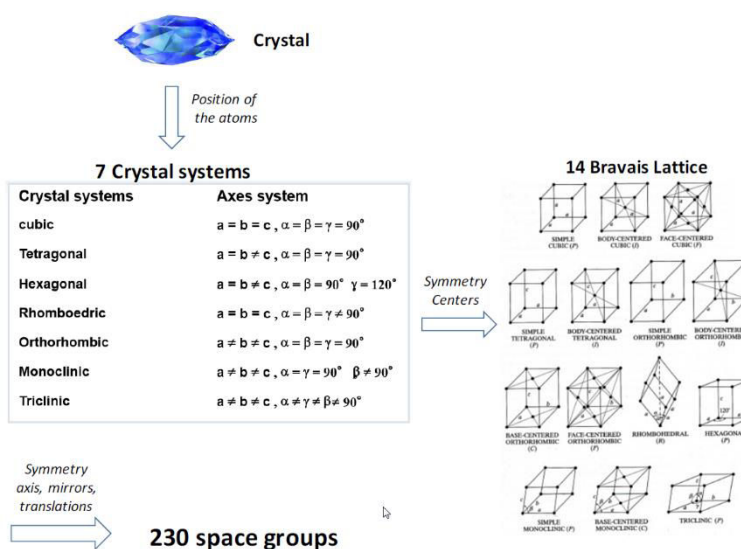


Figure 5.19. Illustration of the crystal systems and Bravais lattice

For SCRD, the inter lattice plan distance is directly given, while for PXRD, a calculation using the Bragg's Law is required. From this data, it is possible to know the crystal properties of the material, i.e the space group. In fact, 7 crystal systems exist in total: from the less "symmetric" one (triclinic, $a \neq b \neq c, \alpha \neq \beta \neq \gamma \neq 90^\circ$) to the more "symmetric" one (cubic, $a = b = c, \alpha = \beta = \gamma = 90^\circ$). From the different symmetry operations that can be involved (face centre, body centre, inversion centre, etc...), we can obtain the Bravais lattice, that are 14 in total. By combining this with additional operations such as the

mirror planes or the translations, we can determine the space group of a crystalline structure. In total, crystals can be formed in 230 different ways. In this chapter, we showed that molecules that are very similar can crystallize in completely different space groups. Furthermore, two materials completely different can crystallize in very similar ways. This explanation is illustrated in **Figure 5.19**.

The PXRD pattern is acquired according to a combination of two parts briefly explained as follow: from the unit cell of a given molecule is stated the position peak (diffraction angle). On the other hand, the containing of the unit cells gives the peaks intensity. These two parts combined together give the final diffractogram. The data process goes towards the opposite way: from the diffractogram, we could obtain the space group. In our research group, we use the state-of-the-art TOPAS software in order to treat PXRD patterns.

TOPAS is a powerful software for profile and structure analysis. The approach of such method requires first the indexing method, in which calculations give, according to measured pattern and a statistical distribution, the highest possibilities of space group and unit cell dimensions. From these values, we can simulate a PXRD pattern, and the closer it is from the actual measured one, the higher is the goodness of fitting. This is quantified by a value, the Rietveld weighted profile (R_{wp}). The lower the R_{wp} , the better the fitting. TOPAS also provides a database with well-known materials, mainly minerals, that can be used for instance for reproducibility tests. In case of a mixture of two different compounds, we can quantify either one crystal from another one, or one crystal from an amorphous structure. Finally, it gives us precious information about the crystallite size.

5.5. Experimental Section

5.5.1 Materials and methods

All the solvents and reagents were used as received from Aldrich, Fluka, TCI and VWR without any further purification. K_2PtCl_4 was purchased from Precious Metal Online (PMO). $PtCl_2(DMSO)_2$ was synthesized according to already reported procedures. All the synthesis and characterization of the ligands and the complexes are described below. Nuclear Magnetic Resonance (NMR) spectra were acquired on a Bruker Avance 400 spectrometer, the NMR chemical shifts were given in ppm. Electro-Spray ionization Mass Spectrometry (ESI-MS) analysis were performed on a Bruker Daltonics microTOF spectrometer (Bruker Daltonik GmbH, Bremen, Germany) equipped with an orthogonal

ESI interface. Calibration was performed using Tunning mix (Agilent Technologies). Sample solutions were introduced into the spectrometer source with a syringe pump (Harvard type 55 1111: Harvard Apparatus Inc., South Natick, MA, USA) with a flow rate of 5 $\mu\text{L}\cdot\text{min}^{-1}$.

5.5.2 Photophysical measurements

All solvents used for spectroscopic characterization were spectrometric grade and purchased by VWR. Absorption spectra were measured on a Shimadzu UV-3600 spectrophotometer double-beam UV–VIS–NIR spectrometer and baseline corrected. Steady-state emission spectra were recorded on a Horiba Jobin–Yvon IBH FL-322 Fluorolog 3 spectrometer equipped with a 450 W xenon arc lamp, double-grating excitation, and emission monochromators (2.1 nm mm^{-1} of dispersion; 1200 grooves mm^{-1}) and a TBX-04 single photon-counting detector. Emission and excitation spectra were corrected for source intensity (lamp and grating) and emission spectral response (detector and grating) by standard correction curves. Time-resolved measurements were performed using the time-correlated single-photon-counting (TCSPC) PicoHarp300 or the Multi Channel Scaling (MCS) electronics NanoHarp 250 of the PicoQuant FluoroTime 300 (PicoQuant GmbH, Germany), equipped with a PDL 820 laser pulse driver. A pulsed laser diode LDH-P-C-405 ($\lambda_{\text{exc}} = 405 \text{ nm}$) was used to excite the sample and mounted directly on the sample chamber at 90° . The photons were collected by a PMA-C-192 photomultiplier(PMT) single-photon-counting detector. The data were acquired by using the commercially available software EasyTau (PicoQuant GmbH, Germany), while data analysis was performed using the commercially available software FluoFit (PicoQuant GmbH, Germany).

PLQY measurements were performed by using an absolute photoluminescence quantum yield spectrometer Quantaaurus C11347 (Hamamatsu, Japan) exciting the sample at $\lambda_{\text{exc}} = 350$ and 400 nm . All solvents were spectrometric grade.

5.5.3 Scanning electron microscopy

SEM images were recorded with a FEI Quanta FEG 250 instrument (FEI corporate, Hillsboro, Oregon, USA) with an acceleration voltage of 20 kV. The sample is prepared by drop-casting solutions of complexes in H_2O or EtOH onto a glass cover slip, subsequently sputter coated with Au (Emitech K575X peltier cooled) for 20 s at 60 mA prior to fixation on an Al support.

5.5.4. Powder X-ray diffraction

PXRD data were acquired using a Bruker D2-PHASER diffractometer using CuK α radiation ($\lambda = 1.5418 \text{ \AA}$) at 300W (30kV, 10mA) power with Ni K β -filter and equipped by a 0.1mm divergence slit and 1mm air scatter screen. The samples were manually grounded in an agate mortar, then deposited on a zero background silicon sample holder. All the measurements were performed in the Bragg-Brentano geometry, with 2 θ values ranging from 5 to 40° with an exposure time of several seconds per step. All samples were measured at room temperature and room pressure. The crystal parameters were determined using Total Pattern Analysis Solution program (TOPAS) after refinement using the indexing method

5.5.5. Synthetic procedures

The pyridine-based ligands (1 eq), the tridentate ligand (1 eq) and the platinum precursor Pt[Cl₂(dmsO)₂] (1 eq) are mixed and dissolved in ethyleneglycol dimethylether. Diisopropyl ethyl amine (DIPEA) is then added (2.5 eq) and the reaction mixture is stirred for 24 hours at 110 °C. Water is added then to the crude and the products precipitate and are isolated after filtration. The products are obtained as yellow (**3a**), orange (**3b**, **3c**) and red (**3d**) powders.

3a: ¹H NMR (400 MHz, CDCl₃) δ : 9.57 (d, 2H), 8.02 (t, 1H), 7.79 (d, 2H), 7.73 (t, 3H), 7.66 (d, 1H), 7.27 (t, 1H). ¹³C NMR (100 MHz, CDCl₃) δ : 153.29, 148.86, 142.95, 142.30, 138.75, 130.45, 129.36, 128.15, 118.18, 118.13. ¹⁹F[¹H] NMR (375 MHz, CDCl₃) δ : -64.20. HR-ESI-MS (m/z): [M]⁺calculated: 703.0301; found: 704.0279.

3b: ¹H NMR (400 MHz, CDCl₃) δ : 9.65 (d, 2H), 8.11 (t, 1H), 7.92 (d, 2H), 7.76 (d, 2H), 7.67 (d, 1H), 7.24 (d, 1H), 7.19 (d, 1H), 6.81 (d, 1H), 2.88 (t, 2H), 1.75 (m, 2H), 1.34 (m, 10H), 0.94 (m, 3H). ¹³C NMR (100 MHz, CDCl₃) δ : 153.64, 153.44, 149.25, 143.5, 142.79, 136.82, 136.07, 135.87, 135.59, 134.97, 134.59, 133.39, 129.03, 125.27, 125.2, 124.58, 121.69, 121.2, 119.48, 118.18, 118.09, 31.78, 31.46, 29.64, 22.58. ¹⁹F[¹H] NMR (375 MHz, CDCl₃) δ : -64.23. HR-ESI-MS (m/z): [M]⁺calculated: 897.1430; found: 898.1472.

3c: ¹H NMR (400 MHz, CDCl₃) δ : 9.66 (d, 2H), 8.08 (t, 1H), 7.91 (d, 2H), 7.76 (d, 2H), 7.68 (d, 1H), 7.54 (s, 1H), 7.47 (m, 2H), 7.16 (d, 2H), 7.08 (t, 1H). ¹³C NMR (100 MHz, DMSO) δ : 182.08, 181.85, 153.55, 150.91, 143.04, 140.56, 138.27, 136.94, 128.89, 128.08, 126.68, 126.42, 126.31, 126.05, 125.56, 125.05, 122.19, 119.76, 118.88. ¹⁹F[¹H] NMR

(375 MHz, CDCl₃) δ : -64.24. HR-ESI-MS (m/z): [M]⁺calculated: 969.0101; found: 967.7304.

3d: ¹H NMR (400 MHz, CDCl₃) δ : 9.56 (d, 2H), 8.06 (t, 1H), 7.84 (d, 2H), 7.44 (d, 2H), 7.23 (d, 1H), 6.99 (dd, 1H), 6.86 (d, 1H), 3.33 (t, 2H), 3.20 (t, 2H). ¹³C NMR (100 MHz, CDCl₃) δ : 163.17, 154.69, 152.85, 142.84, 142.17, 141.24, 127.08, 126.50, 125.04, 124.26, 117.98, 37.15, 29.64. ¹⁹F[¹H] NMR (375 MHz, CDCl₃) δ : -64.29. HR-ESI-MS (m/z): [M]⁺calculated: 731.0614; found: 730.956.

5.6. References

1. Lee, O. P.; Yiu, A. T.; Beaujuge, P. M.; Woo, C. H.; Holcombe, T. W.; Millstone, J. E.; Douglas, J. D.; Chen, M. S.; Fréchet, J. M. J. *Adv. Mater.* **2011**, *23*, 5359.
2. Aytun, T.; Barreda, L.; Ruiz-Carretero, A.; Lehrman, J. A.; Stupp, S. I. *Chem. Mater.* **2015**, *27*, 1201.
3. Ruiz-Carretero, A.; Aytun, T.; Bruns, C. J.; Newcomb, C. J.; Tsai, W.-W.; Stupp, S. I. *J. Mater. Chem. A* **2013**, *1*, 11674.
4. Metrangolo, P.; Meyer, F.; Pilati, T.; Resnati, G.; Terraneo, G. *Angew. Chem. Int. Ed.* **2008**, *47*, 6114.
5. Alessandro, A.; Damiano, G.; Matteo, M.; Luisa, D. C. *Chem. Lett.* **2015**, *44*, 1152.
6. Mauro, M.; Aliprandi, A.; Cebrian, C.; Wang, D.; Kubel, C.; De Cola, L. *Chem. Commun.* **2014**, *50*, 7269.
7. Thomas, T. W.; Underhill, A. E. *Chem. Soc. Rev.* **1972**, *1*, 99.
8. Yeung, M. C.-L.; Yam, V. W.-W. *Chem. Sci.* **2013**, *4*, 2928.
9. Zhang, W.; Jin, W.; Fukushima, T.; Ishii, N.; Aida, T. *Angew. Chem. Int. Ed.* **2009**, *48*, 4747.
10. Chen, Y.; Li, K.; Lu, W.; Chui, S. S.-Y.; Ma, C.-W.; Che, C.-M. *Angew. Chem. Int. Ed.* **2009**, *48*, 9909.
11. Daniele, M. A.; North, S. H.; Naciri, J.; Howell, P. B.; Foulger, S. H.; Ligler, F. S.; Adams, A. A. *Adv. Funct. Mater.* **2013**, *23*, 698.
12. Strassert, C. A.; Chien, C.-H.; Galvez Lopez, M. D.; Kourkoulos, D.; Hertel, D.; Meerholz, K.; De Cola, L. *Angew. Chem. Int. Ed.* **2011**, *50*, 946.
13. Septiadi, D.; Aliprandi, A.; Mauro, M.; De Cola, L. *RSC Advances* **2014**, *4*, 25709.
14. Mauro, M.; Aliprandi, A.; Septiadi, D.; Kehr, N. S.; De Cola, L. *Chem. Soc. Rev.* **2014**, *43*, 4144.
15. Soldati, R.; Aliprandi, A.; Mauro, M.; De Cola, L.; Giacomini, D. *Eur. J. Org. Chem.* **2014**, *2014*, 7113.
16. Connick, W. B.; Marsh, R. E.; Schaefer, W. P.; Gray, H. B. *Inorg. Chem.* **1997**, *36*, 913.

17. Aliprandi, A.; Mauro, M.; De Cola, L. *Nat. Chem.* **2016**, *8*, 10.
18. Kozhevnikov, V. N.; Donnio, B.; Bruce, D. W. *Angew. Chem. Int. Ed.* **2008**, *47*, 6286.
19. Borré, E.; Stumbé, J.-F.; Bellemin-Laponnaz, S.; Mauro, M. *Angew. Chem. Int. Ed.* **2016**, *55*, 1313.
20. Allampally, N. K.; Bredol, M.; Strassert, C. A.; De Cola, L. *Chem. Eur. J.* **2014**, *20*, 16863.
21. Yuen, M.-Y.; Roy, V. A. L.; Lu, W.; Kui, S. C. F.; Tong, G. S. M.; So, M.-H.; Chui, S. S.-Y.; Muccini, M.; Ning, J. Q.; Xu, S. J.; Che, C.-M. *Angew. Chem. Int. Ed.* **2008**, *47*, 9895.
22. Che, C.-M.; Chow, C.-F.; Yuen, M.-Y.; Roy, V. A. L.; Lu, W.; Chen, Y.; Chui, S. S.-Y.; Zhu, N. *Chem. Sci.* **2011**, *2*, 216.
23. Huang, L.-M.; Tu, G.-M.; Chi, Y.; Hung, W.-Y.; Song, Y.-C.; Tseng, M.-R.; Chou, P.-T.; Lee, G.-H.; Wong, K.-T.; Cheng, S.-H.; Tsai, W.-S. *J. Mater. Chem. C* **2013**, *1*, 7582.
24. Kim, D.; Brédas, J.-L. *J. Am. Chem. Soc.* **2009**, *131*, 11371.
25. Ma, B.; Li, J.; Djurovich, P. I.; Yousufuddin, M.; Bau, R.; Thompson, M. E. *J. Am. Chem. Soc.* **2005**, *127*, 28.
26. El Garah, M.; Sinn, S.; Dianat, A.; Santana-Bonilla, A.; Gutierrez, R.; De Cola, L.; Cuniberti, G.; Ciesielski, A.; Samori, P. *Chem. Commun.* **2016**, *52*, 11163.
27. Tsai, W.-W.; Tevis, I. D.; Tayi, A. S.; Cui, H.; Stupp, S. I. *J. Phys. Chem. B* **2010**, *114*, 14778.
28. Coelho, A. *J. Appl. Crystallogr.* **2003**, *36*, 86.
29. Rietveld, H. *J. Appl. Crystallogr.* **1969**, *2*, 65.
30. Uribe-Romo, F. J.; Doonan, C. J.; Furukawa, H.; Oisaki, K.; Yaghi, O. M. *J. Am. Chem. Soc.* **2011**, *133*, 11478.
31. Dinnebier, R. E.; Ding, L.; Ma, K.; Neumann, M. A.; Tanpipat, N.; Leusen, F. J. J.; Stephens, P. W.; Wagner, M. *Organometallics* **2001**, *20*, 5642.

CHAPTER 6:

Tuning Luminescent Properties of Metal-Organic Framework by Metal Complex Inclusion

Abstract

In this chapter, we report the preparation of new emissive materials based on the inclusion of platinum(II) and iridium(III) complexes inside Al(OH)(bipyridinedicarboxylate) metal organic framework (MOF-253). The guest insertion is performed by a ligand substitution leading to the formation of a coordination bond, providing increased robustness to the system compared to guest inclusion by physical diffusion. The powder X-ray diffraction analysis highlights the high degree of crystallinity of the materials, with a complete change of the lattice parameters upon metal complex insertion. The photophysical properties of the resulting materials were thoroughly characterized. We further prove the quality of this synthetic approach by showing that the emission maxima of our materials can be tuned all across the visible range.

Keywords

MOF, metal complexes, luminescence, photophysical properties

6.1. Introduction

Metal Organic Frameworks (MOFs), also known as Porous Coordination Polymers (PCPs), are an emerging class of supramolecular coordination polymers where coordination bonds between one or several metal centres and an organic moiety called ligand or linker, create geometrically well-defined structures. This definition implies that these species are crystalline solids.¹ Up to now, several hundreds of MOFs have been reported.²⁻³ **Figure 6.1** presents the structure of two of them.⁴

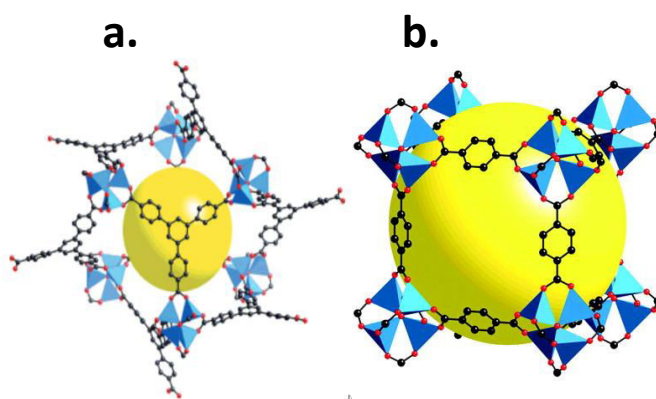
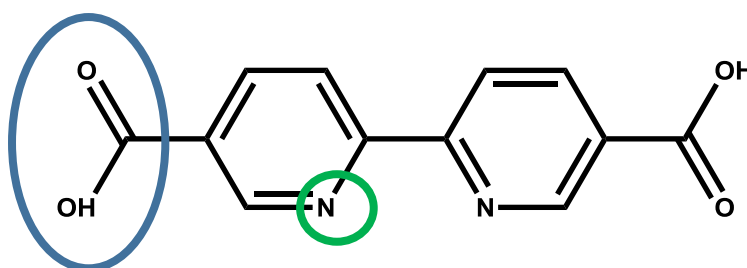


Figure 6.1. Structural representations of MOF-177 (a.) and MOF-5 (b.)

MOFs feature straightforward syntheses, nanoscale process ability, predictable structures and network geometry, possibility of post-synthetic modification, and in most cases a relatively tuneable porosity (with the exception of 0D and 1D MOFs). Due to these characteristics, such hybrid organic-inorganic materials are finding more and more applications in chemistry. They are widely studied in gas separation,⁵ gas storage,⁶⁻⁷ catalysis,⁸⁻⁹ and to a lesser extent in medicine¹⁰⁻¹³ and opto-electronics.¹⁴⁻¹⁵ Notwithstanding the availability of structural and chemical data on MOFs, their photophysical properties are rarely addressed. Indeed, only about 15% of the reported MOFs are described as luminescent, even though this figure has been increasing steadily in the last few years,¹⁶⁻¹⁷ and this mainly involves rare earth elements.¹⁸⁻¹⁹ Like their molecular counterparts, organometallic complexes, excited MOFs can relax through both fluorescence and phosphorescence. Moreover, the luminescence may result from ligand-centred transitions, ligand to metal charge transfers (LMCT) or metal to ligand charge transfer (MLCT) phenomena.¹⁴

As mentioned above, the porosity of MOFs implies the possibility of encapsulating guest molecule inside the pores themselves. However, for most of the systems, the insertion is only performed physically, by guest diffusion into the bulk structure. In 2013, Li *et al.* demonstrated the production of white light by incorporation of a yellow emissive iridium complex inside a blue emissive MOF.²⁰ Despite the efficiency of this material, the complex is not linked to the framework by a real chemical bond, but just diffused inside the host materials, like for inorganic porous materials such as zeolites,²¹ mesoporous silica nanoparticles²² or calcite.²³ Thus, the guest can get out from the host as easily as it entered. The latest approach to overcome this problem is the construction of porous coordination polymers, with a linker bearing several coordination sites. Figure 6.2 represents 2,2'-Bipyridine-5,5'-dicarboxylic acid (bpydc), a common organic linker used in MOF synthesis, including for MOF-253 used in this work (Figure 6.3).

Primary coordination site



Secondary coordination site

Figure 6.2. Representation of bpydc, showing primary and secondary coordination sites

Primary binding sites of the linker form the structure of the MOF itself, while the secondary binding sites could be used for further host-guest interactions. Those interactions depend on the nature of the binding site involved (hydrogen bonding,²⁴ electrostatic interaction, pi-pi stacking,²⁵ covalent bond,²⁶⁻²⁷ coordination bond, ...). The use of coordination bonds is particularly important for metal complexes insertion. This incorporation method, of metal complexes in **MOF-253**, is widely used for catalysis or gas uptake but so far has not been explored for luminescence purposes. Indeed, in the first report of **MOF-253**, Yaghi *et al.* investigated the insertion of PdCl_2 , and $\text{Cu}(\text{BF}_4)_2$ in order to demonstrate the selectivity factor for binding CO_2 over N_2 under typical flue gas conditions.²⁸ Further research involved metal insertion for catalysed reactions such as alcohol oxidations,²⁹ arylations³⁰ or couplings.³¹

Thanks to their luminescence properties, metal complexes of transition metals such as iridium (III) or platinum (II) are very good candidates for optoelectronics applications³². Indeed, they feature high stability, high emission quantum yields and long excited-states lifetimes.

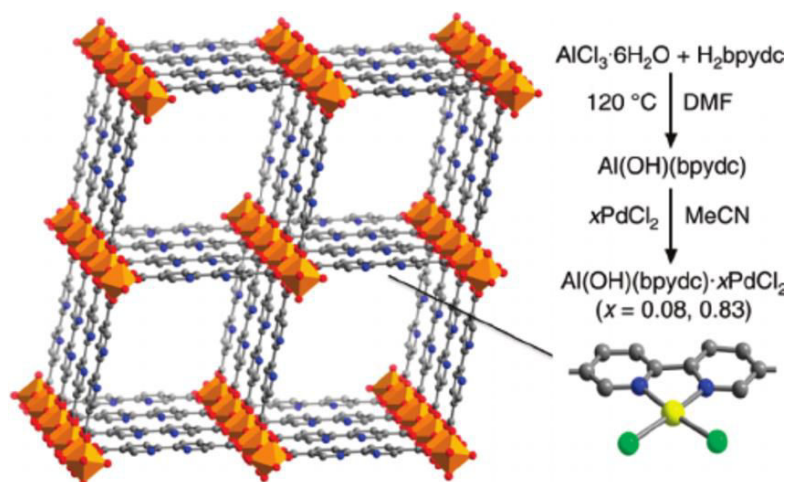
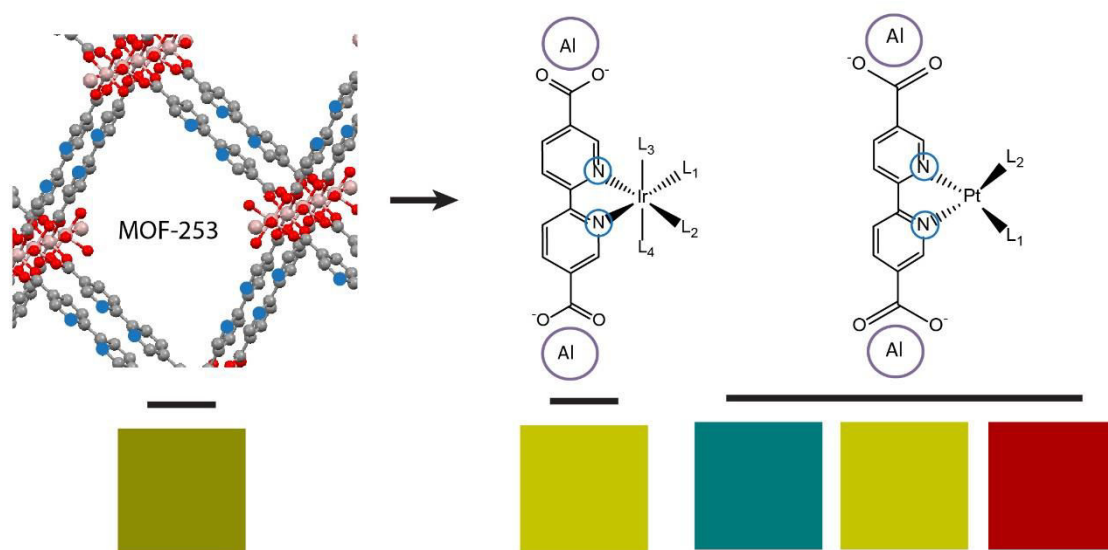


Figure 6.3. Structure and synthetic pathway of MOF253, the MOF used in this chapter

In the case of platinum complexes, due to their square planar geometry, there is a possibility of aggregation through metallophilic and pi-pi stacking interactions.³³ Therefore, they provide a tuneable emission behaviour according to the stacking and the investigation of Pt(II) complexes have taken more and more space in the luminescence field.³⁴

This work starts by reporting the synthesis and characterization of **MOF-253**. This material is then used to incorporate transition metal complexes (TMCs) by a robust coordination with the chelating ligand bpydc. The resulting MOF-metal complexes have been investigated and their photophysical behaviour is described.



Scheme 6.1. Schematic representation of Ir(III) complex and Pt(II) complex attached to **MOF-253**. The coloured squares represent the emission colour of each MOF-TMC hybrid material.

6.2. Results and Discussion

MOF-253 was synthesized according to previous literature.²⁸ The organic linker reacts with AlCl_3 , using DMF as a solvent in order to reach a high temperature. The further Soxhlet extraction in methanol allows the removal of DMF molecules in order to get a material with pores that are the completely empty. Thermogravimetric analysis (TGA, **Figure 6.4**) shows a single weight loss between 450°C to 550°C , accounting for 80% of the total starting mass, confirming the expected weight ratio between aluminum oxide and the **bpydc** ligand.

In order to assay the crystallinity of **MOF-253**, transmission electronic microscopy (TEM) and powder X-ray diffraction (PXRD) analysis have been performed. TEM images, shown in **Figure 6.5**, gives a first indication that we have a crystalline isostructural material, with a size in the micrometers range.

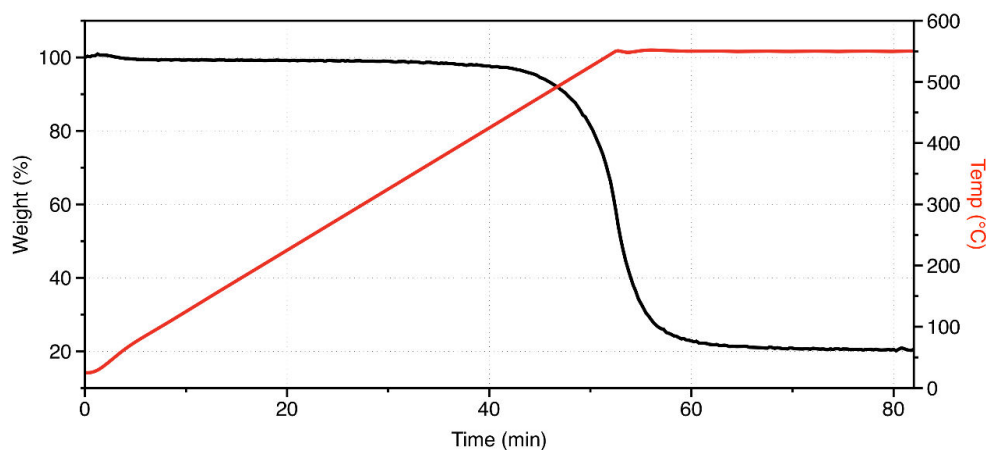


Figure 6.4. TGA profile of **MOF-253**

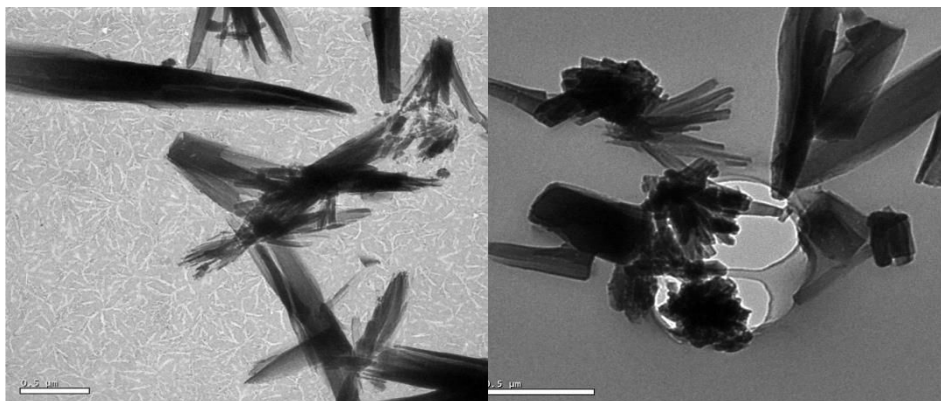


Figure 6.5. TEM pictures of **MOF-253**, scale bar is 500 nm

The PXRD pattern of **MOF-253** is very similar to the one reported by Yaghi *et al.* (**Figure 6.6**).²⁸ with an orthorhombic crystal phase and a *Imma*(74) space group.

The pore size of the **MOF-253** based on the nitrogen adsorption-desorption measurements is 1.2 nm (**Figure 6.7**). This value is close to the expected length of the linker (2,2'-Bipyridine-4-4'-dicarboxylate).

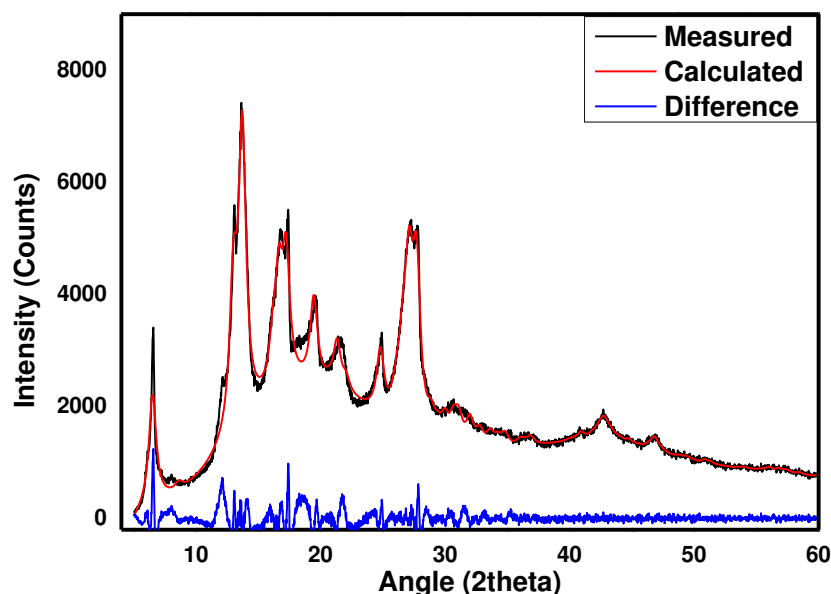


Figure 6.6. Powder XRD diffractogram of **MOF-253**. Black line: Measured diffractogram; Red line: Simulated diffractogram; Blue line: Difference between the measured and the simulated patterns.

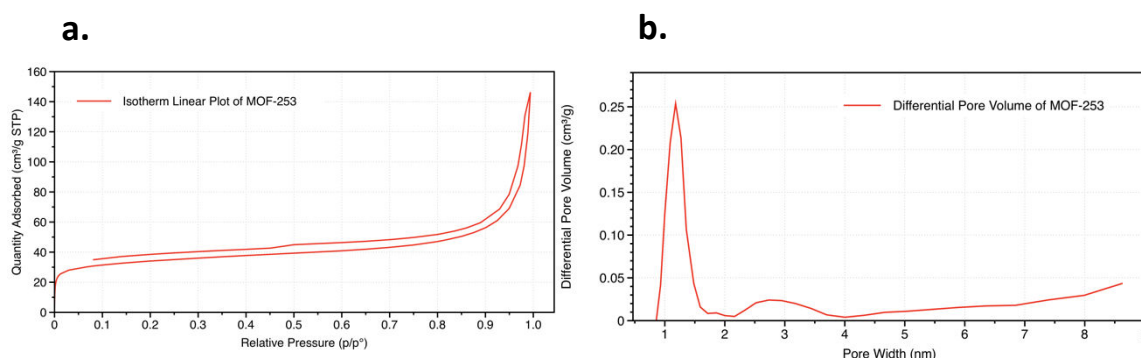


Figure 6.7. a. Isotherm curve of **MOF-253** **b.** Pore size distribution of **MOF-253** calculated by density functional theory

Bipyridine complexes of some transition metal complexes are known for their good stability and interesting luminescence properties. The 5,5' dicarboxylate bipyridine of the MOF possess two chelating sites: the carboxylate moiety engaged in the coordination with aluminium ion while the chelating bipyridine is available for coordinating different metal complex precursors by a ligand substitution between the chloride, of the metal complex precursor, and the 2,2'-bipyridine moieties, the latter belonging to the framework.

In order to study the effects of the coordination on the bipyridine linker on the structure and photophysical properties of **MOF-253**, a series of Pt(II) and Ir(III) complexes, were prepared and inserted in **MOF-253**. These two metals in particular were chosen due to their different geometry and oxidation number. Ir(III) has a d^6 electronic configuration displaying an octahedral geometry, while the d^8 electronic configuration of Pt(II) allows their relative complexes to have a square planar geometry. (**Figure 6.8.**). This phenomenon is stated by the ligand field theory.³⁵ The different complexes inserted inside **MOF-253** are shown in **Figure 6.9**.

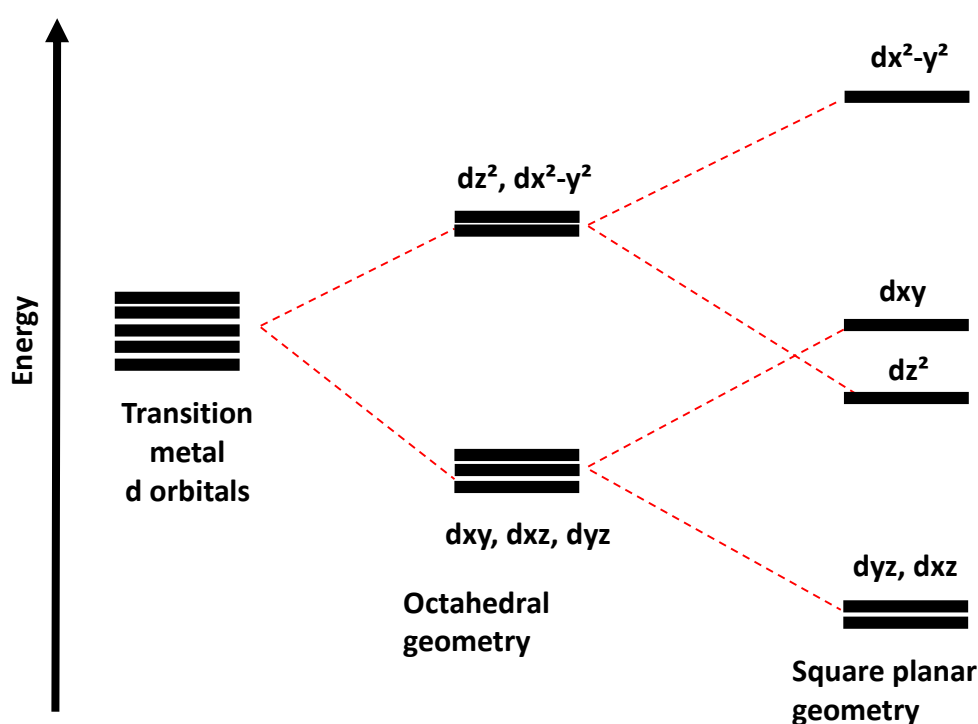


Figure 6.8. Representation of transition metals d orbitals splitting in octahedral and square planar geometries

To understand the size and charge effect of the guest complexes, we explored different iridium complexes possessing neutral or cyclometallated ligands. The influence of the ligands on the spectroscopic properties is of great importance since it determines the energy, i.e. the colour, of the emission upon coordination to the bipyridine. **Ir1**, bearing two bulky, strong sigma donor, monodentate ligands, triphenylphosphines, was chosen in order to evaluate the effect of the steric hindrance during the coordination of Ir(III) complex inside of the MOF pore. **Ir2** was selected to study the electron-

withdrawing effects of the fluorine groups, shifting the emission to higher energy. **Ir3** was used to compare its spectroscopic properties with its known metal complex analogue, $\text{Ir}(\text{ppy})_2(\text{bpy})^+$.^{20, 36} **Pt1** and **Pt3** are interesting to compare, since they have a 2,2-bipyridine and two triphenylphosphine moieties, respectively. Finally, **Pt2** was chosen in order to investigate the effect of oxygen between the platinum and the phosphine.

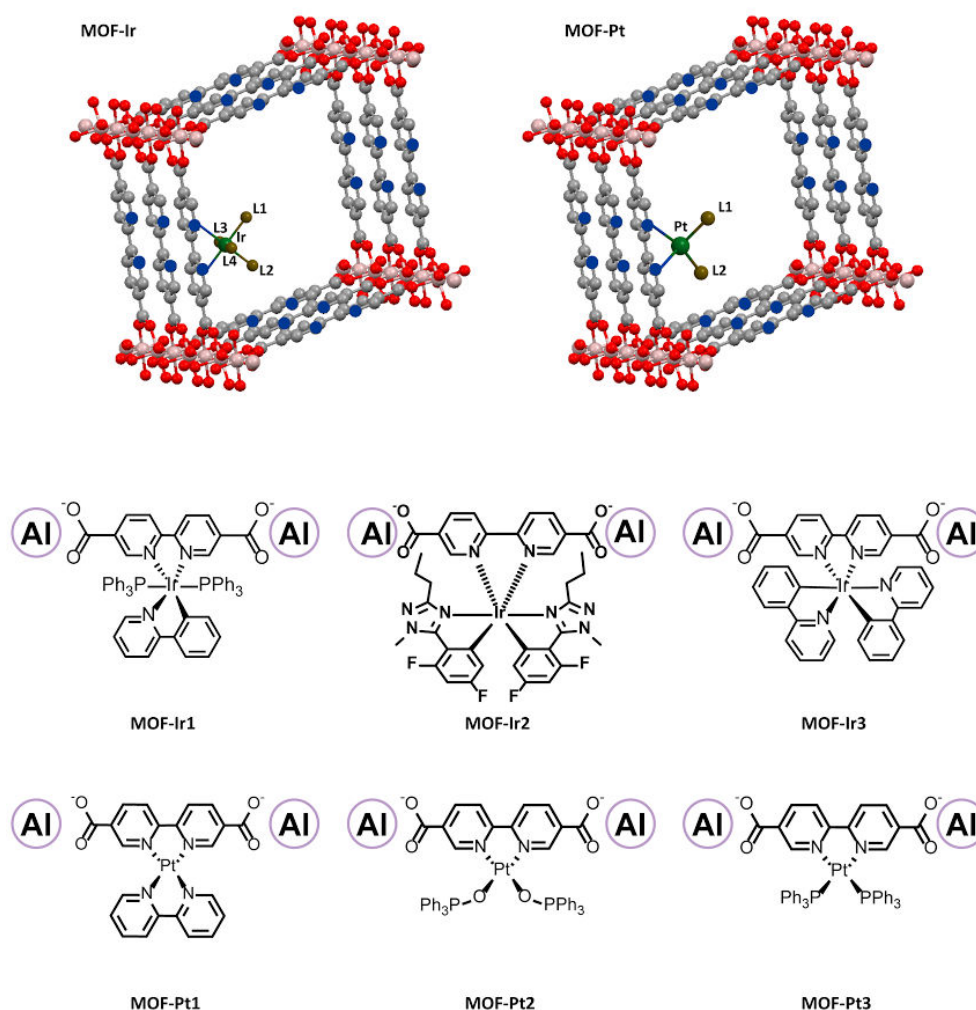


Figure 6.9. Structural schematic representation of the final MOF-TMC systems(top), studied MOF-TMCs systems (bottom)

The inclusion processes have been performed according to the following general reaction Scheme (**Figure 6.10**), all in the same way; in order to yield the final hybrid systems (**Figure 6.9**).

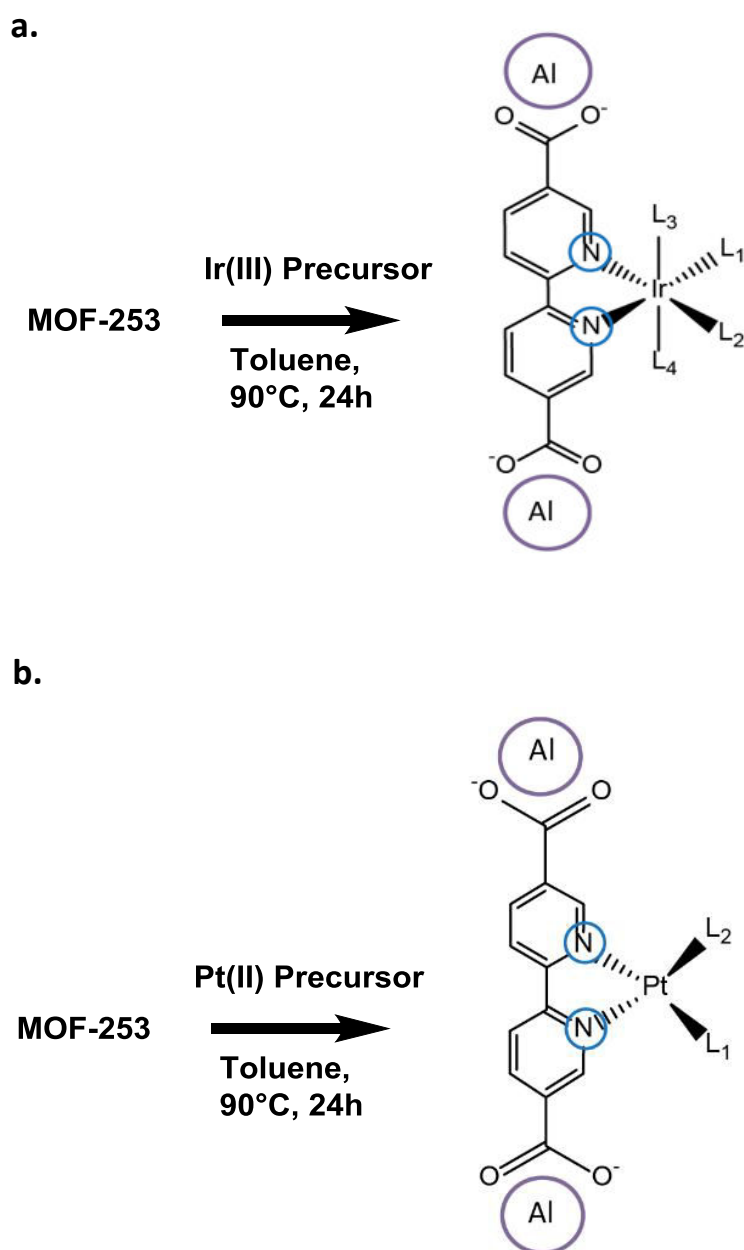
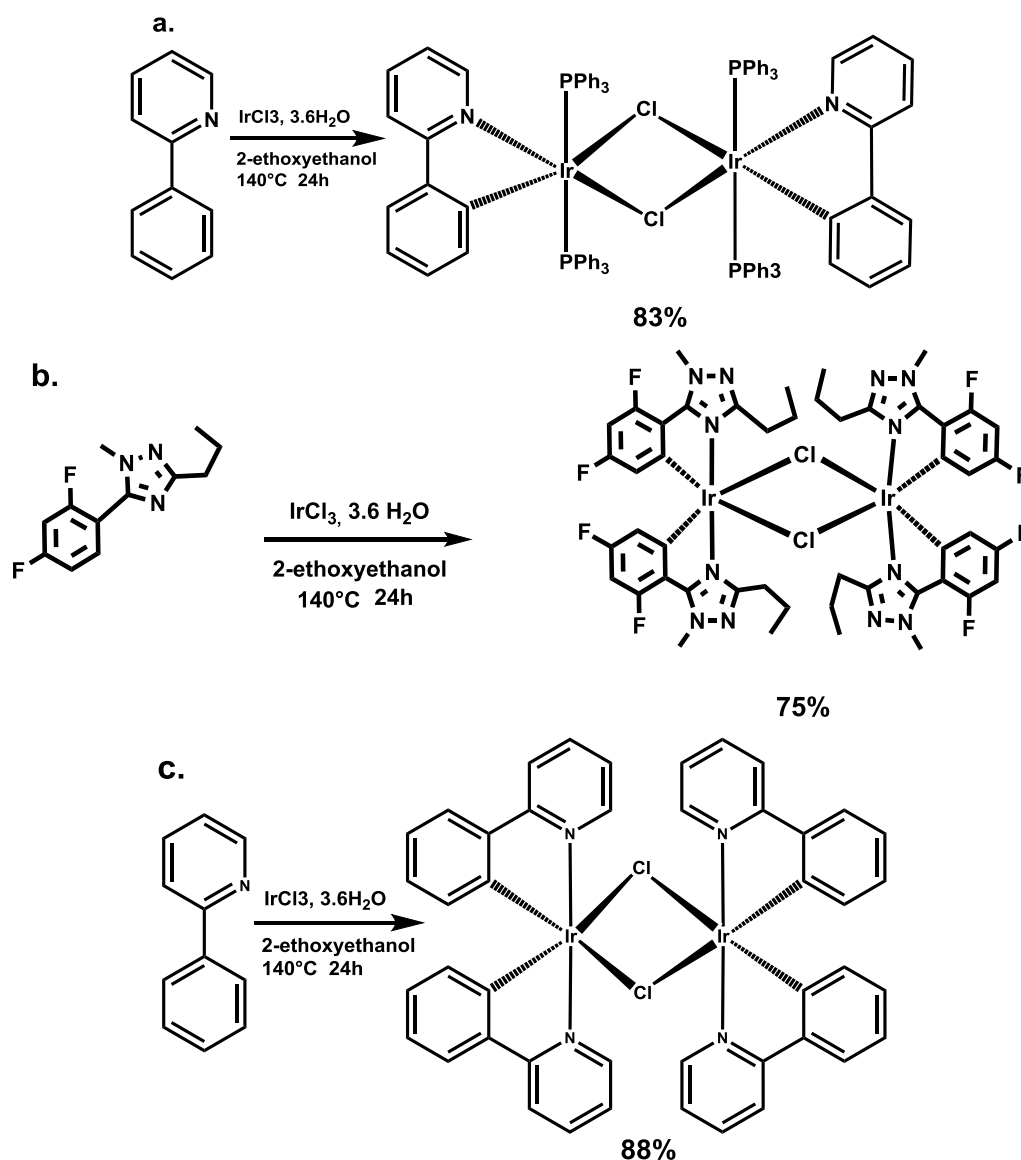


Figure 6.10. Schematic representation of Pt(II) complexes (**a.**) and Ir(III) complexes (**b.**) inclusion process in **MOF-253**

The platinum precursors being commercially available, only the iridium precursors were synthesized and yielded as dimers, as it is already well known in the literature.³⁷⁻³⁸ (**Scheme 6.2**). It is important to point out that in the first case, the trans position of the triphenylphosphines moieties are due to the strong trans effect of such ligands.

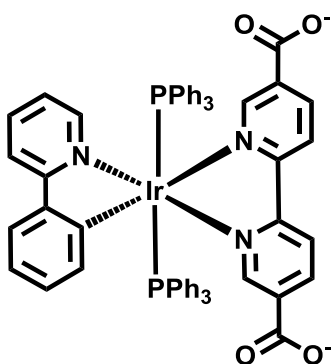


Scheme 6.2. Synthetic pathway for the synthesis of Ir precursors: **a.** Ir1; **b.** Ir2; **c.** Ir3

One of the problems related to the insertion of molecules inside MOFs is their quantification. We have therefore devoted much effort to establish if the TMC is inserted in the framework of the MOF, through coordination with the bipyridine, but also we have quantitatively evaluated the amount of free ligand and metal complex we have for each system. In order to achieve our goal, we have performed elemental analysis of the MOF-TMC systems and core nitrogen scan using XPS. The obtained elemental atomic ratios from the survey spectra are shown in **table 6.1**, chloride being the counter anion.

The elemental analysis from XPS shows that except for **MOF-Ir1**, all the samples contain both Al and the TMC guest, with a transition metal/Al ratio between 0.2 and

0.5 proving that the samples contain both the complex and the framework. The **Ir1** precursor is not inserted within **MOF-253**, while for the other iridium complexes we could obtain **MOF-Ir2** and **MOF-Ir3**. This is confirmed by the XPS data in which the survey does not show aluminum atom (**Table 6.1**). One reason for this observation could be due to the disassembly of the metal organic framework during the coordination process because of the steric hindrance between such ligands in an octahedral geometry, dictated by the bulky phosphines in the octahedral geometry of the complex, prevent the formation of the MOF. In this case, the isolated product is a crystalline iridium complex, having bpydc as ancillary ligand (**Scheme 6.3**). The ^1H and ^{31}P NMR spectra being displayed in **Figure 6.24** and **6.25** (Experimental section), respectively.



Scheme 6.4. Predicted structure of “**MOF-Ir1**”, after the disassembly of the system due to the bulkiness of the guest molecule.

Table 6.1. Elemental ratio obtained from XPS analysis.

Sample	C	N	O	Al	Pt	Ir	F	P	Cl
MOF-253	57.86	8.67	27.67	5.79					
MOF-Ir1	86.58	1.72	6.58	-		1.07		3.06	1.00
MOF-Ir2	59.36	10.39	18.74	3.75		0.87	6.18		0.71
MOF-Ir3	70.57	10.41	9.11	1.66		3.12			5.12
MOF-Pt1	69.57	4.90	18.09	2.63	1.23				3.58
MOF-Pt2	70.25	3.01	19.35	1.92	0.84			2.83	1.80
MOF-Pt3	67.91	5.97	19.13	3.70	0.75			0.71	1.84

The XPS core nitrogen high resolution the binding energy of coordinated and non-coordinated nitrogen in the linker are different. **Figure 6.12** shows respectively XPS N 1s high resolution spectra of **MOF-253** and **MOF-Ir(III)** systems; as well as of **MOF-253** and **MOF-Pt(II)** systems.

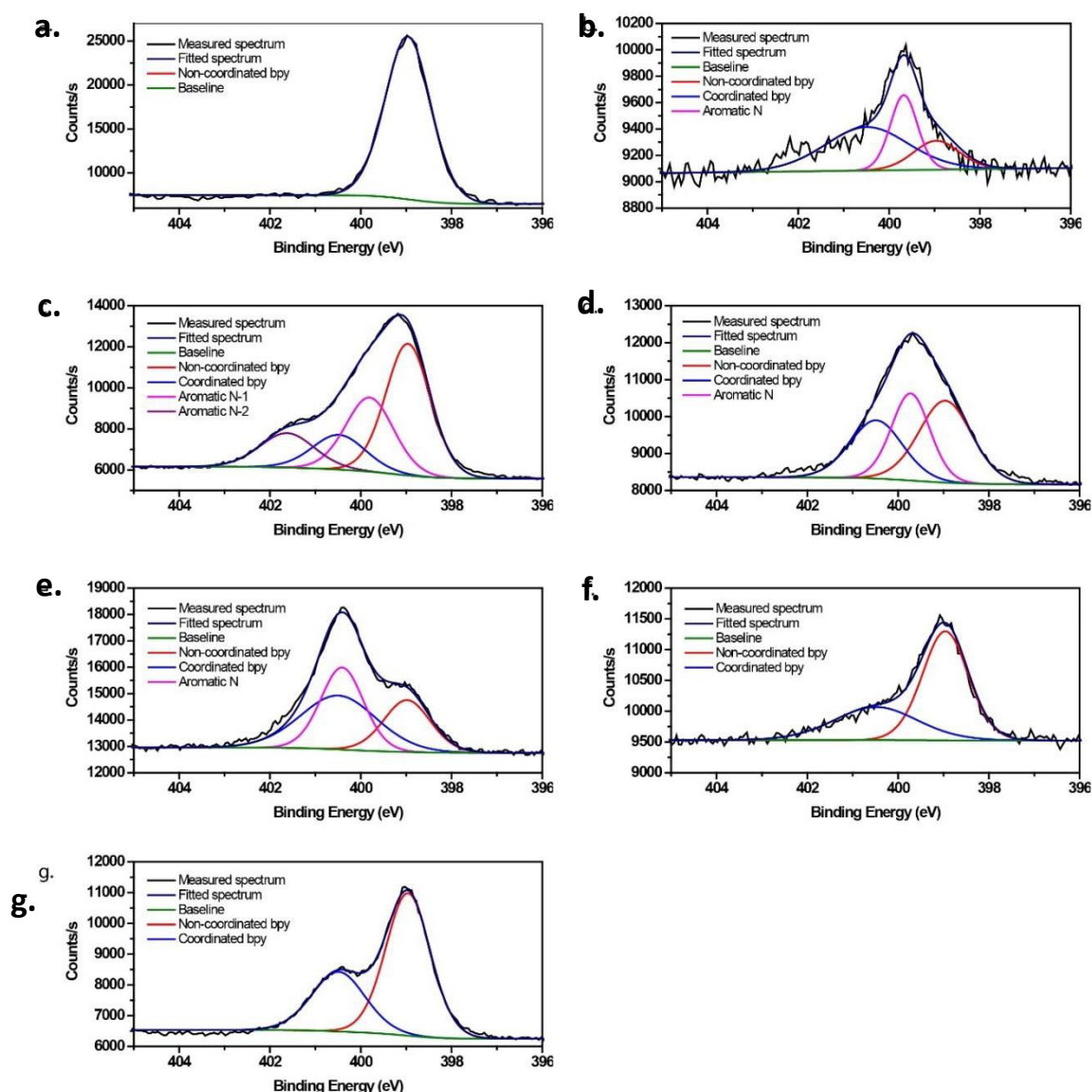


Figure 6.12. XPS N 1s high resolution spectra of MOF-253 (a.), “MOF-Ir1”(b.), MOF-Ir2(c.) and MOF-Ir3(d.)

As can be seen for **MOF-253**, we observe, as expected, a single peak for the bipyridine, with binding energy at 398.98 eV, which matches the reported energy value from literatures for the non-coordinated aromatic nitrogen.³⁹ The MOF-TMCs systems show a more complex band, that after deconvolution process, reveals additional signals at

higher binding energy due to the coordination of the 2,2'-bipyridine to the transition metal. From an accurate analysis, we can conclude that the amount of the transition metal complex successfully loaded in **MOF-253** through a coordinative bond with the structural bipyridine ligand as shown in **Figure 6.9**. This coordination bond is generated by ligand substitution mechanism as reported elsewhere.⁴⁰ Using a similar approach, the loading ratio of the transition metal was then calculated by the quantification of each peak, and the results are shown in **table 6.2**. For clarity, also the non-deconvoluted N1s spectra are shown in **Figure 6.13**. Regarding **MOF-Ir** systems and **MOF-Pt1**, the additional signals are for the free nitrogens on the ligands that are not involved on the insertion process (phenylpyridine, bipyridine, triazole).

Table 6.2. Loading ratio of TMC inserted in MOF-253 by coordination bond.

Material	Non-coordinated bipy (%)	Coordinated bipy (%)
MOF-Ir2	76.06	23.94
MOF-Ir3	58.39	41.61
MOF-Pt1	37.17	62.83
MOF-Pt2	64.46	35.54
MOF-Pt3	66.57	33.43

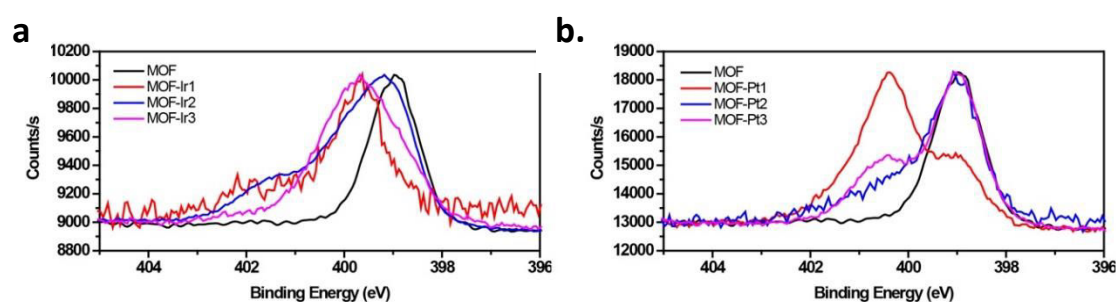


Figure 6.13. Non-deconvoluted N1s spectra of **MOF-253** and MOF-Ir systems (a.); and **MOF-253** and MOF-Pt systems (b.)

In regard to MOF-Ir systems and **MOF-Pt1**, since these complexes contain ligands with nitrogens (phenylpyridine, bipyridine, triazole), additional signals are observed and are indicated in the Figure as aromatic nitrogen. Such peaks are however important since they further confirm the presence of the metal complex coordinated in the MOF.

Interestingly, **MOF-Ir3**, features a stronger tendency towards coordination than **MOF-Ir2**, the substituents groups of the latter likely hinder a high coordination. Moreover, due to the bulkiness of the triphenylphosphines moieties, **MOF-Pt2** and **MOF-Pt3** indicate a less efficient coordination than their pendant **MOF-Pt1**, bearing a much less bulky 1,2-bpy moiety. We can therefore find a certain correlation between the bulkiness of the guest and the loading ratio, concluding that the formation of the coordination bond inside the frame is also dependent on the guest size.

The crystallinity of the materials has been demonstrated by TEM and PXRD. As an example, PXRD diffractogram of **MOF-Ir2** is shown in **Figure 6.14**. Indeed, they all show evidence of crystallinity, and after refinement and indexing using T^OTal Pattern Analysis Solution (TOPAS) program,⁴¹ we were able to determine the crystal phase, as well as the space group and the parameters of one unit cell (**Table 6.3**). Furthermore, the simulated PXRD pattern has been calculated from the lattice parameters and the very striking similarity between both measured and calculated diffractograms has to be mentioned, (**Figure 6.14**); with indeed relatively low Rietveld weighed profiles (R_{wp}) values.

Table 6.3. Crystal parameters of **MOF-253** and MOF-TMC systems

Sample	Crystal system	Space group	a	b	c	α	β	γ	Cryst al size	Rwp
MOF-253	Orthorombic	Imma (74)	20.659	6.953	18.252	90	90	90	13.0	6.25
MOF-Ir1	Orthorombic	P21212 (18)	47.416	8.564	5.100	90	90	90	26.7	21
MOF-Ir2	Monoclinic	P21/n (14)	42.136	15.0201	30.066	90	94.4	90	51.8	6.07
MOF-Ir3	Orthorombic	Ima2	26.664	22.846	23.902	90	90	90	46.5	36.9
MOF-Pt1	Orthorombic	Pbca (61)	15.227	14.789	25.303	90	90	90	64.6	13.96
MOF-Pt2	Monoclinic	P21/n (14)	11.140	31.348	15.619	90	92.8	90	102.7	19.82
MOF-Pt3	Monoclinic	P21/c (14)	18.687	10.086	32.136	90	93.5	90	39.8	11.38

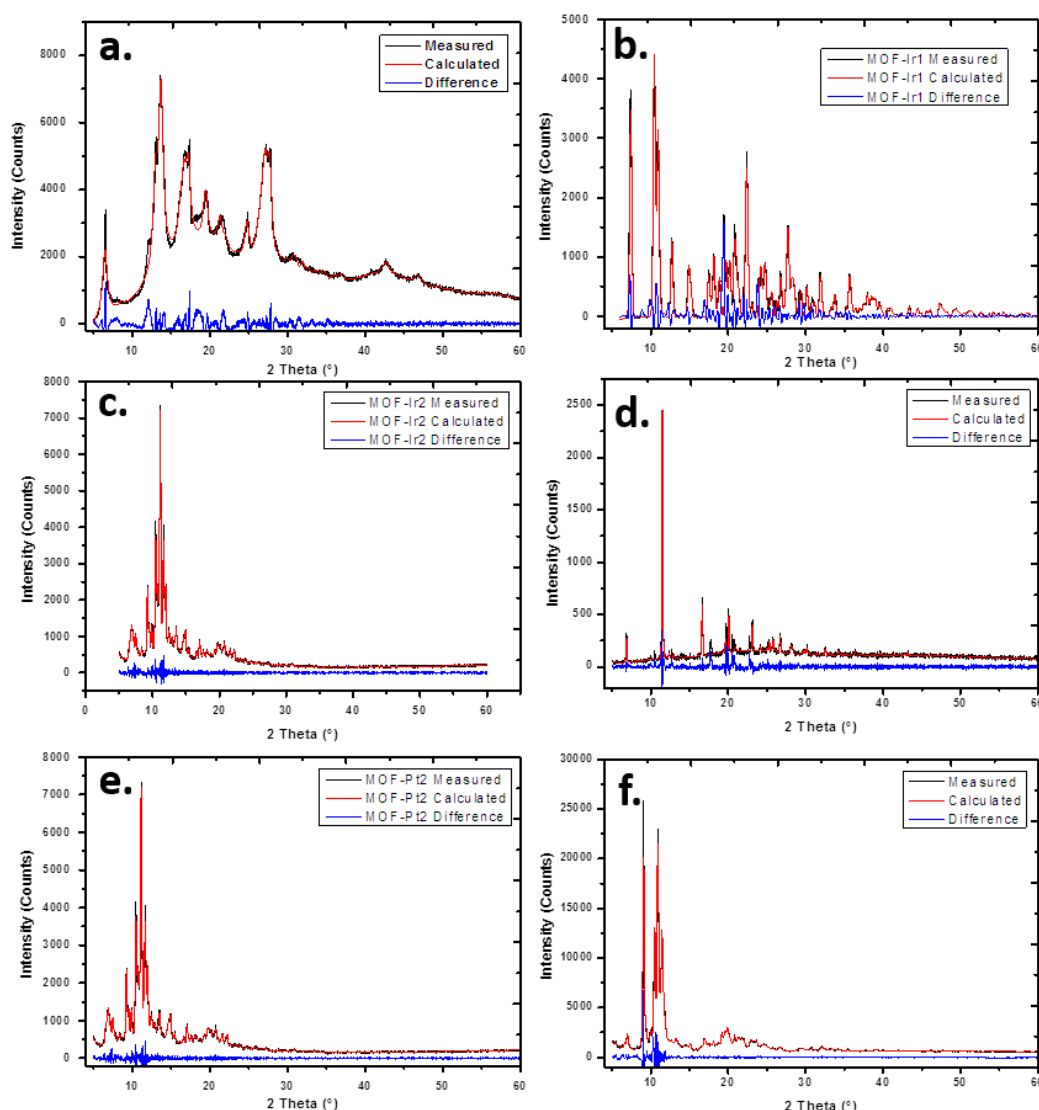


Figure 6.14. PXRD patterns of MOF-complexes systems : Measured: black trace, Calculated: red trace, Difference: blue trace

It is important to point out the fact that after encapsulation of the TMCs inside the cavity of the MOF, the crystal parameters are completely changed. Such phenomena has been, indeed, observed by other research groups.⁴²

TEM images of the MOF-TMCs systems is shown in **Figure 6.15**. This is another proof of the crystallinity of the materials, and it tells us that the crystal has a length in the micron scale. The absence of any crystal from TEM images for **MOF-Ir1**, confirms our hypothesis from XPS measurements, that is to say that there is a disassembly of the network due to a decoordination of the bpydc ligand from the aluminum moiety.

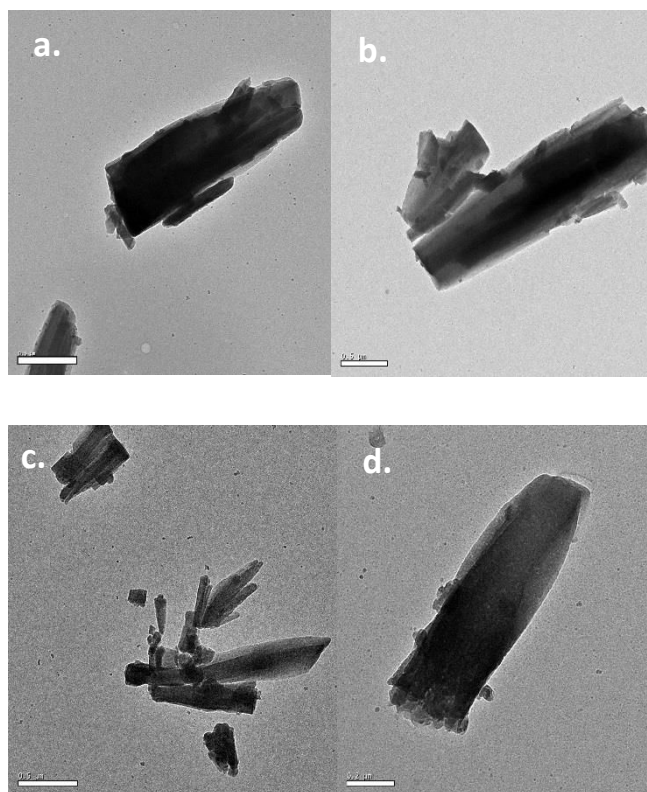


Figure 6.15. TEM pictures of: MOF-Ir2(a.), MOF-Ir3(b.), MOF-Pt1a(c.), MOF-Pt3(d.). **Scale bar: 500nm**

After proving the crystallinity of the materials and determining the crystal parameters of each MOF-TMC material, the photophysical properties of the materials were studied. **MOF-253** is a yellow emissive solid, with a photoluminescence quantum yield (PLQY) of 1% and a nanosecond scale excited state lifetime (ESLT). After post-synthetic modification, the emission colour of the final hybrid material is, in most cases, shifted. Emission and excitation spectra of **MOF-253** and MOF-TMC species are shown in **Figures 6.16** and **6.17**. Noticeably, the shift covers the full visible spectrum, going from the blue (470 nm) to the red (616 nm). The luminescence properties of MOF-TMC systems are summarized in **Table 6.4**.

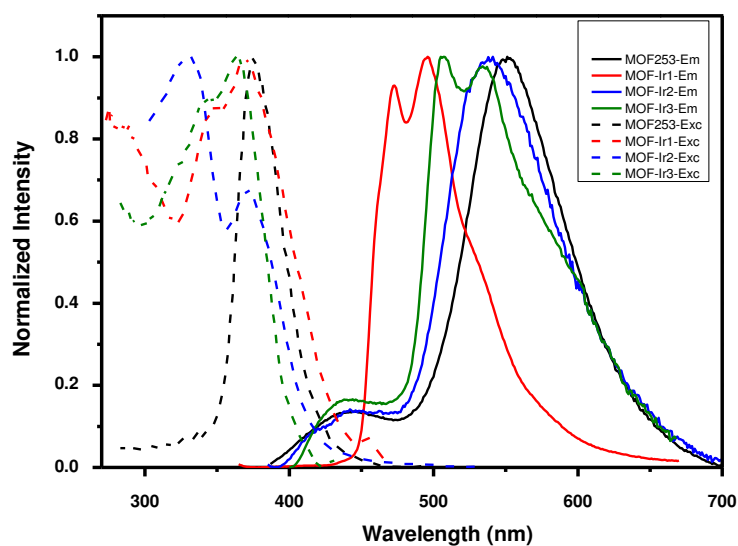


Figure 6.16. Excitation and Emission profiles of **MOF-253** and MOF-Ir systems

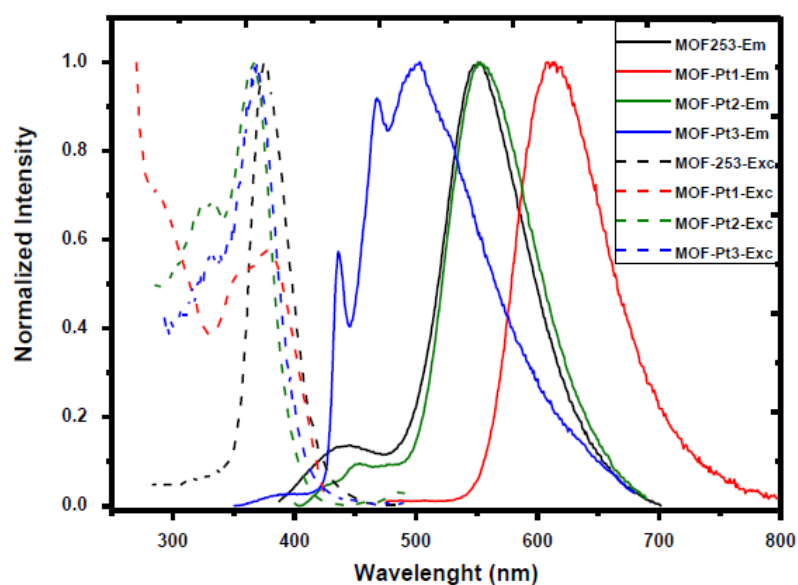


Figure 6.17. Excitation and Emission profiles of **MOF-253** and MOF-Pt systems

Table 6.4. Most important photophysical properties of the investigated materials.

Material	λ_{em} , nm	ϕ	τ , ns
MOF-253	555	1%	6 (87%) 3 (13%)
MOF-Ir1	497	3%	3087 (82.5%) 657 (17.5%)
MOF-Ir2	551	1%	227 (37%) 36 (22%) 3 (41%)
MOF-Ir3	504	1%	5367 (53%) 10 (32.5%) 3016 (14.5%)
MOF-Pt1	616	3%	225 (19.88%) 10 (24.32%) 82 (55.80%)
MOF-Pt2	543	5%	6 (24 %) 3 (76%)
MOF-Pt3	470	3%	388 (44%) 67 (56%)

Confocal microscopy experiments show the evidence of both crystallinity and emission of the materials (**Figure 6.18**).

MOF-253 possesses two emission bands, a lower energy more intense peak at 555 nm and a weak emission at 442 nm. The lowest energy emission is attributed to the Al complex⁴³ and it is a perturbed fluorescence of the coordinated carboxylate ligands. The blue emission is attributed to the fluorescence of the non-coordinated bipyridine and this assignment is corroborated by its disappearance in the MOF-Ir1. The complex displays two bands at 472 nm and 496 nm typical of this Ir(III) compound with excited state lifetimes in the microsecond regime, due to the triplet nature of the emissive excited state. **MOF-Ir2** shows a similar emission profile as the pristine MOF. However, we can exclude that the emission is due purely to the MOF since the excited state lifetime is typical of the iridium complex. The nature of such radiative transition is therefore mainly a triplet metal to ligand charge transfer, ³MLCT, involving the bpy ligand. MOF-Ir3 shows also a charge transfer emission the same emission as its counterpart Ir(ppy)₂(bpy)⁺ reported by other researchers,^{38, 44} with two bands at 504

nm and at 536 nm. The blue shift observed for this compound, which exhibit luminescent $^3\text{MLCT}$ transitions, can be attributed to the rigidochromic effect imposed by the immobilization of the complex in the MOF structure. Such an effect was already reported by Li et al.¹⁹ for a similar complex. The emission decays bi-exponentially in the microsecond range.

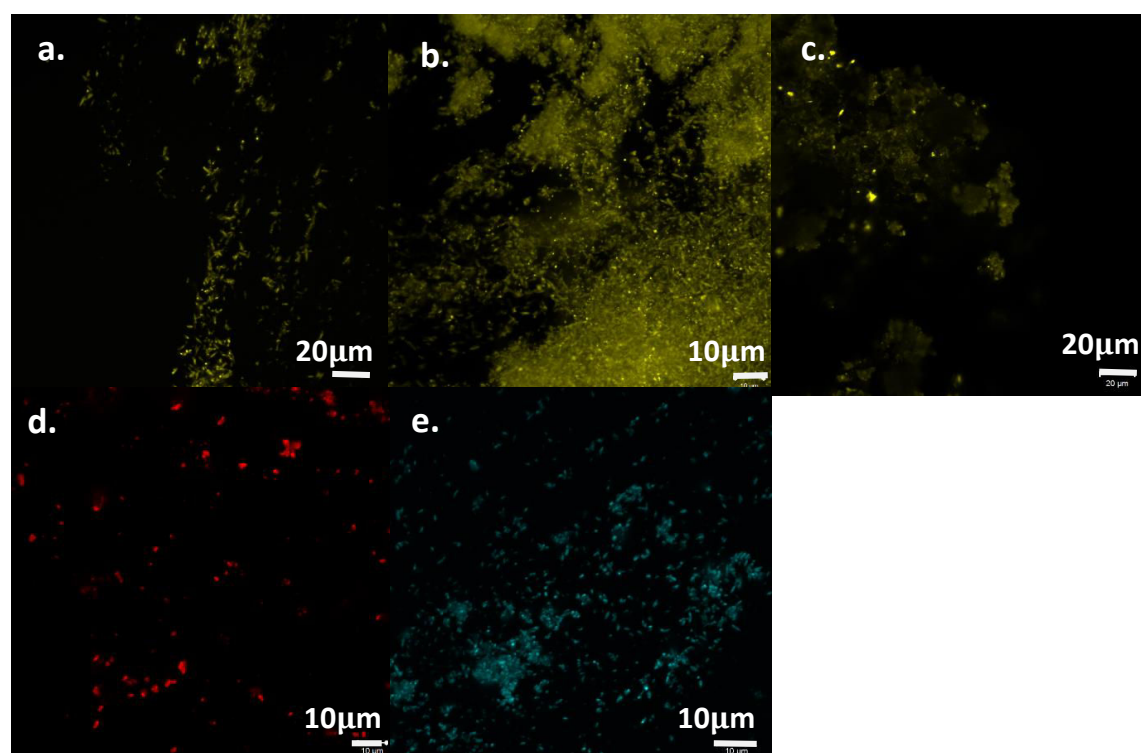


Figure 6.18. Confocal microscope images of **MOF-253** (a), **MOF-Ir2** (b), **MOF-Ir3** (c), **MOF-Pt1** (d), **MOF-Pt3** (e).

Upon insertion of the Pt(II) precursor we have a modulation of the emission that spans from blue to red. The **MOF-Pt1** showed a red luminescence ($\lambda_{\text{em}} = 616$ nm), and this emission is almost identical to the one of the complex **Pt1** not linked to the MOF (Pt(II)bis-2,2'-bipyridine dichloride) (Figure S13). We have attributed this emission to a $^3\text{MLCT}$ transition. **MOF-Pt2** displays the same emission profile and the same excited state lifetime as **MOF-253**. Indeed, the complex is a non-emissive species due to the presence of the oxygen on the phosphine (phosphine oxide). Therefore, the only emission that is recorded is the yellow emission of the free site of the MOF. Finally, **MOF-Pt3** display an emission higher in energy, showing three bands at 436, 467 and 503 nm. The long excited state lifetime can rule out a fluorescence of the MOF but the highly structured emission profile suggests a ligand centered nature of the emission.

6.3. Conclusion

We successfully introduced metal complexes in the MOF framework and were able to tune the luminescence of the MOF-TMC hybrid. The encapsulation was performed according to a smart design by a ligand substitution and the formation of coordinative bonds. The characterizations by X-ray photoelectron spectroscopy and powder X-ray diffraction prove the presence of the complex-type guest encapsulation inside the pores of the **MOF-253**. This work brings new interesting perspectives for encapsulated transition metal complexes in MOFs for different applications.

6.4. Experimental section

6.4.1. Materials and methods

All the chemicals were purchased from Sigma Aldrich, Tokyo Chemical Industry and Alfa Aesar and used without any further purification.

Nuclear magnetic resonance (NMR) spectra were recorded on a Brüker Avance DPX 400 MHz spectrometer.

X-ray Photoelectron Spectroscopic (XPS) measurements were carried out on a Thermo Scientific K-Alpha X-ray Photoelectron Spectrometer using monochromatic AlK α radiation ($h\nu = 1486.6$ eV). Survey measurements were performed with a 200 eV analyser pass energy and a 1 eV energy step size to calculate the atomic concentrations.

The Pore size of MOF-253 was determined by the density functional theory according to nitrogen adsorption-desorption measurements. The latter were performed on a Micromeritics ASAP 2020 surface area and porosity analyser at 77 K.

Thermogravimetric (TG) measurements were performed on a TGA instrument NETZSCH STA 449 F3 Jupiter. TGA scans were done with a heating rate of 10 °C /min from room temperature and hold at 550 °C for 30 min under a synthetic air purge gas flow of 20 mL/min

Powder X-ray diffraction (PXRD) data were acquired using a Bruker D2-PHASER diffractometer using CuK α radiation ($\lambda = 1.5418$ Å) at 300W (30kV, 10mA) power with Ni K β -filter and equipped by a 0.1mm divergence slit and 1mm air scatter screen. The samples were manually ground in an agate mortar, then deposited on a zero background silicon sample holder. All the measurements were performed in the Bragg-

Brentano geometry, with 2θ values ranging from 6 to 60° with an exposure time of several seconds per step. All samples were measured at room temperature and room pressure. The crystal parameters were determined using Total Pattern Analysis Solution program (TOPAS) after refinement using the indexing method.

Steady-state emission spectra were recorded on a HORIBA Jobin-Yvon IBH FL-322 Fluorolog 3 spectrometer equipped with a 450 W xenon arc lamp as the excitation source, double-grating excitation and emission monochromators (2.1 nm mm⁻¹ of dispersion; 1200 grooves mm⁻¹), and a TBX-04 single-photon-counting device as the detector. Emission and excitation spectra were corrected for source intensity (lamp and grating) and emission spectral response (detector and grating) by standard correction curves. Time-resolved measurements were performed using the multichannel scaling electronics (MCS) option on the Fluorolog 3, where a Horiba Jobin Yvon Nano LED source 375 nm used was used to excite the samples. The excitation sources were mounted directly on the sample chamber at 90° to a double-grating emission monochromator (2.1 nm mm⁻¹ of dispersion; 1200 grooves mm⁻¹) and collected by a TBX-04 single-photon-counting detector. Signals were collected using an IBH Data Station Hub photon-counting module, and data analysis was performed using the commercially available DAS6 software (HORIBA Jobin Yvon IBH). The quality of the fit was assessed by minimizing the reduced χ^2 function and by visual inspection of the weighted residuals.

Time-resolved measurements were performed using the TCSPC option (PicoHarp) of a FluoTime 300 “EasyTau” apparatus (PicoQuant) equipped with subnanosecond LDH sources (375, 405, 440, 510 and 640 nm, with 50–100 ps pulse-width) powered by a PicoQuant PDL 820 variable (0.2–80 MHz) pulsed power supply. For this work, only the 375 nm laser has been used to excite the samples. The laser was mounted directly on the sample chamber at 90° to a Czerny-Turner type emission monochromator (2.7 nm mm⁻¹ of dispersion; 1200 grooves mm⁻¹) and collected by a PMA-C192M single-photon-counting detector.

The luminescence decays were analysed by means of PicoQuant FluoFit Global Fluorescence Decay Analysis Software (PicoQuant GmbH, Germany).

Confocal imaging experiments were performed by a Zeiss 710 confocal microscope system with a 63x magnification objective lens (Zeiss GmbH). The samples were prepared as grains on a glass colourless plate and excited by continuous wave (cw) laser at 375 nm. In addition, the lambda-mode acquisition technique was performed

to observe the emission spectra of the different materials. False colours were adjusted for clarity reasons.

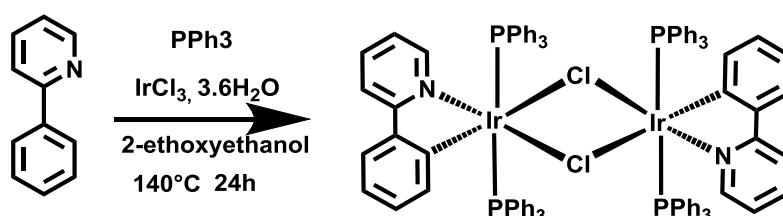
6.4.2. Synthesis of MOF-253

The synthesis of **MOF-253** has been done according to O. Yaghi et al.²⁸

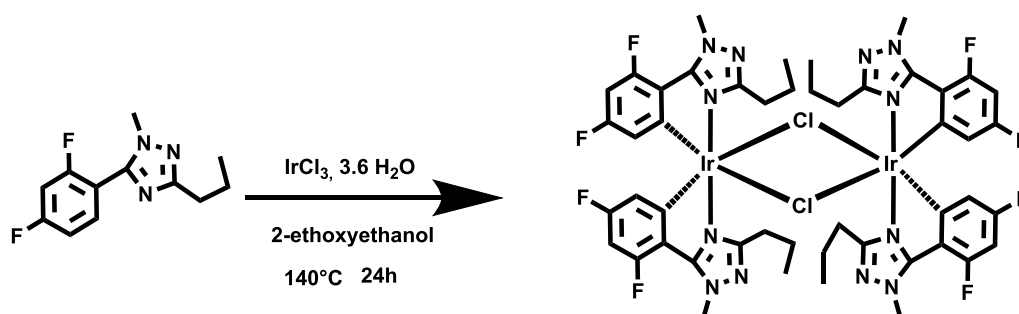
A solution of $\text{AlCl}_3 \cdot 6\text{H}_2\text{O}$ (302 mg, 1.25 mmol) and glacial acetic acid (1.7 mL, 30.0 mmol) in 20 mL *N,N'*-dimethylformamide was added to a Teflon-capped containing 2,2'-bipyridine-5,5'-dicarboxylic acid (306 mg, 1.25 mmol). The mixture was heated on a hot plate at 120 °C for 24 h. The resulting white crystalline powder was then filtered and washed with DMF and washed with methanol by a Soxhlet extraction for 24 h, after which the powder was collected by filtration and dried under vacuum on a Schlenk line for 24h to yield a white crystalline powder. The final material has been characterized by Thermogravimetric analysis, Powder x-ray diffraction, X-ray photoelectron spectroscopy, Nitrogen adsorption-desorption, Transmission electron microscopy.

6.4.3. Synthesis of Ir(III) precursors

All the platinum precursors have been purchased in Sigma-Aldrich and Alfa Aesar. The Iridium precursors have been synthesized according to previous reports.³⁷⁻³⁸



Iridium trichloride hydrate (181mg, 0.5 mmol, 1eq), 2-phenylpyridine (233 mg, 1.5mmol, 3eq) and triphenylphosphine (393 mg, 1.5mmol, 3eq) were added into a mixture of 2-ethoxyethanol and water (3:1) and the reaction media was reflux and stirred under nitrogen atmosphere for 12h and then cooled to room temperature. The obtained yellow precipitate was filtered and washed with water and ethanol several times and purified by column chromatography on silica gel with dichloromethane/ethyl acetate (5:1) as solvent to give a pale yellow solid. (0.35 mg, 0.37 mmol, 74%).



Iridium trichloride hydrate (0.3g, 0.82mmol, 1eq) and 5-difluorophenyl-1-methyl-3-propyl-1,2,4-triazole were added into a mixture of 2-ethoxyethanol and water (3:1) and the reaction was allowed to reflux and to stir under nitrogen atmosphere for 12h and the cooled to room temperature. The obtained slight yellow solid was filtered and washed with water and ethanol (0.89 g, 0.64 mmol, 78%).

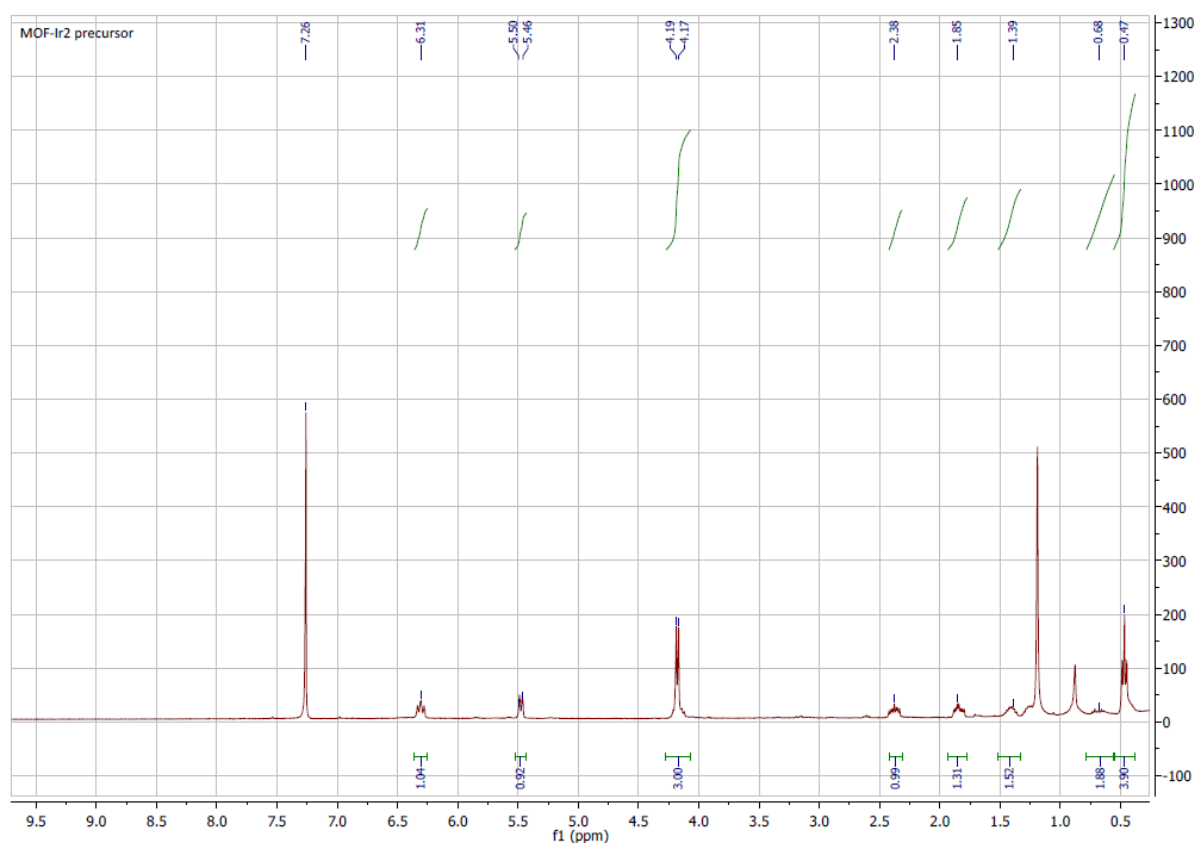


Figure 6.19. ¹H NMR spectrum of MOF-Ir2 precursor

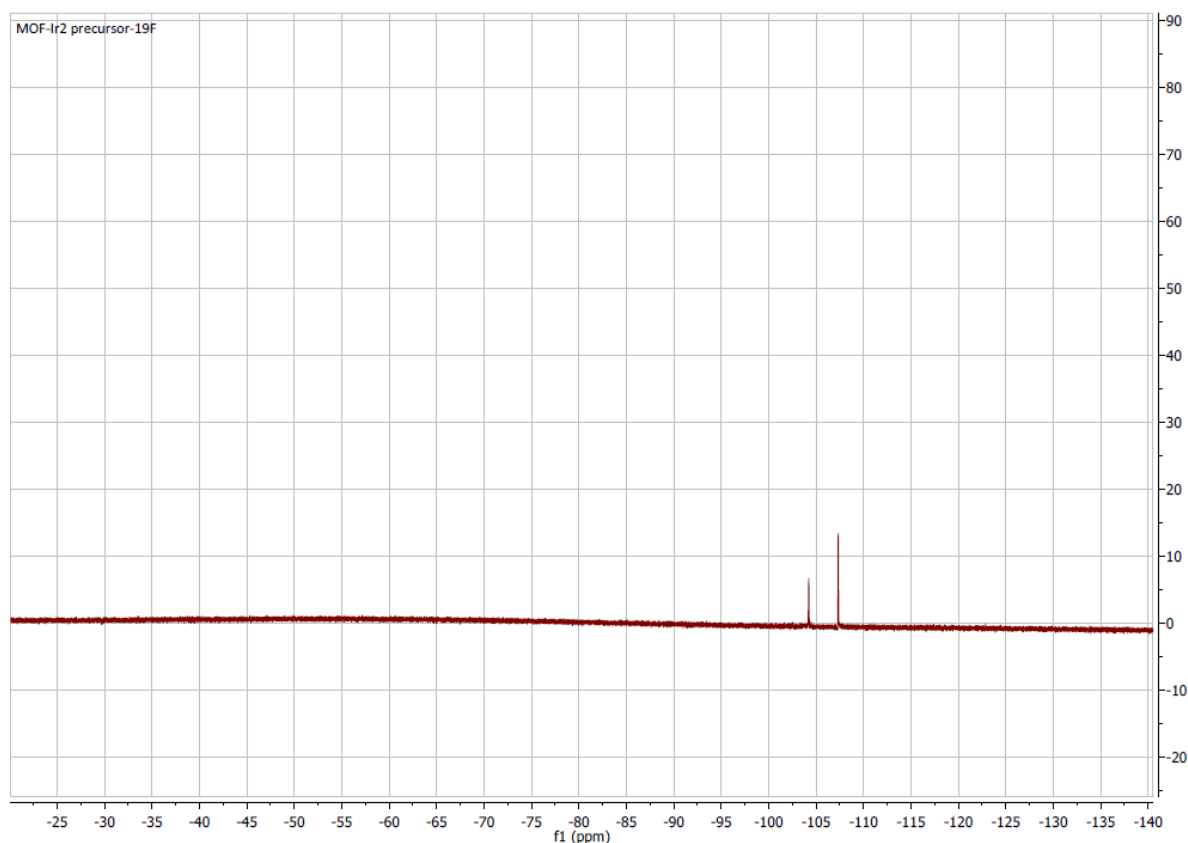


Figure 6.20. ^{19}F NMR spectrum of MOF-Ir2 precursor

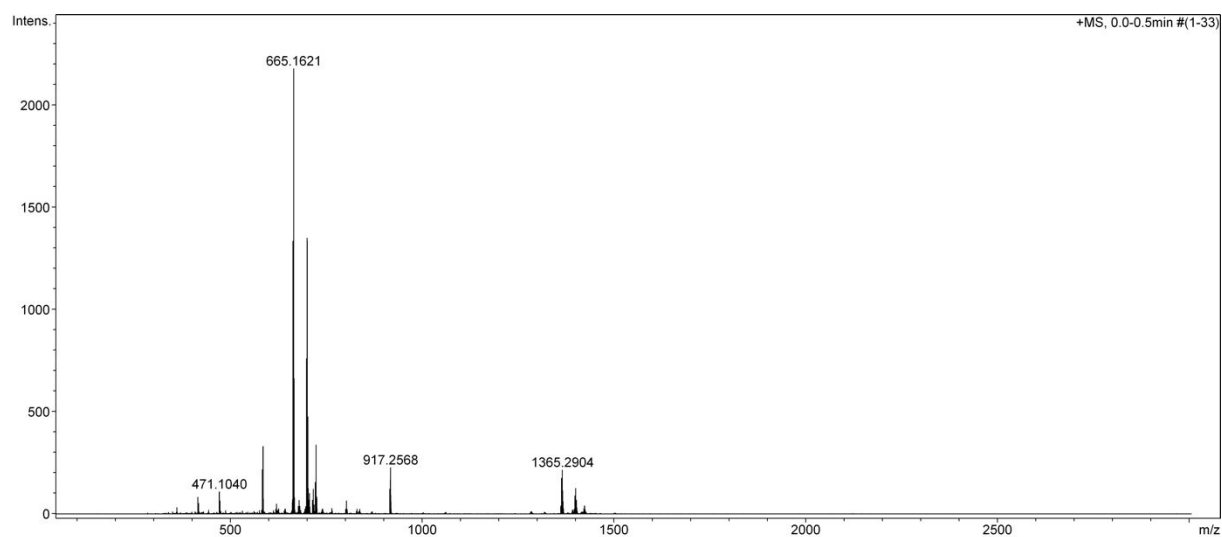
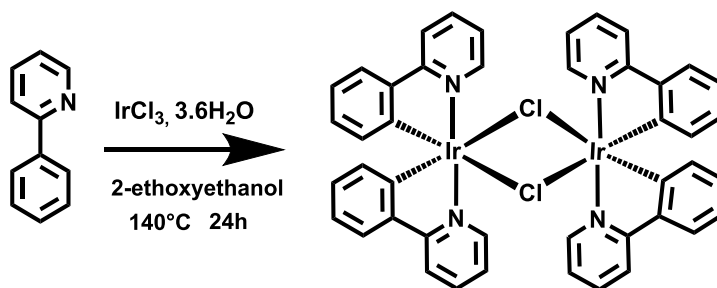


Figure 6.21. ESI-MS spectrum of MOF-Ir2 precursor



Iridium trichloride hydrate (0.5 g, 1.40 mmol) was combined with 2-phenylpyridine (0.8 mL, 5 mmol) in 40 mL of a mixture of 2-ethoxyethanol and water (3:1). And reflux for 24h. The solution was cooled to room temperature, and the yellow precipitate was collected on a glass filter frit. The precipitate was washed with water, ethanol and diethylether. The solid was dissolved in dichloromethane (50mL) and filtered, which was then concentrated under vacuum and cooled to give dark yellow crystals and dark yellow powder of $[\text{Ir}(\text{ppy})_2\text{Cl}]_2$, (1.18g, 1.1 mmol, 80%).

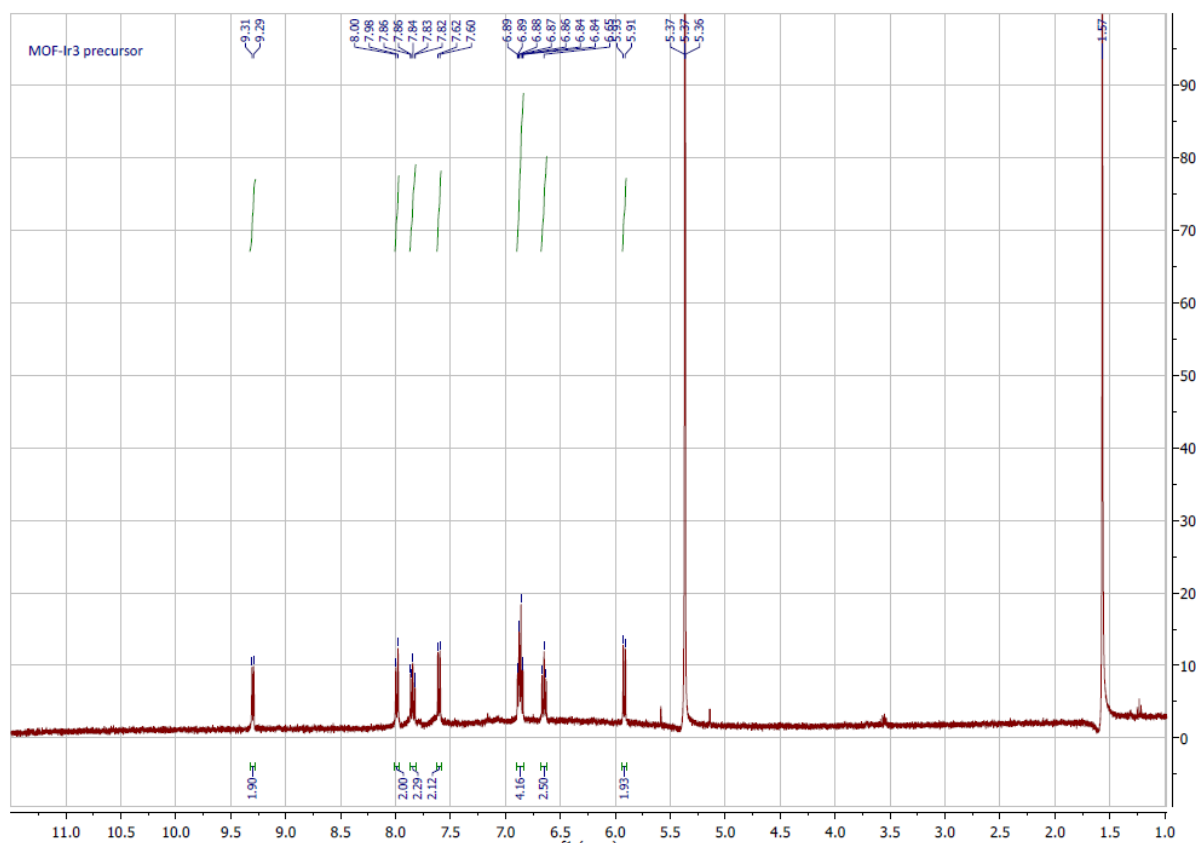
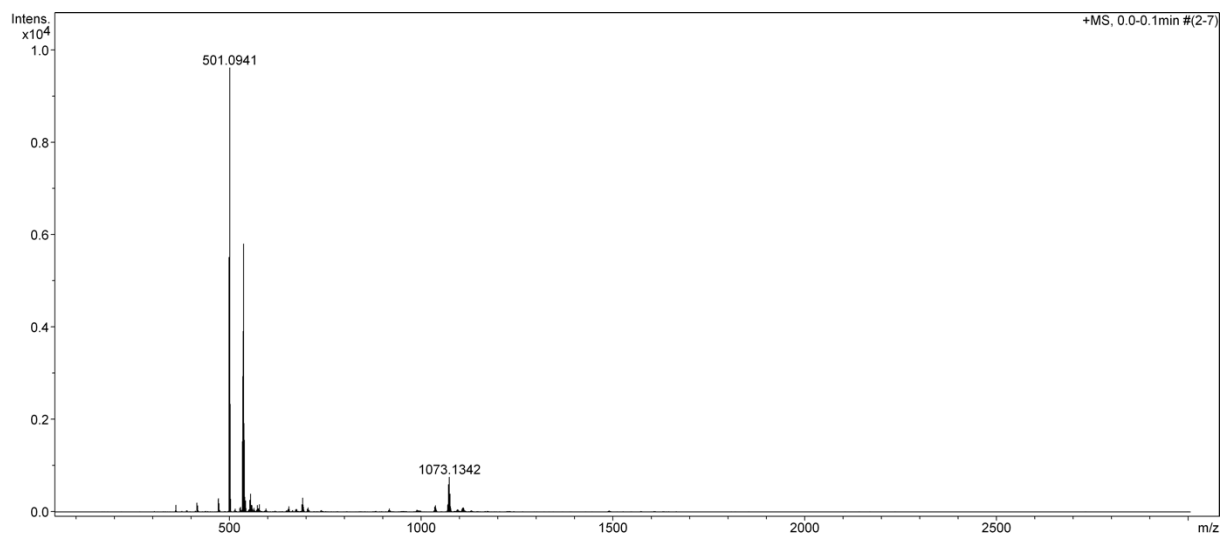
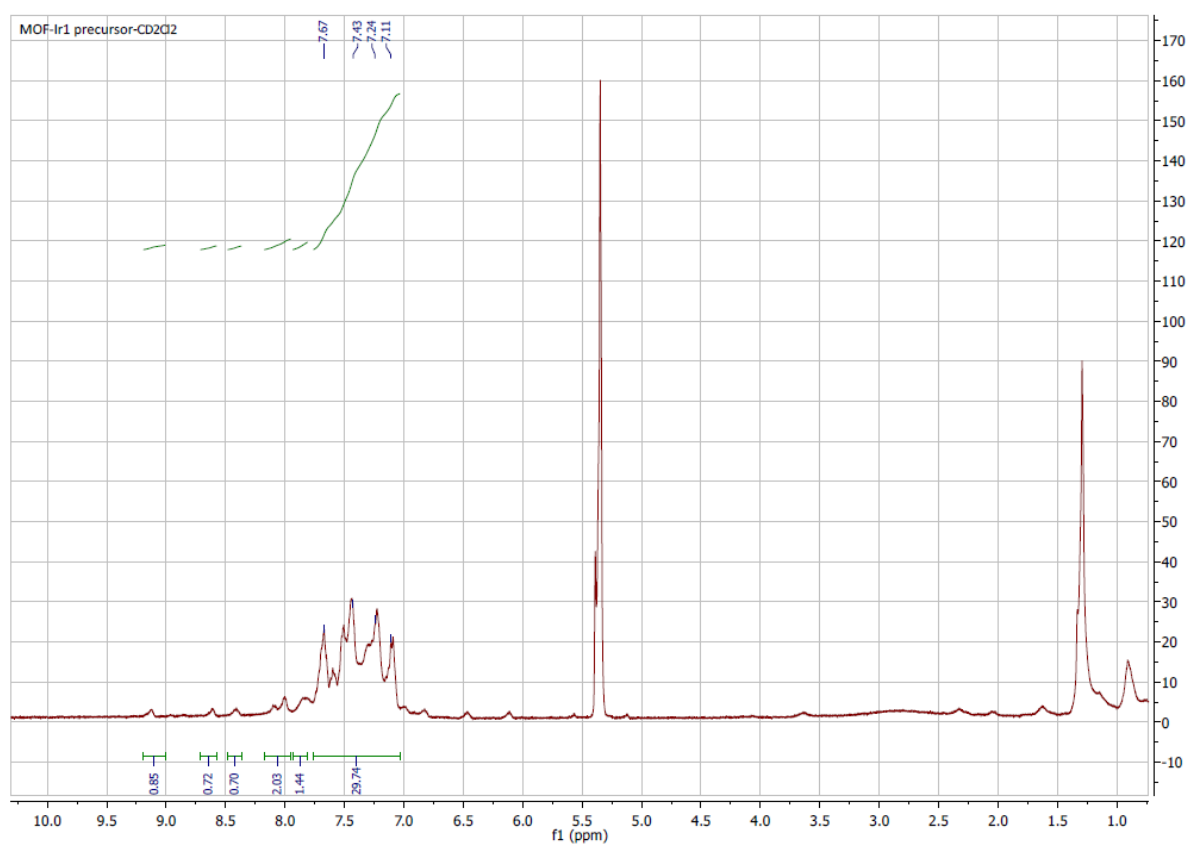


Figure 6.22. ^1H NMR spectrum of MOF-Ir3 precursor

**Figure 6.23.** ESI-MS spectrum of **MOF-Ir3** precursor**Figure 6.24.** ¹H NMR spectrum of Ir1(bpydc)

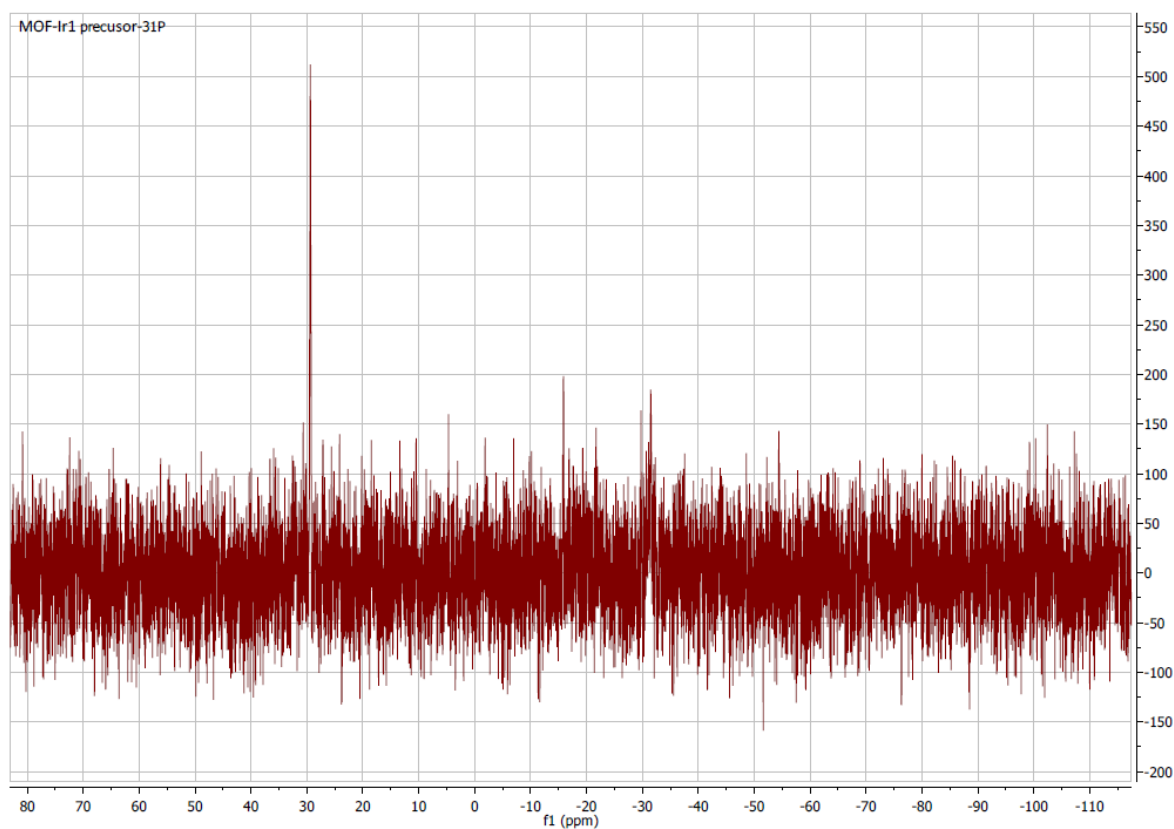


Figure 6.25. ^{31}P NMR spectrum of Ir1(bpydc)

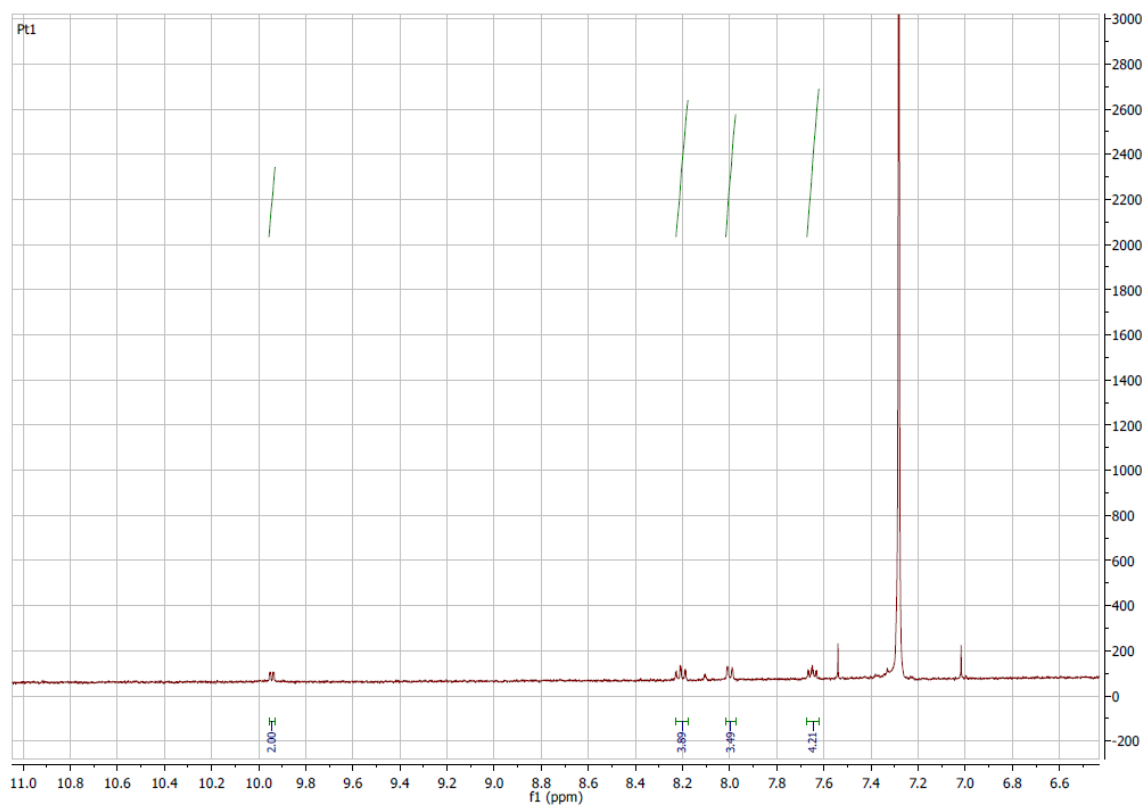


Figure 6.26. ^1H NMR spectrum of **Pt1** (Pt(II)bisbipyridine dichloride)

6.4.4. Procedure for metal inclusion inside MOF-253

To a dispersion of metal precursor (0.09625 mmol, 1.1 eq) in 10 mL of toluene was added **MOF-253** (25mg, 0.0875 mmol, 1eq). The mixture was stirred at 90°C for 24h, and cooled down at 0°C. The resulting precipitate was filtered under vacuum, washed twice with toluene and dried under vacuum.

6.5. References

1. Rowsell, J. L. C.; Yaghi, O. M., *Microporous Mesoporous Mater.* **2004**, 73 (1-2), 3.
2. Gangu, K. K.; Maddila, S.; Mukkamala, S. B.; Jonnalagadda, S. B., *Inorg. Chim. Acta* **2016**, 446, 61.
3. Zhou, H.-C.; Kitagawa, S., *Chem. Soc. Rev.* **2014**, 43, 4.
4. Rowsell, J. L. C.; Yaghi, O. M., *Angew. Chem. Int. Ed.* **2005**, 44 (30), 4670.
5. Mason, J. A.; Veenstra, M.; Long, J. R., *Chem. Sci.* **2014**, 5 (1), 32.
6. Li, Y.; Yang, R. T., *Langmuir* **2007**, 23 (26), 12937.
7. Zhao, Z.; Ma, X.; Kasik, A.; Li, Z.; Lin, Y. S., *Ind. Eng. Chem. Res.* **2012**, 52 (3), 1102.
8. Wang, C.; Wang, J. L.; Lin, W., *J. Am. Chem. Soc.* **2012**, 134 (48), 19895.
9. Sawano, T.; Ji, P.; McIsaac, A. R.; Lin, Z.; Abney, C. W.; Lin, W., *Chem. Sci.* **2015**, 6 (12), 7163.
10. Horcajada, P.; Chalati, T.; Serre, C.; Gillet, B.; Sebrie, C.; Baati, T.; Eubank, J. F.; Heurtaux, D.; Clayette, P.; Kreuz, C.; Chang, J.-S.; Hwang, Y. K.; Marsaud, V.; Bories, P.-N.; Cynober, L.; Gil, S.; Férey, G.; Couvreur, P.; Gref, R., *Nat. Mater.* **2010**, 9 (2), 172.
11. McKinlay, A. C.; Morris, R. E.; Horcajada, P.; Férey, G.; Gref, R.; Couvreur, P.; Serre, C., *Angew. Chem. Int. Ed.* **2010**, 49 (36), 6260.
12. Tsotsalas, M.; Liu, J.; Tettmann, B.; Grosjean, S.; Shahnas, A.; Wang, Z.; Azucena, C.; Addicoat, M.; Heine, T.; Lahann, J.; Overhage, J.; Bräse, S.; Gliemann, H.; Wöll, C., *J. Am. Chem. Soc.* **2014**, 136 (1), 8.
13. Rowe, M. D.; Thamm, D. H.; Kraft, S. L.; Boyes, S. G., *Biomacromolecules* **2009**, 10 (4), 983.
14. Allendorf, M. D.; Bauer, C. A.; Bhakta, R. K.; Houk, R. J. T., *Chem. Soc. Rev.* **2009**, 38 (5), 1330.
15. Allendorf, M. D.; Schwartzberg, A.; Stavila, V.; Talin, A. A., *Chem. Eur. J.* **2011**, 17 (41), 11372.
16. Wu, J.; Zhang, H.; Du, S., *J. Mater. Chem. C* **2016**, 4 (16), 3364.

17. Liu, J. J.; Shan, Y. B.; Fan, C. R.; Lin, M. J.; Huang, C. C.; Dai, W. X., *Inorg. Chem.* **2016**, 55 (7), 3680.
18. Serre, C.; Millange, F.; Thouvenot, C.; Gardant, N.; Pelle, F.; Ferey, G., *J. Mater. Chem.* **2004**, 14 (10), 1540.
19. Rao, X.; Huang, Q.; Yang, X.; Cui, Y.; Yang, Y.; Wu, C.; Chen, B.; Qian, G., *J. Mater. Chem.* **2012**, 22 (7), 3210.
20. Sun, C.-Y.; Wang, X.-L.; Zhang, X.; Qin, C.; Li, P.; Su, Z.-M.; Zhu, D.-X.; Shan, G.-G.; Shao, K.-Z.; Wu, H.; Li, J., *Nat. Commun.* **2013**, 4, 2717.
21. Lülff, H.; Bertucci, A.; Septiadi, D.; Corradini, R.; De Cola, L., *Chem. Eur. J.* **2014**, 20 (35), 10845.
22. de Barros e Silva Botelho, M.; Fernandez-Hernandez, J. M.; de Queiroz, T. B.; Eckert, H.; De Cola, L.; de Camargo, A. S. S., *J. Mater. Chem.* **2011**, 21 (24), 8829.
23. Kim, Y.-Y.; Carloni, J. D.; Demarchi, B.; Sparks, D.; Reid, D. G.; Kunitake, M. E.; Tang, C. C.; Duer, M. J.; Freeman, C. L.; Pokroy, B.; Penkman, K.; Harding, J. H.; Estroff, L. A.; Baker, S. P.; Meldrum, F. C., *Nat Mater* **2016**, 15 (8), 903.
24. Sadakiyo, M.; Yamada, T.; Kato, K.; Takata, M.; Kitagawa, H., *Chem. Sci.* **2016**, 7 (2), 1349.
25. Mukherjee, S.; Joarder, B.; Manna, B.; Desai, A. V.; Chaudhari, A. K.; Ghosh, S. K., *Sci. Rep.* **2014**, 4, 5761.
26. Zhenqiang Wang, S. M. C., *J. Am. Chem. Soc* **2007**, 129, 2.
27. Gadzikwa, T.; Farha, O. K.; Mulfort, K. L.; Hupp, J. T.; Nguyen, S. T., *Chem. Commun.* **2009**, (25), 3720.
28. Bloch, E. D.; Britt, D.; Lee, C.; Doonan, C. J.; Uribe-Romo, F. J.; Furukawa, H.; Long, J. R.; Yaghi, O. M., *J. Am. Chem. Soc.* **2010**, 132 (41), 14382.
29. Man Wang, B. Y., Tongmei Ma, Huanfeng Jiang Yingwei Li, *RSC Advances* **2012**, 2, 3.
30. Gao, J.; Song, Q.-W.; He, L.-N.; Yang, Z.-Z.; Dou, X.-Y., *Chem. Commun.* **2012**, 48 (14), 2024.
31. Carson, F.; Agrawal, S.; Gustafsson, M.; Bartoszewicz, A.; Moraga, F.; Zou, X.; Martin-Matute, B., *Chem. Eur. J.* **2012**, 18 (48), 15337.
32. Vezzu, D. A. K.; Deaton, J. C.; Jones, J. S.; Bartolotti, L.; Harris, C. F.; Marchetti, A. P.; Kondakova, M.; Pike, R. D.; Huo, S., *Inorg. Chem.* **2010**, 49 (11), 5107.
33. Miskowski, V. M.; Houlding, V. H., *Inorg. Chem.* **1989**, 28 (8), 1529.
34. Aliprandi, A.; Mauro, M.; De Cola, L., *Nat. Chem.* **2016**, 8 (1), 10.
35. Atkins, P., *Shriver and Atkins' inorganic chemistry*. Oxford University Press, USA: 2010.
36. Ladouceur, S.; Zysman-Colman, E., *Eur. J. Inorg. Chem.* **2013**, 2013 (17), 2985.
37. Eum, M.-S.; Chin, C. S.; Kim, S. y.; Kim, C.; Kang, S. K.; Hur, N. H.; Seo, J. H.; Kim, G. Y.; Kim, Y. K., *Inorg. Chem.* **2008**, 47 (14), 6289.

38. Garces, F. O.; King, K. A.; Watts, R. J., *Inorg. Chem.* **1988**, 27 (20), 3464.
39. Jansen, R. J. J.; van Bekkum, H., *Carbon* **1995**, 33 (8), 1021.
40. F. Basolo, J. C., H. B. Gray, R. G. Pearson and B. L. Shaw *J. Chem. Soc* **1961**, 9.
41. Coelho, A. A., *J. Appl. Cryst.* **2003**, 36, 10.
42. Raatikainen, K.; Rissanen, K., *Chem. Sci.* **2012**, 3 (4), 1235.

CHAPTER 7:

Instrumental Techniques

Abstract

In order to successfully complete all the studies, experimental chemistry requires a lot of physical characterization techniques. According to the yielded product (single molecule, self-assembly, nanomaterial,) and to the information one wants to get, the chosen analytic method, and thus the analytic instrument is different. Here we describe the different characterization principles, as well as the instruments used to perform these analytical experiments. It is worthwhile to mention that the XRD part is not described here, but rather in chapter 5.

7.1. Nuclear Magnetic Resonance (NMR)

NMR is without any doubt the most common and most widely used technique to characterize organic molecules, and to a lesser extent organometallic complexes.

Upon a magnetic field, a sample can absorb an electromagnetic radiation in the radiofrequencies range ($\lambda \approx 1\text{m}$). the absorption depends on the nuclei in the molecule.

Each nucleus has a spin, which describes the surrounding magnetic dipole charge (0, 1/2, 1, 3/2, etc...). Essentially, this spin makes the nuclei behaving as a magnet. In organic chemistry, the two most common nuclei are ^1H and ^{13}C . They both have a spin of 1/2, and we will only focus on this value of spin (**Figure 7.1**). Upon an external magnetic field, there are two energy levels called +1/2 (**1**) and -1/2 (**2**)

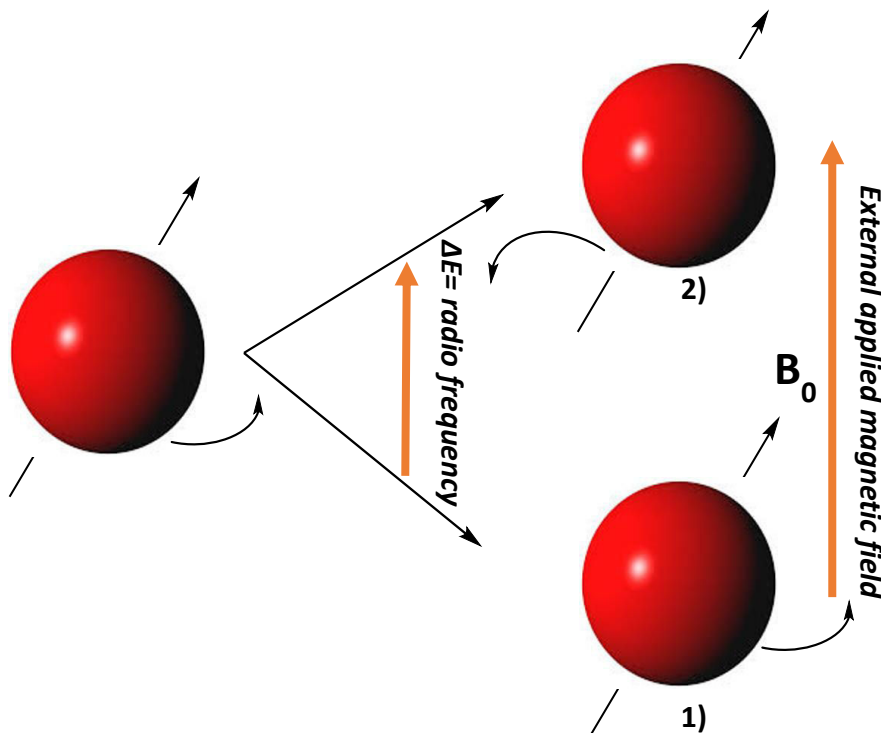


Figure 7.1. Schematic representation of two energy levels of proton in a magnetic field

The energy gap ΔE is given, according to Boltzmann distribution, by the following equation:

$$\Delta E = \left(\frac{h\gamma}{2\pi} \right) B_0 \quad (7.1)$$

Where h is the Planck's constant ($6.62607004 \cdot 10^{-34} \text{ m}^2 \cdot \text{kg} \cdot \text{s}^{-1}$) and γ is the gyromagnetic ratio, which can be defined as the ratio of its magnetic momentum in an atom to its angular momentum (for ^1H nucleus, $\gamma = 267.513 \text{ rad} \cdot \text{s}^{-1} \cdot \text{T}^{-1}$).¹ From this equation we show that ΔE is proportional to the magnetic field B_0 .

Once established this principle, it is possible to provide energy as radiofrequency radiation ν , in order to get a transition between 1) and 2) in a magnetic field. Indeed, $\Delta E = h\nu$ and therefore:

$$\nu = \left(\frac{\gamma}{2\pi} \right) B_0 \quad (7.2)$$

Where ν is given in MHz. For the proton, if $B_0 = 2.35 \text{ T}$, $\nu = 100 \text{ MHz}$. The energy is absorbed by the nucleus, the latter is hence brought to the highest energy state and the spectrum is recorded. This phenomenon is called *resonance*.

We can distinguish two kind of spectrometers: the continuous wave (CW) and the Fourier transform (FT). In the CW spectrometer, The spectrometer scans through a range of frequencies. The sample is measured with one frequency at a time. As the frequency range is scanned, a plot of signal intensity (or the absorbed energy) vs. frequency is generated.

Regarding the FT spectrometer, the sample is measured with a range of several frequencies at once. The decay of the signal over time is observed as a so-called "Free Induction Decay" (FID). A FT changes the signal vs. time plot into a signal vs. frequency plot. In a FT instrument, the sample is irradiated with a specified range of frequencies (sweep width) for a specified period of time (pulse width). One of the main parameters of such instruments is the so-called "relaxation time". This is needed the time for the sample to go back to its ground state before irradiating again. This allows us to make sure that the signal is reproducible.

7.2. Electrospray Ionization-Mass Spectrometry (ESI-MS)

The ESI (electrospray ionization) source belongs to the category of API (atmospheric pressure ionization) ion sources, which ionize the sample at atmospheric pressure and then transfer the ions into the mass analyser. The first work that recognized the possibility to generate gas-phase ions from macromolecules by formation of a spray at the exit of an electrically charged capillary was delivered by Dole in 1968;² however, the worldwide success of the ESI source began when Fenn (Nobel Prize in Chemistry, 2002), in 1985, he started to develop the electrospray ionization technique,

proposing it as a real interface for mass spectrometry, and then showing the possibility of obtaining multiply charged ions from biological macromolecules.³ The ESI process is nowadays among the key methods for the analysis of molecules, macromolecules and biopolymers through the determination of the molecular weight. Mass spectrometry measures the mass/charge ratio (m/z) of the ions: for instance, an ion of mass 10000 Da displaying 10 charges will be detected at m/z 1000. ESI-MS mechanism is schematized in **Figure 7.2**.

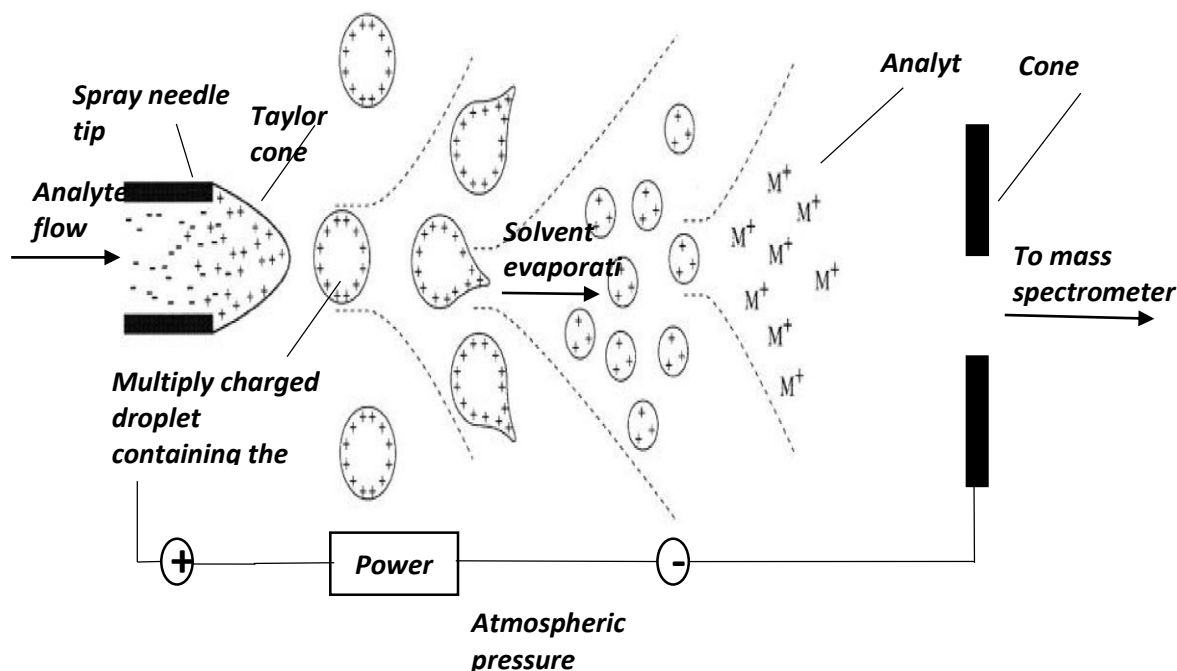


Figure 7.2. Mechanistic representation of an ESI source

It is produced by applying a strong electric field, under atmospheric pressure, to a liquid passing through a capillary tube with a weak flow. The electric field is obtained by inducing a potential difference of 3-6 kV between this capillary and the counter electrode; inducing a charge accumulation at the liquid surface located at the end of the capillary, which breaks to form highly charged droplets.

Under the pressure of the accumulating charges at the tip of the needle, the nascent drop tends to elongate till the surface tension is broken and the shape of the profile changes to the so-called “Taylor cone”, with the appearance of the spray. A gas injected coaxially at a low flow rate helps the dispersion of the spray to be limited in space. The droplets then pass through a heated capillary transfer to remove the last solvent molecules, producing the gas phase ions that will be guided to the mass

analyser. A fair range of possible mass analysers can be found in modern instruments depending on the user's needs, the most common being single and triple quadrupoles, ion traps, time-of-flight (TOF) analysers, and advanced combination of these.

With the fact that one can working at atmospheric pressure and be able to ionize liquid sample, ESI source also represents the keystone that makes it possible to interface a liquid chromatography system with mass spectrometry (LC-MS), thus allowing for introducing a separation technique at the early stage. This indeed plays a crucial role offering the possibility to analyse complex mixtures by separating the different composing species, and then to identify and to characterize each of them by recording the mass spectrum, offering excellent sensitivity and selectivity. For this thesis, the ESI-MS analysis have been performed using a Bruker Daltonics microTOF spectrometer (Bruker Daltonik GmbH, Bremen, Germany) equipped with an orthogonal electrospray (ESI) interface.

7.3. UV-Visible absorption spectroscopy (UV)

When light passes through a medium, it is absorbed and the absorbance (A_s) of a medium at the given wavelength (λ) corresponds to:

$$A_s(\lambda) = -\log(I_s/I_0) \quad (7.3)$$

where I_s is the intensity of the light that has passed through the sample, I_0 is the intensity of incident light before passing through the sample. Without the scattering and the aggregation of samples problems, the absorbance follows the Lambert-Beer law as following equation:

$$A_s(\lambda) = -\log(I_s/I_0) = \epsilon(\lambda) \cdot l \cdot c \quad (7.4)$$

where ϵ is the molar absorption coefficient (in $L \cdot mol^{-1} \cdot cm^{-1}$), l is the path length of the light through the medium (in cm), and c is the concentration (in $mol \cdot L^{-1}$). However, the Lambert-Beer law is limited to measure in low concentration samples. In high concentration samples, the linear relationship is not valid anymore. Normally the measured absorbance should be below 1.00.

Figure 7.3 presents the most used double beam setup for absorption measurements. The incident light is split in two beams and directed through each of two cuvettes, one with the sample solution and the other containing solvent as a reference. Absorption spectra shown in this thesis were recorded on the UV 3600 UV-VIS-NIR

spectrophotometer from Shimadzu.

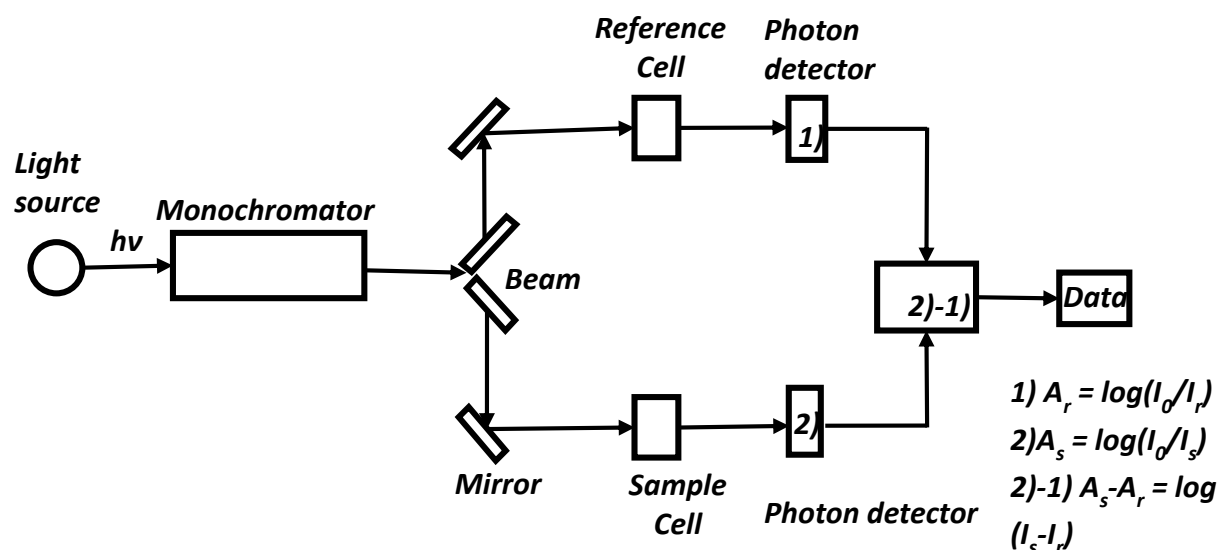


Figure 7.3. Schematic representation of UV-Vis instrument

7.4. Steady-state emission spectroscopy

An emission spectrum is the wavelength distribution of an emission measured at a single constant excitation wavelength. Conversely, an excitation spectrum is the dependence of emission intensity, measured at a single emission wavelength, upon scanning the excitation wavelength. Such spectra can be presented on either a wavelength scale or a wavenumber scale. Light of a given energy can be described in terms of its wavelength λ , frequency ν , or wavenumber. The usual units for wavelength are nanometers, and wavenumbers are given in units of cm^{-1} .

Because the spectral output of the light sources and the wavelength-dependent efficiency of the monochromators and detector tubes are not uniform, the available instruments do not yield true excitation or emission spectra. The polarization or anisotropy of the emitted light can also affect the measured fluorescence intensities because the efficiency of gratings depends on polarization. Emission spectra recorded on different instruments can be different because of the wavelength-dependent sensitivities of the instruments. Emission of the sample, collected at 90° with respect to the incident light, passes through another monochromator (2.1 nm/mm dispersion; 1200 grooves/mm) before reaching the detector. Different detectors were used

depending on the considered region of the light spectrum: for the UV-Vis range, a TBX-04 single photon-counting detector was used whereas for the NIR a Hamamatsu R2658P photomultiplier was used. The excitation spectra are corrected from source intensity (lamp and excitation grating) and for detector spectral response and emission grating by standard correction curves. Optical Filters are used, to remove unwanted wavelengths in the excitation beam, or to remove scattered light from the emission channel. In this thesis, steady-state emission spectra were recorded on a HORIBA Jobin-Yvon IBH FL-322 Fluorolog 3 spectrometer equipped with a 450 W xenon arc lamp as a source of exciting light which passes through a monochromator (2.1 nm/mm dispersion; 1200 grooves/mm) and is directed to a reference detector and to the sample. The schematic representation of such instrument is shown in **Figure 7.4**

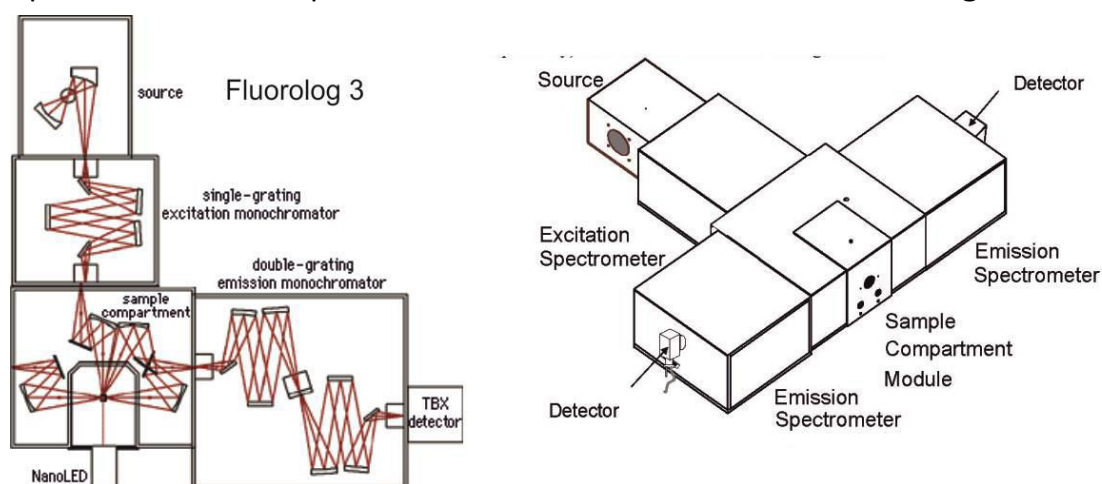


Figure 7.4. Schematic representation of the fluorescence spectrophotometer Fluorolog 3 model FL3-12 from Horiba Scientific (source: www.horiba.com)

7.5. Absolute photoluminescence quantum yield

Integrating sphere method has been more and more used for measuring optical properties of samples. A schematic representation of the principle of the integrating sphere is shown in **Figure 7.5**.

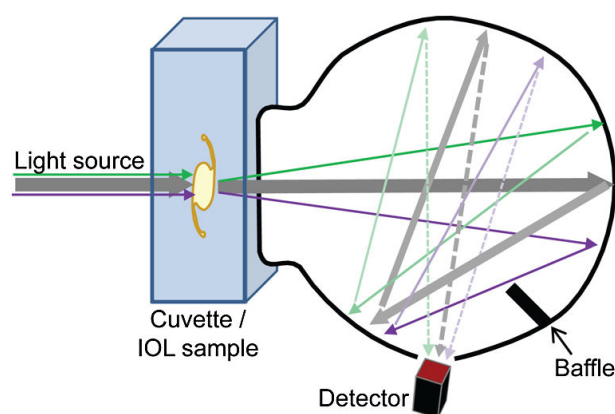


Figure 7.5. Schematic representation of Integrating sphere setup

The light coming from an external source is passing through a slit having a known diameter and reflected for a succession of times on the surface of the integrating sphere. For studies in the visible domain, in order to get a maximum reflectance, the inner part of the sphere is white, mostly made by barium sulfate (BaSO_4). After a certain time, the light hits the detector, giving the absolute quantum yield.

The benefit of this approach is the lack of sensitivity to scattering and the geometry of the sample. In this thesis, all the quantum yields were performed at a fixed range of excitation wavelengths by using a Hamamatsu Photonics absolute PLQY measurements system (C11347-11) equipped with L9700-01 CW Xenon light source (150 W), monochromator, integrating sphere, and a photonics multi-channel analyzer. (Hamamatsu Photonics Ltd., Shizuoka, Japan)

7.6. Time-resolved emission spectroscopy

Time-resolved experiments, were carried out by time-correlated single-photon counting (TCSPC). The schematic diagram of the setup is shown in Figure 7.6. The experiment starts with the excitation pulse (either a flash lamp or a laser) which excites the samples and sends a signal to the electronics. This signal is passed through a constant function discriminator (CFD), which accurately measures the arrival time of the pulse.

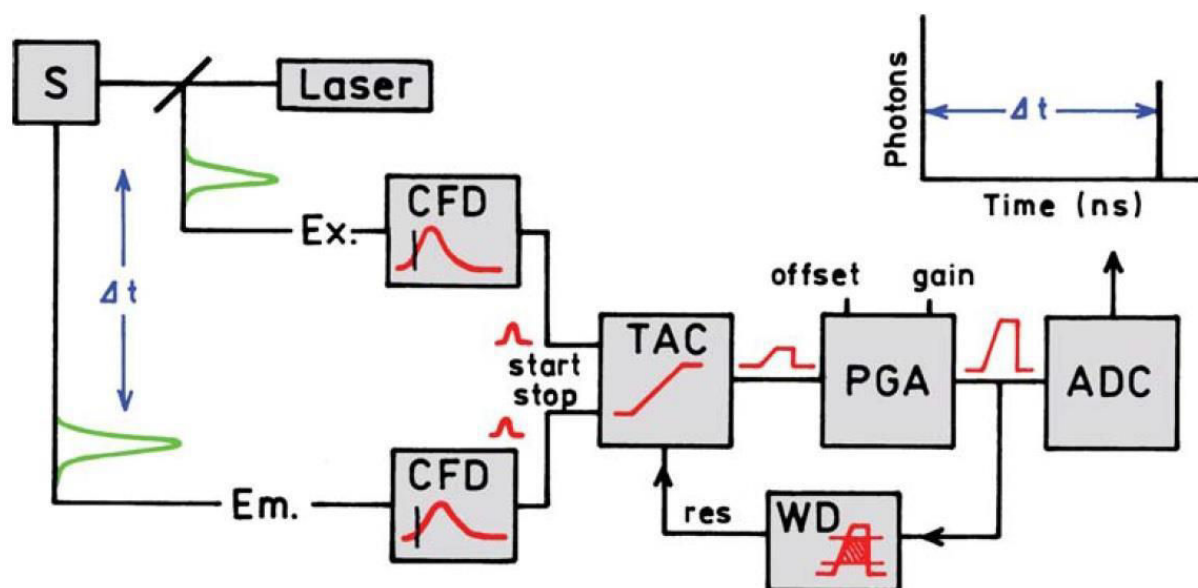


Figure 7.6. Schematic representation for TCSPC (source: Joseph R. Lakowicz, *Principles of Fluorescence Spectroscopy*, Third Edition, p. 104)

The signal (START) is passed to a time-to-amplitude converter (TAC), which starts the charging of the capacitor by generating a voltage ramp. The voltage increases linearly with time on the nanosecond timescale. A second channel detects the pulse from the single detected photon (STOP). The arrival time of the signal is also accurately determined using a CFD, which sends a signal to stop the voltage ramp. TAC now contains a voltage proportional to the time delay and is stored in a histogram in which the x-axis in the histogram is the time difference between START and STOP signal and the y-axis is the number of photons detected for this time difference. As needed the voltage is amplified by a programmable gain amplifier (PGA) and converted to a numerical value by the analog-to-digital converter (ADC). To minimize false readings, the signal is restricted to given range of voltages. If the signal is not within this range the event is suppressed by a window discriminator (WD). The voltage is converted to a digital value that is stored as a single event with the measured time delay. By repetitive measurements a statistical time distribution of emitted photons is obtained. Time-resolved measurements up to $\sim 10\mu\text{s}$ were performed using the TCSPC option (PicoHarp) of a FluoTime 300 “EasyTau” apparatus (PicoQuant) equipped with subnanosecond LDH sources (375, 405, 440, 510 and 640 nm, with 50–100 ps pulse-width) powered by a PicoQuant PDL 820 variable (0.2–80 MHz) pulsed power supply.

7.7. X-ray photoelectron spectroscopy (XPS)

X-ray photoelectron spectroscopy is a powerful surface analytical technique due to the extreme sensitivity and ability to distinguish the signal from the vast majority of atoms present in the sample.

The basic principle of XPS has been discovered in 1887 by Heinrich Rudolf Hertz and was elucidated in 1905 by Albert Einstein (Nobel Prize in Physics 1921). Two years later, in 1907, P.D. Innes was able to record broad recording the first XPS spectrum.

Several decades later, Kai Siegbahn (Nobel Prize laureate in physics in 1981)) developed several significant improvements in the equipment, and in 1956 recorded the first high-energy-resolution XPS spectrum of cleaved sodium chloride.⁴ The potential of XPS has been widely investigated and in 1967, Siegbahn published a comprehensive study of XPS, bringing instant recognition of the utility of XPS. In 1969, at Hewlett-Packard produced the first commercial monochromatic XPS.

Figure 7.7 shows the XPS principle and a schematic representation of an XPS instrument, when an incident X-ray (200~2000eV) is applied under vacuum, a 1s electron is ejected from the atom. The photoelectron is then collected by the electron multiplier detector and analysed by the electron spectrometer to acquire the kinetic energy (E_{ph}).

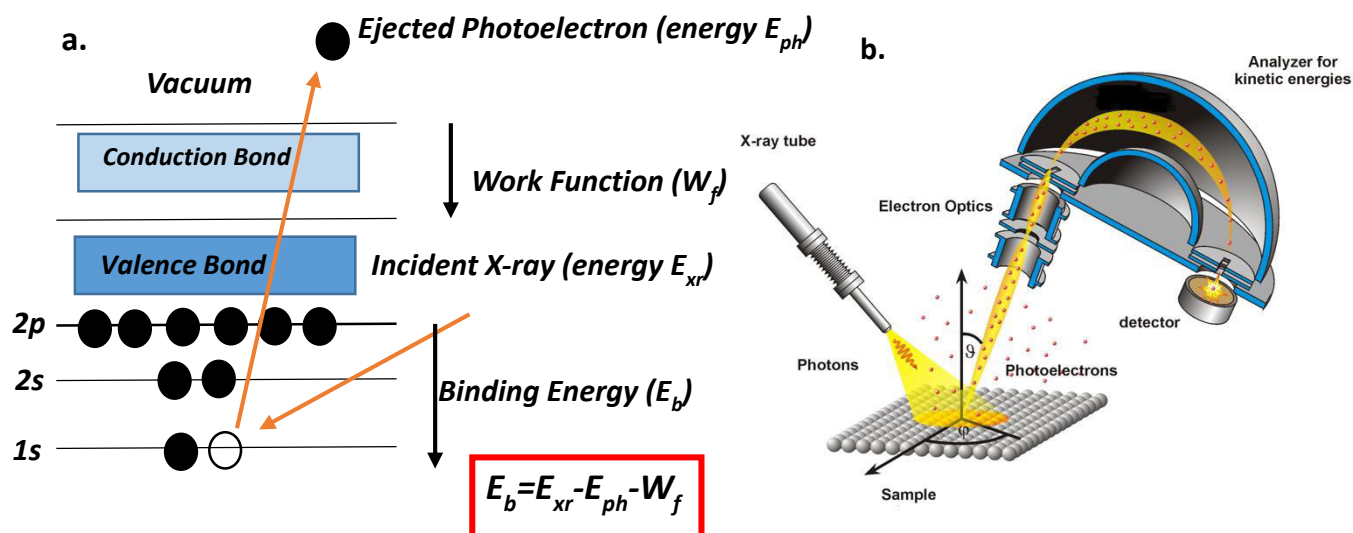


Figure 7.7. XPS principle(a.) and schematic representation of an XPS instrument (b.)

The binding energy of the electron (EB) can identify the electron both from its parent element and the atomic energy level. It can be described as below:

$$Eb = E_{xr} - E_{ph} - W_f \quad (7.5)$$

where E_{xr} is the X-Ray energy, E_{ph} is the kinetic energy of the photoelectron and W_f the spectrometer work function. The binding energy can be therefore determined from those three parameters which are either known constants, or measurable.

For the works of this thesis, the XPS measurements were done by a Thermo Scientific K-Alpha X-ray Photoelectron Spectrometer using a monochromatic $AlK\alpha$ radiation ($h\nu = 1486.6$ eV; $\lambda = 8.340113\text{\AA}$). Survey measurements were performed with a 200 eV analyzer pass energy and a 1 eV energy step size to calculate the atomic concentrations. Element scans were performed with a 50 eV analyzer pass energy and a 0.1 eV energy step size to obtain the chemical state information. All the obtained binding energies were referenced from carbon 1s peak, coming from the residual CO_2 , at 284.80 eV.

7.8. Scanning electron microscopy (SEM)

The SEM is a type of microscope that uses electrons to create high resolved images of the sample. Since their development in the early 1950's, scanning electron microscopes have developed new areas of study in the medical and physical science communities. The SEM uses a focused beam of high-energy electrons which is placed at the top of the electron column and accelerated thanks to an anode (voltage: 1 to 50 kV) before passing by a system of lenses that causes a repulsive electric field and a condensation of the electrons, focusing them on the following aperture. The secondary electrons reach then the surface of the sample, prior metallized (Ag, Au, Pt...). After passing through the condenser lens, the beam is divergent and must be refocused on the sample. This is done by means of the focusing lens, which are located just above the sample.

Two types of electron sources are generally used in SEM-instruments: Thermoionic-Sources and Field-Emission-Sources. Thermoionic-Sources are based on a thin conductive wire (usually tungsten), which is heated to temperatures where the energy of the weakest bounded electrons exceeds the work function of the material, thus allowing for the electron emission. Field-Emission Sources use high electric fields between a cathode and an anode, in a way that if the applied electric field is big enough, the work function of the cathode dramatically decreases and electron emission is possible even at room temperature. The signals that come from electron-

sample interactions give especially information about the external morphology of the sample and its chemical composition (EDX module). Secondary electrons are then torn off and deviated towards the so-called “scintillation counter”, transformed into impulsions by a photomultiplier and the image is seen on a screen. Due to the very low energy, only secondary electrons near the surface can be detach from the sample and produce the output signal. The volume in which secondary electrons are produced is relatively small, which leads to a high axial resolution (a few nm). The final image is thus a map of the secondary electron density depending on the properties of the sample. The images are collected over a selected area of the surface of the specimen, and a 2-dimensional image is generated that displays spatial variations in the sample properties with respect to the interaction with the electron beam. As the number of detected electrons at each spot of the sample is a function of h the beam-surface, the picture is in relief. The angle Areas ranging from approximately 1 cm to few microns in width can be imaged in a scanning mode using conventional SEM techniques, having magnification up to more than 500000x and resolution of few nanometers. When speaking about the fundamental principles of SEM, accelerated electrons in an SEM carry significant amounts of kinetic energy, and this energy is dissipated as a variety of signals produced by electron-sample interactions when the incident electrons are decelerated in the solid sample.

Schematic draw of SEM setup is shown in **Figure 7.8**.

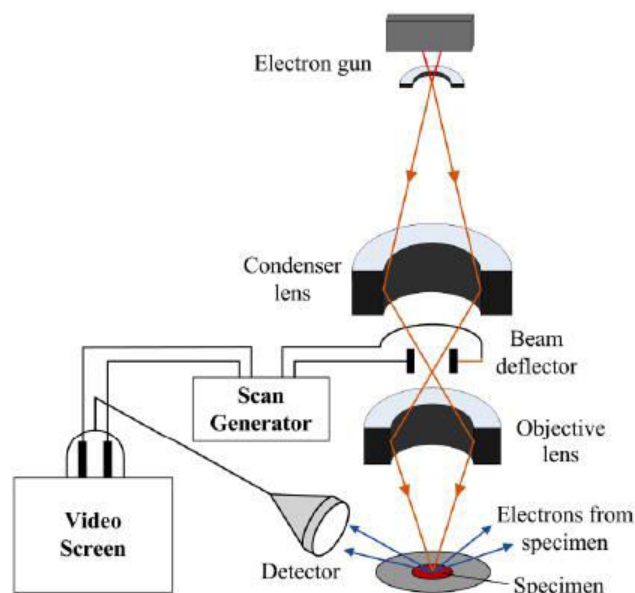


Figure 7.8. Schematic representation of SEM setup

In this thesis, SEM experiments have been performed using a FEI Quanta FEG 250 instrument.

7.9 Transmission electron microscopy (TEM)

This microscope technique is used to analyze very small objects, down to the angstrom scale. An electron beam that is produced by an anode under vacuum and passes at a very high speed through the sample and to the cathode. This beam is condensed by electromagnetic lenses, and electrons are stopped or not by the structures they collide with. The lenses then widen the obtained picture and projected on a fluorescent screen.

The vacuum is maintained during the entire experiment to avoid electrons dispersion. Therefore, a cooling system is also used, typically with liquid nitrogen. Nowadays, TEM microscopes are equipped by a camera, allowing a better data acquisition.

TEM offers the advantage of pushing the limit of resolution down to 50 pm, with possible

magnification in the order of 10^7 times, making it possible to work at the atomic scale.

A schematically view of the electron path in a TEM instrument is shown in **Figure 7.9**.

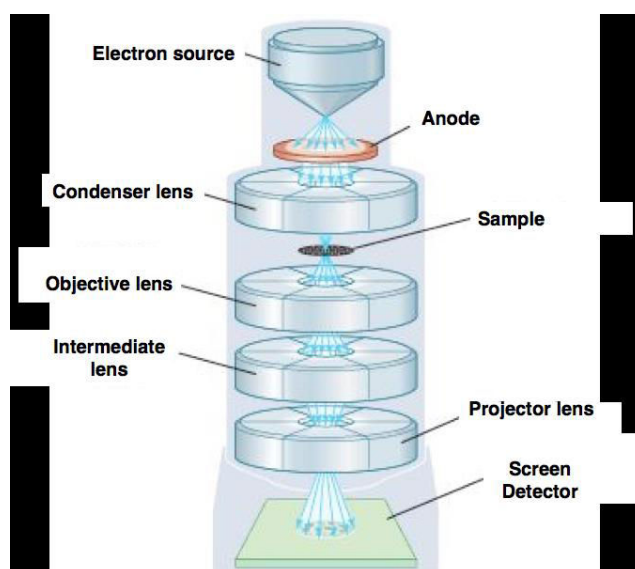


Figure 7.9 Schematic draw showing the components of a TEM instrument.

Once the electron beam passes through the sample, it reaches the objective lens, which generates the first intermediate image of the sample, the quality of which determines the resolution of the final image. The intermediate image is an inverted initial one, which then is subsequently magnified by the intermediate lens, and

produces a second intermediate image. The latter is collected by the projector lens, which forms the final image onto a fluorescent screen or a recording device.

7.10. Scanning transmission electron microscope (STEM)

Excepting TEM, scanning transmission electron microscope (STEM) also gains a lot of attention in examining the samples in atomic scale. As a result, the STEM technique has image resolution up to sub-Å range, providing information on the element composition and electronic structure. **Figure 7.10** is a schematic representation of STEM setup.⁵

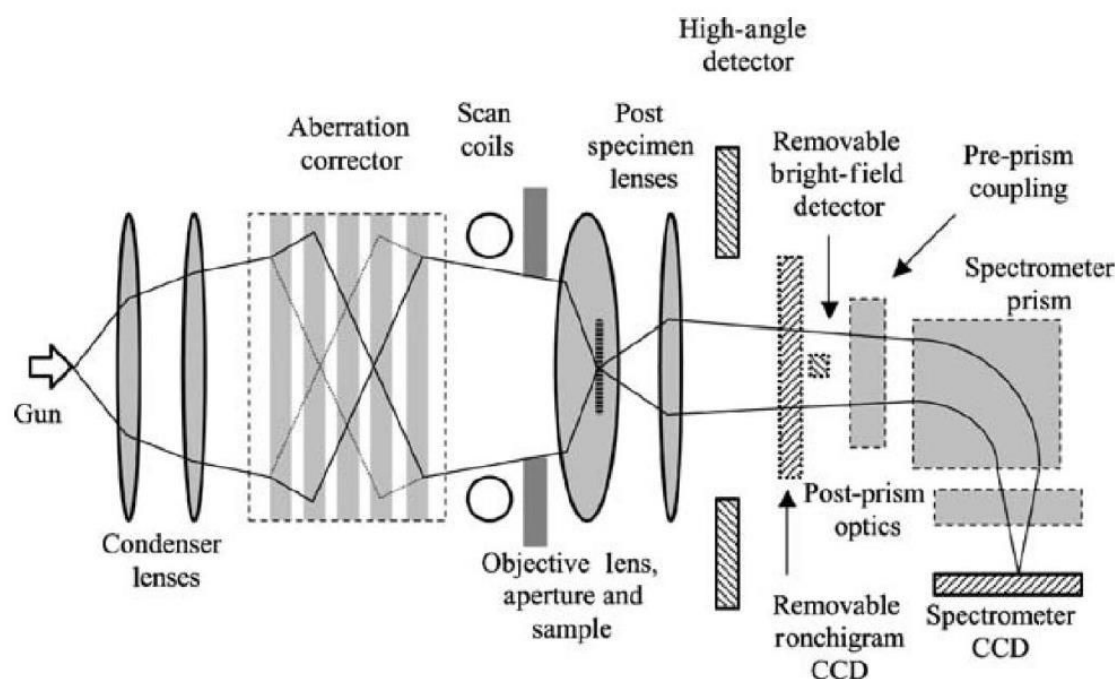


Figure 7.10 Schematic representation of STEM setup.

The difference between STEM and TEM is that for TEM, a large area of sample is illuminated, the transmitted electron beam is magnified by the lens system after the sample and collected the whole image at once. However, for in STEM, the electron beam condenses to a tiny probe in an order of 1\AA before reaching to the sample and scan the sample in the specific area. Then the electrons are collected to form the image as function of position. Also, STEM has multiple detectors can be used simultaneously, bright field (BF) detector collects the transmitted electron beam and performs the image as in TEM; annual dark field (ADF) detector, surrounds the transmitted beam,

collects the scattered electrons in different angles. To have a high contrast image, the high-angle annular dark field (HAADF) detector can be used. The reason is that the high Z (atomic number) atoms scatter the electron to high angles stronger than lighter atoms, resulting the contrast in the image is proportional to Z^2 .

7.11. Confocal microscope

Confocal microscopy offers many advantages over conventional optical epifluorescence microscopy, including the ability to control depth of field, elimination or reduction of background information away from the focal plane, and the capability to collect serial optical sections from thick sample. The basic key to the confocal strategy is the use of spatial filtering techniques to eliminate out-of-focus light. The confocal principle in fluorescence laser scanning microscopy is schematically shown in **Figure 7.11**. Coherent light emitted by the laser system (excitation source) passes through an excitation pinhole aperture that is placed in a conjugate plane (confocal) with a scanning point on the specimen and a second pinhole aperture located in front of the detector. When the laser is reflected by a dichromatic mirror and scanned across the specimen in a defined focal plane through the objective, secondary fluorescence emitted from points on the sample (in the same focal plane) pass back through the dichromatic mirror and are focused as a confocal point at the detector pinhole aperture.

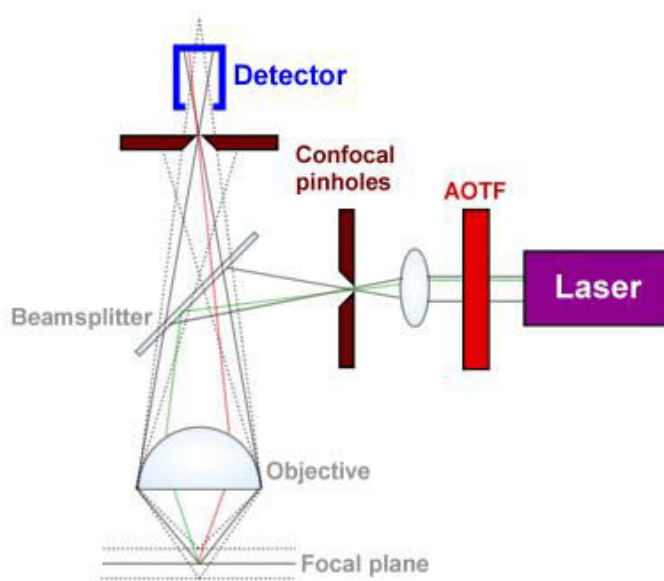


Figure 7.11. Schematic representation of confocal microscopy principle

The amount of fluorescence emission that occurs at points above and below the objective focal plane is not confocal with the pinhole. Since only a small fraction of the out-of-focus fluorescence emission is delivered through the pinhole aperture, most of this extraneous light is not detected by the photomultiplier and does not contribute to the resulting image. The dichromatic mirror, barrier filter, and excitation filter perform similar functions to the analog components in an epifluorescence microscope. Refocusing the objective in a confocal microscope shifts the excitation and emission points on a specimen to a new plane that becomes confocal with the pinhole apertures of the light source and detector. In traditional fluorescence microscopy, the entire sample is exposed to intense illumination from the source lamp, and the resulting image of secondary fluorescence emission is generally projected onto the surface of an electronic array detector. In contrast, the mechanism of image formation in a confocal microscope is essentially different. The confocal fluorescence microscope consists of

multiple laser excitation sources, a scan head with optical and electronic components, electronic detectors (usually photomultipliers), and a computer for acquisition, processing, analysis, and display of images. These properties actually allow the user to record 3D-images using different combinations of excitation and emission wavelengths as long as the emission spectra of the diverse species do not completely overlap, which is a key tool when analyzing bio-samples that require the use of multiple labels. In this thesis, Confocal imaging experiments were performed by a Zeiss 710 confocal microscope system with a 63x magnification objective lens (Zeiss GmbH). The samples were prepared as grains on a glass colourless plate and excited by continuous wave (cw) laser at 375 nm. In addition, the lambda-mode acquisition technique was performed to observe the emission spectra of the different materials. False colours were adjusted for clarity reasons.

7.12. Dynamic light scattering (DLS)

Dynamic light scattering (DLS) is a widely spread technique used to determine the size of particles in dispersion. Particles suspended in liquids are in Brownian motion due to random collisions with solvent molecules. This motion causes the particles to diffuse through the medium. The diffusion coefficient, D , is inversely proportional to the particle size according to the Stokes-Einstein equation:

$$D = \frac{kT}{3\pi\eta d} \quad (7.6)$$

In which D is the diffusion coefficient ($\text{m}^2.\text{s}^{-1}$), k is the Boltzmann's constant ($1.38064852 \cdot 10^{-23} \text{ J.K}^{-1}$), T stands for the temperature of the medium (K), η is the viscosity of the medium ($\text{kg.s}^{-1}.\text{m}^{-1}$) and d the hydrodynamic diameter (m).

This equation shows that, for large particles, D will be relatively small, and, thus, the particles will move slowly, while for smaller particles, D will be larger and the particles will move more rapidly. Therefore, by observing the motion and determining the diffusion coefficient of particles in liquid media, it is possible to determine their size. When a laser light is focused onto the particles, the resulted scattered light comes from a collection of scattering elements, so that the observed intensity of the scattered light at any instant is a result of the interference of light scattered by each element. Hence, it will depend on the relative positions of the elements. If the particles are in motion, the relative positions of particles will change in time; and thus, fluctuations in time of the scattered light intensity will be observed. Because particles in Brownian motion move relatively randomly, the scattered intensity fluctuations are random. The intensity fluctuates faster for smaller particles and slower for bigger particles. The fluctuations of the scattered light are analyzed using the autocorrelation function (ACF).

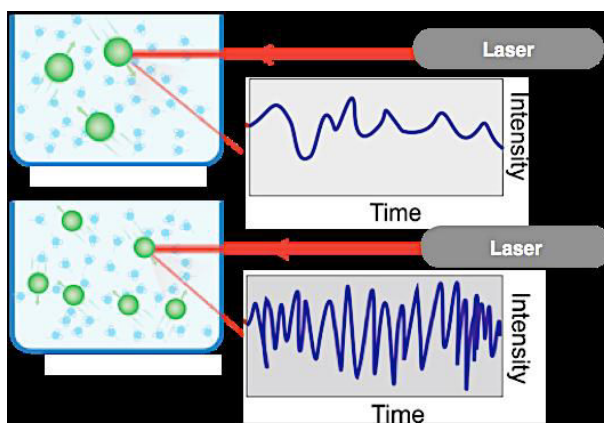


Figure 7.12. Representation of the random intensity fluctuations of the scattered laser obtained from a dispersion of bigger particles (top) and smaller particles (bottom).

The ACF is a function that decays as a function of delay time. **Figure 7.13** shows that for small particles with rapid motion and rapid intensity fluctuations, the autocorrelation function is a rapidly decaying exponential function with a large decay

constant, while for large particles the exponential decays more slowly with a smaller decay constant.

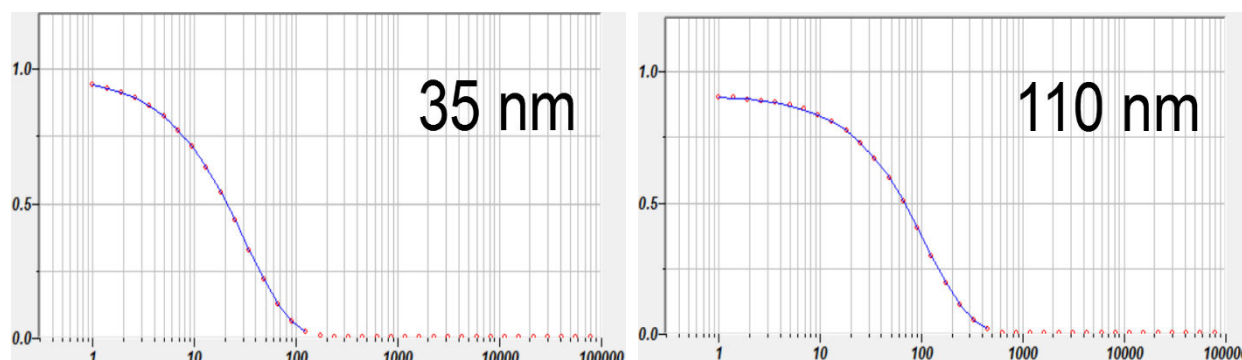


Figure 7.13 ACF function's decay for a 35 nm particle (left) and a 110 nm particle (right)

The ACF is then used to calculate the diffusion coefficient and therefore the size of the particles. The particle size is finally given in the form of a statistical distribution sorted by scattering intensity, volume or number of particles. The directly measured (and thus more reliable) parameter is always the intensity distribution, while the volume and the number distributions are subsequently calculated via software from the intensity distribution by using Mie theory. The intensity distribution is thus the general and most common way used to show DLS data.

In this thesis, DLS experiments were done with a Delsa Nano C Particle Analyzer (Beckman Coulter, Brea, CA, USA).

7.13. Thermogravimetric analysis (TGA)

Thermogravimetric analysis measures mass changes in a material as a function of temperature (or time) under a controlled atmosphere. Its principle uses include measurement of a material's thermal stability, filler content in polymers, moisture and solvent content, and the percent composition of components in a compound, particularly for hybrid organic inorganic materials. A TGA analysis is performed by gradually raising the temperature of a sample in a furnace as its weight is measured on an analytical scale that remains outside of the furnace (**Figure 7.14**). In TGA, mass loss is observed if a thermal event involves loss of a volatile component. Chemical reactions, such as combustion, involve mass losses, whereas physical changes, such as melting, do not. The weight of the sample is plotted against temperature or time to illustrate thermal transitions in the material – such as loss of solvent and plasticizers in

polymers, water of hydration in inorganic materials, and, finally, decomposition of the material.

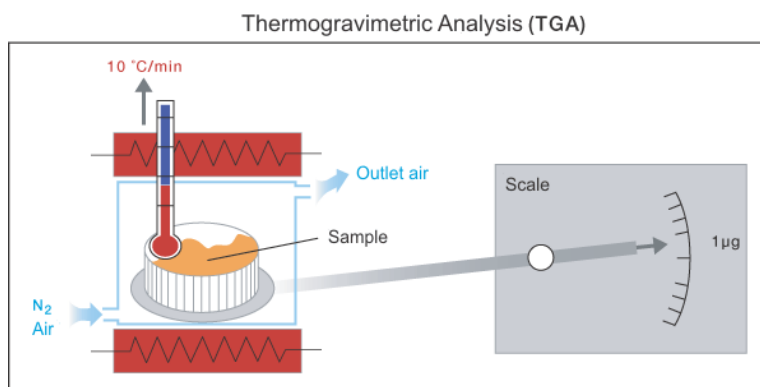


Figure 7.14. Schematic representation of TGA analysis

7.14. References

1. Rabi, I. I.; Zacharias, J. R.; Millman, S.; Kusch, P., *Phys. Rev.* **1938**, 53 (4), 318.
2. Dole, M.; Mack, L. L.; Hines, R. L.; Mobley, R. C.; Ferguson, L. D.; Alice, M. B., *The Journal of Chemical Physics* **1968**, 49 (5), 2240.
3. Whitehouse, C. M.; Dreyer, R. N.; Yamashita, M.; Fenn, J. B., *Anal. Chem.* **1985**, 57 (3), 675.
4. Siegbahn, K.; Edvarson, K., *Nucl. Phys.* **1956**, 1 (8), 137.
5. Varela, M.; Lupini, A. R.; Benthem, K. v.; Borisevich, A. Y.; Chisholm, M. F.; Shibata, N.; Abe, E.; Pennycook, S. J., *Annual Review of Materials Research* **2005**, 35 (1), 539.

Acknowledgement

To end of this thesis, I am more convinced that research is not a lonely work. Indeed, during my Ph.D. time, which is quite long, but paradoxically passed so quickly, I had the opportunity to meet so many people coming from all parts of the world. All these people extended my general and scientific knowledge and opened my mind more than it was; and without their daily help and their good mood, I would not have been able to perform such Ph.D work.

First I would like to thank Prof. Luisa De Cola for having given me the opportunity to work in her group. I have been very happy to have the honour to learn from you, to have almost all the instruments that I needed to achieve my work, to have the chance to attend to trainings, schools, conferences... Thank you.

Thanks also to the financial support from SACS project, and to everybody related to this consortium.

Eko, thank you for all your help and your kindness, for always being very patient with me, for all the interesting discussion, for giving me your time and your broad knowledge, for making me feeling comfortable in this group, for making me trusting myself... I learnt more from you than from anybody else, and thank you for this.

Loïc, je te dois beaucoup, plus que tu ne le penses : les explications scientifiques, avec cette capacité à transformer un truc qui paraît très compliqué en truc super simple. Les délires stupides, les voyages partout en Europe (je t'ai lâché pour le meeting à Marburg, ne m'en veux pas ça avait pas l'air chouette...), ta grande capacité à (dé)motiver aussi ... Plus sérieusement, j'ai beaucoup appris en ta présence. Un grand Cimer !!! et « Wesh Alooors !!! »

Ahora, mil gracias a mis amigas hispanohablantes. Las palabras no son suficiente fuertes para describir a que punto quiero agradecerlos. Amparo, ma chouchou pote, como te digo siempre, tu ayuda fue muy preciosa, desde el primero día hasta el ultimo. He aprendido mucho de ti, el español, la química, como hacer un poster, una presentación, y también de tu felicidad de vivir. Merci!

Ingrid, fuiste (y eres) una colega (una amiga) muy preciosa. Has hecho tan para mi, y te debo mucho. Nunca olvidaré los momentos contigo, ni la felicidad que he tenido cuando he visto Oli . Gracias por todo, y sobretodo, quédate así!

Leti, gracias por mantener tu sonrisa que me da animo y fuerza, incluso durante los mementos difíciles. Merci mon amie!

My dear “Asian crew”: thanks for the time spending together, in the lab, the 6th floor or outside... Also for the several travels we had together as well!

Chien-Wei, thank you for all the advice, the knowledge and the tricks you gave me during these years. It has been a great pleasure to share the lab and the office with you.

Dedy, thanks for always being available for me, in the the lab (explanations, trainings...) or outside (Saiko time, thé à la menthe, football... I have to admit you are a good striker, even though a bit lazy...). Even though I still did not understand your laser story, I believe it's pretty cool! I am trying to write something nice about Real Madrid, but I just can't, sorry...

Pengkun, thanks for the precious help in the lab, for the nice discussion sharing together, for the several diners you cooked for me, for the basketball games... but more general... Thanks for being yourself! I think this is just impossible to forget you!

Hiroki, thank you very much for all your kindness. I really appreciated it!

Veronika, you got the award of “kindest person I have ever met in my life” thank you for being so nice and so helpful with me. I will never forget.

Claire, je ne saurais pas comment te remercier... Tous les services, les aides de dernière minute, toutes les fois où tu as dû nous couvrir... Merci à Sandro aussi, car c'est le meilleur!

Ines, thank you for all your patience towards me (and us in general), for being so kind, so helpful and so available. Thanks to Maurice as well, always so nice and so polite with people.

Un grand merci à mes amies italiennes, du fond du cœur : mes étudiantes de français, Federica et Nadia; j'espère avoir été un bon enseignant... Fede, je tiens à te remercier pour les discussions sympas, pour ton honnêteté, ta gentillesse, et ton aide. Tu mérites plein de réussite. Nadia, j'ai passé deux années vraiment super avec toi au labo, tu es une personne très attachante ! Je garde beaucoup de bons souvenirs. Merci à vous.

Bea, merci d'avoir apporté ton sourire, ta bonne humeur, ta gentillesse dans le labo. J'ai beaucoup apprécié les moments passés avec toi.

Sere, la personne la plus cool du labo !! Tu sais déjà tout le bien que je pense de toi, tu sais que tu m'as donné beaucoup de sourire quand je n'étais pas bien, tu es vraiment

une personne chère à mes yeux. Je ne te remercierai jamais assez pour tout ce que tu as fait pour moi.

Etienne, merci d'avoir été toujours disponible, et merci pour les nombreux matchs de football ensemble.

Mike, merci pour toujours avoir été super sympa avec moi, pour les parties de foot (où je me débrouille un peu mieux que toi), pour les parties de basket (où la par contre je suis archi nul), pour les soirées SIG (et la poisse qui va avec...) Merci aussi pour la "carte magique"...

Remi, merci pour les nombreuses discussions, les « night sessions » au labo, pour ta bonne humeur, pour les matchs de ligue des champions, pour ce voyage super sympa à tes côtés.

Stephan, mon pote, merci pour toute l'aide, les discussions (scientifiques ou non), les idées, les cours d'allemand, mais aussi les super matchs de football, les soirées soupes chez toi... Merci à Elisabeth et à Tristan pour toujours m'accueillir avec le sourire.

Alberto, tío, gracias para todo lo que hiciste para mi, el español que me has enseñado, el buen humor... Eres un crack! Merci mon pote.

My two best English speaking friends: Many thanks to both of you, and one more time, I apologize for my English which is not always correct, as well as my awful "French accent"

Becky, Thanks to you for always being so kind with me, in the lab but also outside. It has been always a pleasure to discuss with you, to have lunch together.

John, mon frère, thanks for being always available for me, for the nice time, the football debates (Leicester!!!), the scientific discussion. I still want to get the copyrights for the "lumisicles".

Simone, thank you for all the advice you gave me, all your kindness, your several explanations, your help. I learnt a lot from you!

Christelle, merci pour ta gentillesse et ta joie de vivre. C'était vraiment sympa de travailler à tes côtés, même si ce n'était pas pour une longue période.

Alessandro A. and Matteo M., thanks for introducing me to the platinum world, for all your explanations related to this and for sharing your knowledge with me.

I would like to also thank the two internship students that I had the chance to work with: Mateusz and Hélène: Thank you to both of you, I could not have expected better student than you!

Thanks to all my other colleagues, everybody who passed by the lab during these years; the list is very long: Henning, Deane, Laura, Valentin, Nina, René, Damiano, Angélique,

Marine, Vito, Tommaso, Matteo B., Valentina, Giuseppe, Ariana, Maurizio, Frank, Luca, Francesca, Christof, Yevhen, Alessandra, Camilla, Ligia...

It is also important for me to thank my bachelor's and master's colleagues, as well as my internships supervisors those people with whom everything started: Yusuf, Bilgehan, Sami, Dimby, Mustapha, Anaëlle, Hassiba, Nico, Amara, Patrick, Thomas, Lucas, Elliot, Elisa, Cécile, Solène, Pit, Alain, Rachid, Jessie, Jean-Pierre, Elena, Eric, and the list goes on...

J'ai également eu la chance, durant ma thèse, d'effectuer quelques missions d'enseignement qui m'ont été très enrichissantes. A ce sujet, je tiens à remercier plusieurs personnes : Pierre, Valérie, Christophe, Antoinette, Jean-Marc, Michel, Frédéric, Alain, et j'en passe... Particulièrement, je remercie Aurélia: ta gentillesse à mon égard, ta détermination et ton envie de réussir qui m'ont donné de la force, ta bonne humeur... tu m'as aidé bien plus que tu ne le penses, et je te souhaite le meilleur. Du fond du coeur, merci.

I also would like to thank everyone in ISIS who was involved in, one way or another, in making this Ph.D. as successful as it is: Muriel, Fabienne, Fabien, Jean-Louis, Philippe, Thierry, Ania, Nathalie, Jordi, Emilie, Amélie, Raghavan, Aika, Jorge, Vincent, Alessandro S., Thomas "jefe", Akihiro, Hadi, Oussama, Thibault, Eloïse, Mohamed, Joel, Joseph, Elena, Vuk, Ed, Jeremy, Regis, Paco, Paul, Seb, and the list goes on...

Bien entendu, merci à ma famille, pour tout le soutien sans faille apporté durant cette période pas toujours facile : Mes parents Mohamed et Fatna, ainsi que mes frères Yacine, Yahia, Omar, Sohaïb, et ma sœur, la meilleure sœur, Fatima.

Enfin, Eda, je te remercie pour tout ce que tu as fait pour moi, l'aide et le soutien sans arrêt dont j'ai pu bénéficier grâce à ta gentillesse, ta générosité, ta patience ... Je n'ai pas toujours été la personne la plus facile à vivre durant cette période, mais si j'ai pu réaliser tout ce travail, c'est aussi grâce à toi. Merci Canim.

Last but not least, un tcha et un merci infini à Ricardo. Pendant ces 9 années passées à se voir presque tous les jours, des amphis jusqu'à maintenant, en passant par les révisions intenses (et moins intenses) à la bibliothèque, les nombreuses aides, les galères, les vacances, ton humour pourri, les foots, les baskets, les sorties, les bouffes, les promenades en villes, les services rendus... Je pourrais écrire une seconde thèse sur toi. Merci pour tout le meilleur ami !